Silicon Anodes in Lithium-Ion Batteries

Ian P. E. Roper
St Anne's College
University of Oxford

A thesis submitted for the degree of
Doctor of Philosophy

Trinity 2019

Acknowledgements

Firstly, I would like to thank both of my supervisors: Professors S. Jon Chapman and Colin Please. Thank you, Jon for having the patience to sit through many gritty derivations and having the patience and creativity to explain concepts to me in half a dozen different ways until I understand. Colin, thank you for always making time in your busy schedule, your many insightful nuggets of wisdom and helping me through difficult times in the project.

Thank you also to my industrial supervisor, Bill Macklin, firstly for setting up the project in the first place, but also for the many discussions on how to bring the mathematics back to the batteries.

I would especially like to thank my girlfriend, Tahnee, who has been by my side throughout this endeavour. Forever reminding me of the days when things went well on those days which they did not, and convincing me I could finish this if I put my mind to it.

Thank you to my parents for always supporting me in whatever I do, and also to my brother Alan, and my sister Kim, for encouraging me throughout.

I would like to thank the fantastic friends within the Mathematical Institute that I have met over the last four years. Chatting over tea, cake and doughnuts has always been enjoyable and thought-provoking. Special thanks go to my fellow members of Cohort 2. From the hellish first year of 2am Sunday night report-writing, to fantastic holidays in Romanian mountains, German beer festivals and French chalets; it has been a wonderful four years with you all.

Lastly, thank you to everyone who has been a part of Oxford Ultimate and Oxford University Ultimate throughout the last four years. You were always around to distract me with a round piece of plastic.

Abstract

In this thesis we consider the chemo-mechanical response of a multi-material lithium-ion battery anode nano-particle at equilibrium. The stresses are induced by lithium being intercalated into the nano-particle, causing the anode materials to expand. The presence of several anode materials expanding to different extents induces stress even at equilibrium. The model we primarily study is a linear elasticity model derived under the assumption that the stress-free expansion of each anode material is small. We couple the mechanical model to a diffusion-based model governing the transport of lithium in each material through stress-assisted diffusion. At equilibrium, the chemical potential of the lithium, which depends both on the lithium concentration and the hydrostatic stress, is uniform throughout the nano-particle, governing the distribution of lithium between the materials.

Silicon is a promising anode material with a high capacity for lithium, but it expands to around 380% its original size when fully lithiated, leading to several issues during battery usage. We apply our equilibrium model to a nano-particle consisting of a silicon core and a surrounding graphite shell. The aim of using both materials is to mitigate the expansion of silicon without sacrificing too much capacity. We analyse the lithium concentration, displacement and stresses within each material, and use the results to optimise the volume of the silicon core based on several measures of success. Void spaces and porous silicon are introduced into the nano-particle design, using the method of multiple scales, to improve on the simple core–shell design, to moderate success. We extend the model to a geometrically nonlinear elastic model, and analyse this after finding that solutions cease to exist above a certain state of charge. Finally, we incorporate yielding and fracture of both materials into the linear model, based on perfect plasticity.

Contents

Nomenclature

Accents

$\hat{}$	Microscale (Chapter 3)

Domains

Ω	Domain
Γ	Boundary
$\mathbf{n}$	Outwards-facing normal

Subscripts

a	General anode material
b	General anode material distinct from a
Si	Silicon
C	Graphite
ϕ	Porous silicon
rr	Radial direction
$\theta\theta$	Hoop direction
$i, j, k, l, m, n, p, r, s$	Suffix notation

Superscripts

*	Dimensional quanitity
max	Maximum
e	Elastic
SF	Stress-free
p	Pulverised/plastic
$+$	Positively charged/positive side of boundary
$-$	Negatively charged/negative side of boundary
(0)	Leading order
(1)	First order
$(0,1)$	Leading order in ϵ but first order in S^d_{Si}

Variables

$\boldsymbol{u}$	Displacement
c	Lithium concentration
$\boldsymbol{\sigma}$	Cauchy stress tensor

μ	Chemical potential
r	Radius
u	Radial displacement
c_0	State of charge (SOC)
$\boldsymbol{\sigma}^0$	1st Piola–Kirchhoff stress tensor
s	Position of pulverised/plastic front

Dimensionless Quantities

γ	Ratio of expansion parameters (2.13)
S^d	Stress-assisted diffusion parameter (2.40)
$\mathbb{C}$	Ratio of general anisotropic stiffness tensor to shear modulus of unlithiated silicon
λ	Ratio of 1st Lamé parameter to shear modulus of unlithiated silicon
G	Ratio of shear modulus to shear modulus of unlithiated silicon
Λ	$3\lambda + 2G$
R	Outer radius of domain relative to outer radius of nano-particle
V	Volume of domain/relative expanded volume (2.82)
Q	Relative amount of lithium (2.80)
σ^Y	Yield stress

Chapter 1

Introduction

1.1 Lithium-ion Batteries

Lithium-ion batteries (LIBs) are one of the leading technologies for energy storage [59] due to the benefits of using lithium ions (Li^+) as the charge carrier. Lithium has the lowest reduction potential of any element, is the third lightest element and its positive ion, Li^+, has one of the smallest radii of any singly charged ion. All these properties make lithium ideal as a charge-carrying ion in a battery and mean that LIBs have an extremely high capacity. The capacity of a battery is a measure of how much energy it can deliver from a single charge, which is directly related to the amount of lithium which can be stored. Typically, this is measured per unit volume (volumetric capacity) or per unit mass (gravimetric capacity). A high volumetric capacity and gravimetric capacity make LIBs ideal for use in portable electronic devices such as laptops, mobile phones and electric vehicles. A growing use of LIBs is for renewable energy storage: the temperamental nature of many of the sources of renewable energy means that energy storage is essential to meet the energy demand at all times.

LIBs comprise one or more cells joined in series with each other to increase the voltage the battery produces. Each cell induces an electrical current by the following mechanism. When the cell is fully charged and at rest, lithium atoms are stored in the anode at a higher chemical potential than if they were stored in the cathode. The lithium is stored by intercalation within the crystal structure of the anode material. When an electrical circuit is connected between the cathode and the anode, the lithium atoms in the anode are oxidised at the anode-electrolyte surface to form Li^+ ions and electrons. The Li^+ ions pass through the electrolyte towards the cathode, whereas the electrons must travel through the anode towards the current collector attached to the anode. The electrons are then conducted through the current collector and around an external circuit which causes the electrical current. The electrons arrive

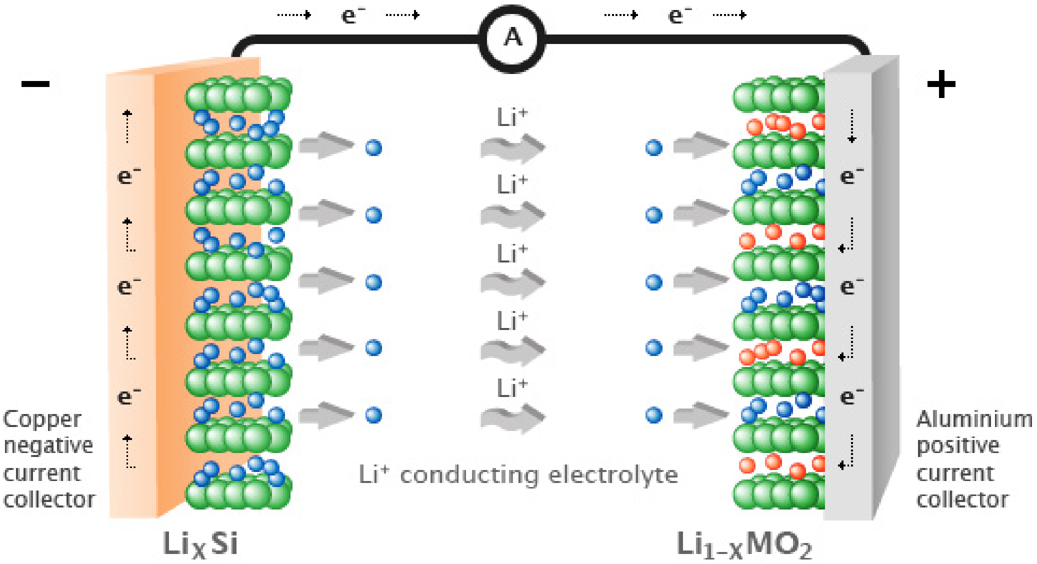

Figure 1.1: Schematic of the movement of Li^+ ions and electrons in a lithium-ion battery during operation. The anode is on the left and the cathode is on the right. Taken from [79].

at the opposite current collector, travel into the cathode and reform with Li^+ ions at the cathode-electrolyte surface to form lithium atoms, which are intercalated into the cathode. When the battery is recharged, the induced potential difference causes the lithium atoms to split again at the cathode surface and the opposite process occurs until the lithium atoms are intercalated back into the anode. The process of Li^+ and electron movement when a circuit is attached is shown in Figure 1.1.

A desirable property of LIBs, aside from having high capacity, is their ability to deliver high power. Power is determined by how quickly the LIB is able to deliver the stored energy to the circuit, which is related to how quickly the lithium can be deintercalated from the anode and intercalated into the cathode. This determines how quickly electrons move through the external circuit and increasing these rates, increases the current, and thus the power. As the lithium is only intercalated or deintercalated at the surfaces of the electrodes, power therefore increases with surface area of the electrodes. In addition, typically the diffusion of lithium is considerably faster through the electrolyte than through the electrodes and so minimising the distance a lithium atom needs to move through the electrode will also increase the power. Therefore, instead of two large electrodes with electrolyte between the two as shown schematically in Figure 1.1, batteries are manufactured with porous electrodes as depicted in Figure 1.2. This gives the electrodes large surface areas and small

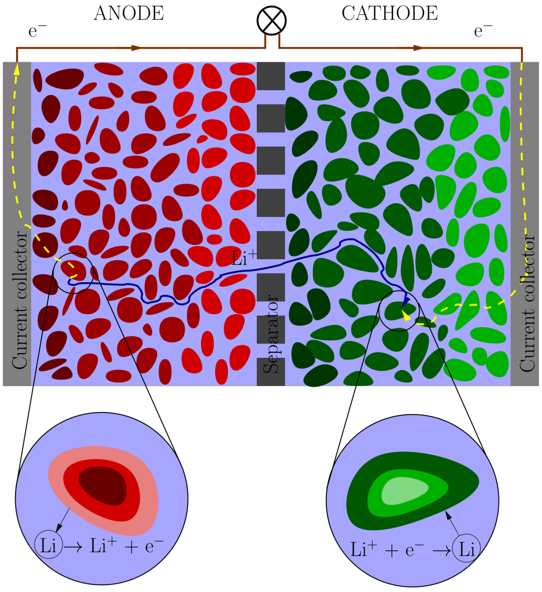

Figure 1.2: Schematic of the movement of Li^+ ions and electrons in LIBs with porous electrodes. Current collectors are at each end, and the separator is in the centre. The blue line shows the movement of Li^+ from the anode to the cathode and the yellow dashed lines show the movement of the electrons, which would move solely through the electrode particles, binder or conductive additives, in three dimensions. The circles at the bottom show the surface reactions occurring in each electrode.

distances from within particles to the reaction surface. The two electrodes now must be separated by a separator to ensure they do not touch which would result in a short-circuit. Additionally, a binder is added to keep the electrode particles in place, along with a conductive additive to ensure the electrons can flow towards the current collector easily. The movement of the Li^+ and electrons in this case is shown in Figure 1.2.

1.2 Silicon Anodes

Nexeon Ltd seeks to include silicon into the anode materials they produce. The reason for this is the extremely large capacity for lithium (both volumetric and gravimetric) that silicon has compared to other common anode materials. When fully lithiated, silicon can accommodate 3.75 lithium atoms per silicon atom, forming the alloy $Li_{3.75}Si$ at room temperature [45]. This is a very large improvement over the commonly-used graphite which can accommodate one lithium atom per six carbon atoms (0.167 lithium atoms per carbon atom) when it forms the alloy LiC_6 [13]. The

	Si	C_6	$Li_4Ti_5O_{12}$	Sn	SnO_2	Ge
Grav. Cap. ($mAhg^{-1}$)	3500[45]	372[62]	175[130]	994[130]	790[68]	963[96]
Volume Change (%)	280[66]	10[86]	1[130]	260[130]	240[50]	270[123]

Table 1.1: Gravimetric capacities and volume changes of anode materials.

gravimetric capacities for silicon, graphite and other common anode materials are given in Table 1.1.

However, silicon has a significant limitation to its use as an anode material. When fully lithiated, silicon expands to up to 400% its original volume due to the changes in the crystal structure that occur to accommodate the lithium atoms [66]. This can cause mechanical stresses because of geometrical constraints within the anode and the rest of the battery, but also because of concentration gradients of lithium within the anode particles causing non-uniform expansion. The expansion of the anode material can result in loss of connection within the cell due to the displacement of other components of the battery, and the high stresses within the anode material may cause it to crack [5, 107]. This loss of connection can lead to parts of the anode being electrically disconnected, which reduces the capacity of the battery after several charge/discharge cycles, commonly known as capacity fade. High levels of expansion also occur in other high-capacity anode materials, especially alloy anodes [130], and we include them in the table of anode material properties in Table 1.1.

Experimental efforts to make silicon a viable anode material have involved using nano-structures within the anode design. These small structures decrease the diffusion length of the lithium into the anode, decreasing the gradients in the lithium concentration and thus decreasing the internal stresses caused by the non-uniform expansion. Some examples of nanoscale designs are nano-particles [55, 66, 72], nanowires [14, 47, 126] and nano-tubes [103, 112]. Additionally, there are many nanostructure designs which attempt to constrain the expansion of the silicon, for example in a core–shell structure [102, 121, 124], yolk–shell structure [64, 113], or using self-healing polymers [110].

A further limitation of using silicon as an anode material is the growth of a solid–electrolyte interphase (SEI) layer. An SEI layer forms on the surface of an anode during cycling when an anode is in contact with the electrolyte. This can decrease the capacity of the battery over time due to the loss of lithium to this layer [84, 101] and can reduce the power of the battery due to the increased diffusion length for the lithium to reach the reaction surface. Silicon is particularly susceptible to SEI growth,

Figure 1.3: Schematics and SEM images of experimentally made nano-structured anode designs. Top left: Silicon nano-tubes [103], top right: Yolk–shell design [64], bottom left: Self-healing polymer cages [110], bottom right: Pomegranate structure [63].

so minimising the surface area of silicon which is in contact with the electrolyte is also important. Therefore, the constraining structures described above are also used to protect the silicon from coming into contact with the electrolyte.

Nano-structures and constraining mechanisms are often used in conjunction with each other. For example, Wang et al. showed that for a silicon oxide shell which is thick enough, inwards growth can be induced in silicon nanotubes [112]. Schematics of some of these structures are shown in Figure 1.3.

In this thesis, we focus on the use of silicon in conjunction with graphite to form a multi-material anode. The simultaneous use of both silicon and graphite in anodes has been investigated experimentally in an attempt to increase the capacity of graphite anodes but not cause them to expand to an unreasonable extent. Dölle [30] reviews several methods of producing silicon–graphite anodes, presents experimental results for their performance, and formulates a basic mathematical model to describe and explain the behaviour of the anode. The two materials are often used in two ways; i) covering the silicon with graphite to constrain the silicon's expansion and protect it from the electrolyte, or ii) including small particles of silicon within the graphite to increase the capacity. The geometries used to constrain the silicon include wrapping a graphite nanotube around silicon nano-particles [119] and by wrapping silicon nanowires in a sheet of graphite [23]. Both these anode geometries retained their capacity over several cycles more than using just silicon, suggesting the stresses are reduced by the graphite coverage, making cracking less likely. Slightly increasing the capacity of graphitic anodes has been attempted in experiments by adding silicon coatings on the outside of carbon nanotubes [49] and attaching small nano-particles of silicon to graphitic frames [69]. These designs are shown to have a large capacity increase compared to using solely graphite with a minimal change to the expansion upon lithiation. As silicon's expansion is so large, in almost all practical applications it is not viable to use for the entire anode, hence the use of multi-material anodes seems one of the few viable ways to utilise the high capacity of silicon. A full review of the developments in silicon-based anode design from 1990 to 2016 is given in [140], describing the new void-based designs emerging recently.

1.3 Modelling of Lithium-ion Batteries

Mathematical modelling of LIBs is a powerful tool in developing both new battery designs and improving battery operation. Models can be formulated on a wide range of different spatial scales. At the microscale, models focus on the intercalation of individual lithium atoms into the crystal structure of the electrodes. These models often utilise density functional theory (DFT) to derive different properties of the electrode materials ab initio [81, 129]. At the mesoscale, models usually focus on a single cell consisting of an anode, cathode, separator, electrolyte, and two current collectors. These models usually approximate the position of the lithium atoms and ions as a continuum, calculating the concentration of lithium and the electrical potential as a function of space and time throughout each electrode and the electrolyte [40, 94]. Finally, at the macroscale, full batteries of several cells in series are often modelled using equivalent circuit models, modelling the loads on a circuit as resistances in series and analysing how these loads change the idealised voltage from the battery [76, 139]. All these models have advantages and disadvantages, depending on the importance of understanding the physical basis of the behaviour, the need for accuracy, and the computational costs due to complexity. A review of models at different scales can be found in [100]. Within this thesis, we focus on the mesoscale models.

Mesoscale models typically aim to predict the concentration of lithium within the cell. A common model for the movement of lithium atoms in the electrode is by Fickian diffusion, for example in [9, 13, 25, 40, 131]. However, in recent years experimental evidence suggests that electrode materials undergo phase separation between a fully lithiated phase and an unlithiated or poorly-lithiated phase [65, 66, 72, 73, 111]. This phase-separation is better described by the Cahn-Hilliard equation [12, 17, 128] but can also be modelled by prescribing the position of the phase boundary [15, 51, 118]. The movement of lithium-ions within the electrolyte is governed by both Fickian diffusion and forces caused by gradients in the electric potential. The movement of electrons in the anode is modelled as a current density satisfying Ohm's law [77]. Finally, the rate of the reaction at the surface of each electrode is usually modelled using Butler–Volmer kinetics [77]. This uses an Arrhenius-type law depending on the difference in electrical potential between the electrode and electrolyte to model the rate of intercalation.

There are many flaws to this modelling framework, especially the Butler–Volmer kinetics [87], but due to the multiple scales which this model spans, it is already sufficiently complicated that several reductions need to be made before it can be solved in an adequately small time. The most famous of these simplifications, and most commonly used, is the pseudo-2D (P2D) model derived by Doyle, Fuller and Newman [40]. This models each electrode as an agglomeration of spherical particles each with an 'effective radius' and treats the processes occurring at the particle level and those at the cell level separately. The diffusion problem in the electrode particles is solved at every spatial point in the cell, and the particle and cell problems are coupled by Butler–Volmer kinetics determining the rate of (de)intercalation of lithium into (and out of) each particle at the particle boundary.

Since this seminal paper, there have been many other reductions of the full model, attempting to capture the processes occurring at all scales using formal homogenisation methods. The first homogenised models for nonhomogeneous LIB anodes were by Ciucci and Lai using volume averaging [57] and the method of multiple scales [22]. Ciucci and Lai homogenise the Poisson–Nernst–Planck (PNP) equations to describe the movement of ions in the electrolyte and use Butler–Volmer dynamics to describe the movement of lithium ions between the electrodes and the electrolyte. The resulting homogenised equations for the diffusion of the ionic species are very similar to those in the P2D model [40]. A very similar model was formulated by Richardson *et al.*, however, they then proceed to analyse ways to solve the resulting model using asymptotic methods [89]. In some applications, the computational cost of solving the P2D model is still too high to be useful. Therefore, a further simplification is taken to assume that each particle can be modelled in the same way, yielding the single-particle model (SPM) [2, 7, 80]. This was shown to be reasonably accurate for slow charge/discharge rates, but breaks down at higher rates. Most recently, systematic asymptotic reductions to the P2D model have recovered the SPM for small charging rates [71], and for large changes in overpotential during charging [90]. Both these studies include a higher-order correction term capturing the effects of variations in the electrolyte, providing much better accuracy of this model at higher charging rates.

In addition to these multiscale model reductions, recent research has also focussed on including more physical phenomena into the battery models. One such phenomenon is the temperature variation that occurs within the cell during operation, mainly due to Joule heating by the resistances within the cell and the entropic changes when intercalating and deintercalating [3]. Models that include these temperature effects have been developed [56, 82] and asymptotically reduced, for example in [46]. Secondly, the SEI layer formation on the surface has been a focus of recent modelling efforts due to its large contribution to battery degradation [108]. Finally, mechanical stresses caused by the expansion of electrodes have also been considered. It is this last effect which will be our main focus in this thesis.

A comprehensive review of the electro-chemo-mechanical modelling of lithium-ion batteries can be found in [135]; we highlight some areas of the research field relevant to the work in this thesis here. The most common approach to modelling the mechanical behaviour of an anode is to model it as an elastic solid which isotropically expands in proportion to the concentration of lithium. This is similar to a conventional thermoelastic model with lithium concentration playing the role of temperature. The first model to incorporate stress into the standard cell model was by Christensen and Newman [21] in which a graphite sphere was considered. Due to the small expansion of graphite, linear elasticity theory was used, which is a common approximation as it greatly simplifies the equations involved [15, 92, 131]. However, for electrode materials with larger expansions, such as silicon, the assumption of small strains used in linear elasticity theory is no longer valid for all states of charge. Thus finite strain models using geometrically nonlinear elasticity have been used when considering these materials [9, 13, 17, 25, 42]. The solving of these models is often simplified by assuming some symmetry of the anode nano-structure, typically using spherical [25, 136] or cylindrical [13, 136] geometries. However, the finite strain models are sufficiently complicated that they often must be solved numerically, even with these geometrical simplifications.

Most anode materials are not elastic for very large elastic strains: eventually at large enough deviatoric stresses, the anode material yields in some way. Sethuraman *et al.* showed experimentally that silicon exhibits plastic flow at sufficiently large deviatoric stress [98]. This has been included into the mathematical modelling of anodes, especially silicon, by being incorporated into linear elastic models [118], into the finite strain models [9, 13, 25, 17], and by neglecting the elasticity of the silicon altogether and modelling the material as solely plastic [53, 132, 133]. Many anode materials do not plasticise at high deviatoric stress but instead crack once their yield stresses have been reached. Analysing the appearance and propagation of these cracks has also been a large area of research within the anode modelling field [15, 32, 42, 95, 118, 120].

The coupling between the lithium distribution and the stress is a two-way phenomenon, since in addition to lithiation causing expansion, lithium transport also depends on the internal stress within the anode through a phenomenon known as stress-assisted diffusion. Stress-assisted diffusion is typically included into lithium transport models by considering the chemical potential of the lithium in the anode to be a sum of a stress-independent chemical potential and a stress-dependent chemical potential. If a part of the anode is under compressive stress, the chemical potential of the lithium in that region will increase making it more difficult for the anode to intercalate the lithium. Conversely, if a part of the anode is under tensile stress, the chemical potential of lithium in that region will decrease, enhancing its ability to intercalate lithium.

With the high stress that occurs in silicon-based anodes, stress-assisted diffusion is very important, and should be included in any model. The first model of this phenomenon was formulated by Larche and Cahn with applications outside the context of LIBs, instead modelling the movement of chemical species in a solid under stress [58]. This work introduced a stress-dependent chemical potential proportional to the hydrostatic stress (the trace of the Cauchy stress tensor) and this approach has been utilised in many works in the context of LIB electrodes [15, 27, 41, 92]. In more recent years, Wu showed that for finite-strain models, the Eshelby tensor should be used in place of the Cauchy stress tensor [117]. Then, Cui *et al.* incorporated a concentration-dependent stiffness into the chemical potential, resulting in a more general framework for stress-assisted diffusion [25]. Cui's form of the stress-dependent chemical potential reduces to those proposed by Wu, Larche and Cahn under appropriate conditions. This general stress-assisted diffusion framework has more recently been applied to finite strain models, for example in [13, 26].

The modelling focus of this thesis is the mechanical effects of lithiation within the anode. We would like to gain insight into the stresses generated across the whole porous anode, using a multiscale model similar to the P2D model. However, to make analytical progress, we focus on the displacement and stresses generated in a single anode nano-particle, approximated to be spherical. The stresses generated by lithium inhomogeneities in a single nano-particle of a single material is well studied [21, 131]. We consider a core–shell geometry for the nano-particle, consisting of multiple materials. Models for this nano-particle design have also been studied [44, 53, 106], but these often model the shell as a hard boundary, generating stress in the expanding core, or by assuming the shell material does not chemically interact with the core. Chemo-mechanically modelling the core–shell design in which both materials are electrochemically active has recently been studied by Wu and Lu [115]. In this work, Wu and Lu model the materials as linearly elastic and compute the stresses, lithium concentrations and chemical potentials in each material as lithium diffuses through each material in the nano-particle. In this thesis, we also model the stresses generated by the presence of multiple active anode materials in a nano-particle, but at chemical equilibrium. We focus on the coupling between stress and lithiation through stress-assisted diffusion and the effect the equilibrium stresses have on lithium distribution between the multiple materials, using several models. Although many of the ideas apply to general anode materials, we consider the core to be silicon and the shell to be graphite throughout the thesis to demonstrate the type of behaviour that occurs in these core–shell designs. The overall aim of the models we derive in this thesis is to improve the design of the nano-particles according to the expansion, stress and capacity at equilibrium.

1.4 Thesis Overview

We begin in Chapter 2 by deriving the quasi-static chemo-mechanical model that will be the basis of all the work in this thesis before applying this model to a spherical core–shell geometry. We solve the model in a spherical anode nano-particle consisting of a silicon core and graphite shell and analyse the displacement, stresses and lithium concentrations within each material. By including stress-assisted diffusion into the model, we show the role that stress has in the distribution of lithium between the silicon and graphite at equilibrium. Using the equilibrium chemical potential of each material, we produce an effective open-circuit voltage for the multi-material anode. We then seek to find an optimal initial volume of the silicon core using this equilibrium model by considering several different relevant performance measures.

In Chapter 3, we explore the inclusion of porous materials and voids into the nano-particle and in particular, porous silicon. We first consider a particle with a central void and find incorporating a small void can reduce the expansion compared to a nano-particle without a void, while maintaining the same capacity. We then derive a multiple-scales formulation of the chemo-mechanical model from Chapter 2 to calculate effective mechanical parameters for porous silicon and how these vary with porosity. As the resulting multiple-scales problem needed to derive these effective parameters is nonlinear, we consider the limits of small and large stress-assisted diffusion, finding the problem only becomes linear if other features of the model are removed. We calculate the mechanical parameters of fully lithiated porous silicon using the multiple-scales formulation, as the resulting cell problems are linear in this case. We calculate the expansion and capacity of nano-particles containing various layers of porous silicon and find that using a porous silicon core and including a porous silicon layer between the silicon core and the graphite shell can reduce the expansion of the nano-particle at a given capacity. We find that in the porous layer case, these improvements predicted by the linear elasticity model only occur when there is unphysical behaviour, which we discuss.

The unphysical results motivate us to extend the model and so we consider a geometrically nonlinear elastic model for the spherical particle in Chapter 4. This model is found to have no solutions for a range of lithium concentrations. We therefore further extend the model by using a nonlinear constitutive law as well as geometric nonlinearity and this permits solutions to exist for all concentrations. We use two particular nonlinear constitutive laws to solve the porous silicon layer problem from Chapter 3, which yield physically viable solutions.

In Chapter 5, we extend the linear elasticity model in a different direction by considering possible yielding mechanisms for the materials. Firstly we incorporate fracturing of the graphite shell into the model of the spherical nano-particle geometry with a silicon core. We calculate the growth of the fractured graphite region as a function of the state of charge for a range of volumes of silicon core and calculate the critical volume of silicon core which will cause the entire graphite shell to fracture when the nano-particle is fully lithiated. We then consider a silicon core with a central void which can yield plastically. We calculate how the yielding behaviour of each material depends on the yield stress of each material and the geometry of the nano-particle. This allows us to determine whether a central void can increase the lithium that the nano-particle can accommodate before the graphite fully fractures. Finally, in Chapter 6, we summarise the results found in the thesis, make some comments on the modelling techniques used, and conclude.

Chapter 2

Silicon–Graphite Nano-Particle

In this chapter, we present the chemo-mechanical model for a multi-material anode particle which we will use throughout this thesis and proceed to show how this can be linearised for small stress-free expansions. The quasi-static diffusion model for the lithium concentration is presented and we explain how we can obtain the stress-independent chemical potential of the lithium within an anode material from its open-circuit voltage (OCV). We then apply this quasi-static linear chemo-mechanical model to a spherical, radially-symmetric anode nano-particle consisting of a silicon core surrounded by a graphite shell.

The chemo-mechanical model for a radially-symmetric core–shell nano-particle we present is very similar to that used by Wu and Lu [115]. In Wu's work, the diffusion of lithium is considered and the lithium concentration is coupled to the stress through stress-assisted diffusion. The stresses, lithium concentrations and displacements are calculated in both materials during lithiation and delithiation. The resulting stresses are then used to quantify the likelihood of shell fracture and core–shell debonding using energy release rates. The effects of changing the shell thickness, core size and applied current density on the stress and energy release rates are then studied, finding a feasible parameter space for the geometrical parameters based on a critical energy release rate.

In our work, we consider the quasi-steady state valid for very slow charging rates, so the nano-particle is in chemical equilibrium and thus the chemical potential is uniform throughout the anode. We show that the lithium concentration is also uniform in each material for spherically symmetric geometries at equilibrium and this result allows us to write an algebraic equation for the concentration in each material, decoupled from the stress. In contrast, the time-dependent problem in [115] results in integral equations for the concentration in each material, which are significantly more difficult to solve. We focus on the effect of stress-assisted diffusion in the chemical model by demonstrating the large difference this makes to both the lithium distribution between the core and the shell and the chemical potential of the nano-particle. The calculated chemical potential is then shown to act as an effective open-circuit potential for the hybrid anode nano-particle, taking the stresses at equilibrium into account. We plot the displacements and stresses throughout the spherical nano-particles and analyse how this varies with state of charge (SOC) and the initial volume of the silicon core, showing qualitatively similar results to the time-independent case in [115].

Using this model, we make design recommendations for the nano-particle, based on the volume of the silicon core. In the time-dependent case in [115], the solution to the model is dependent on the length-scale of the entire nano-particle as the diffusion through the nano-particle depends on the diffusion length. In the equilibrium case studied in this chapter, the length-scale of the entire nano-particle is factored out, and we have only two independent variables: the SOC and the *relative* volume of the silicon core compared to that of the entire nano-particle. We find the optimal initial volume of the silicon core at various states of charge according to several performance measures which are based on volumetric capacity and maximising the capacity subject to expansion and stress constraints. We note here though, that our optimal solutions in the case of silicon take the deformation outside the regime in which the linear model is valid.

2.1 Mechanical Model

We derive the mechanical model from fully nonlinear elasticity theory, but then immediately linearise this model by assuming a parameter, which we will define below, is small. We do this to show the origin of the equations we use, but also to show the parameter regimes in which our model is valid. We will also return to this fully nonlinear model in Chapter 4.

2.1.1 Geometry

We begin by introducing notation for the domains and boundaries within the general multi-material anode particle we consider. We denote the domain of the entire anode particle as Ω and the domain occupied by each anode material as Ω_a with $a = 1, \dots, n$, where n is the number of different materials in the multi-material anode. We assume the anode particle is surrounded by electrolyte, ignoring the binder in this geometry, so we denote the boundary between the anode and the electrolyte by Γ_e. Lastly, we denote the boundaries between different anode materials as Γ_{ab} where $a \neq b$ and $a, b \in \{1, \ldots, n\}$.

2.1.2 Nonlinear Mechanical Model

When a solid body becomes mechanically deformed, each point of the initial, undeformed configuration at position $\boldsymbol{X}^*$, is displaced to a point $\boldsymbol{x}^*(\boldsymbol{X}^*)$. Thus, we may write the displacement, $\boldsymbol{u}^*$, as

$$\boldsymbol{u}^*(\boldsymbol{X}^*) = \boldsymbol{x}^*(\boldsymbol{X}^*) - \boldsymbol{X}^*. \tag{2.1}$$

We then define the deformation gradient, $\mathbf{F}$, by

$$\mathbf{F} := \frac{\partial \boldsymbol{x}^*}{\partial \boldsymbol{X}^*} = \mathbf{1} + \frac{\partial \boldsymbol{u}^*}{\partial \boldsymbol{X}^*}, \tag{2.2}$$

where $\mathbf{1}$ is the identity matrix.

The deformation of an anode occurs due to lithiation during the charging process. We assume the deformation is firstly due to the expansion associated with lithiation, and secondly due to the elastic response to this expansion due to the stiffness of the material. To account for the two different effects leading to deformation, we multiplicatively decompose $\mathbf{F}$, as was first proposed by Stojanović *et al.* [104]. The decomposition allows us to write $\mathbf{F}$ as the product of a stress-free deformation gradient caused by the volumetric expansion, $\mathbf{F}^{\mathrm{SF}}$, and an elastic deformation gradient, $\mathbf{F}^{e}$, such that $\mathbf{F} = \mathbf{F}^{e}\mathbf{F}^{\mathrm{SF}}$. We assume the stress-free expansion is isotropic; thus we may write it as

$$\mathbf{F}^{\mathrm{SF}} = (J^c_a)^{1/3}\mathbf{1} \qquad \text{in } \Omega_a, \tag{2.3}$$

where J^c_a is the Jacobian of the stress-free deformation gradient $\mathbf{F}^{\mathrm{SF}}$ in material a, due to the intercalated lithium. This Jacobian is a measure of the volume change due to the stress-free expansion. A simple model is to assume this expansion is proportional to the amount of lithium intercalated into the material at each point, so that we write[†]

$$J^c_a = 1 + 3\eta_a V^m_a c^*_a. \tag{2.4}$$

Here, c^*_a is the concentration of lithium measured in mol m^{-3}, V^m_a is the molar volume of the material with zero lithium absorbed, measured in m^3 mol^{-1}, and η_a is the coefficient of compositional expansion (CCE) which is a measure of the volumetric expansion due to lithiation [105].

[†] So $x_a = c^*_a V^m_a$ is the stoichiometric value of Li in the lithiated anode material alloy $\mathrm{Li}_{x_a}\mathrm{A}$.

The mechanical strain, $\mathbf{E}$, is related to the deformation gradient, $\mathbf{F}$, by

$$\mathbf{E} = \frac{1}{2}\Big(\mathbf{F}^{\mathrm{T}}\mathbf{F} - \mathbf{1}\Big). \tag{2.5}$$

We also define the elastic strain as

$$\mathbf{E}^{e} = \frac{1}{2}\Big((\mathbf{F}^{e})^{\mathrm{T}}\mathbf{F}^{e} - \mathbf{1}\Big). \tag{2.6}$$

From the multiplicative decomposition of $\mathbf{F}$, we can write $\mathbf{F}^{e} = (J_a^c)^{-1/3}\mathbf{F}$, and hence (2.6) becomes

$$\begin{aligned}\mathbf{E}^{e} &= \frac{1}{2}\bigg[(J_a^c)^{-2/3}\mathbf{F}^{\mathrm{T}}\mathbf{F} - \mathbf{1}\bigg],\\ &= \frac{1}{2}\bigg[(1 + 3\eta_a V_a^m c_a^*)^{-2/3}\bigg\{\mathbf{1} + \left(\frac{\partial \boldsymbol{u}^*}{\partial \boldsymbol{X}^*}\right)^{\mathrm{T}} + \frac{\partial \boldsymbol{u}^*}{\partial \boldsymbol{X}^*} + \left(\frac{\partial \boldsymbol{u}^*}{\partial \boldsymbol{X}^*}\right)^{\mathrm{T}}\frac{\partial \boldsymbol{u}^*}{\partial \boldsymbol{X}^*}\bigg\} - \mathbf{1}\bigg] \quad \text{in } \Omega_a.\end{aligned} \tag{2.7}$$

Lastly, the Cauchy stress tensor, $\boldsymbol{\sigma}^*$, is related to the elastic strain by some constitutive law, which shall remain general for now.

2.1.3 Linear Elastic Stress Derivation

We shall now nondimensionalise the lithium concentration, the spatial coordinate in the reference configuration, $\boldsymbol{X}^*$, and the displacement, $\boldsymbol{u}^*$, using

$$c_a^* = c_a^{\max} c_a, \qquad \boldsymbol{X}^* = L\boldsymbol{X}, \qquad \boldsymbol{u}^* = L\eta_1 V_1^m c_1^{\max}\boldsymbol{u}, \tag{2.8}$$

where L is a characteristic length scale of the anode particle. The lithium concentration in each material is nondimensionalised relative to the maximum concentration able to be intercalated *in that material.* The lithium concentration variables in each material are therefore distinct. The displacement, $\boldsymbol{u}$, is nondimensionalised by the variables η, V^m and $c^{\max}$ of one of the materials, which we have denoted using $a = 1$. Substituting (2.8) into the elastic strain (2.7) yields

$$\begin{aligned}\mathbf{E}^{e} = \frac{1}{2}\bigg[(1 + 3\eta_a V_a^m c_a^{\max} c_a)^{-2/3}\bigg\{\mathbf{1} + \eta_1 V_1^m c_1^{\max}\bigg[\left(\frac{\partial \boldsymbol{u}}{\partial \boldsymbol{X}}\right)^{\mathrm{T}} + \frac{\partial \boldsymbol{u}}{\partial \boldsymbol{X}}\bigg]\\ + (\eta_1 V_1^m c_1^{\max})^2\left(\frac{\partial \boldsymbol{u}}{\partial \boldsymbol{X}}\right)^{\mathrm{T}}\frac{\partial \boldsymbol{u}}{\partial \boldsymbol{X}}\bigg\} - \mathbf{1}\bigg] \quad \text{in } \Omega_a.\end{aligned} \tag{2.9}$$

Now, we consider the case in which $\eta_a V_a^m c_a^{\max}$ is small for all materials a, corresponding to small volumetric expansion. This encourages a scaling of the strain with $\eta_1 V_1^m c_1^{\max}$. Thus we define

$$\mathbf{E}^e = \eta_1 V_1^m c_1^{\max} \bar{\mathbf{E}}^e. \tag{2.10}$$

We can now approximate $(1 + 3\eta_a V_a^m c_a^{\max} c_a)^{-2/3} \approx 1 - 2\eta_a V_a^m c_a^{\max} c_a$ and neglect the quadratic deformation gradient term, simplifying (2.9) to

$$\begin{aligned} \eta_1 V_1^m c_1^{\max} \bar{\mathbf{E}}^e = \frac{1}{2}\eta_1 V_1^m c_1^{\max} \left[\left(\frac{\partial \boldsymbol{u}}{\partial \boldsymbol{X}} \right)^{\mathrm{T}} + \frac{\partial \boldsymbol{u}}{\partial \boldsymbol{X}} \right] &- \eta_a V_a^m c_a^{\max} c_a \mathbf{1} \\ &+ \mathcal{O}((\eta_a V_a^m c_a^{\max})^2) \quad \text{in } \Omega_a, \end{aligned} \tag{2.11}$$

$$\implies \bar{\mathbf{E}}^e = \frac{1}{2}\left[\left(\frac{\partial \boldsymbol{u}}{\partial \boldsymbol{X}} \right)^{\mathrm{T}} + \frac{\partial \boldsymbol{u}}{\partial \boldsymbol{X}} \right] - \gamma_a c_a \mathbf{1} + \mathcal{O}(\eta_a V_a^m c_a^{\max}) \qquad \text{in } \Omega_a, \tag{2.12}$$

where

$$\gamma_a = \frac{\eta_a V_a^m c_a^{\max}}{\eta_1 V_1^m c_1^{\max}}. \tag{2.13}$$

Due to the choice of nondimensionalisation of the displacement, small $\eta_a V_a^m c_a^{\max}$ implies the displacements are small compared to the characteristic length scale. This is known as geometric linearity and a key implication of this is that there is no need to distinguish between the variables $\boldsymbol{X}^*$ and $\boldsymbol{x}^*$ (known as the Langrangian and the Eulerian frames, respectively). Thus, we have

$$\mathbf{F} = \mathbf{1} + \frac{\partial \boldsymbol{u}^*}{\partial \boldsymbol{X}^*} \approx \mathbf{1} + \frac{\partial \boldsymbol{u}^*}{\partial \boldsymbol{x}^*}, \tag{2.14}$$

which we will now write as $\mathbf{F} = \mathbf{1} + \boldsymbol{\nabla}^* \boldsymbol{u}^* = \mathbf{1} + \eta_1 V_1^m c_1^{\max} \boldsymbol{\nabla} \boldsymbol{u}$. Therefore, we can write the linearised elastic strain (2.12) as

$$\bar{\mathbf{E}}^e = \frac{1}{2}\Big[\big(\boldsymbol{\nabla} \boldsymbol{u} \big)^{\mathrm{T}} + \boldsymbol{\nabla} \boldsymbol{u} \Big] - \gamma_a c_a \mathbf{1} \qquad \text{in } \Omega_a. \tag{2.15}$$

We relate the stress at a point in a material a to its strain by Hooke's law, where the constant of proportionality is a rank-4 elastic stiffness tensor, $\mathbb{C}_a^*$. In general, $\mathbb{C}_a^*$ depends on the lithium concentration within the material, c_a. We relate the Cauchy stress $\boldsymbol{\sigma}^*$ to the elastic strain (2.15) by

$$\bar{\boldsymbol{\sigma}}^* = \mathbb{C}_a^* : \bar{\mathbf{E}}^e \qquad \text{in } \Omega_a, \tag{2.16}$$

where : represents the double dot product and we have scaled the Cauchy stress tensor by $\boldsymbol{\sigma}^* = \eta_1 V_1^m c_1^{\max} \bar{\boldsymbol{\sigma}}^*$ to ensure balancing of terms. We assume the anode materials are isotropic, giving the stiffness tensor the form

$$\mathbb{C}_a^* = c_{ijkl}^{a,*} = \lambda_a^* \delta_{ij} \delta_{kl} + G_a^* \delta_{ik} \delta_{jl} + G_a^* \delta_{il} \delta_{jk}, \tag{2.17}$$

using suffix notation. Here, λ_a^* and G_a^* are the Lamé parameters of material a, measured in GPa, which are in general dependent on c_a. This isotropy assumption allows us to simplify the constitutive relation (2.16) to

$$\bar{\boldsymbol{\sigma}}^* = \mathbb{C}_a^* : \big(\boldsymbol{\nabla u} - \gamma_a c_a \mathbf{1}\big) \quad \text{in } \Omega_a. \tag{2.18}$$

Finally, we nondimensionalise the stress $\boldsymbol{\sigma}^*$ using

$$\boldsymbol{\sigma}^* = G_1^*(0)\eta_1 V_1^m c_1^{\max}\boldsymbol{\sigma} \implies \bar{\boldsymbol{\sigma}}^* = G_1^*(0)\boldsymbol{\sigma}, \tag{2.19}$$

where $G_1^*(0)$ is the dimensional shear modulus of material 1 when unlithiated. This gives the nondimensional stress $\boldsymbol{\sigma}$ as

$$\boldsymbol{\sigma} = \mathbb{C}_a : \big(\boldsymbol{\nabla u} - \gamma_a c_a \mathbf{1}\big) \quad \text{in } \Omega_a, \tag{2.20}$$

where

$$\mathbb{C}_a = \lambda_a \delta_{ij}\delta_{kl} + G_a \delta_{ik}\delta_{jl} + G_a \delta_{il}\delta_{jk}, \tag{2.21}$$

and

$$\lambda_a = \frac{\lambda_a^*}{G_1^*(0)}, \quad \text{and} \quad G_a = \frac{G_a^*}{G_1^*(0)}. \tag{2.22}$$

Using (2.21), the stress (2.20) is given in suffix notation by

$$\sigma_{ij} = \lambda_a \delta_{ij}\frac{\partial u_k}{\partial x_k} + G_a\left(\frac{\partial u_i}{\partial x_j} + \frac{\partial u_j}{\partial x_i}\right) - \gamma_a c_a (3\lambda_a + 2G_a)\delta_{ij} \quad \text{in } \Omega_a. \tag{2.23}$$

2.1.4 Equilibrium Equations and Boundary Conditions

We assume the anode is in mechanical and chemical equilibrium and thus the forces on the anode are balanced. Neglecting gravity, inertial effects and body forces, the conservation of momentum equation then states that

$$\boldsymbol{\nabla} \cdot \boldsymbol{\sigma} = \mathbf{0} \qquad \text{in } \Omega. \tag{2.24}$$

Neglecting surface tractions, the boundary condition between the anode and the electrolyte is given by

$$\boldsymbol{\sigma} \cdot \mathbf{n}_e = \mathbf{0} \qquad \text{on } \Gamma_e, \tag{2.25}$$

where $\mathbf{n}_e$ is the unit normal vector to Γ_e. This assumes that the electrolyte is easily compressible and does not apply any force to the anode material. This assumption is also reasonable in the presence of binder as the bulk modulus of binders tend to be much lower than that of anode materials [39]. We assume that there is no delamination and so the displacement is continuous at the boundaries between anode materials. Additionally, as the anode is in mechanical equilibrium, the normal stresses between materials are also continuous. These conditions are given by

$$[\boldsymbol{u}]_-^+ = [\boldsymbol{\sigma} \cdot \mathbf{n}_{ab}]_-^+ = \mathbf{0} \qquad \text{on } \Gamma_{ab}\, \forall a \neq b \in [1, n], \tag{2.26}$$

respectively, where $\mathbf{n}_{ab}$ is the unit normal vector between anode materials a and b.

2.2 Chemical Model

We now derive the equations which govern the lithium transport in each of the materials for a multi-material anode. We begin with a diffusion-based model and then introduce the limiting case we consider in this thesis. We state the stress-dependent chemical potential of the anode materials under constitutively and geometrically linear elasticity. The details of the derivation of this chemical potential from the internal energy and the simplification from nonlinear elasticity are presented in appendix A.

2.2.1 Diffusion

The transport of lithium through an anode material a is governed by the diffusion equation, given by

$$\frac{\partial c_a^*}{\partial t^*} + \boldsymbol{\nabla}^* \cdot \mathbf{j}_a^* = 0 \qquad \text{in } \Omega_a, \tag{2.27}$$

where $\mathbf{j}_a^*$ is the dimensional flux of the lithium, given by

$$\mathbf{j}_a^* = -\frac{D_a}{R_g T} c_a^* \boldsymbol{\nabla}^* \mu_a^*. \tag{2.28}$$

In (2.28), D_a is the diffusion coefficient of lithium in anode material a, R_g is the gas constant $= 8.314$ J mol^{-1} K^{-1}, T is the temperature which we assume to be at a constant 298 K, and μ_a^* is the chemical potential of the lithium atoms in anode material a, which we define in Section 2.2.2.

The flux of lithium from the electrolyte into the anode through Γ_e is dictated by the rate of the reaction occurring at the anode surface. This reaction is given by

$$\text{Li} \leftrightharpoons \text{Li}_{\text{el}}^+ + e^-, \tag{2.29}$$

where Li_{el}^+ represents the lithium ions in the electrolyte, e^- the electrons in the anode, and Li the lithium atoms intercalated into the anode. The rate of this reaction is often modelled using Butler–Volmer kinetics [77] which is dependent on the difference between the electrochemical potential of the anode and the equilibrium potential. This difference is known as the overpotential. Lastly, the chemical potential is continuous across boundaries between anode materials, given by

$$\mu_a^* = \mu_b^* \qquad \text{on } \Gamma_{ab}. \tag{2.30}$$

Now, to simplify these equations, we focus on a time-scale much slower than any dynamics in the system and thus we consider steady state solutions to the diffusion equation (2.27), given by

$$\boldsymbol{\nabla}^* \cdot \mathbf{j}_a^* = 0 \qquad \text{in } \Omega_a. \tag{2.31}$$

Additionally, we suppose that there is no net flux of lithium between the anode and the electrolyte, giving

$$\mathbf{j}_a^* \cdot \mathbf{n} = 0 \qquad \text{on } \Gamma_e \, \forall \, a \in [1, n]. \tag{2.32}$$

As $\mathbf{j}_a^*$ can be written as a gradient using (2.28), combining (2.31) and (2.32) implies that $\mathbf{j}_a^* = \mathbf{0} \; \forall \, a \in [1, n]$. Using (2.28), we have

$$c_a^* \boldsymbol{\nabla}^* \mu_a^* = 0 \quad \text{in } \Omega_a. \tag{2.33}$$

Therefore, either the lithium concentration is zero throughout each anode material or the chemical potential is uniform throughout each anode material. Finally, from (2.30), we have that the chemical potential is uniform across the entire anode in equilibrium, and we denote this chemical potential by μ^*.

2.2.2 Chemical Potential

In the linear elastic model we consider in this thesis, the chemical potential of the lithium intercalated into anode material a is given by

$$\mu^* = \tilde{\mu}_a^{\mathrm{SF},*}(c_a^*) - \eta_a V_a^m \mathrm{tr}(\boldsymbol{\sigma}^*) \quad \text{in } \Omega_a. \tag{2.34}$$

This is the sum of the stress-free chemical potential, $\tilde{\mu}_a^{\mathrm{SF},*}(c_a^*)$ and the stress-dependent chemical potential under linear elasticity assumptions, $-\eta_a V_a^m \mathrm{tr}(\boldsymbol{\sigma}^*)$.

The stress-dependent term in (2.34) is from the inclusion of stress-assisted diffusion into the model, coupling the chemical model to the mechanical model. This phenomenon causes the chemical potential of the lithium intercalated into the anode to increase if the anode is under compression and to decrease if the anode is under tension. The trace of the Cauchy stress tensor is negative when the anode is under compression and positive when the anode is under tension and thus subtracting this term provides these effects. In Appendix A, we derive the stress-dependent chemical potential of lithium in a mechanically-deformed solid from the internal energy and show how the second term in (2.34) is obtained under the assumptions made in Section 2.1.3.

For the remainder of this section, we explain how the stress-free chemical potential, $\tilde{\mu}_a^{\mathrm{SF},*}(c_a^*)$, can be obtained from the open-circuit voltage of an anode material using a similar approach to Bazant [4]. The open-circuit voltage of an anode material is a measurement of the difference between the electrochemical potential of the electrons in the anode compared to that in the cathode. This is often a function of the lithium concentrations in each electrode and is measured by recording the open-circuit voltage while charging the anode extremely slowly. This is to ensure that the battery remains approximately in equilibrium. Because the chemical reaction at the surface (2.29) is in equilibrium during this charging, we can equate the electrochemical potentials of the reactants on each side. This electrochemical potential balance gives

$$\hat{\mu}_{\mathrm{Li},a}^{\mathrm{SF},*}(c_{\mathrm{Li},a}^*) = \underbrace{\mu_{\mathrm{Li}^+,\mathrm{el}}^*(c_{\mathrm{Li}^+,\mathrm{el}}^*) + ze\phi_{\mathrm{el}}^*}_{\text{Electrochem. pot. of Li}^+\text{ in electrolyte}} + \underbrace{\mu_{e^-,a}^*(c_{e^-,a}^*) - ze\phi_a^*,}_{\text{Electrochem. pot. of e}^-\text{ in anode}} \tag{2.35a}$$

$$\hat{\mu}_{\mathrm{Li},c}^{\mathrm{SF},*}(c_{\mathrm{Li},c}^*) = \underbrace{\mu_{\mathrm{Li}^+,\mathrm{el}}^*(c_{\mathrm{Li}^+,\mathrm{el}}^*) + ze\phi_{\mathrm{el}}^*}_{\text{Electrochem. pot. of Li}^+\text{ in electrolyte}} + \underbrace{\mu_{e^-,c}^*(c_{e^-,c}^*) - ze\phi_c^*,}_{\text{Electrochem. pot. of e}^-\text{ in cathode}} \tag{2.35b}$$

for the reactions occurring at the surface of the anode and cathode, respectively. In (2.35), ϕ^* is the electrical potential where the subscript denotes the phase, a denoting anode, c denoting cathode and el denoting electrolyte. The chemical potential is denoted by μ^* where the first subscript denotes the chemical species and the second subscript denotes the phase which the species is in. Lastly, the charge number of Li^+ is $z = 1$ and e is the fundamental charge, 1.60217×10^{-19}C.

We make the distinction between the chemical potential of a single lithium atom in the anode, given by $\hat{\mu}_{\mathrm{Li},a}^{\mathrm{SF},*}(c_{\mathrm{Li},a}^*)$ in (2.35), and the chemical potential of lithium per mole, given by $\tilde{\mu}_a^{\mathrm{SF},*}(c_a^*)$ in (2.34). Secondly, we neglect the stress-dependent chemical potential of the lithium in the anode in (2.35) as the charging is occurring slowly such that any stresses caused by non-uniform concentrations are negligible and we are only considering the charging of one anode material so there are no stresses in this equilibrium state.

The measurement that the OCV produces, E^{OCV}, in volts, is equivalent to the difference between the electrochemical potential of the electrons in the anode and that in the cathode, divided by the charge on the electron $-e$ [77]. We write this as

$$E^{\text{OC}} = -\frac{\mu^*_{e,a}(c^*_{e,a})}{e} + z\phi^*_a + \frac{\mu^*_{e,c}(c^*_{e,c})}{e} - z\phi^*_c, \tag{2.36}$$

and rearrange (2.35) to obtain an expression for the chemical potential of the lithium in the anode in terms of the OCV, given by

$$\hat{\mu}^{\text{SF},*}_{\text{Li},a}(c^*_{\text{Li},a}) = -eE^{\text{OC}} + \mu^{\text{SF},*}_{\text{Li},c}(c^*_{\text{Li},c}). \tag{2.37}$$

We then convert $\hat{\mu}^{\text{SF},*}_{\text{Li},a}$, measured in J, to $\tilde{\mu}^{\text{SF},*}_a$, measured in J mol^{-1}, by multiplying by Avagadro's number, 6.02214086 $\times 10^{23}$ mol^{-1}.

The chemical potential for the lithium in the cathode, $\mu^{\text{SF},*}_{\text{Li},c}(c^*_{\text{Li},c})$, in (2.37) does not concern the work in this thesis for two reasons. Firstly, the cathode material used to measure the OCV of the anode material is often lithium metal. In this case, the reaction (2.29) at the surface of the cathode simply plates lithium and this does not affect the chemical potential of the lithium already in the cathode. Thus, in this case, $\mu^{\text{SF},*}_{\text{Li},c}$ is not dependent on $c^*_{\text{Li},c}$ and is an additive constant, shifting the reference potential for $\hat{\mu}^{\text{SF},*}_{\text{Li},a}$. Secondly, we are only concerned with comparing the potentials of different anode materials or of anode materials at different states of charge. Therefore, as long as the cathode used when calculating the OCV of the different materials is the same, this additive constant will cancel when comparing them.

2.2.3 Nondimensionalisation

We nondimensionalise the total chemical potential μ^* and the stress-free chemical potential $\tilde{\mu}^{\text{SF},*}_a(c^*_a)$ in (2.34) using

$$\mu^* = R_g T \mu, \qquad \mu^{\text{SF},*}_a(c^*_a) = R_g T \mu^{\text{SF}}_a(c_a), \tag{2.38}$$

respectively. Lastly, we nondimensionalise the Cauchy stress by (2.19). This gives the expression for the nondimensional chemical potential for the lithium in material a as

$$\mu = \mu^{\text{SF}}_a(c_a) - S^d_a \text{tr}(\boldsymbol{\sigma}) \quad \text{in } \Omega_a, \tag{2.39}$$

where

$$S^d_a = \frac{\eta_a \eta_1 V^m_a V^m_1 c^{\max}_1 G^*_1(0)}{R_g T}. \tag{2.40}$$

This parameter can be interpreted as the ratio of the elastic energy of the solid to thermal noise.

2.2.4 State of Charge Condition

We close the system of equations for the lithium concentration by prescribing the total amount of intercalated lithium within the anode. We describe this as a proportion of the maximum amount of intercalated lithium possible using the SOC parameter $c_0 \in [0, 1]$, where $c_0 = 0$ denotes there is no intercalated lithium and $c_0 = 1$ denotes a fully lithiated anode. Therefore, we impose

$$\begin{aligned} c_0 \sum_{a=1}^{n} \left(\int_{\Omega_a} c_a^{\max} \, \mathrm{d}V \right) &= \sum_{a=1}^{n} \left(\int_{\Omega_a} c_a^{*} \, \mathrm{d}V \right) \\ &= \sum_{a=1}^{n} \left(c_a^{\max} \int_{\Omega_a} c_a \, \mathrm{d}V \right). \end{aligned} \tag{2.41}$$

We conclude this section with a summary of the model. The full mechanical model is given by the governing equation (2.24), the Cauchy stress (2.20) and the boundary conditions (2.25)-(2.26). The full chemical model is given by the chemical potential (2.39) being uniform across the anode, and the SOC condition (2.41). Given a value of $c_0 \in [0, 1]$, we seek to calculate the concentration profile in each material, c_a, and displacement profile, $\boldsymbol{u}$, from the model.

2.2.5 Summary of Model in General Geometry

A summary of the governing equations and boundary conditions for the general linearised model derived so far in this chapter is given by

$$\boldsymbol{\nabla} \cdot \boldsymbol{\sigma} = \mathbf{0} \quad \text{in } \Omega, \tag{2.42a}$$

$$\sigma_{ij} = \lambda_a \delta_{ij} \frac{\partial u_k}{\partial x_k} + G_a \left(\frac{\partial u_i}{\partial x_j} + \frac{\partial u_j}{\partial x_i} \right) - \gamma_a c_a (3\lambda_a + 2G_a) \delta_{ij} \quad \text{in } \Omega_a, \tag{2.42b}$$

$$\mu = \mu_a^{\mathrm{SF}}(c_a) - S_a^d \mathrm{tr}(\boldsymbol{\sigma}) \quad \text{in } \Omega_a, \tag{2.42c}$$

$$\boldsymbol{\sigma} \cdot \mathbf{n}_e = \mathbf{0} \quad \text{on } \Gamma_e, \tag{2.42d}$$

$$[\boldsymbol{u}]_-^+ = [\boldsymbol{\sigma} \cdot \mathbf{n}_{ab}]_-^+ = \mathbf{0} \quad \text{on } \Gamma_{ab} \, \forall a \neq b \in [1, n], \tag{2.42e}$$

$$c_0 \sum_{a=1}^{n} \left(\int_{\Omega_a} c_a^{\max} \, \mathrm{d}V \right) = \sum_{a=1}^{n} \left(c_a^{\max} \int_{\Omega_a} c_a \, \mathrm{d}V \right). \tag{2.42f}$$

This system is solved for a given SOC, c_0.

2.3 Radial Symmetry

In the previous section, we derived a quasi-static chemo-mechanical model for multi-material anode lithiation for a general geometry of anode. We now simplify this model by applying it to a spherical, radially-symmetric geometry inspired by anode nano-particles. This simplifies the PDEs in the general case of Section 2.1 to ODEs, allowing us to use analytical methods to solve the resulting equations.

Due to the radial symmetry, we can assume that the displacement is in the radial direction and only varies with the radial coordinate, r. Similarly, the symmetry implies the lithium concentration, c_a, only varies in the radial direction so that

$$\boldsymbol{u} := u(r)\boldsymbol{e}_r, \qquad c_a := c_a(r), \tag{2.43}$$

where $\boldsymbol{e}_r$ is the radial basis vector. We now wish to solve the mechanical problem for the scalar displacement, u, as a function of the radius, r. In spherical coordinates and with radial symmetry, the Cauchy stress tensor (2.20) can be simplified to [48]

$$\boldsymbol{\sigma} = \mathbb{C}_a : \begin{bmatrix} \frac{\mathrm{d}u}{\mathrm{d}r} - \gamma_a c_a & 0 & 0 \\ 0 & \frac{u}{r} - \gamma_a c_a & 0 \\ 0 & 0 & \frac{u}{r} - \gamma_a c_a \end{bmatrix} \quad \text{in } \Omega_a, \tag{2.44}$$

which, using (2.21), gives

$$\boldsymbol{\sigma} = \operatorname{diag} \begin{bmatrix} \lambda_a\left(\frac{\mathrm{d}u}{\mathrm{d}r} + \frac{2u}{r}\right) + 2G_a\frac{\mathrm{d}u}{\mathrm{d}r} - \gamma_a(3\lambda_a + 2G_a)c_a \\ \lambda_a\left(\frac{\mathrm{d}u}{\mathrm{d}r} + \frac{2u}{r}\right) + 2G_a\frac{u}{r} - \gamma_a(3\lambda_a + 2G_a)c_a \\ \lambda_a\left(\frac{\mathrm{d}u}{\mathrm{d}r} + \frac{2u}{r}\right) + 2G_a\frac{u}{r} - \gamma_a(3\lambda_a + 2G_a)c_a \end{bmatrix} \quad \text{in } \Omega_a. \tag{2.45}$$

We denote these diagonal entries of $\boldsymbol{\sigma}$ as σ_{rr}, $\sigma_{\theta\theta}$ and $\sigma_{\phi\phi}$, respectively, and in this radially-symmetric case, we have $\sigma_{\theta\theta} = \sigma_{\phi\phi}$, as seen in (2.45).

We now derive the equilbrium equation (2.24) in spherical coordinates. The divergence of the Cauchy stress $\boldsymbol{\sigma}$ in spherical coordinates with only the σ_{rr}, $\sigma_{\theta\theta}$ and $\sigma_{\phi\phi}$ terms being non-zero and each only depending on r is given by

$$\boldsymbol{\nabla} \cdot \boldsymbol{\sigma} = \left(\frac{1}{r^2}\frac{\mathrm{d}(r^2\sigma_{rr})}{\mathrm{d}r} - \frac{\sigma_{\theta\theta} + \sigma_{\phi\phi}}{r}\right)\boldsymbol{e}_r. \tag{2.46}$$

As we have $\sigma_{\theta\theta} = \sigma_{\phi\phi}$, we can write the mechanical equilibrium equation (2.24) as

$$\frac{\mathrm{d}\sigma_{rr}}{\mathrm{d}r} + \frac{2(\sigma_{rr} - \sigma_{\theta\theta})}{r} = 0 \qquad \text{in } \Omega, \tag{2.47}$$

and we can write (2.39) as

$$\mu = \mu_a^{\mathrm{SF}}(c_a) - S_a^d(\sigma_{rr} + 2\sigma_{\theta\theta}) \qquad \text{in } \Omega_a. \tag{2.48}$$

Substituting (2.45) into (2.47) yields

$$(\lambda_a + 2G_a)\frac{\mathrm{d}}{\mathrm{d}r}\left(\frac{1}{r^2}\frac{\mathrm{d}}{\mathrm{d}r}(r^2 u)\right) + K_1\frac{\mathrm{d}c_a}{\mathrm{d}r} = 0 \qquad \text{in } \Omega_a, \tag{2.49}$$

where

$$K_1 = \left(\frac{\mathrm{d}u}{\mathrm{d}r} + \frac{2u}{r}\right)\frac{\mathrm{d}\lambda_a}{\mathrm{d}c_a} + 2\frac{\mathrm{d}u}{\mathrm{d}r}\frac{\mathrm{d}G_a}{\mathrm{d}c_a} - \gamma_a\frac{\mathrm{d}(3\lambda_a + 2G_a)}{\mathrm{d}c_a}c_a - \gamma_a(3\lambda_a + 2G_a). \tag{2.50}$$

Differentiating (2.48) with respect to r yields

$$K_2\frac{\mathrm{d}c_a}{\mathrm{d}r} - S_a^d(3\lambda_a + 2G_a)\frac{\mathrm{d}}{\mathrm{d}r}\left(\frac{1}{r^2}\frac{\mathrm{d}}{\mathrm{d}r}(r^2 u)\right) = 0 \qquad \text{in } \Omega_a, \tag{2.51}$$

where

$$\begin{aligned} K_2 = \frac{\mathrm{d}\mu_a^{\mathrm{SF}}}{\mathrm{d}c_a} - S_a^d\bigg[&3\frac{\mathrm{d}\lambda_a}{\mathrm{d}c_a}\left(\frac{\mathrm{d}u}{\mathrm{d}r} + \frac{2u}{r}\right) + 2\frac{\mathrm{d}u}{\mathrm{d}r}\frac{\mathrm{d}G_a}{\mathrm{d}c_a} + 4\frac{\mathrm{d}G_a}{\mathrm{d}c_a}\frac{u}{r} \\ &- 3\gamma_a\frac{\mathrm{d}(3\lambda_a + 2G_a)}{\mathrm{d}c_a}c_a - 3\gamma_a(3\lambda_a + 2G_a)\bigg], \end{aligned} \tag{2.52}$$

and we have used the fact that the total chemical potential, μ, is uniform in each material. Substituting (2.49) into (2.51) yields

$$\frac{\mathrm{d}c_a}{\mathrm{d}r}\left[K_2 + \frac{S_a^d(3\lambda_a + 2G_a)}{\lambda_a + 2G_a}K_1\right] = 0 \qquad \text{in } \Omega_a. \tag{2.53}$$

Therefore, either the concentration in each material is independent of r or the terms in the bracket are zero. We take the case that the concentration in each material is uniform and discuss other solutions in Appendix B. This is similar to the results in [115] in which the lithium concentrations are approximately uniform in each material for the time-dependent case. This uniform concentration result allows us to remove the final term of the left-hand side of (2.49) as we have shown that c_a is independent of r. Our mechanical equilibrium equation (2.49) is now given by

$$\frac{\mathrm{d}}{\mathrm{d}r}\left(\frac{1}{r^2}\frac{\mathrm{d}}{\mathrm{d}r}(r^2 u)\right) = 0 \quad \text{in } \Omega, \tag{2.54}$$

which can be integrated twice to yield

$$u = A_a r + \frac{B_a}{r^2} \quad \text{in } \Omega_a, \tag{2.55}$$

where A_a and B_a are integration constants. Using (2.45), we can now write the stress components for each material as

$$\sigma_{rr} = (3\lambda_a + 2G_a)(A_a - \gamma_a c_a) - \frac{4G_a B_a}{r^3} \qquad \text{in } \Omega_a, \tag{2.56a}$$

$$\sigma_{\theta\theta} = \sigma_{\phi\phi} = (3\lambda_a + 2G_a)(A_a - \gamma_a c_a) + \frac{2G_a B_a}{r^3} \qquad \text{in } \Omega_a. \tag{2.56b}$$

These expressions are substituted into (2.39) to yield the chemical potential of the lithium in anode material a in terms of c_a as

$$\mu = \mu_a^{\mathrm{SF}}(c_a) - 3S_a^d(3\lambda_a + 2G_a)(A_a - \gamma_a c_a) \quad \text{in } \Omega_a. \tag{2.57}$$

The boundary conditions (2.25) and (2.26) in spherical coordinates are given by

$$\sigma_{rr} = 0 \quad \text{on } \Gamma_e, \tag{2.58a}$$

$$[u]_-^+ = [\sigma_{rr}]_-^+ = 0 \quad \text{on } \Gamma_{ab}\ \forall a \neq b \in [1, n], \tag{2.58b}$$

where the boundaries Γ_e and Γ_{ab} are spherical surfaces with radii depending on the exact geometry of the spherical anode. The SOC condition (2.41) is now given by

$$c_0 \sum_{a=1}^{n} \left(c_a^{\max} \int_{\Omega_a} r^2 \, \mathrm{d}r \right) = \sum_{a=1}^{n} \left(c_a^{\max} c_a \int_{\Omega_a} r^2 \, \mathrm{d}r \right). \tag{2.59}$$

2.3.1 Summary of Spherically-Symmetric Model

The displacement and stresses in a spherically symmetric geometry are given in terms of the integration constants A_a and B_a, and the lithium concentrations c_a, by

$$u = A_a r + \frac{B_a}{r^2} \quad \text{in } \Omega_a, \tag{2.60a}$$

$$\sigma_{rr} = (3\lambda_a + 2G_a)(A_a - \gamma_a c_a) - \frac{4G_a B_a}{r^3} \quad \text{in } \Omega_a, \tag{2.60b}$$

$$\sigma_{\theta\theta} = \sigma_{\phi\phi} = (3\lambda_a + 2G_a)(A_a - \gamma_a c_a) + \frac{2G_a B_a}{r^3} \quad \text{in } \Omega_a. \tag{2.60c}$$

The integration constants A_a and B_a for $a \in [1, n]$ are calculated in terms of c_a for $a \in [1, n]$ using the mechanical boundary conditions given by

$$\sigma_{rr} = 0 \quad \text{on } \Gamma_e, \tag{2.61a}$$

$$[u]_-^+ = [\sigma_{rr}]_-^+ = 0 \quad \text{on } \Gamma_{ab}\ \forall a \neq b \in [1, n]. \tag{2.61b}$$

Finally, the lithium concentrations are calculated for a given SOC, c_0, using the uniform chemical potential condition and the SOC condition, given by

$$\mu = \mu_a^{\mathrm{SF}}(c_a) - 3S_a^d(3\lambda_a + 2G_a)(A_a - \gamma_a c_a) \quad \text{in } \Omega_a, \tag{2.62}$$

and

$$c_0 \sum_{a=1}^{n} \left(c_a^{\max} \int_{\Omega_a} r^2 \, \mathrm{d}r \right) = \sum_{a=1}^{n} \left(c_a^{\max} c_a \int_{\Omega_a} r^2 \, \mathrm{d}r \right), \tag{2.63}$$

respectively.

2.4 Silicon Core, Graphite Shell Problem

We now apply the spherically symmetric results of Section 2.3 to a specific geometry of anode nano-particle consisting of a silicon core surrounded by a graphite shell. This model can be used for any core and shell materials, however, we use silicon and graphite here as an example of a core with a large expansion constrained by a shell with a small expansion.

2.4.1 Domains and Boundaries

We denote the dimensional outer radius of the spherical anode nano-particle as R^*_{C}, and the dimensional outer radius of the silicon core before expansion as R^*_{Si}. Both the core and the entire nano-particle are spheres centered at the origin. Our characteristic length scale in this geometry is the radius of the whole nano-particle, R^*_{C}, and thus we substitute $L = R^*_{\mathrm{C}}$ into the nondimensionalisation of the displacement (2.8). Our nondimensional spatial variable is therefore $r = r^*/R^*_{\mathrm{C}}$ and we define $R_{\mathrm{Si}} = R^*_{\mathrm{Si}}/R^*_{\mathrm{C}}$ where we are interested in the cases where $0 < R_{\mathrm{Si}} < 1$. The domains for the entire nano-particle, the silicon core and the graphite shell are therefore denoted by

$$\Omega = \{r : 0 \leq r \leq 1\}, \tag{2.64a}$$

$$\Omega_{\mathrm{Si}} = \{r : 0 \leq r \leq R_{\mathrm{Si}}\}, \tag{2.64b}$$

$$\Omega_{\mathrm{C}} = \{r : R_{\mathrm{Si}} < r \leq 1\}, \tag{2.64c}$$

respectively.

Note here that we have $a = \{\mathrm{Si}, \mathrm{C}\}$ rather than $a = 1, \ldots, n$ as in the general derivation in Section 2.3. The boundary between the anode and the electrolyte, Γ_{e}, is now $r = 1$ and we denote the boundary between the silicon core and the graphite shell as $\Gamma_{\mathrm{Si,C}}$ at $r = R_{\mathrm{Si}}$. A two-dimensional slice of this geometry is shown in Figure 2.1.

2.4.2 Displacement, Stresses and Chemical Potentials

The displacement in each material of the anode is of the form of (2.55), therefore the expressions for the displacement in the silicon and graphite are

$$u = A_{\mathrm{Si}} r + \frac{B_{\mathrm{Si}}}{r^2} \qquad \text{in } \Omega_{\mathrm{Si}}, \tag{2.65a}$$

$$u = A_{\mathrm{C}} r + \frac{B_{\mathrm{C}}}{r^2} \qquad \text{in } \Omega_{\mathrm{C}}, \tag{2.65b}$$

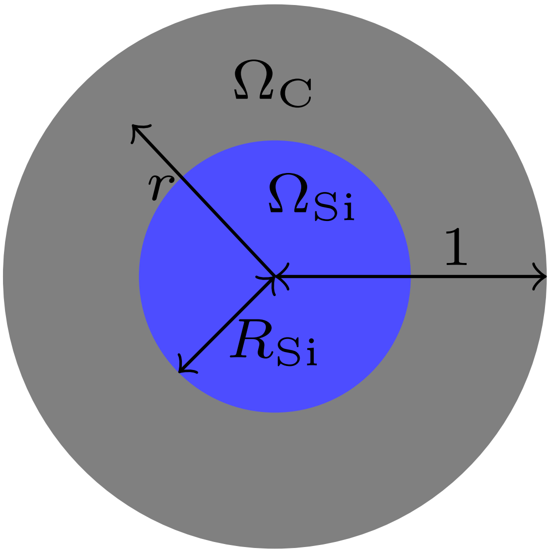

Figure 2.1: Schematic of a two-dimensional slice through a spherical nano-particle with a spherical central silicon core denoted by Ω_{Si} and a graphite shell denoted by Ω_{C}. The outer radii of the two regions are labelled as R_{Si} and 1, respectively, and the direction of the spatial variable r is labelled.

respectively. The stress components in each material are given in the same form as (2.56) by

$$\sigma_{rr} = (3\lambda_{\mathrm{Si}} + 2G_{\mathrm{Si}})(A_{\mathrm{Si}} - \gamma_{\mathrm{Si}} c_{\mathrm{Si}}) - \frac{4G_{\mathrm{Si}} B_{\mathrm{Si}}}{r^3} \qquad \text{in } \Omega_{\mathrm{Si}}, \tag{2.66a}$$

$$\sigma_{rr} = (3\lambda_{\mathrm{C}} + 2G_{\mathrm{C}})(A_{\mathrm{C}} - \gamma_{\mathrm{C}} c_{\mathrm{C}}) - \frac{4G_{\mathrm{C}} B_{\mathrm{C}}}{r^3} \qquad \text{in } \Omega_{\mathrm{C}}, \tag{2.66b}$$

$$\sigma_{\theta\theta} = \sigma_{\phi\phi} = (3\lambda_{\mathrm{Si}} + 2G_{\mathrm{Si}})(A_{\mathrm{Si}} - \gamma_{\mathrm{Si}} c_{\mathrm{Si}}) + \frac{2G_{\mathrm{Si}} B_{\mathrm{Si}}}{r^3} \qquad \text{in } \Omega_{\mathrm{Si}}, \tag{2.66c}$$

$$\sigma_{\theta\theta} = \sigma_{\phi\phi} = (3\lambda_{\mathrm{C}} + 2G_{\mathrm{C}})(A_{\mathrm{C}} - \gamma_{\mathrm{C}} c_{\mathrm{C}}) + \frac{2G_{\mathrm{C}} B_{\mathrm{C}}}{r^3} \qquad \text{in } \Omega_{\mathrm{C}}, \tag{2.66d}$$

where λ_{Si}, λ_{C}, G_{Si} and G_{C} are all dependent on the lithium concentration. The potential in each material (2.57) is given by

$$\mu = \mu_{\mathrm{Si}}^{\mathrm{SF}}(c_{\mathrm{Si}}) - 3S_{\mathrm{Si}}^{d}(3\lambda_{\mathrm{Si}} + 2G_{\mathrm{Si}})(A_{\mathrm{Si}} - \gamma_{\mathrm{Si}} c_{\mathrm{Si}}) \qquad \text{in } \Omega_{\mathrm{Si}}, \tag{2.67a}$$

$$\mu = \mu_{\mathrm{C}}^{\mathrm{SF}}(c_{\mathrm{C}}) - 3S_{\mathrm{C}}^{d}(3\lambda_{\mathrm{C}} + 2G_{\mathrm{C}})(A_{\mathrm{C}} - \gamma_{\mathrm{C}} c_{\mathrm{C}}) \qquad \text{in } \Omega_{\mathrm{C}}. \tag{2.67b}$$

Lastly, the SOC condition (2.59) is given by

$$c_0 \left[c_{\mathrm{Si}}^{\max} R_{\mathrm{Si}}^3 + c_{\mathrm{C}}^{\max} \left(1 - R_{\mathrm{Si}}^3\right) \right] = c_{\mathrm{Si}}^{\max} R_{\mathrm{Si}}^3 c_{\mathrm{Si}} + c_{\mathrm{C}}^{\max} (1 - R_{\mathrm{Si}}^3) c_{\mathrm{C}}. \tag{2.68}$$

2.4.3 Boundary Conditions

To find the integration constants A_{Si}, B_{Si}, A_{C} and B_{C}, we must solve the boundary conditions to the mechanical problem (2.58). Additionally to these, we prescribe the displacement to be zero at $r = 0$ as we do not account for cavitation. The full system of boundary conditions is given by

$$u = 0 \text{ at } r = 0, \tag{2.69a}$$

$$[u]_-^+ = 0 \text{ at } r = R_{\mathrm{Si}}, \tag{2.69b}$$

$$[\sigma_{rr}]_-^+ = 0 \text{ at } r = R_{\mathrm{Si}}, \tag{2.69c}$$

$$\sigma_{rr} = 0 \text{ at } r = 1. \tag{2.69d}$$

Using (2.65) and (2.66), we can write these as

$$B_{\mathrm{Si}} = 0, \tag{2.70a}$$

$$A_{\mathrm{Si}} R_{\mathrm{Si}} = A_{\mathrm{C}} R_{\mathrm{Si}} + \frac{B_{\mathrm{C}}}{R_{\mathrm{Si}}^2}, \tag{2.70b}$$

$$(3\lambda_{\mathrm{Si}} + 2G_{\mathrm{Si}})(A_{\mathrm{Si}} - \gamma_{\mathrm{Si}} c_{\mathrm{Si}}) = (3\lambda_{\mathrm{C}} + 2G_{\mathrm{C}})(A_{\mathrm{C}} - \gamma_{\mathrm{C}} c_{\mathrm{C}}) - \frac{4G_{\mathrm{C}} B_{\mathrm{C}}}{R_{\mathrm{Si}}^3}, \tag{2.70c}$$

$$(3\lambda_{\mathrm{C}} + 2G_{\mathrm{C}})(A_{\mathrm{C}} - \gamma_{\mathrm{C}} c_{\mathrm{C}}) = 4G_{\mathrm{C}} B_{\mathrm{C}}, \tag{2.70d}$$

where (2.70a) has been used to simplify (2.70b) and (2.70c).

2.4.4 Solutions

The system of linear equations (2.70) can be solved to give the integration constants in terms of the concentrations c_{Si} and c_{C} and the Lamé parameters λ_a and G_a. These are given by

$$\begin{aligned} A_{\mathrm{Si}} = \frac{1}{\omega}\Big[&(3\lambda_{\mathrm{Si}} + 2G_{\mathrm{Si}})\big((3\lambda_{\mathrm{C}} + 2G_{\mathrm{C}}) + 4G_{\mathrm{C}} R_{\mathrm{Si}}^3\big)\gamma_{\mathrm{Si}} c_{\mathrm{Si}} \\ &+ 4G_{\mathrm{C}}(3\lambda_{\mathrm{C}} + 2G_{\mathrm{C}})(1 - R_{\mathrm{Si}}^3)\gamma_{\mathrm{C}} c_{\mathrm{C}}\Big], \end{aligned} \tag{2.71a}$$

$$\begin{aligned} A_{\mathrm{C}} = \frac{1}{\omega}\Big[&(3\lambda_{\mathrm{C}} + 2G_{\mathrm{C}})\big(4G_{\mathrm{C}}(1 - R_{\mathrm{Si}}^3) + (3\lambda_{\mathrm{Si}} + 2G_{\mathrm{Si}})\big)\gamma_{\mathrm{C}} c_{\mathrm{C}} \\ &+ 4G_{\mathrm{C}}(3\lambda_{\mathrm{Si}} + 2G_{\mathrm{Si}}) R_{\mathrm{Si}}^3 \gamma_{\mathrm{Si}} c_{\mathrm{Si}}\Big], \end{aligned} \tag{2.71b}$$

$$B_{\mathrm{C}} = \frac{1}{\omega}\Big[(3\lambda_{\mathrm{Si}} + 2G_{\mathrm{Si}})(3\lambda_{\mathrm{C}} + 2G_{\mathrm{C}})(\gamma_{\mathrm{Si}} c_{\mathrm{Si}} - \gamma_{\mathrm{C}} c_{\mathrm{C}}) R_{\mathrm{Si}}^3\Big], \tag{2.71c}$$

where

$$\begin{aligned} \omega = {}&(3\lambda_{\mathrm{Si}} + 2G_{\mathrm{Si}})(3\lambda_{\mathrm{C}} + 2G_{\mathrm{C}}) \\ &+ 4G_{\mathrm{C}}\big((3\lambda_{\mathrm{C}} + 2G_{\mathrm{C}})(1 - R_{\mathrm{Si}}^3) + (3\lambda_{\mathrm{Si}} + 2G_{\mathrm{Si}}) R_{\mathrm{Si}}^3\big). \end{aligned} \tag{2.72}$$

To solve the chemical problem, (2.71a) and (2.71b) are substituted into (2.67) and these are equated to find an algebraic equation relating c_{Si} and c_{C} given by

$$\begin{aligned}\mu_{\mathrm{Si}}^{\mathrm{SF}}(c_{\mathrm{Si}}) - 3S_{\mathrm{Si}}^{d}(3\lambda_{\mathrm{Si}} + 2G_{\mathrm{Si}})(A_{\mathrm{Si}} - \gamma_{\mathrm{Si}}c_{\mathrm{Si}}) \\ = \mu_{\mathrm{C}}^{\mathrm{SF}}(c_{\mathrm{C}}) - 3S_{\mathrm{C}}^{d}(3\lambda_{\mathrm{C}} + 2G_{\mathrm{C}})(A_{\mathrm{C}} - \gamma_{\mathrm{C}}c_{\mathrm{C}}).\end{aligned} \tag{2.73}$$

We rearrange the SOC condition (2.68) to read

$$c_{\mathrm{Si}} = c_0 + \frac{c_{\mathrm{C}}^{\max}}{c_{\mathrm{Si}}^{\max}}\left(1 - R_{\mathrm{Si}}^{-3}\right)(c_{\mathrm{C}} - c_0), \tag{2.74}$$

and we substitute this into (2.73) to obtain a single algebraic equation in c_{C} for a given SOC, c_0. When solving this equation numerically it is important to note that c_{Si} and c_{C} must be between zero and one and we can use (2.74) to place bounds on c_{C} to find that

$$\max\left\{0, \frac{(1-c_0)c_{\mathrm{Si}}^{\max}R_{\mathrm{Si}}^3}{c_{\mathrm{C}}^{\max}(R_{\mathrm{Si}}^3 - 1)} + c_0\right\} < c_{\mathrm{C}} < \min\left\{1, c_0 - \frac{c_0 c_{\mathrm{Si}}^{\max}R_{\mathrm{Si}}^3}{c_{\mathrm{C}}^{\max}(R_{\mathrm{Si}}^3 - 1)}\right\}. \tag{2.75}$$

The first and second elements of the maximum and minimum functions in (2.75) ensure that $c_{\mathrm{C}} \in [0,1]$ and $c_{\mathrm{Si}} \in [0,1]$, respectively.

After c_{C} is found, we use (2.74) to calculate c_{Si}, then calculate the Lamé parameters for each material at c_{Si} and c_{C} and substitute these into (2.71) to find the integration constants. Lastly, we substitute the integration constants into (2.65) and (2.66) to yield the displacement and stresses, fully solving the problem.

2.5 Mechanical and Chemical Results

In this section, we plot the lithium concentration, chemical potential, displacement and stresses within the nano-particle consisting of a silicon core and a graphite shell, as shown in Figure 2.1. We present results for different initial volumes of the silicon core and for different states of charge.

2.5.1 Parameter Derivation

In Table 2.1, we present all the parameters we will be using in the remainder of this thesis. The relative expanded volume, J_a^c, maximum stoichiometric ratio of lithium $x_a^{\max}$ and molar volume V_a^m are all taken from the literature based on experimental results. We can then calculate the theoretical maximum lithium concentrations $c_{\mathrm{Si}}^{\max}$ and $c_{\mathrm{C}}^{\max}$ by

$$c_a^{\max} = \frac{x_a^{\max}}{V_a^m} \qquad \text{for } a = \mathrm{Si}, \mathrm{C}, \tag{2.76}$$

Parameter	Description	Silicon	Graphite
J_a^c	Expanded volume at $c_a = 1$	3.8[66]	1.1[86]
$x_a^{\max}$	Max. stoichiometric ratio of Li	3.75[45]	0.167[13]
V_a^m	Molar volume ($\mathrm{m^3 mol^{-1}}$)	1.205×10^{-5}[25]	8.69×10^{-6}[125]
$c_a^{\max}$	Maximum Li conc. ($\mathrm{mol\ m^{-3}}$)	3.11×10^5	1.92×10^4
η_a	CCE	0.2489	0.2
ν_a	Poisson's ratio	0.29[86]	0.32[86]
E_a^0	Young's modulus at $c_a = 0$ (GPa)	96[86]	32[86]
E_a^1	Young's modulus at $c_a = 1$ (GPa)	41[86]	109[86]
η_a^E	Variation of E with Li conc.	-0.1528	14.4375
γ_a	Eq. 2.13	1.0	0.0357
S_a^d	Eq. 2.40	42.046	24.362

Table 2.1: Material parameters of silicon and graphite.

giving the values seen in Table 2.1. The coefficients of compositional expansion (CCE), η_a, can be calculated by rearranging (2.4) to yield

$$\eta_a = \frac{J_a^c - 1}{3V_a^m c_a^{\max}} = \frac{J_a^c - 1}{3x_a^{\max}} \quad \text{for } a = \mathrm{Si}, \mathrm{C}. \tag{2.77}$$

It is well known that the Young's moduli of some anode materials vary with the SOC [86]. For silicon and graphite specifically, the Young's moduli vary linearly with lithium concentration [99, 85]. The Poisson's ratios of each material, ν_{Si} and ν_{C}, have been shown to only have a small lithium concentration dependence and thus we take these as constant [25, 86]. Therefore, we define the dimensional Lamé parameters of each material as

$$\lambda_a^* = \frac{E_a^0(1 + \eta_a^E x_a^{\max} c_a)\nu_a}{(1+\nu_a)(1-2\nu_a)}, \quad G_a^* = \frac{E_a^0(1 + \eta_a^E x_a^{\max} c_a)}{2(1+\nu_a)} \quad \text{for } a = \mathrm{Si}, \mathrm{C}, \tag{2.78}$$

where E_a^0 is the Young's modulus at zero lithiation, η_a^E is the linear variation of the Young's modulus with concentration and ν_a is the Poisson's ratio. These parameters are then nondimensionalised to λ_a and G_a using (2.22). We take the values for E_a^0 from the zero lithiation values calculated by Qi *et al.* using DFT calculations [86] as shown in Table 2.1. We then derive the η_a^E values by using the Young's moduli of fully lithiated silicon and graphite, E_a^1, again calculated by Qi *et al.* [86], by rearranging the expression for the Young's modulus to give

$$\eta_a^E = \frac{1}{x_a^{\max}}\left(\frac{E_a^1}{E_a^0} - 1\right), \tag{2.79}$$

giving the values in Table 2.1.

2.5.1.1 Extracting μ_a^{SF} from data

Despite the complexity of the majority of mathematical models for lithium-ion battery anodes which almost unanimously require numerical methods to solve, the stress-free chemical potential, μ_a^{SF}, is very often approximated using a fitted function instead of interpolating experimental data [13, 25, 97]. These approximations fail to capture the large steps in chemical potential that occur at transitions in the structure of the intercalated anode, particularly apparent in the OCV of graphite [6]. In this thesis, we do not use a simple fitted function for μ_a^{SF} but instead use an interpolated function of the OCV data points. Here we explain exactly how the experimentally obtained OCV data are converted to the $\mu_a^{\mathrm{SF}}(c_a)$ function used in the model.

We take data for silicon from Figure 4c of [60] which measures the potential of the silicon anode during the second lithiation of the anode (this is called the second discharge in [60]). The silicon is believed to be crystalline before lithiation and becomes amorphous during the first charge–discharge cycle as shown in [60]. We have assumed isotropy in both the silicon and graphite, which is a good assumption for amorphous silicon but not crystalline silicon, and thus we take data from the second lithiation. We take data for the OCV of graphite from Figure 1 of [88] taking the charging data, as opposed to the discharging data because we are interested in the stresses caused when charging instead of discharging[†]. Both of these plots are not exact OCVs as this is impossible to achieve in practice but are measured at very low charging rates. The charging rates are measured using C-rates, defined by the current through the battery compared to the theoretical current under which the battery would deliver its capacity in one hour. Therefore, a battery charged to full capacity in 2 hours is being charged at a C-rate of $C/2$. The data for silicon in [60] is measured at a C-rate of $C/100$ and the data for graphite in [88] at $C/50$, because of this they are technically pseudo-OCVs. Both of the pseudo-OCVs for the anodes are measured against a lithium metal cathode, which is standard for these types of measurements, allowing us to ignore the last term in (2.37) when comparing them.

We extract the (x, y) coordinates from the figures in [60] and [88] using the software `grabit` [29] and normalise the x-coordinate values such that the SOC varies between zero (not lithiated) to one (fully lithiated). This has a large implication for the silicon data as in [60], the voltage is plotted against specific capacity and after the first cycle, the anode cannot be fully delithiated again but remains at a capacity

---

[†] As we only consider elasticity in this chapter, the charging and discharging behaviours are identical. However, when we study yielding mechanisms in Chapter 5, this becomes an important distinction.

of around 1117 mAhg^{-1}. The reasoning for the normalisation in this case is because the minimum capacity stays reasonably close to this value for the subsequent cycles, meaning this is the practical range of lithiation states after the first cycle. Therefore, after this normalisation, a capacity of 1117 mAhg^{-1} corresponds to zero SOC. We then multiply the y-coordinate values by $-e$ and Avagadro's constant using (2.37), nondimensionalise using (2.38) and linearly interpolate between the data points. We plot the linearly interpolated nondimensional chemical potentials as functions of lithium concentration for silicon and graphite in Figure 2.2.

As the materials have a minimum and maximum lithium concentration they can tolerate, if the chemical potential that is induced in the anode material is less than the minimum chemical potential recorded in the OCV data (≈ -57 kJ mol^{-1} for silicon, ≈ -28 kJ mol^{-1} for graphite), we take $c_a = 0$. Similarly, if the induced potential is greater than the maximum chemical potential recorded (≈ 0 kJ mol^{-1} for both silicon and graphite), we prescribe $c_a = 1$. When functions of lithium concentration, c, are fitted to analytic functions instead, this behaviour is usually accounted for using logarithmic terms which are singular at $c = 0$ and $c = 1$. This is more physically accurate as anodes can never be completely lithiated in practice. The procedure outlined here is one of the disadvantages to using interpolated functions for the stress-free chemical potential as opposed to fitting functions.

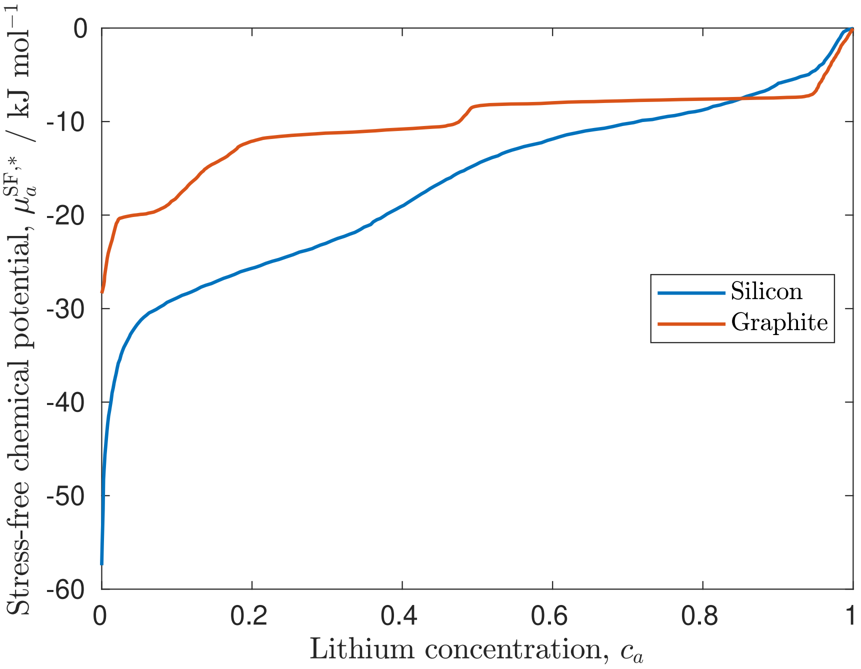

Figure 2.2: Stress-free chemical potential $\mu^{\mathrm{SF},*}$ as a function of nondimensional concentration for each material, c_{Si} and c_{C}.

2.5.2 Chemical Results

In Figure 2.3 we plot c_{Si} and c_{C} against c_0 for different initial volumes of the silicon core, $V_{\mathrm{Si}} = R_{\mathrm{Si}}^3$, using the method described in Section 2.4.4. It can be seen that the graphite is saturated ($c_{\mathrm{C}} = 1$) at fairly low c_0 values, especially for large silicon cores, whereas the lithium concentration in the silicon, c_{Si}, remains relatively low until the graphite is saturated. As c_0 increases past the value at which the graphite is saturated, all the lithium being intercalated must be intercalated into the silicon and thus c_{Si} is linear in c_0 in this region of Figure 2.3.

The saturation of the graphite and the low c_{Si} values at low SOC are due to the hydrostatic stresses induced in the silicon core and graphite shell. The trace of the Cauchy stress in each material, given by $3(3\lambda_a + 2G_a)(A_a - \gamma_a c_a)$, which is uniform in r, is plotted against c_0 in Figure 2.4 for different initial volumes of silicon core, V_{Si}. As $\gamma_{\mathrm{Si}} \gg \gamma_{\mathrm{C}}$, the expansion of the silicon is much greater than that of the graphite. Therefore, when lithiated, the expanding silicon is being constrained by the graphite shell, inducing a compressive stress in the silicon, causing $\mathrm{tr}(\boldsymbol{\sigma})$ to be negative in Ω_{Si}. Conversely, the graphite is being stretched by the large expansion of silicon, inducing a tensile stress, causing $\mathrm{tr}(\boldsymbol{\sigma})$ to be positive in Ω_{C}.

From (2.39), the tensile stress in the graphite lowers the chemical potential of the

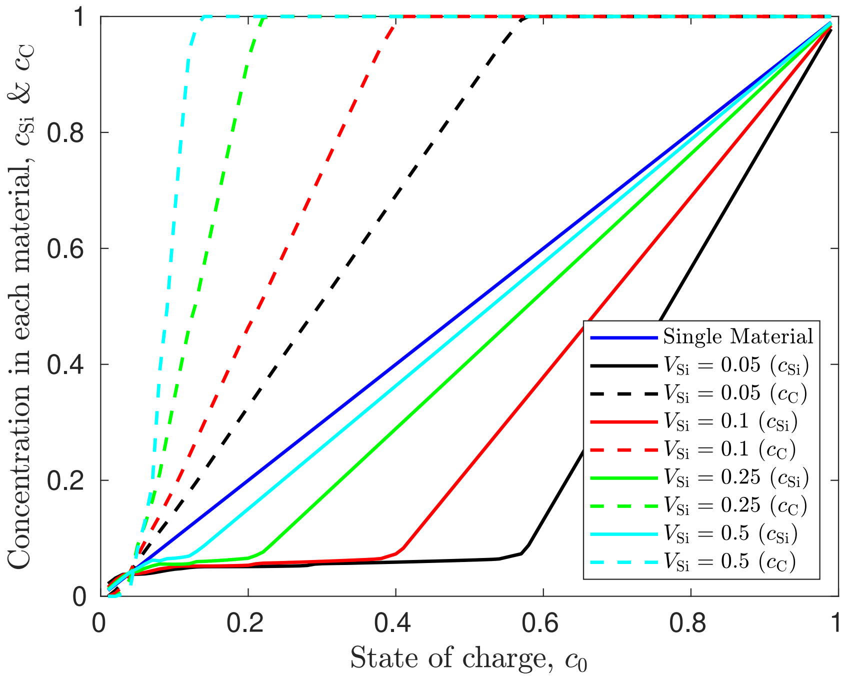

Figure 2.3: Nondimensional concentrations in each material, c_{Si} and c_{C}, against SOC, c_0, for different initial volumes of the silicon core, V_{Si}.

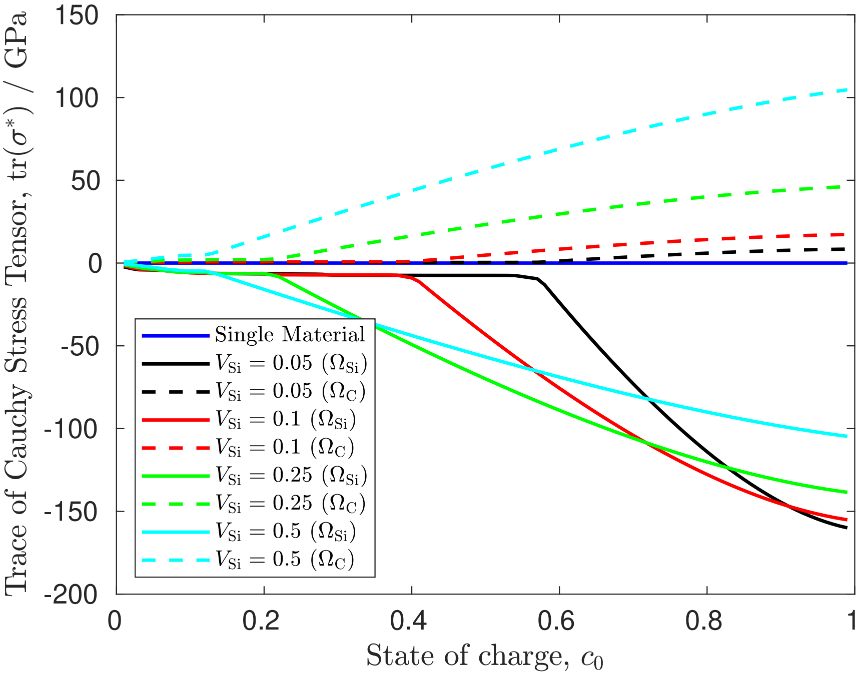

Figure 2.4: Trace of the Cauchy stress tensor, $\sigma^*_{rr} + 2\sigma^*_{\theta\theta}$, against SOC, c_0, for silicon (solid lines) and graphite (dashed lines) for different initial volumes of the silicon core, V_{Si}.

lithium whereas the compressive stress in the silicon increases the chemical potential of the lithium. For the chemical potential of the lithium to be equal in each material, $\mu^{\mathrm{SF}}_{\mathrm{Si}}(c_{\mathrm{Si}})$ must therefore decrease and $\mu^{\mathrm{SF}}_{\mathrm{C}}(c_{\mathrm{C}})$ must increase. As $\mu^{\mathrm{SF}}_{\mathrm{Si}}(c_{\mathrm{Si}})$ and $\mu^{\mathrm{SF}}_{\mathrm{C}}(c_{\mathrm{C}})$ are monotonically increasing functions of c_{Si} and c_{C}, respectively, c_{Si} must decrease and c_{C} must increase. Returning to Figure 2.3, the lithium concentration in the graphite saturates at larger c_0 values as the initial volume of the silicon core decreases. This is because the graphite shell gets thicker as the initial silicon core volume decreases and the smaller silicon cores induce less stress, as seen in Figure 2.4.

In Figure 2.5 we plot the chemical potential, μ, of the lithium in the nano-particle against c_0 for different initial volumes of the silicon core, V_{Si}. Given the condition (2.73), this is the same in each material and thus we denote this as the multi-material anode potential. It can be seen from the left plot of Figure 2.5, that for c_0 values for which the graphite is saturated, the chemical potential is much greater than that of the individual materials. This is because if the graphite is saturated at a certain SOC and more lithium is then intercalated, the lithium concentration in the silicon must increase. This increases $\mu^{\mathrm{SF}}_{\mathrm{Si}}(c_{\mathrm{Si}})$, but also decreases $\mathrm{tr}(\boldsymbol{\sigma})$ as seen in Figure 2.4, causing the chemical potential to increase rapidly with increasing SOC. In practice, the battery would not be charged at a low enough voltage to achieve these high

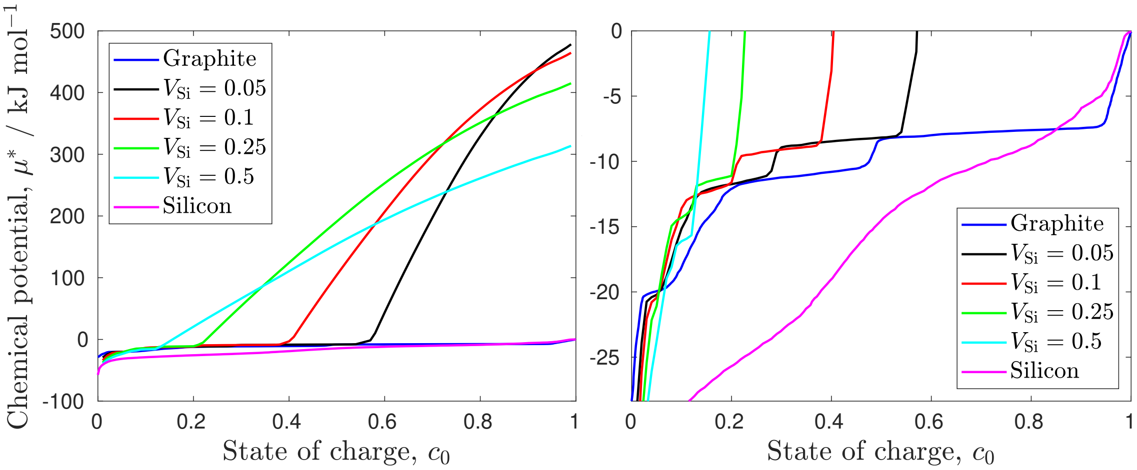

Figure 2.5: Chemical potential, μ^*, of the multi-material nano-particle against SOC, c_0, for different initial volumes of the silicon core, V_{Si}. The right plot is identical to the left plot with a smaller range of μ^*.

lithium concentrations and either the lithium will not intercalate into the silicon, or other mechanisms will occur, such as cracking of the graphite to allow the silicon to continue to be lithiated. However, even for states of charge at which the graphite is not saturated, the multi-material chemical potential deviates significantly from the stress-free chemical potentials of the individual materials as seen in the right plot of Figure 2.5.

In Figures 2.6 and 2.7 we replicate Figures 2.3 and 2.5, respectively, without stress-assisted diffusion by setting $S_a^d = 0$ for $a = \mathrm{Si}, \mathrm{C}$. This is to highlight the differences caused by including stress-assisted diffusion into the chemical model. It can be seen in Figure 2.6 that $c_{\mathrm{Si}} > c_{\mathrm{C}}$ for $c_0 \lessapprox 0.85$ when $S_a^d = 0$, which is very different to the result found in Figure 2.3 in which $c_{\mathrm{Si}} < c_{\mathrm{C}}$ for $c_0 \gtrapprox 0.05$. The behaviour of c_{Si} and c_{C} in Figure 2.6 is solely due to $\mu_{\mathrm{Si}}^{\mathrm{SF}}(c_{\mathrm{Si}})$ being less than $\mu_{\mathrm{C}}^{\mathrm{SF}}(c_{\mathrm{C}})$ for $c_a \lessapprox 0.85$, as seen in Figure 2.2.

In Figure 2.7, the chemical potential of the lithium in the multi-material nano-particle, μ, is bounded by $\mu_{\mathrm{Si}}^{\mathrm{SF}}(c_{\mathrm{Si}})$ and $\mu_{\mathrm{C}}^{\mathrm{SF}}(c_{\mathrm{C}})$. This is because the high compressive stresses in the silicon causing the chemical potential to increase for high SOC are not present in the chemical potential for $S_a^d = 0$. At each SOC, the lithium is shared between the two materials. Therefore, one material has concentration $c_a < c_0$ and the other has $c_a > c_0$, or $c_{\mathrm{Si}} = c_{\mathrm{C}} = c_0$. As the stress-free potential is monotonically increasing, the multi-material effective chemical potential in this case must therefore be bounded between the two single-material chemical potentials.

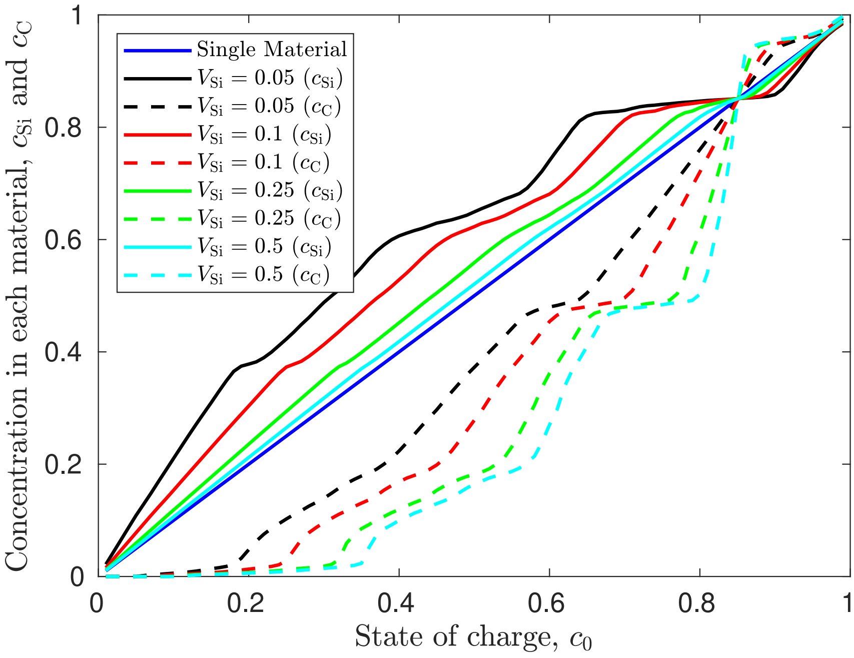

Figure 2.6: Nondimensional concentrations in each material, c_{Si} and c_{C}, against SOC, c_0, for different initial volumes of the silicon core, V_{Si}, without stress-assisted diffusion ($S_a^d = 0$).

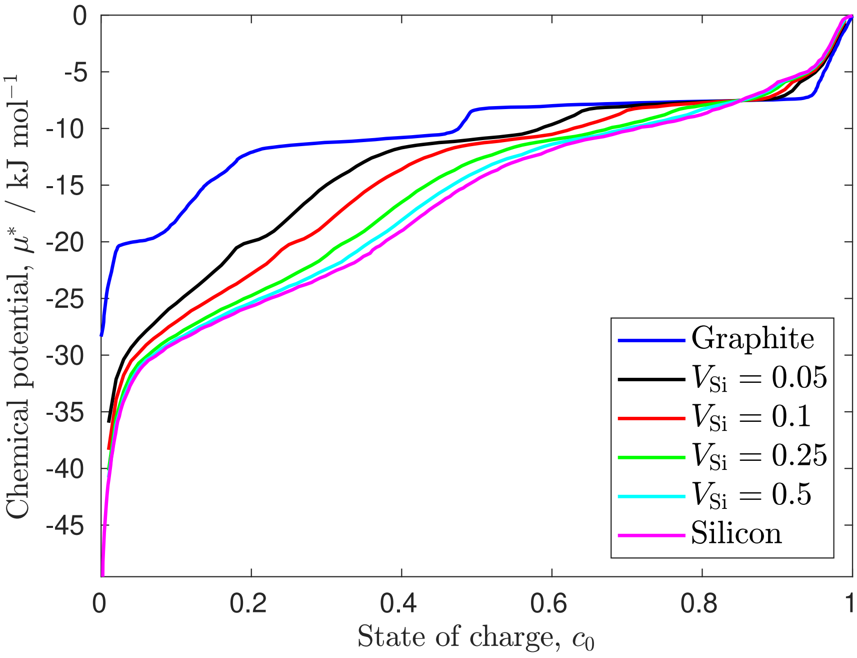

Figure 2.7: Chemical potential, μ^*, of the nano-particle against SOC, c_0, for different initial volumes of the silicon core, V_{Si}, without stress-assisted diffusion ($S_a^d = 0$).

2.5.3 Mechanical Results

In Figure 2.8, we plot the dimensional displacement relative to the outer radius, u^*/R^*_{C}, as a function of the radius, $r = r^*/R^*_{\mathrm{C}}$, for different states of charge, c_0, and for different initial volumes of silicon core, V_{Si}. As expected from the solution (2.65) and the boundary condition (2.70a), the displacement in the silicon is linear in r but not in the graphite because $B_{\mathrm{C}} \neq 0$. In Figures 2.9 and 2.10, we plot the dimensional radial stress, σ^*_{rr}, and hoop stress, $\sigma^*_{\theta\theta}$, against the radius, r, for different states of charge, c_0, and for different initial volumes of silicon core, V_{Si}. The stress in the silicon is uniform in r because $B_{\mathrm{Si}} = 0$ removes the radial dependence in the second term of (2.66a) and (2.66c). The displacement and stress profiles are qualitatively very similar to those in the time-dependent case in Figure 2d-f in [115].

Intuitively, the maximum displacement inside the nano-particle increases with the initial volume of the silicon core, V_{Si}. However, the maximum stresses in the silicon decrease with V_{Si}. This also agrees with the results in Figure 4a of [115]. This is due to the graphite shell being thinner when the silicon core is larger, causing the expansion of the silicon to be less restricted, decreasing the magnitude of the compressive stress in the silicon. The maximum hoop stress in the graphite increases with increasing V_{Si} due to the graphite shell being stretched in the azimuthal direction more by a larger silicon core.

For small V_{Si}, the displacement and stresses in the silicon are very similar for all $c_0 \lessapprox 0.5$, whereas for larger silicon cores, the displacement and stress profiles increase approximately linearly with c_0 across the entire domain, Ω. This is due to c_{Si} remaining approximately constant until the graphite is saturated, as shown in Figure 2.3, and this saturation of the graphite occurs at lower states of charge for larger values of V_{Si}. For constant c_{Si} the expansion of the silicon also remains constant, whereas the expansion of the graphite is increasing as c_{C} increases. As the graphite has a relatively low expansion, this does not induce a large stress in the silicon, meaning the stresses also remain approximately constant.

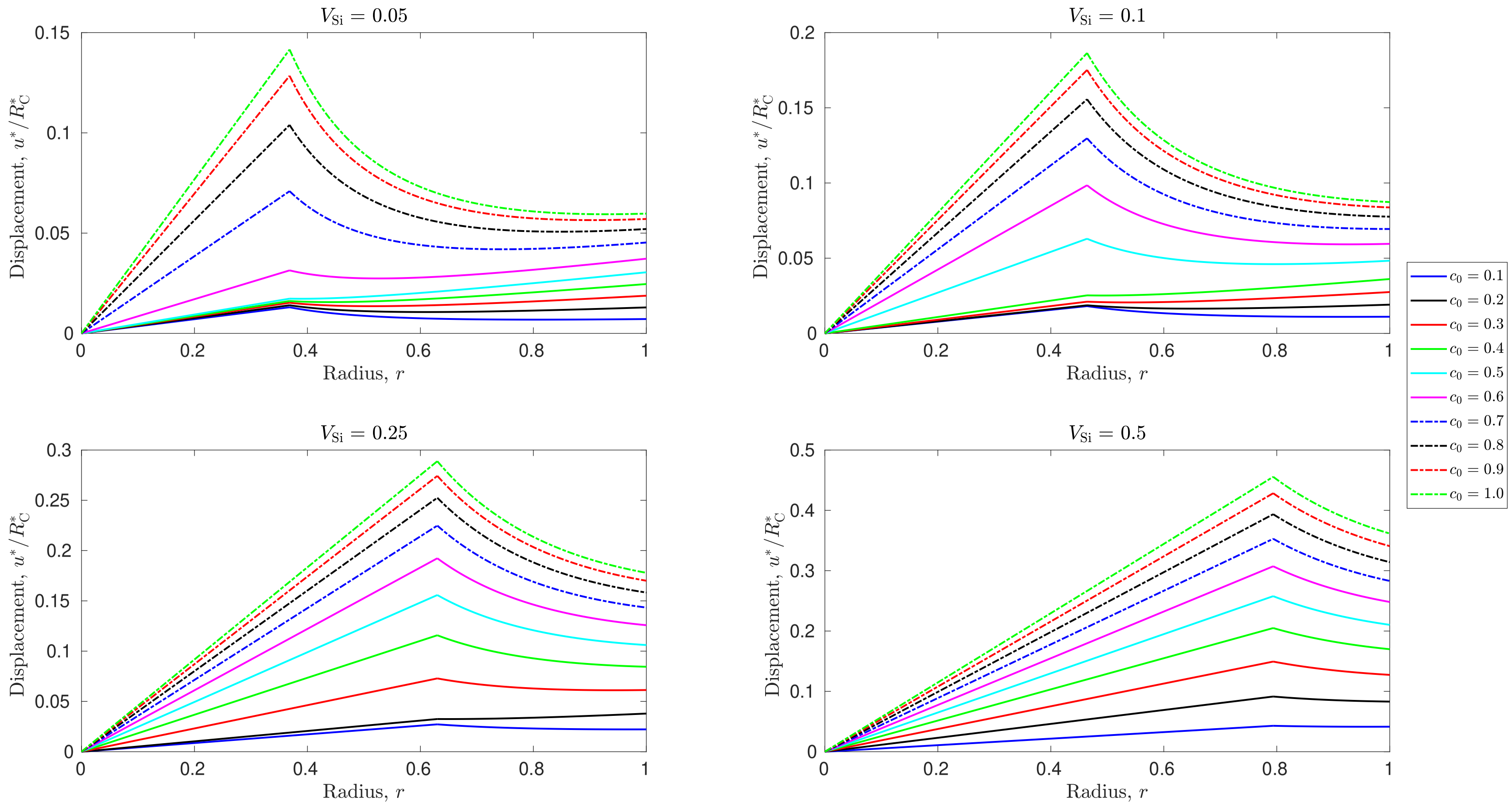

Figure 2.8: Displacement relative to the radius of the nano-particle, u^*/R^*_{C}, against radius, $r = r^*/R^*_{\mathrm{C}}$, for different initial volumes of the silicon core, V_{Si}, and for different states of charge, c_0. Note the change of vertical axis in each subplot.

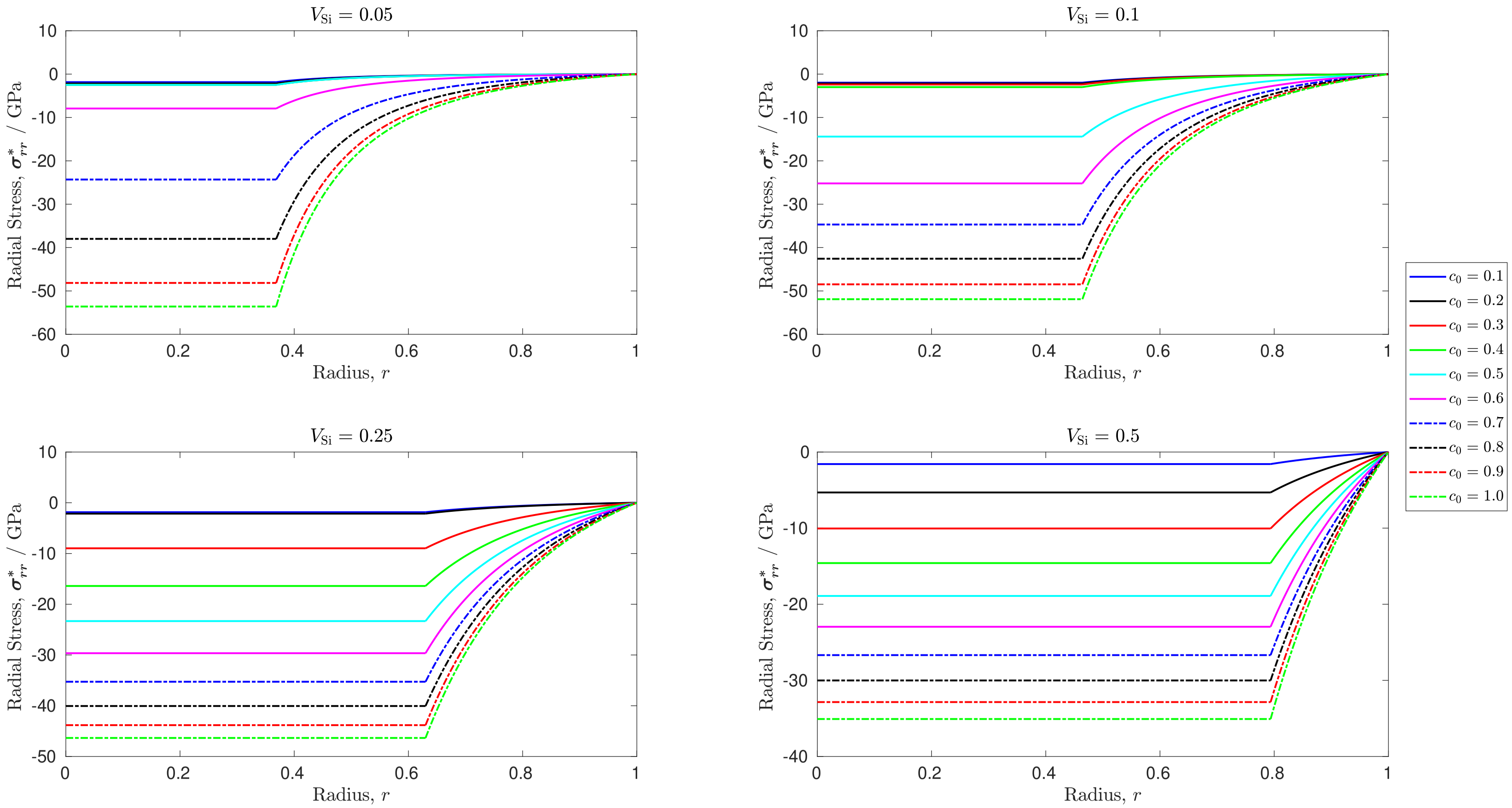

Figure 2.9: Radial stress, σ^*_{rr}, against radius, $r = r^*/R^*_{\mathrm{C}}$, for different initial volumes of the silicon core, V_{Si}, and for different states of charge, c_0. Note the change of vertical axis in each subplot.

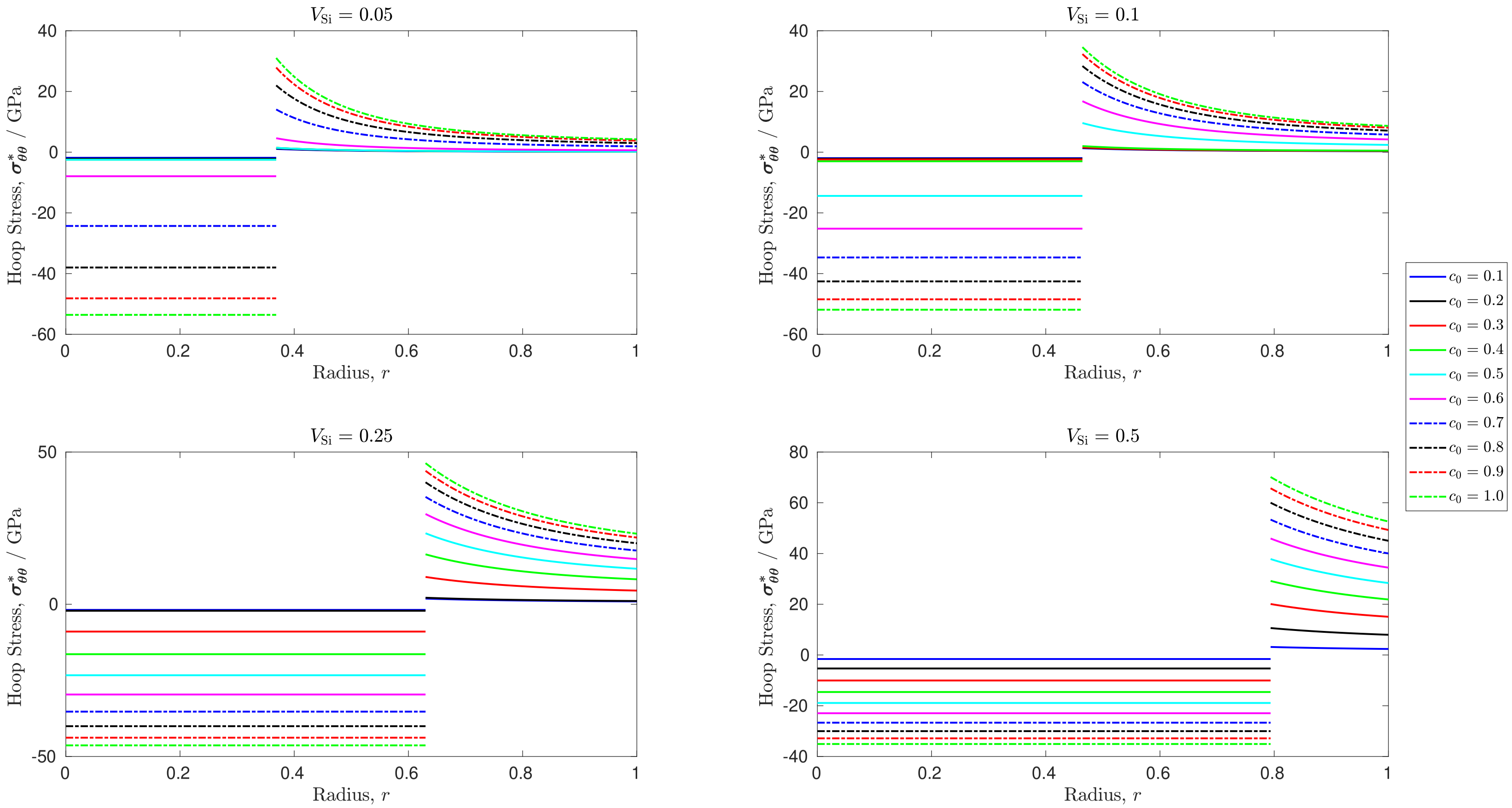

Figure 2.10: Hoop stress, $\sigma^*_{\theta\theta}$, against radius, $r = r^*/R^*_{\mathrm{C}}$, for different initial volumes of the silicon core, V_{Si}, and for different states of charge, c_0. Note the change of vertical axis in each subplot.

2.6 Silicon Core Volume Optimisation

In this section, we aim to find the optimal initial volume of the silicon core in the nano-particle in Figure 2.1, based on the results of the model presented in this chapter. We introduce three performance measures: the relative amount of lithium, the expanded volume and the maximum induced stress. We then investigate the optimal initial core volume according to three criteria based on these performance measures: volumetric capacity, and maximising the amount of lithium subject to constraints on the expanded volume and the induced stress.

2.6.1 Performance Measures

To define the objective functions we will use in the optimisation of the initial silicon core volume, it is helpful to define three performance measures. The measures we use are the relative amount of lithium, the relative expanded volume of the nano-particle and the maximum induced stress inside the nano-particle.

2.6.1.1 Relative Amount of Lithium

The capacity of a lithium-ion battery is closely related to the amount of lithium that the anode can accommodate and thus this is a very important performance measure of a lithium-ion battery anode. For a general anode with domain Ω and different anode materials $i = 1, \ldots, n$, each with domain Ω_i, we measure the total amount of intercalated lithium relative to a fully lithiated anode of material 1 and domain Ω. The relative amount of lithium is therefore given by

$$Q = \frac{\sum_{i=1}^{n} \int_{\Omega_i} c_i^* \, \mathrm{d}V}{\int_{\Omega} c_1^{\max} \, \mathrm{d}V}. \tag{2.80}$$

For the nano-particle comprising a silicon core and a graphite shell which we consider in this section, (2.80) is given by

$$Q = c_{\mathrm{Si}} R_{\mathrm{Si}}^3 + c_{\mathrm{C}} \frac{c_{\mathrm{C}}^{\max}}{c_{\mathrm{Si}}^{\max}} (1 - R_{\mathrm{Si}}^3). \tag{2.81}$$

2.6.1.2 Expanded Volume

We now consider the expansion of the anode by calculating the volume of the expanded nano-particle compared to its original volume and denote this as V. For a nano-particle with a silicon core and graphite shell, V can be calculated as

$$V = \frac{\frac{4\pi}{3}(R_{\mathrm{C}}^* + u^*(R_{\mathrm{C}}^*))^3}{\frac{4\pi}{3} R_{\mathrm{C}}^{*3}} = \left(1 + \eta_{\mathrm{Si}} V_{\mathrm{Si}}^m c_{\mathrm{Si}}^{\max} u(1)\right)^3, \tag{2.82}$$

where $u^* = \eta_{\mathrm{Si}} V_{\mathrm{Si}}^m c_{\mathrm{Si}}^{\max} R_{\mathrm{C}}^* u$ is the dimensional displacement. In the linearised model we use in this chapter, we assume that $\eta_{\mathrm{Si}} V_{\mathrm{Si}}^m c_{\mathrm{Si}}^{\max} \ll 1$. Using this assumption, we approximate (2.82) by

$$V \approx 1 + 3\eta_{\mathrm{Si}} V_{\mathrm{Si}}^m c_{\mathrm{Si}}^{\max} u(1). \tag{2.83}$$

We plot the linearised V (2.83) against V_{Si} for different states of charge in Figure 2.11. It can be seen that V increases with V_{Si} and this trend becomes more prominent for larger V_{Si}. Additionally, a greater SOC causes a greater V for all values of V_{Si}.

In Figure 2.12, we plot the exact V (2.82), and the linearised V (2.83), against V_{Si} for different states of charge. We can see that for small V_{Si} and for small c_0, the linearised and exact V are similar. However, for large silicon cores and high states of charge, the exact V exceeds $J_{\mathrm{Si}}^c = 3.8$, which is counter-intuitive as this is the expanded volume of unconstrained silicon. This is because we required that $\eta_a x_a^{\max} \ll 1$ for $a =$ Si, C, to make the approximation that the anode behaves according to linear elasticity. However, $\eta_{\mathrm{Si}} x_{\mathrm{Si}}^{\max} = 0.933$, so the linearisation of the model assuming that $\eta_{\mathrm{Si}} V_{\mathrm{Si}}^m c_{\mathrm{Si}}^{\max} \ll 1$ breaks down for high states of charge and large silicon cores. This causes much larger displacements than physically expected at high states of charge and so the nonlinear elasticity formulation should be retained to produce

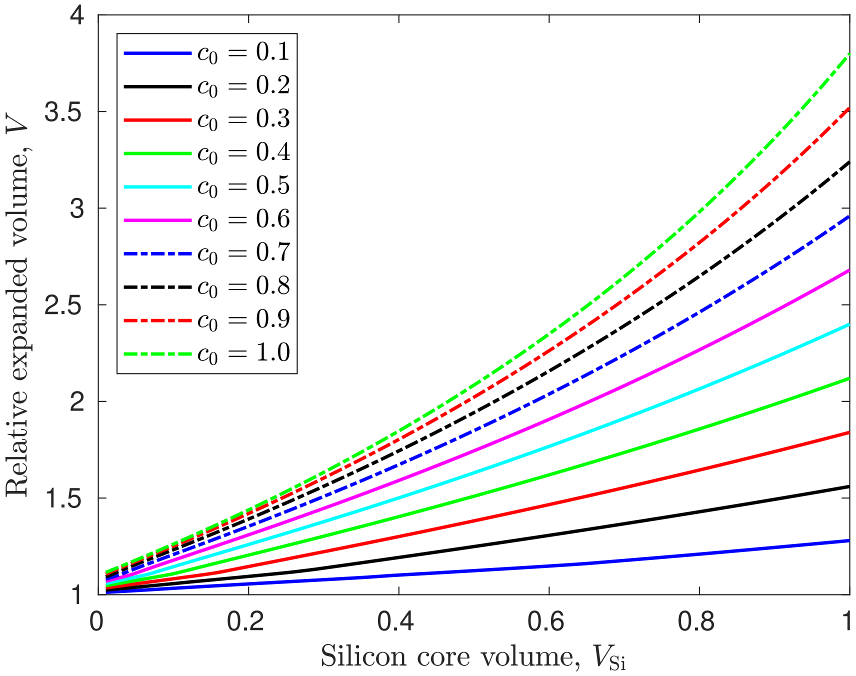

Figure 2.11: Linearised relative expanded volume, V, given by (2.83), against the initial volume of the silicon core, V_{Si}, and for different states of charge, c_0.

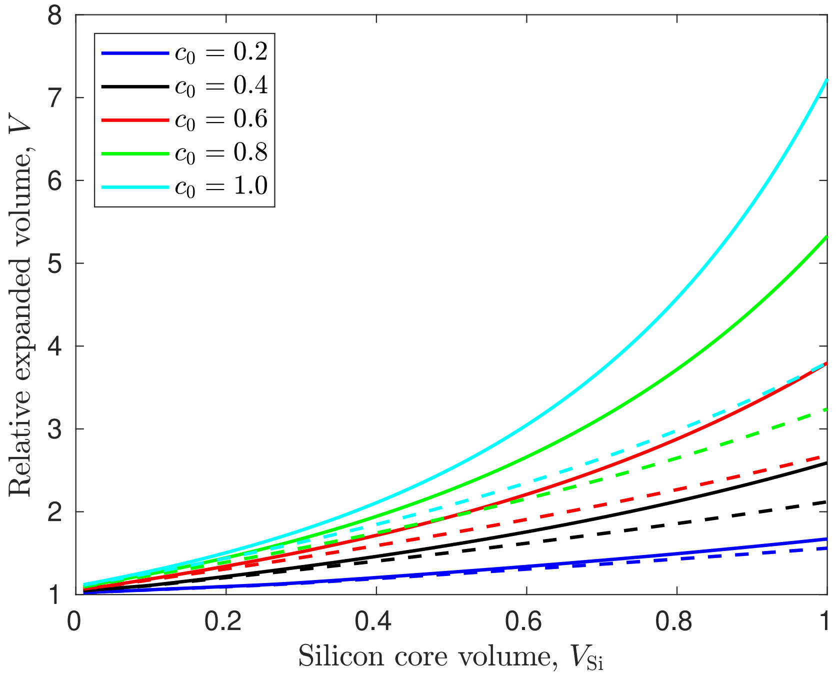

Figure 2.12: Exact relative expanded volume using (2.82) (solid lines) and the linearised relative expanded volume using (2.83) (dashed lines), against the initial volume of the silicon core, V_{Si}, and for different states of charge, c_0.

quantitatively accurate results for silicon at high concentrations. We take the linearised volume expansion (2.83) in the subsequent optimisation problems in order to be consistent with the linear model in this chapter.

2.6.1.3 Maximum Induced Stress

Capacity fade exhibited by expanding anode materials after cycling is often attributed to cracks in the anode material [75]. These cracks are caused by high stresses and thus the final performance measure we define is the maximum induced stress within the nano-particle. We use the von Mises stress [48] as a scalar effective stress measure. For a general anode geometry, this is given by

$$\sigma^*_{\text{eff}} = \left(\frac{(\sigma^*_{11} - \sigma^*_{22})^2 + (\sigma^*_{22} - \sigma^*_{33})^2 + (\sigma^*_{33} - \sigma^*_{11})^2 + 6(\sigma^{*2}_{12} + \sigma^{*2}_{23} + \sigma^{*2}_{31})}{2} \right)^{\frac{1}{2}}. \tag{2.84}$$

In radial symmetry, the von Mises stress (2.84) can be written as

$$\sigma^*_{\text{eff}} = |\sigma^*_{rr} - \sigma^*_{\theta\theta}|. \tag{2.85}$$

From (2.19) and (2.56), we can write this effective stress as

$$\sigma^*_{\text{eff}} = \frac{6G^*_{\text{Si}}(0)\eta_{\text{Si}} V^m_{\text{Si}} c^{\max}_{\text{Si}} G_a |B_a|}{r^3} \quad \text{for } a = \text{Si}, \text{C}. \tag{2.86}$$

As we have $B_{\text{Si}} = 0$, the effective stress is only non-zero in Ω_{C}. The r^{-3} dependence shows that this effective stress is greatest at the minimum value of r in Ω_{C}, which is $r = R_{\text{Si}}$. Therefore, the maximum induced stress is given by

$$\sigma^*_{\text{eff}}(R_{\text{Si}}) = \frac{6\eta_{\text{Si}} V^m_{\text{Si}} c^{\max}_{\text{Si}} G^*_{\text{C}} |B_{\text{C}}|}{R^3_{\text{Si}}}. \tag{2.87}$$

In Figure 2.13, we plot $\sigma^*_{\text{eff}}(R_{\text{Si}})$ against V_{Si} for different states of charge, c_0. For all states of charge, $\sigma^*_{\text{eff}}(R_{\text{Si}})$ decreases as V_{Si} approaches zero. A single-material anode nano-particle will not induce any stress in equilibrium and thus a nano-particle made solely from either material will have $\sigma^*_{\text{eff}}(R_{\text{Si}}) = 0$.

2.6.2 Optimisation

We now use the performance measures defined in the last section to optimise the initial volume of the silicon core according to three different criteria.

2.6.2.1 Amount of Lithium per Expanded Volume

The performance of anode materials are often measured by their volumetric or gravimetric capacity. The first objective function we use to optimise the initial silicon core volume is the amount of lithium per expanded volume which is closely related

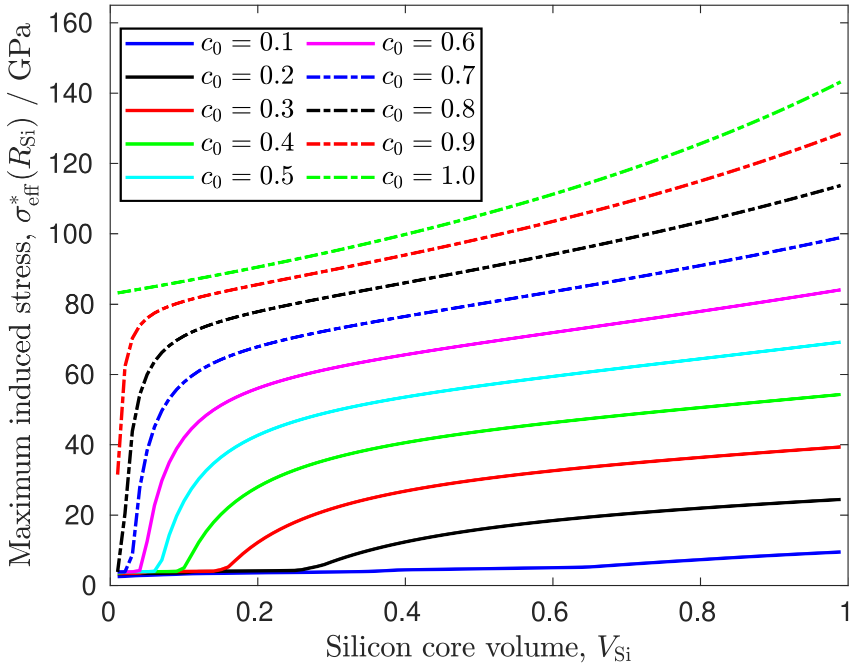

Figure 2.13: Maximum induced stress, $\sigma^*_{\text{eff}}(R_{\text{Si}})$, given by (2.87), against the initial volume of the silicon core, V_{Si} for different states of charge, c_0.

to the volumetric capacity. We calculate the amount of lithium per expanded volume by dividing the relative amount of lithium, Q, in (2.81), by the linearised relative expanded volume, V, in (2.83), giving

$$\frac{Q}{V} = \frac{c_{\text{Si}} R_{\text{Si}}^3 + c_{\text{C}} \frac{c_{\text{C}}^{\max}}{c_{\text{Si}}^{\max}} (1 - R_{\text{Si}}^3)}{1 + 3\eta_{\text{Si}} V_{\text{Si}}^m c_{\text{Si}}^{\max} u(1)}. \tag{2.88}$$

As we assume $\eta_{\text{Si}} V_{\text{Si}}^m c_{\text{Si}}^{\max} \ll 1$, we should Taylor expand the denominator for small $\eta_{\text{Si}} V_{\text{Si}}^m c_{\text{Si}}^{\max}$. However, as the parameters for silicon are not in the appropriate regime, we calculate Q/V using (2.88) instead to keep the results physically meaningful.

We plot Q/V for different initial volumes of silicon core and different states of charge in Figure 2.14. We can see from this plot that Q/V is maximised by a fully lithiated nano-particle ($c_0 = 1$) with a silicon core of $V_{\text{Si}} \approx 0.75$. However, for small c_0 values, Q/V has a more linear relationship with V_{Si}, and thus if the nano-particle is only lithiated a small amount, a fully silicon nano-particle is the optimal design according to the Q/V measure.

The reason that Q/V is not optimised by a nano-particle of solely silicon at full lithiation is that the amount of lithium, Q, is linear in V_{Si} $(= R_{\text{Si}}^3)$, whereas the expanded volume, V, increases more rapidly with V_{Si} at large values of V_{Si}, than for smaller values. Therefore, as V_{Si} becomes larger, the extra lithium that can be

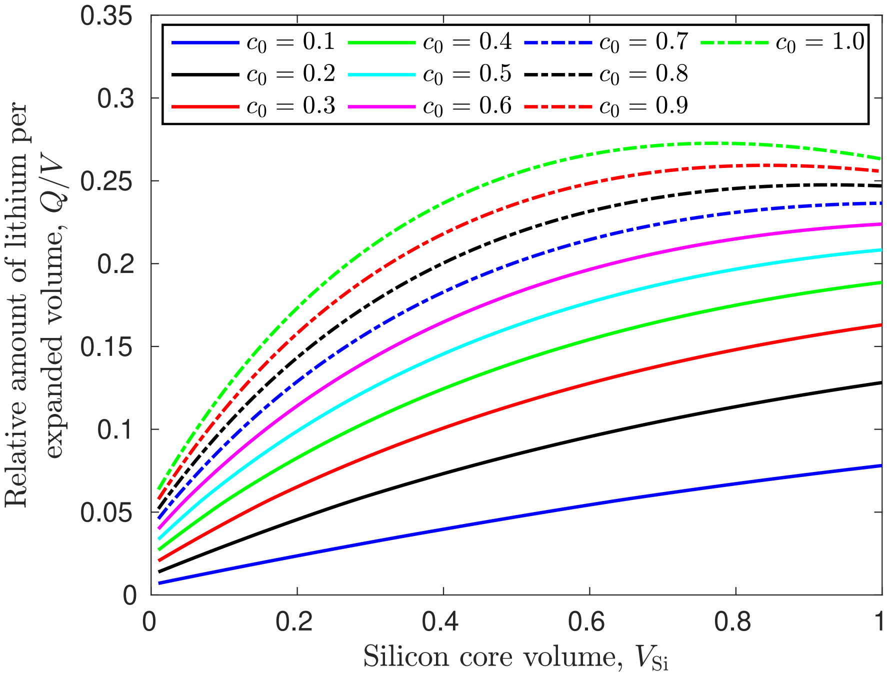

Figure 2.14: Relative amount of lithium per expanded volume Q/V against the initial volume of the silicon core, V_{Si}, and for different states of charge c_0.

intercalated is out-weighed by the increased expansion and Q/V begins to decrease with V_{Si}.

This can also be seen from substituting $u(1) = A_{\mathrm{C}} + B_{\mathrm{C}}$, $c_{\mathrm{Si}} = c_{\mathrm{C}} = 1$, (2.71b) and (2.71c) into (2.88). This yields an expression for Q/V of

$$\frac{Q}{V} = \frac{\rho_1 V_{\mathrm{Si}}^2 + \rho_2 V_{\mathrm{Si}} + \rho_3}{\rho_4 V_{\mathrm{Si}} + \rho_5}, \tag{2.89}$$

where ρ_j, $j = 1, \dots 5$ depends on λ_a, G_a, γ_a for $a = \mathrm{Si}, \mathrm{C}$ and $\eta_{\mathrm{Si}} V_{\mathrm{Si}}^m c_{\mathrm{Si}}^{\max}$. The denominator, $\rho_4 V_{\mathrm{Si}} + \rho_5$ is positive and ρ_1 is given by

$$\rho_1 = 4G_{\mathrm{C}}\big((3\lambda_{\mathrm{Si}} + 2G_{\mathrm{Si}}) - (3\lambda_{\mathrm{C}} + 2G_{\mathrm{C}})\big)\left(1 - \frac{c_{\mathrm{C}}^{\max}}{c_{\mathrm{Si}}^{\max}}\right). \tag{2.90}$$

At full lithiation, $\lambda_{\mathrm{C}} > \lambda_{\mathrm{Si}}$ and $G_{\mathrm{C}} > G_{\mathrm{Si}}$ due to the graphite parameters increasing with c_{C} and the silicon parameters decreasing with c_{Si}. Therefore, $\rho_1 < 0$ and Q/V is a negative quadratic, causing the maximum at $V_{\mathrm{Si}} \approx 0.75$. If the lithiation-dependency of the mechanical parameters is ignored, a solely silicon nano-particle would be optimal for the Q/V measure.

2.6.2.2 Maximum Amount of Lithium Under Expansion Constraint

We now consider maximising the amount of lithium intercalated into the nano-particle subject to constraints on the expanded volume and the maximum effective stress. We begin with the expanded volume constraint. Thus, we want to maximise Q, given by (2.81), subject to $V \leq V_{\max}$, for some prescribed $V_{\max} > 1$.

For a given V_{Si}, Q is maximised by maximising the SOC, c_0, because from Figure 2.11, we see that the expansion V is monotonically increasing with c_0 for each value of V_{Si}. Thus, for a given V_{Si}, the maximum viable c_0 value, which we denote as $\check{c}_0$, occurs when $V = V_{\max}$, unless the fully lithiated volume is less than the constraint, in which case $\check{c}_0 = 1$ and $V < V_{\max}$. Therefore, for each $V_{\mathrm{Si}} \in [0, 1]$, we must find $\check{c}_0$ such that

$$V_{c_0=\check{c}_0} = \min\left[V_{c_0=1}, V_{\max}\right]. \tag{2.91}$$

We then maximise the corresponding $Q_{\max} = Q(\check{c}_0)$ over V_{Si} to find the optimal value of V_{Si}.

We denote the value of V_{Si} at which $V_{c_0=\check{c}_0}$ changes from $V_{c_0=1}$ to $V_{\max}$ in (2.91) by $\mathcal{V}_{\mathrm{Si}}^V$. This is the initial volume of silicon core such that a fully lithiated nano-particle yields an expansion of $V = V_{\max}$. We can calculate this by substituting (2.65b) into (2.83) for $c_1 = c_2 = r = 1$ and equating to the prescribed $V_{\max}$, giving

$$1 + 3\eta_{\mathrm{Si}} V_{\mathrm{Si}}^m c_{\mathrm{Si}}^{\max}\big(A_{\mathrm{C}}|_{c_0=1} + B_{\mathrm{C}}|_{c_0=1}\big) = V_{\max}, \tag{2.92}$$

where $A_{\mathrm{C}}|_{c_0=1}$ and $B_{\mathrm{C}}|_{c_0=1}$ are given by (2.71b) and (2.71c), respectively, with $c_{\mathrm{Si}} = c_{\mathrm{C}} = 1$. Substituting A_{C} and B_{C} from (2.71b) and (2.71c) into (2.92) yields

$$V_{\max} = 1 + 3\bar{\eta}_{\mathrm{Si}} \frac{\Lambda_{\mathrm{C}}\big(4G_{\mathrm{C}}(1-\mathcal{V}_{\mathrm{Si}}^{V}) + \Lambda_{\mathrm{Si}}\big)\gamma_{\mathrm{C}} + 4G_{\mathrm{C}}\mathcal{V}_{\mathrm{Si}}^{V}\Lambda_{\mathrm{Si}}\gamma_{\mathrm{Si}} + \Lambda_{\mathrm{Si}}\Lambda_{\mathrm{C}}(\gamma_{\mathrm{Si}} - \gamma_{\mathrm{C}})\mathcal{V}_{\mathrm{Si}}^{V}}{\Lambda_{\mathrm{Si}}\Lambda_{\mathrm{C}} + 4G_{\mathrm{C}}\big(\Lambda_{\mathrm{C}}(1-\mathcal{V}_{\mathrm{Si}}^{V}) + \Lambda_{\mathrm{Si}}\mathcal{V}_{\mathrm{Si}}^{V}\big)}, \tag{2.93}$$

where $\Lambda_{\mathrm{Si}} = 3\lambda_{\mathrm{Si}} + 2G_{\mathrm{Si}}$, $\Lambda_{\mathrm{C}} = 3\lambda_{\mathrm{C}} + 2G_{\mathrm{C}}$, $\bar{\eta}_{\mathrm{Si}} = \eta_{\mathrm{Si}} V_{\mathrm{Si}}^{m} c_{\mathrm{Si}}^{\max}$, and we have substituted R_{Si}^{3} from (2.71b) and (2.71c) with $\mathcal{V}_{\mathrm{Si}}^{V}$. This can be rearranged to give

$$\mathcal{V}_{\mathrm{Si}}^{V} = \frac{(\Lambda_{\mathrm{Si}}\Lambda_{\mathrm{C}} + 4G_{\mathrm{C}}\Lambda_{\mathrm{C}})\big(V_{\max} - 1\big) - 3\bar{\eta}_{\mathrm{Si}}\Lambda_{\mathrm{C}}\gamma_{\mathrm{C}}(\Lambda_{\mathrm{Si}} + 4G_{\mathrm{C}})}{3\bar{\eta}_{\mathrm{Si}}\big[\Lambda_{\mathrm{Si}}\Lambda_{\mathrm{C}}(\gamma_{\mathrm{Si}} - \gamma_{\mathrm{C}}) + 4G_{\mathrm{C}}(\Lambda_{\mathrm{Si}}\gamma_{\mathrm{Si}} - \Lambda_{\mathrm{C}}\gamma_{\mathrm{C}})\big] - 4G_{\mathrm{C}}(\Lambda_{\mathrm{Si}} - \Lambda_{\mathrm{C}})\big(V_{\max} - 1\big)}. \tag{2.94}$$

For $V_{\mathrm{Si}} < \mathcal{V}_{\mathrm{Si}}^{V}$, we can simply calculate $Q_{\max}$ by substituting V_{Si} and $c_{\mathrm{Si}} = c_{\mathrm{C}} = 1$ into (2.81). For $V_{\mathrm{Si}} > \mathcal{V}_{\mathrm{Si}}^{V}$, we must numerically solve

$$1 + 3\eta_{\mathrm{Si}} V_{\mathrm{Si}}^{m} c_{\mathrm{Si}}^{\max}\big(A_{\mathrm{C}} + B_{\mathrm{C}}\big) = V_{\max}, \tag{2.95}$$

to find $\check{c}_0$ before finding the corresponding c_{Si} and c_{C} values for $c_0 = \check{c}_0$, and substituting these concentrations into (2.81) to find $Q_{\max}$.

In Figure 2.15 we plot $Q_{\max}$ against V_{Si} for four different values of $V_{\max}$. The V_{Si} values for which $V_{\mathrm{Si}} < \mathcal{V}_{\mathrm{Si}}^{V}$ can be seen by the straight line on the left side of the plot.

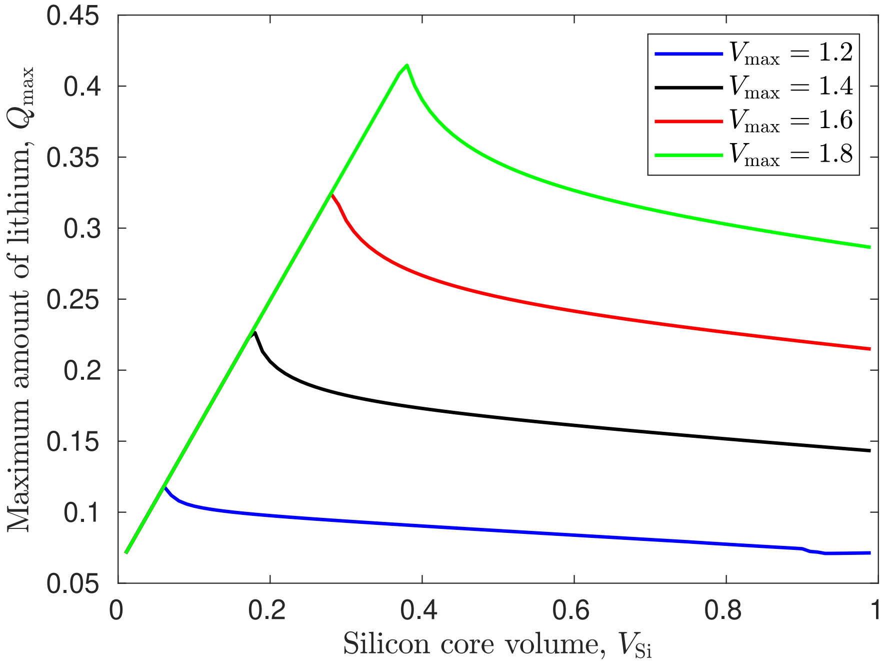

Figure 2.15: Maximum amount of lithium able to be intercalated, $Q_{\max}$, under the constraint $V \leq V_{\max}$ against the initial volume of the silicon core, V_{Si}, for several values of the expanded volume constraint, $V_{\max}$.

This is because for $c_1 = c_2 = 1$, (2.81) is a linear function of V_{Si}. Immediately to the right of this region, $Q_{\max}$ decreases for $V_{\text{Si}} > \mathcal{V}_{\text{Si}}^{V}$ because the additional capacity due to the increase in the initial silicon core volume does not outweigh the decrease in the amount of lithium caused by reducing c_{Si} to ensure that $V \leq V_{\max}$. Additionally, if more silicon is incorporated into the nano-particle, the shell is thinner, leading to the silicon being less compressed so it could accommodate more lithium, instead of the lithium being intrecalated into the graphite. This would cause V to increase a lot as c_{Si} has increased, so to meet the expansion constraint, less lithium overall can be intercalated into the nano-particle.

Therefore, the V_{Si} value which yields the largest $Q_{\max}$ is $V_{\text{Si}} = \mathcal{V}_{\text{Si}}^{V}$. However, for this solution to be feasible, we require $0 \leq \mathcal{V}_{\text{Si}}^{V} \leq 1$. We can substitute (2.94) into this inequality and rearrange to obtain a condition on $V_{\max}$ such that $0 \leq \mathcal{V}_{\text{Si}}^{V} \leq 1$ given by

$$\frac{3\bar{\eta}_{\text{Si}}\Lambda_{\text{C}}\gamma_{\text{C}}(\Lambda_{\text{Si}} + 4G_{\text{C}})}{\Lambda_{\text{Si}}\Lambda_{\text{C}} + 4G_{\text{C}}\Lambda_{\text{C}}} + 1 < V_{\max} < 1 + 3\bar{\eta}_{\text{Si}}\gamma_{\text{Si}}. \tag{2.96}$$

We note that other core and shell materials and other $V_{\max}$ values, $V_{\text{Si}} = \mathcal{V}_{\text{Si}}^{V}$ may not be the optimal solution and numerical optimisation may have to be utilised.

2.6.2.3 Maximum Amount of Lithium Under Maximum Stress Constraint

We now wish to maximise the amount of intercalated lithium such that the maximum induced stress, defined in (2.87), is less than some prescribed constraint $\sigma_{\max}$. As with the expanded volume constraint in Section 2.6.2.2, for each V_{Si}, we must find the maximum c_0, denoted by $\check{c}_0$, such that the maximum induced stress $\sigma_{\text{eff}}^{*}(R_{\text{Si}})$ is less than $\sigma_{\max}$. Then we calculate $Q_{\max} = Q(\check{c}_0)$ using (2.81) and maximise $Q_{\max}$ over V_{Si}. In Figure 2.16, we plot $\sigma_{\text{eff}}^{*}(R_{\text{Si}})$ against c_0 for different values of V_{Si}. It can be seen that $\sigma_{\text{eff}}^{*}(R_{\text{Si}})$ is a monotonically increasing function of c_0 for each V_{Si} value. Therefore, the maximal c_0 value for a given V_{Si} under the constraint $\sigma_{\text{eff}}^{*}(R_{\text{Si}}) < \sigma_{\max}$ will be such that $\sigma_{\text{eff}}^{*}(R_{\text{Si}}) = \sigma_{\max}$.

In Figure 2.17, we plot $Q_{\max}$ against V_{Si} for several different values of $\sigma_{\max}$. It can be seen that $V_{\text{Si}} = 1$ gives the greatest $Q_{\max}$ value for each value of $\sigma_{\max}$. However, for $\sigma_{\max} = 4.0$ and 5.0 GPa, $Q_{\max}$ is not monotonic in V_{Si}, thus there are local maxima of $Q_{\max}$. These non-monotonicities are caused by the steps in the stress-free chemical potential of graphite, as shown by the labelled c_{C} values in Figure 2.17. The sharp decreases in $Q_{\max}$ with V_{Si} stem from c_{C} decreasing rapidly for a small change to the chemical potential. The smaller c_{C} value reduces the amount of expansion in the graphite, causing more stress in the graphite as the stress-free expansion caused by

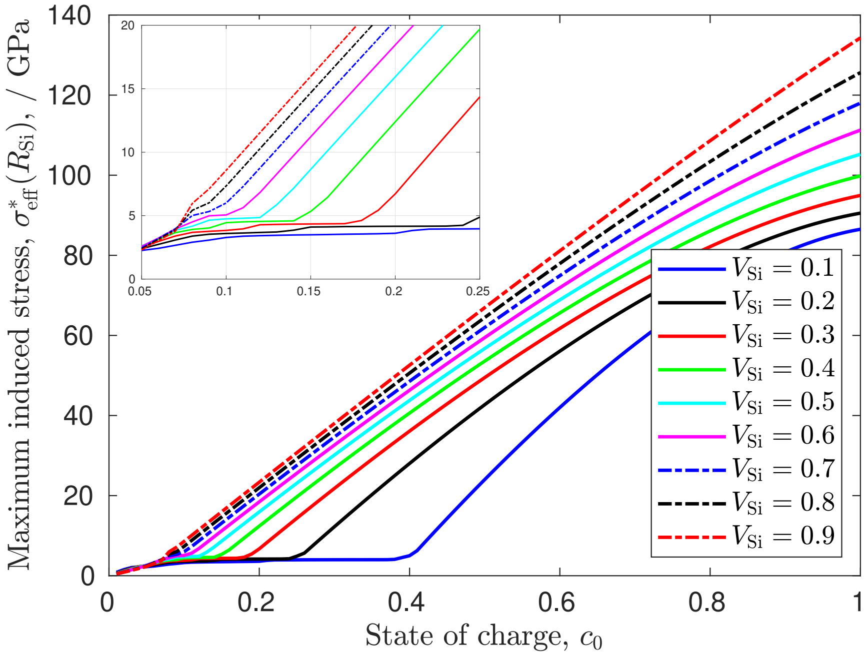

Figure 2.16: Maximum induced stress, $\sigma^*_{\mathrm{eff}}(R_{\mathrm{Si}})$, against SOC, c_0, for different initial silicon core volumes, V_{Si}. The inset plot is focussed on $0 < \sigma^*_{\mathrm{eff}}(R_{\mathrm{Si}}) < 20.0$ GPa to show more clearly that it is monotonically increasing in c_0 for these values.

lithiation of the graphite is no longer mitigating the stress caused by the expanding silicon core. Therefore, the amount of lithium that can be intercalated drops rapidly at these values of V_{Si}. This non-monotonicity is useful for design purposes in the presence of other constraints. For example, if the maximum stress permitted is $\sigma_{\max} = 4.0$ GPa, but we must also restrict V_{Si} to be less than 0.25 due to expansion constraints, $V_{\mathrm{Si}} = 0.05$ would allow a larger amount of lithium to be intercalated than $V_{\mathrm{Si}} = 0.2$.

Similarly to the maximum expansion constraint in Section 2.6.2.2, for sufficiently large $\sigma_{\max}$, there are V_{Si} values for which a fully lithiated nano-particle ($c_0 = 1$) does not produce stresses as large as $\sigma_{\max}$. Therefore, the linear relationship for small V_{Si} in Figure 2.15 is also seen for large values of $\sigma_{\max}$. However, the $\sigma_{\max}$ values illustrated in Figure 2.17 are too small to see this behaviour; all of the plots have $\check{c}_0 < 1$. We denote the initial silicon core volume at which the maximum induced stress at $c_0 = 1$ is equal to $\sigma_{\max}$ as $\mathcal{V}^{\sigma}_{\mathrm{Si}}$. We can find the value of $\mathcal{V}^{\sigma}_{\mathrm{Si}}$ by substituting B_{C} from (2.71c) into (2.87) with $c_{\mathrm{Si}} = c_{\mathrm{C}} = 1$ to give

$$\sigma_{\max} = \frac{6\eta_{\mathrm{Si}} V^m_{\mathrm{Si}} c^{\max}_{\mathrm{Si}} G^*_{\mathrm{C}} \Lambda_{\mathrm{Si}} \Lambda_{\mathrm{C}} |\gamma_{\mathrm{Si}} - \gamma_{\mathrm{C}}|}{\Lambda_{\mathrm{Si}}\Lambda_{\mathrm{C}} + 4G_{\mathrm{C}}\big(\Lambda_{\mathrm{C}}(1 - \mathcal{V}^{\sigma}_{\mathrm{Si}}) + \Lambda_{\mathrm{Si}}\mathcal{V}^{\sigma}_{\mathrm{Si}}\big)}, \tag{2.97}$$

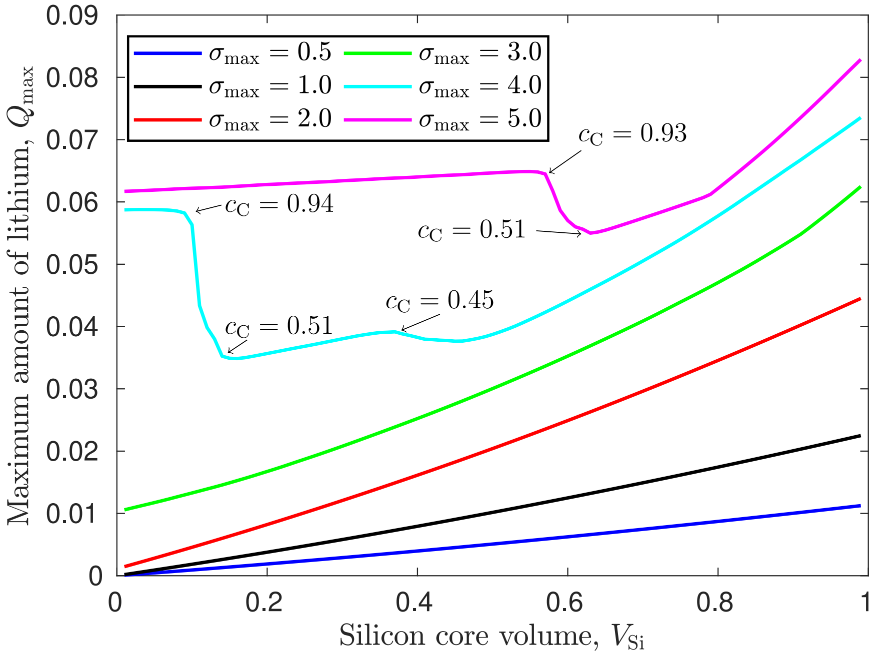

Figure 2.17: Maximum amount of lithium able to be intercalated, $Q_{\max}$, against the initial volume of the silicon core, V_{Si}, for different values of the maximum permitted effective stress, $\sigma_{\max}$. The lithium concentration in the graphite shell at the points where there are sudden changes are marked.

which can be rearranged to find

$$\mathcal{V}_{\mathrm{Si}}^{\sigma} = \frac{\Lambda_{\mathrm{Si}}\Lambda_{\mathrm{C}}(6\eta_{\mathrm{Si}}V_{\mathrm{Si}}^{m}c_{\mathrm{Si}}^{\max}G_{\mathrm{C}}^{*}|\gamma_{\mathrm{Si}}-\gamma_{\mathrm{C}}|-\sigma_{\max})-4G_{\mathrm{C}}\Lambda_{\mathrm{C}}\sigma_{\max}}{4G_{\mathrm{C}}(\Lambda_{\mathrm{Si}}-\Lambda_{\mathrm{C}})\sigma_{\max}}. \tag{2.98}$$

The bounds on $\sigma_{\max}$ such that the linear relationship for small V_{Si} is observed are given by substituting (2.98) into $0 < \mathcal{V}_{\mathrm{Si}}^{\sigma} < 1$ to yield

$$\frac{6\eta_{\mathrm{Si}}V_{\mathrm{Si}}^{m}c_{\mathrm{Si}}^{\max}G_{\mathrm{C}}^{*}\Lambda_{\mathrm{Si}}\Lambda_{\mathrm{C}}|\gamma_{\mathrm{Si}}-\gamma_{\mathrm{C}}|}{\Lambda_{\mathrm{Si}}\Lambda_{\mathrm{C}}+4G_{\mathrm{C}}\Lambda_{\mathrm{C}}} < \sigma_{\max} \tag{2.99a}$$

$$\text{and } \sigma_{\max} < \frac{6\eta_{\mathrm{Si}}V_{\mathrm{Si}}^{m}c_{\mathrm{Si}}^{\max}G_{\mathrm{C}}^{*}\Lambda_{\mathrm{Si}}\Lambda_{\mathrm{C}}|\gamma_{\mathrm{Si}}-\gamma_{\mathrm{C}}|-4G_{\mathrm{C}}(\Lambda_{\mathrm{Si}}-\Lambda_{\mathrm{C}})}{\Lambda_{\mathrm{Si}}\Lambda_{\mathrm{C}}+4G_{\mathrm{C}}\Lambda_{\mathrm{C}}}. \tag{2.99b}$$

The $\sigma_{\max}$ values plotted for in Figure 2.17 are much greater than the tensile strength of graphite, $\sigma_{\mathrm{C}}^{Y,*}$, typically given in the literature to be between 8 and 12 MPa [70]. If the tensile strength of graphite is exceeded, it will crack, which can be extremely detrimental to the integrity of the nano-particle. The results for the constraint $\sigma_{\max} = \sigma_{\mathrm{C}}^{Y}$ are qualitatively similar to that of $\sigma_{\max} = 0.5$ GPa in Figure 2.17 such that $Q_{\max}$ is monotonically increasing with a maximum as $V_{\mathrm{Si}} \to 1$. Therefore, to avoid the yielding or cracking of the graphite at the interface, the optimal design is as large a silicon core as possible. For $V_{\mathrm{Si}} = 0.99$, the silicon can only be lithiated to around $c_{\mathrm{Si}} = 2.2 \times 10^{-4}$ for $\sigma^*_{\mathrm{eff}}(R_{\mathrm{Si}})$ to remain under the tensile strength, $\sigma_{\mathrm{C}}^{Y,*}$, while the graphite remains unlithiated. This achieves a $Q_{\max}$ value also of around 2.2×10^{-4} (as $c_{\mathrm{C}} = 0$ in this case). As the graphite is not lithiated in this optimal design, this suggests there are other materials better suited for the shell material because the desirable property that the graphite is an active material is not being utilised. A stronger material, or a material with the same strength as graphite but a lower stress-free potential than silicon, so that it is lithiated first at low states of charge, would be more beneficial.

2.7 Conclusions

In this chapter, we have derived the linear chemo-mechanical model for the lithiation of a lithium-ion battery anode that we base most of the work of this thesis on. We have shown how this model is simplified when applied to a radially-symmetric spherical geometry, allowing us to decouple the chemical and mechanical models. We have fully solved the model for a nano-particle consisting of a silicon core and a graphite shell, analysing the lithium concentration profiles, chemical potential, displacement and stresses within the nano-particle. We then were able to produce an effective OCV for the multi-material anode particle taking into account stresses at equilibrium. Lastly, we have used the linear model to find the optimal size of the silicon core compared to the graphite shell based on maximising the capacity.

We have linearised a geometrically nonlinear elasticity model by assuming that the quantity $\eta_a x_a^{\max}$ is small. Physically, this corresponds to assuming that the expanded volume is approximately equal to the original volume such that $J_a^c \approx 1$. Although this is not the case for silicon, we have used this assumption to gain insight into the behaviour of core–shell anode nano-particles used to constrain the expansion of the core material. Due to the simplifications that arise from the linearisation, the model can be solved almost entirely analytically. This allows the chemical, mechanical and optimisation results in Section 2.6 to be much better understood. Furthermore, we are able to solve the linear model quickly, allowing for many numerical experiments to be carried out at a reasonable computational cost.

The significant results of this chapter arise from the inclusion of multiple materials into the nano-particle, taking into account the intercalation of lithium in both materials. The derivation of the effective OCV of the multi-material anode, taking into account the stresses induced in each of the materials in equilibrium, is a novel contribution to the field and the fundamental idea could be applied to more accurate models for silicon. The optimisation of the size of the silicon core based on the capacity of the resulting nano-particle is another useful application of this model, and the simple geometry allows us to plot the objective function due to the initial volume of the silicon core being the only geometrical variable to optimise over. This concept of maximising capacity subject to certain constraints can also be applied to nonlinear models given sufficient computational power to solve them. Both the effective OCV and geometry optimisation results in this chapter can be useful in practice for industrialists aiming to perfect anode designs.

We found the optimal geometry depends on the performance measure chosen. The volumetric capacity measure we use, Q/V, is maximised by a fully lithiated nano-particle with a silicon core of $V_{\mathrm{Si}} = 0.75$. To maximise the capacity, Q, subject to a maximum volumetric expansion, V_{max}, we have shown that the optimal initial volume of silicon core is that which has a volume expansion of V_{max} at full lithiation. However, if any silicon within the nano-particle causes the expansion to be greater than the maximum permitted, a solely graphitic nano-particle is optimal. To maximise the capacity subject to a maximum stress the optimal nano-particle design is one with a very large silicon core with a low lithiation. We note though that for large silicon cores, and high states of charge, the deformation and stress is no longer in the linear regime we have assumed, so these optimal solutions may not be quantitatively accurate. Furthermore, the model is assumed to be static and there are several physical effects missing from the model. Therefore, these optimal designs may not be accurate for use in battery function with high charging rates causing lithium inhomogeneities, cracking and other mechanisms.

In the next chapter, we introduce several changes to the core–shell nano-particle geometry in this chapter, including void spaces and porous silicon. We then attempt to find designs using these voids and pores to improve on the optimal designs found in Section 2.6.

Chapter 3

Porosity

In this chapter, we incorporate a central void and porosity into the spherical nano-particle design consisting of a silicon core and a graphite shell, used in Chapter 2. Void spaces within lithium-ion anode nano-particles have been explored experimentally using yolk–shell designs [28, 64] and central voids [19, 35, 127], and modelled using spherically-symmetric models [53, 67, 137]. The purpose of including voids within the anode is so that the anode will hopefully expand into the voids instead of outwards. We begin this chapter by investigating the effect of including a void in the centre of the silicon core using the linear model derived in the last chapter, seeking a void size which reduces the expansion of the nano-particle while retaining the high capacity. We find that the inclusion of a small void can reduce the expanded volume under the linear elastic approximation, but have the same high capacity as the solid core case.

We also try to limit the expansion of the silicon core without sacrificing too much capacity by incorporating pores into the silicon itself with the intention of allowing the graphite to restrain the weakened porous silicon more easily. We consider a porous silicon design consisting of a periodic lattice of interconnected cubic pores, which allows us to use of the method of multiple scales to determine effective material parameters for the porous silicon. This method is well established for calculating effective mechanical parameters of periodic media [11, 48]. It has been applied to porous anodes in several ways, mostly to calculate effective diffusion properties of the electrolyte and electrodes [22, 89]. However, it has rarely been used to incorporate anode expansion. One study utilised the method to model the degradation of the binder surrounding the anode particles [38, 39]. Lastly, a linear chemo-mechanical model similar to that presented here has been applied to an array of single-material nano-particles [116].

We determine the assumptions under which the method of multiple scales can be applied to the quasi-static model of Chapter 2 to find effective mechanical parameters for this porous silicon. In contrast to previous works we include the effect of stress-assisted diffusion, which makes the resulting cell problems nonlinear. We consider separately the limits in which the stress-assisted diffusion effect is large or small.

To study the effect of including the porous silicon into the nano-particle, we derive the effective parameters for fully lithiated porous silicon, removing several complications in the multiple-scales formulation. We then study how incorporating porous silicon affects the expansion at full lithiation and the maximum capacity of two new designs of nano-particle. We find that using porous silicon in place of the non-porous silicon core does reduce expansion when we take the silicon to be highly porous. We also find that including a layer of porous silicon between a non-porous core and the graphite shell is very successful in reducing the expansion. However, when we examine these predictions in detail we find that this is caused by an unphysical overlap of materials due to the linear elasticity assumption, motivating the nonlinear model in Chapter 4.

3.1 Voids

We now study the effect of including a central void into the nano-particle studied in Chapter 2. We denote the radius of the void as R_V^* and nondimensionalise using the outer radius of the nano-particle, R_{C}^*, so that the non-dimensional radius is $R_V = R_V^*/R_{\mathrm{C}}^*$. As in Figure 2.1, the outer radii of the silicon and graphite domains are given by R_{Si} and 1, respectively. A schematic of a slice through the centre of the nano-particle with a central void is shown in Figure 3.1.

The linear elasticity model applied to this nano-particle design is solved using the method outlined in Section 2.3. We assume that the void does not impose any stress on the anode material and so have a zero traction boundary condition at $r = R_V$, along with the continuity of displacement and radial stress at $r = R_{\mathrm{Si}}$ and zero traction at $r = 1$. Using the general solution in each material (2.55), these boundary conditions give the system of linear equations

$$(3\lambda_{\mathrm{Si}} + 2G_{\mathrm{Si}})(A_{\mathrm{Si}} - \gamma_{\mathrm{Si}} c_{\mathrm{Si}}) = \frac{4G_{\mathrm{Si}} B_{\mathrm{Si}}}{R_V^3}, \tag{3.1a}$$

$$A_{\mathrm{Si}} R_{\mathrm{Si}} + \frac{B_{\mathrm{Si}}}{R_{\mathrm{Si}}^2} = A_{\mathrm{C}} R_{\mathrm{Si}} + \frac{B_{\mathrm{C}}}{R_{\mathrm{Si}}^2}, \tag{3.1b}$$

$$(3\lambda_{\mathrm{Si}} + 2G_{\mathrm{Si}})(A_{\mathrm{Si}} - \gamma_{\mathrm{Si}} c_{\mathrm{Si}}) - \frac{4G_{\mathrm{Si}} B_{\mathrm{Si}}}{R_{\mathrm{Si}}^3} = (3\lambda_{\mathrm{C}} + 2G_{\mathrm{C}})(A_{\mathrm{C}} - \gamma_{\mathrm{C}} c_{\mathrm{C}}) - \frac{4G_{\mathrm{C}} B_{\mathrm{C}}}{R_{\mathrm{Si}}^3}, \tag{3.1c}$$

$$(3\lambda_{\mathrm{C}} + 2G_{\mathrm{C}})(A_{\mathrm{C}} - \gamma_{\mathrm{C}} c_{\mathrm{C}}) = 4G_{\mathrm{C}} B_{\mathrm{C}}. \tag{3.1d}$$

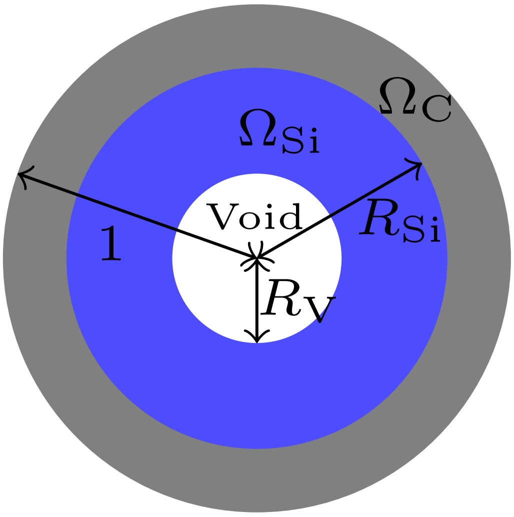

Figure 3.1: Diagram of a slice through a spherical nano-particle with a central void, silicon layer (Ω_{Si}) and graphite shell (Ω_{C}) with the nondimensional radii of each component labelled as R_V, R_{Si} and 1, respectively.

We solve (3.1) to find A_{Si}, B_{Si}, A_{C} and B_{C}, given by

$$\begin{aligned} A_{\mathrm{Si}} = \frac{1}{\omega_V}\Big\{&4G_{\mathrm{Si}}G_{\mathrm{C}}\Lambda_{\mathrm{C}}(1-R_{\mathrm{Si}}^3)R_{\mathrm{Si}}^3\gamma_{\mathrm{C}}c_{\mathrm{C}} \\ &+\big[G_{\mathrm{C}}\Lambda_{\mathrm{Si}}\Lambda_{\mathrm{C}}R_V^3(1-R_{\mathrm{Si}}^3)+G_{\mathrm{Si}}\Lambda_{\mathrm{Si}}(R_{\mathrm{Si}}^3-R_V^3)(4G_{\mathrm{C}}R_{\mathrm{Si}}^3+\Lambda_{\mathrm{C}})\big]\gamma_{\mathrm{Si}}c_{\mathrm{Si}}\Big\}, \end{aligned} \tag{3.2a}$$

$$\begin{aligned} A_{\mathrm{C}} = \frac{1}{\omega_V}\Big\{&4G_{\mathrm{Si}}G_{\mathrm{C}}\Lambda_{\mathrm{Si}}R_{\mathrm{Si}}^3(R_{\mathrm{Si}}^3-R_V^3)\gamma_{\mathrm{Si}}c_{\mathrm{Si}} \\ &+\big[G_{\mathrm{Si}}\Lambda_{\mathrm{Si}}\Lambda_{\mathrm{C}}(R_{\mathrm{Si}}^3-R_V^3)+G_{\mathrm{C}}\Lambda_{\mathrm{C}}(1-R_{\mathrm{Si}}^3)(4G_{\mathrm{Si}}R_{\mathrm{Si}}^3+\Lambda_{\mathrm{Si}}R_V^3)\big]\gamma_{\mathrm{C}}c_{\mathrm{C}}\Big\}, \end{aligned} \tag{3.2b}$$

$$B_{\mathrm{Si}} = \frac{1}{\omega_V}\big\{G_{\mathrm{C}}\Lambda_{\mathrm{Si}}\Lambda_{\mathrm{C}}R_{\mathrm{Si}}^3R_V^3(1-R_{\mathrm{Si}}^3)(\gamma_{\mathrm{C}}c_{\mathrm{C}}-\gamma_{\mathrm{Si}}c_{\mathrm{Si}})\big\}, \tag{3.2c}$$

$$B_{\mathrm{C}} = \frac{1}{\omega_V}\big\{G_{\mathrm{Si}}\Lambda_{\mathrm{Si}}\Lambda_{\mathrm{C}}R_{\mathrm{Si}}^3(R_{\mathrm{Si}}^3-R_V^3)(\gamma_{\mathrm{Si}}c_{\mathrm{Si}}-\gamma_{\mathrm{C}}c_{\mathrm{C}})\big\}, \tag{3.2d}$$

where

$$\begin{aligned} \omega_V = \Lambda_{\mathrm{Si}}\Lambda_{\mathrm{C}}\big[G_{\mathrm{Si}}(R_{\mathrm{Si}}^3-R_V^3)+&G_{\mathrm{C}}R_V^3(1-R_{\mathrm{Si}}^3)\big] \\ &+4G_{\mathrm{Si}}G_{\mathrm{C}}R_{\mathrm{Si}}^3\big[\Lambda_{\mathrm{Si}}(R_{\mathrm{Si}}^3-R_V^3)+\Lambda_{\mathrm{C}}(1-R_{\mathrm{Si}}^3)\big], \end{aligned} \tag{3.2e}$$

and $\Lambda_a = 3\lambda_a + 2G_a$ for $a = \mathrm{Si}, \mathrm{C}$.

We now calculate the capacity and expansion for this nano-particle design at full lithiation ($c_0 = 1$) to determine whether the inclusion of the central void decreases the expanded volume without decreasing the theoretical maximum capacity of the nano-particle. We denote the maximum capacity as Q_1 which is defined as the amount of lithium intercalated at $c_0 = 1$, relative to a fully lithiated silicon nano-particle with unit initial volume, without a central void. As $c_0 = 1$, we have $c_{\mathrm{Si}} = c_{\mathrm{C}} = 1$. For a spherical geometry with a central void, we have

$$Q_1 = R_{\mathrm{Si}}^3 - R_V^3 + \frac{c_{\mathrm{C}}^{\max}}{c_{\mathrm{Si}}^{\max}}(1 - R_{\mathrm{Si}}^3). \tag{3.3}$$

The expanded volume at full lithiation, denoted by V_1, is calculated using the linearised expression for V, given by (2.83), with $c_{\mathrm{Si}} = c_{\mathrm{C}} = 1$. In (2.83), $u(1) = A_{\mathrm{C}}+B_{\mathrm{C}}$, and in this geometry, A_{C} and B_{C} are given by (3.2b) and (3.2d), respectively.

As the void affects both the capacity and the expansion for a given value of R_{Si}, directly comparing nano-particle designs with equal capacities provides more insight than comparing designs with equal values of R_{Si}, as in Section 2.6. In Figure 3.2 we plot the relative expanded volume at full lithiation, V_1, against the maximum capacity, Q_1, for several initial volumes of the central void, $V_V = R_V^3$. For each value of V_V, Q_1 is increased by increasing R_{Si}. We can see that for a given maximum capacity, Q_1, nano-particles with large voids have a greater expanded volume than those without. This is because the graphite shell must be thinner in nano-particles with void spaces to achieve the same capacity, because R_{Si} must be greater. This thinner shell does not

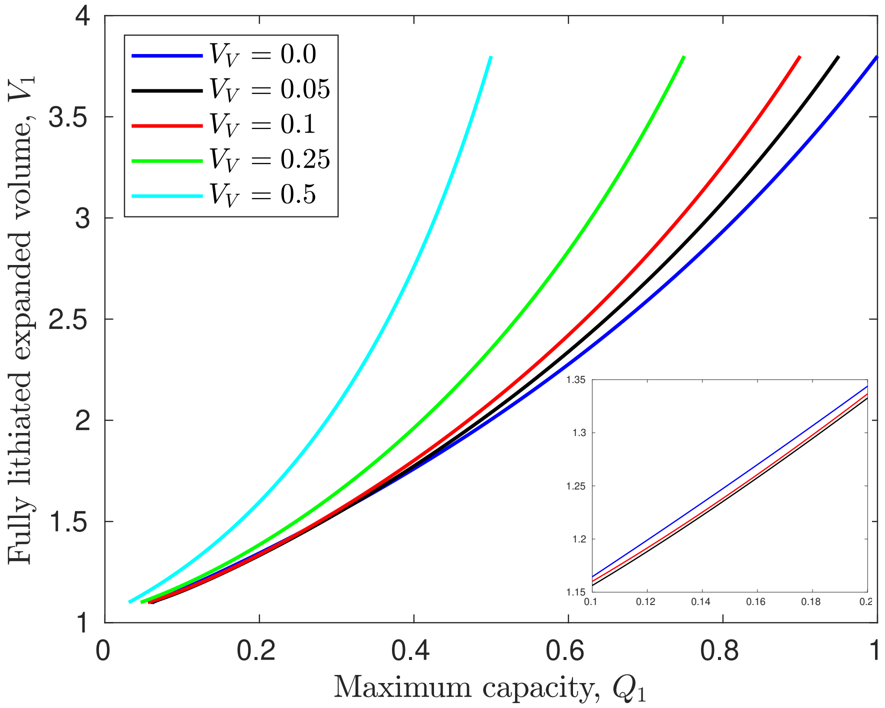

Figure 3.2: Fully lithiated expanded volume, V_1, against maximum capacity, Q_1, the nano-particle geometry in Figure 3.1, for different initial void volumes, $V_V = R_V^3$. The inset plot shows a range of capacities for which a central void with $V_V = 0.05$ and $V_V = 0.1$ can reduce the expansion of the nano-particle.

restrain the silicon as effectively and thus the nano-particle expands outwards more. For smaller voids, for example $V_V = 0.05$ and $V_V = 0.1$, there are geometries in which the expansion of the nano-particles with central voids is less than those without voids having the same capacity. This is due to the silicon being able to expand into the central void, decreasing the outward expansion, while not sacrificing much capacity because the void is small. At full lithiation, the Young's modulus of graphite is much greater than that of silicon or unlithiated graphite. Therefore, at full lithiation, a sufficiently thick graphite shell is strong enough to encourage the silicon to expand into the void. However, at lower states of charge, or for weaker materials, this is not necessarily the case.

These results show that a small central void can reduce the expansion of the nano-particle without decreasing the maximum capacity. In this model we are assuming the materials deform according to linear elasticity without deform plastically or fracturing. We revisit this geometry with a model incorporating plastic yielding of the silicon and pulverisation of the graphite in Chapter 5.

3.2 Porous Silicon

We now wish to investigate whether the inclusion of porous silicon can improve on the designs explored so far, since the graphite will be able to constrain the weaker silicon more easily. We do this by considering the porous silicon material to consist of silicon with a very fine periodic array of interconnected cubic pores, shown in Figure 3.3. Solving the linear elasticity model on this domain would require using computational methods with high cost due to the complicated domain. Instead, we approximate effective mechanical parameters and expansion parameters of the porous silicon using the method of multiple scales. This allows us to model the porous silicon as a single homogeneous material which we may use in the radially-symmetric ODEs derived in Section 2.3.

We begin by applying this method to the linearised chemo-mechanical model derived in Sections 2.1 and 2.2, including a lithiation-dependent general stiffness tensor, $\mathbb{C}_{\mathrm{Si}}$, and stress-assisted diffusion. We find the coupling of the stress to the concentration through stress-assisted diffusion causes the multiple-scales problem to be non-linear. We consider the limits of small and large stress-assisted diffusion parameter for the silicon, S^d_{Si}, to try to simplify the problem. In Section 3.2.5, we then consider the macroscale problem in which the nano-particle is fully lithiated, which allows us to ignore the stress-assisted diffusion coupling and the concentration-dependence of the mechanical parameters, greatly simplifying the multiple-scales formulation. We also reintroduce the isotropic stiffness tensor (2.17) and using several symmetry arguments, we derive effective Lamé parameters for the fully lithiated silicon to use in the radially-symmetric macroscale problem.

3.2.1 Method of Multiple Scales Formulation

The method of multiple scales [52] assumes that the macroscale domain, in this case the domain occupied by the porous silicon, consists of a periodic lattice of a repeating structure, known as a unit cell. For the porous silicon in Figure 3.3, these unit cells are a cage structure, an example of which is shown in Figure 3.4. We denote the volume of each unit cell as $\hat{L}^3$ and the porosity of the silicon is determined by the thickness of the 'pillars' of the cage, $\hat{l}$. We shall use the position vectors denoted by $\mathbf{x} = (x, y, z)$ for the macroscale porous silicon and recall from (2.42) that the governing equations for the linear quasi-static chemo-mechanical problem in the silicon domain are given by

$$\begin{aligned} \boldsymbol{\sigma} &= \mathbb{C}_{\text{Si}}(c_{\text{Si}}) : \big(\boldsymbol{\nabla}\boldsymbol{u} - \gamma_{\text{Si}} c_{\text{Si}} \mathbf{1}\big) && \text{in } \Omega_{\text{Si}}, && (3.4\text{a}) \\ \boldsymbol{\nabla} \cdot \boldsymbol{\sigma} &= \mathbf{0} && \text{in } \Omega_{\text{Si}}, && (3.4\text{b}) \\ \mu_{\text{Si}}^{\text{SF}}(c_{\text{Si}}) - S_{\text{Si}}^{d} \operatorname{tr}(\boldsymbol{\sigma}) &= \mu && \text{in } \Omega_{\text{Si}}, && (3.4\text{c}) \end{aligned}$$

where μ is the constant chemical potential across the entire anode nano-particle. We write the stiffness of the silicon, $\mathbb{C}_{\text{Si}}$, as a function of the lithium concentration, c_{Si}.

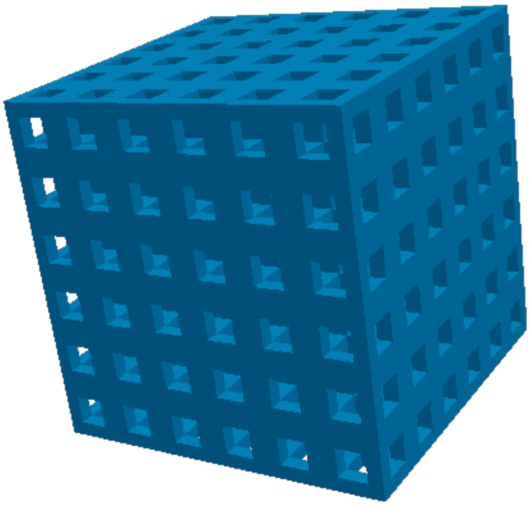

Figure 3.3: Domain of the porous silicon.

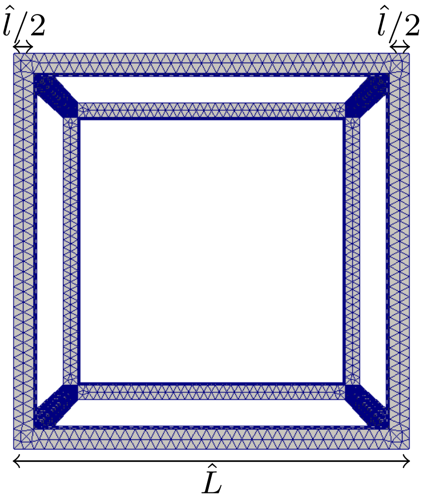

Figure 3.4: Unit cell of porous silicon.

As we assume that the pores and the electrolyte do not induce stress in the silicon, we have the boundary condition

$$\boldsymbol{\sigma} \cdot \mathbf{n}_e = \mathbf{0} \qquad \text{on } \Gamma_e, \tag{3.4d}$$

where Γ_e is the boundary between the silicon and the pores or between the silicon and the electrolyte if the porous silicon is in contact with the electrolyte surrounding the anode-particle.

We assume the porous silicon consists of many unit cells in each spatial dimension of the macroscale porous silicon, implying $\hat{L} \ll L$, where L is the lengthscale of the porous silicon domain in the macroscale. For example, in the case of a porous silicon core of radius R_ϕ, we have $L = R_\phi$. We exploit the difference in the length scales of the porous silicon domain and the unit cell to define the small parameter $\epsilon = \hat{L}/L$. Using the difference in these length scales, we introduce a microscale spatial variable $\hat{\mathbf{x}}$, where

$$\hat{\mathbf{x}} = \frac{\mathbf{x}}{\epsilon}, \tag{3.5}$$

and treat the two space variables $\mathbf{x}$ and $\hat{\mathbf{x}}$ as independent. We prescribe that the displacement, $\boldsymbol{u}$, the concentration, c_{Si}, and the stress, $\boldsymbol{\sigma}$, are periodic with period 1 in the microscale variable $\hat{\mathbf{x}}$. This periodicity condition eliminates the extra degree of freedom introduced by this new independent variable.

We expand each variable asymptotically in ϵ, giving

$$\boldsymbol{u} = \boldsymbol{u}^{(0)}(\mathbf{x}, \hat{\mathbf{x}}) + \epsilon \boldsymbol{u}^{(1)}(\mathbf{x}, \hat{\mathbf{x}}) + \epsilon^2 \boldsymbol{u}^{(2)}(\mathbf{x}, \hat{\mathbf{x}}) + \ldots, \tag{3.6a}$$

$$c_{\mathrm{Si}} = c_{\mathrm{Si}}^{(0)}(\mathbf{x}, \hat{\mathbf{x}}) + \epsilon c_{\mathrm{Si}}^{(1)}(\mathbf{x}, \hat{\mathbf{x}}) + \epsilon^2 c_{\mathrm{Si}}^{(2)}(\mathbf{x}, \hat{\mathbf{x}}) + \ldots, \tag{3.6b}$$

$$\boldsymbol{\sigma} = \boldsymbol{\sigma}^{(0)}(\mathbf{x}, \hat{\mathbf{x}}) + \epsilon \boldsymbol{\sigma}^{(1)}(\mathbf{x}, \hat{\mathbf{x}}) + \epsilon^2 \boldsymbol{\sigma}^{(2)}(\mathbf{x}, \hat{\mathbf{x}}) + \ldots. \tag{3.6c}$$

The differential operator $\boldsymbol{\nabla}$ is now split into a macroscale gradient $\boldsymbol{\nabla}$ and a microscale gradient $\hat{\boldsymbol{\nabla}}$, so we make the substitution

$$\boldsymbol{\nabla} \to \boldsymbol{\nabla} + \frac{1}{\epsilon} \hat{\boldsymbol{\nabla}}. \tag{3.7}$$

Now, $\boldsymbol{\nabla}$ denotes a spatial derivative with respect to $\mathbf{x}$ and $\hat{\boldsymbol{\nabla}}$ denotes a spatial derivative with respect to $\hat{\mathbf{x}}$. We Taylor expand $\mathbb{C}_{\mathrm{Si}}$ about $c_{\mathrm{Si}}^{(0)}$ to give

$$\mathbb{C}_{\mathrm{Si}}(c_{\mathrm{Si}}) \approx \mathbb{C}_{\mathrm{Si}}\big(c_{\mathrm{Si}}^{(0)}\big) + \epsilon \mathbb{C}'_{\mathrm{Si}}\big(c_{\mathrm{Si}}^{(0)}\big) c_{\mathrm{Si}}^{(1)} + \ldots, \tag{3.8}$$

where

$$\mathbb{C}'_{\mathrm{Si}}\big(c_{\mathrm{Si}}^{(0)}\big) = \left. \frac{\mathrm{d}\mathbb{C}_{\mathrm{Si}}}{\mathrm{d}c_{\mathrm{Si}}} \right|_{c_{\mathrm{Si}} = c_{\mathrm{Si}}^{(0)}}, \tag{3.9}$$

which we assume to be $o(1/\epsilon)$.

Substituting (3.6) into (3.4) yields the leading-order system of equations

$$\hat{\boldsymbol{\nabla}} \cdot \boldsymbol{\sigma}^{(0)} = 0, \qquad \text{in } \Omega_{\mathrm{Si}}, \tag{3.10a}$$

$$\mathbb{C}_{\mathrm{Si}}\big(c_{\mathrm{Si}}^{(0)}\big) : (\hat{\boldsymbol{\nabla}} \boldsymbol{u}^{(0)}) = 0, \qquad \text{in } \Omega_{\mathrm{Si}}, \tag{3.10b}$$

$$\mu_{\mathrm{Si}}^{\mathrm{SF}}(c_{\mathrm{Si}}^{(0)}) - S_{\mathrm{Si}}^{d}\mathrm{tr}(\boldsymbol{\sigma}^{(0)}) = \mu, \qquad \text{in } \Omega_{\mathrm{Si}}, \tag{3.10c}$$

$$\boldsymbol{\sigma}^{(0)} \cdot \mathbf{n} = 0, \qquad \text{on } \Gamma_{e}, \tag{3.10d}$$

Equation (3.10b) restricts the leading-order displacement, $\boldsymbol{u}^{(0)}$, to rigid-body displacements. The periodicity we have assumed $\boldsymbol{u}$ has with respect to $\hat{\mathbf{x}}$ then means that $\boldsymbol{u}^{(0)}$ must be independent of the microscale variable, $\hat{\mathbf{x}}$.

The system of equations at next order are given by

$$\boldsymbol{\nabla} \cdot \boldsymbol{\sigma}^{(0)} + \hat{\boldsymbol{\nabla}} \cdot \boldsymbol{\sigma}^{(1)} = 0 \qquad \text{in } \Omega_{\mathrm{Si}}, \tag{3.11a}$$

$$\boldsymbol{\sigma}^{(0)} = \mathbb{C}_{\mathrm{Si}}(c_{\mathrm{Si}}^{(0)}) : \big\{\hat{\boldsymbol{\nabla}} \boldsymbol{u}^{(1)} + \boldsymbol{\nabla} \boldsymbol{u}^{(0)} - \gamma_{\mathrm{Si}} c_{\mathrm{Si}}^{(0)} \mathbf{1}\big\} \qquad \text{in } \Omega_{\mathrm{Si}}, \tag{3.11b}$$

$$c_{\mathrm{Si}}^{(1)} \left.\frac{\partial \mu_{\mathrm{Si}}^{\mathrm{SF}}}{\partial c_{\mathrm{Si}}}\right|_{c_{\mathrm{Si}}=c_{\mathrm{Si}}^{(0)}} = S_{\mathrm{Si}}^{d}\mathrm{tr}(\boldsymbol{\sigma}^{(1)}) \qquad \text{in } \Omega_{\mathrm{Si}}, \tag{3.11c}$$

$$\boldsymbol{\sigma}^{(1)} \cdot \mathbf{n} = 0 \qquad \text{on } \Gamma_{e}, \tag{3.11d}$$

where (3.11c) is the result of a Taylor expansion of $\mu_{\mathrm{Si}}^{\mathrm{SF}}$ about $c_{\mathrm{Si}}^{(0)}$ and the $\big(\mathbb{C}'_{\mathrm{Si}}(c_{\mathrm{Si}}^{(0)}) : \hat{\boldsymbol{\nabla}} \boldsymbol{u}^{(0)}\big)$ term that should appear in (3.11b) is zero due to the independence of $\boldsymbol{u}^{(0)}$ in $\hat{\mathbf{x}}$. Substituting the leading-order stress (3.11b) into the leading-order equilibrium equation (3.10a) and the leading-order boundary condition (3.10d) yields the relationship between $\boldsymbol{u}^{(0)}$ and $\boldsymbol{u}^{(1)}$

$$\hat{\boldsymbol{\nabla}} \cdot \big(\mathbb{C}_{\mathrm{Si}}(c_{\mathrm{Si}}^{(0)}) : \hat{\boldsymbol{\nabla}} \boldsymbol{u}^{(1)}\big) = \hat{\boldsymbol{\nabla}} \cdot \big(\mathbb{C}_{\mathrm{Si}}(c_{\mathrm{Si}}^{(0)}) : \gamma_{\mathrm{Si}} c_{\mathrm{Si}}^{(0)} \mathbf{1}\big) \qquad \text{in } \Omega_{\mathrm{Si}}, \tag{3.12a}$$

$$\big(\mathbb{C}_{\mathrm{Si}}(c_{\mathrm{Si}}^{(0)}) : \hat{\boldsymbol{\nabla}} \boldsymbol{u}^{(1)}\big)\mathbf{n} = -\Big(\mathbb{C}_{\mathrm{Si}}(c_{\mathrm{Si}}^{(0)}) : \big(\boldsymbol{\nabla} \boldsymbol{u}^{(0)} - \gamma_{\mathrm{Si}} c_{\mathrm{Si}}^{(0)} \mathbf{1}\big)\Big)\mathbf{n} \qquad \text{on } \Gamma_{e}, \tag{3.12b}$$

where $\boldsymbol{u}^{(0)}$ does not appear in the PDE (3.12a) as it is independent of $\hat{\mathbf{x}}$. The leading-order lithium concentration, $c_{\mathrm{Si}}^{(0)}$, is given by rearranging (3.10c) to give

$$\begin{aligned} c_{\mathrm{Si}}^{(0)} &= \mu_{\mathrm{SF}}^{-1}\big(\mu + S_{\mathrm{Si}}^{d}\mathrm{tr}(\boldsymbol{\sigma}^{(0)})\big) \\ &= \mu_{\mathrm{SF}}^{-1}\bigg(\mu + S_{\mathrm{Si}}^{d}\mathrm{tr}\Big[\mathbb{C}_{\mathrm{Si}}(c_{\mathrm{Si}}^{(0)}) : \big\{\hat{\boldsymbol{\nabla}} \boldsymbol{u}^{(1)} + \boldsymbol{\nabla} \boldsymbol{u}^{(0)} - \gamma_{\mathrm{Si}} c_{\mathrm{Si}}^{(0)} \mathbf{1}\big\}\Big]\bigg), \end{aligned} \tag{3.13}$$

where μ_{SF}^{-1} is the inverse of the stress-free chemical potential function for silicon, $\mu_{\mathrm{Si}}^{\mathrm{SF}}$, derived in Section 2.2.2. As the only material we consider in the multiple-scales problem is silicon, we drop the subscript Si notation for this inverse function.

To find the effective parameters of the homogenised anode, we integrate the governing equilibrium equation at first order (3.11a) over the unit cell. We denote $\hat{\Omega}_{\mathrm{Si}}$ as the domain occupied by silicon in the unit cell and write the homogenised equation as

$$\int_{\hat{\Omega}_{\mathrm{Si}}} \boldsymbol{\nabla} \cdot \boldsymbol{\sigma}^{(0)} + \hat{\boldsymbol{\nabla}} \cdot \boldsymbol{\sigma}^{(1)} \; \mathrm{d}V = 0. \tag{3.14}$$

The boundary of $\hat{\Omega}_{\mathrm{Si}}$ is split into the boundary between the silicon and the pore, given by $\hat{\Gamma}_e$, and the boundary between the silicon in one unit cell and the silicon in an adjacent unit cell, which we denote as $\hat{\Gamma}_{\mathrm{Si}}$. Physically, $\hat{\Gamma}_{\mathrm{Si}}$ is the union of the planes half way through the 'pillars' within the cage structure in Figure 3.3. Using Green's theorem in (3.14) and splitting the surface integral into the integral over $\hat{\Gamma}_e$ and $\hat{\Gamma}_{\mathrm{Si}}$ gives

$$\boldsymbol{\nabla} \cdot \int_{\hat{\Omega}_{\mathrm{Si}}} \boldsymbol{\sigma}^{(0)} \; \mathrm{d}V + \int_{\hat{\Gamma}_e} \underbrace{\mathbf{n} \cdot \boldsymbol{\sigma}^{(1)}}_{=0 \text{ by } (3.11\mathrm{d})} \; \mathrm{d}S + \underbrace{\int_{\hat{\Gamma}_{\mathrm{Si}}} \mathbf{n} \cdot \boldsymbol{\sigma}^{(1)} \; \mathrm{d}S}_{=0 \text{ by periodicity of } \boldsymbol{\sigma}^{(1)} \text{ in } \hat{\mathbf{x}}} = 0, \tag{3.15}$$

where we can rearrange the divergence and integration of $\boldsymbol{\sigma}^{(0)}$ because we assume $\mathbf{x}$ and $\hat{\mathbf{x}}$ are independent. In the last integral, $\mathbf{n}$ is the normal vector pointing out of the unit cell being considered. The periodicity in $\hat{\mathbf{x}}$ requires continuity between boundaries of adjacent unit cells. Therefore the final integral in (3.15) is zero as the normal vectors are of opposite sign on opposite sides of the unit cell. Therefore, we find that the homogenised equation (3.14) is simply

$$\boldsymbol{\nabla} \cdot \int_{\hat{\Omega}_{\mathrm{Si}}} \boldsymbol{\sigma}^{(0)} \; \mathrm{d}V = 0, \tag{3.16}$$

and substituting (3.11b) yields

$$\boldsymbol{\nabla} \cdot \left[\int_{\hat{\Omega}_{\mathrm{Si}}} \mathbb{C}_{\mathrm{Si}}(c_{\mathrm{Si}}^{(0)}) : \left\{ \hat{\boldsymbol{\nabla}} \boldsymbol{u}^{(1)} + \boldsymbol{\nabla} \boldsymbol{u}^{(0)} - \gamma_{\mathrm{Si}} c_{\mathrm{Si}}^{(0)} \mathbf{1} \right\} \; \mathrm{d}V \right] = 0. \tag{3.17}$$

We wish to find $\boldsymbol{u}^{(1)}$ as a function of $\boldsymbol{u}^{(0)}$ and $c_{\mathrm{Si}}^{(0)}$ by solving (3.12) and (3.13). The solution $\boldsymbol{u}^{(1)}$, $\boldsymbol{u}^{(0)}$ and $c_{\mathrm{Si}}^{(0)}$ are then substituted into (3.11b) which is integrated over $\hat{\Omega}_{\mathrm{Si}}$ to find the effective stress in the porous silicon. The coupling between the stress and the concentration due to the stress-assisted diffusion, given in (3.13), causes the relationship between $\boldsymbol{u}^{(0)}$ and $\boldsymbol{u}^{(1)}$ to be nonlinear. Therefore, in general the microscale displacement, $\boldsymbol{u}^{(1)}$, needs to be calculated by solving (3.12) at every macroscale point due to $\boldsymbol{\nabla} \boldsymbol{u}^{(0)}$ and $c_{\mathrm{Si}}^{(0)}$ being functions of $\mathbf{x}$. Depending on the discretisation of the macroscale problem, this can reduce the computational cost of solving the governing equations on the complicated porous silicon domain. However, if the cell problems are linear in $\boldsymbol{\nabla} \boldsymbol{u}^{(0)}$ and $c_{\mathrm{Si}}^{(0)}$, we are able to remove these macroscale variables from the cell problems. This would allow us to solve the cell problem only once for a given geometry of unit cell, greatly reducing the computational cost.

In an attempt to linearise the cell problems by simplifying the coupling between the stress and the concentration, we investigate two different asymptotic limits of this formulation, taking the stress-assisted diffusion parameter, S_{Si}^d, to be small and to be large. This parameter, S_{Si}^d, is the ratio of the elastic energy to the thermal noise, defined in (2.40). We find that this can be achieved in the small S_{Si}^d case if $\mathbb{C}_{\mathrm{Si}}$ is independent of $c_{\mathrm{Si}}^{(0)}$. However, in the large S_{Si}^d case we arrive at a different nonlinear cell problem.

3.2.2 Small S_{Si}^d Limit

For the small S_{Si}^d case, it is useful to write the microscale displacement, $\boldsymbol{u}^{(1)}$, as the solution to a problem F given by (3.12) and (3.13), parametrised by S_{Si}^d,

$$\boldsymbol{u}^{(1)} = F(\boldsymbol{u}^{(0)}, c_{\mathrm{Si}}^{(0)}, S_{\mathrm{Si}}^d). \tag{3.18}$$

We Taylor expand in S_{Si}^d, giving

$$\boldsymbol{u}^{(1)} \approx F_0(\boldsymbol{u}^{(0)}, c_{\mathrm{Si}}^{(0)}) + S_{\mathrm{Si}}^d F_1(\boldsymbol{u}^{(0)}, c_{\mathrm{Si}}^{(0)}), \tag{3.19}$$

where F_0 is the $S_{\mathrm{Si}}^d = 0$ case and F_1 is the first-order correction.

We must now derive the F_0 and F_1 problems. Expanding $\boldsymbol{u}^{(1)}$ and $c_{\mathrm{Si}}^{(0)}$ in S_{Si}^d gives

$$\boldsymbol{u}^{(1)} = \boldsymbol{u}^{(1,0)} + S_{\mathrm{Si}}^d \boldsymbol{u}^{(1,1)} + (S_{\mathrm{Si}}^d)^2 \boldsymbol{u}^{(1,2)} + \dots, \tag{3.20a}$$

$$c_{\mathrm{Si}}^{(0)} = c_{\mathrm{Si}}^{(0,0)} + S_{\mathrm{Si}}^d c_{\mathrm{Si}}^{(0,1)} + (S_{\mathrm{Si}}^d)^2 c_{\mathrm{Si}}^{(0,2)} + \dots. \tag{3.20b}$$

Equating each term in (3.20b) to the Taylor expansion of $c_{\mathrm{Si}}^{(0)}$ in (3.13), yields

$$c_{\mathrm{Si}}^{(0,0)} = \mu_{\mathrm{SF}}^{-1}(\mu), \tag{3.21a}$$

$$c_{\mathrm{Si}}^{(0,1)} = \left.\frac{\partial \mu_{\mathrm{SF}}^{-1}}{\partial \mu_{\mathrm{Si}}^{\mathrm{SF}}}\right|_{\mu_{\mathrm{Si}}^{\mathrm{SF}} = \mu} \operatorname{tr}\Big(\mathbb{C}_{\mathrm{Si}}(c_{\mathrm{Si}}^{(0,0)}) : \big\{\hat{\boldsymbol{\nabla}} \boldsymbol{u}^{(1,0)} + \boldsymbol{\nabla} \boldsymbol{u}^{(0)} - \gamma_{\mathrm{Si}} c_{\mathrm{Si}}^{(0,0)} \mathbf{1}\big\}\Big). \tag{3.21b}$$

For the lithiation-dependent stiffness case, we find that the F_0 problem is still nonlinear in $c_{\mathrm{Si}}^{(0,0)}$ and the F_1 problem is still nonlinear in both $c_{\mathrm{Si}}^{(0,0)}$ and $\boldsymbol{\nabla} \boldsymbol{u}^{(0)}$. As we ignore the lithiation-dependence of the stiffness tensor when solving the linear model with porous silicon, as explained in Section 3.2.5, we make this simplification now and leave the derivation with a lithiation-dependent stiffness tensor to Appendix C.

3.2.2.1 $\boldsymbol{F_0}$ Problem

The F_0 problem is equivalent to neglecting stress-assisted diffusion. Substituting (3.20) into (3.12) yields

$$\hat{\boldsymbol{\nabla}} \cdot \big(\mathbb{C}_{\mathrm{Si}} : \hat{\boldsymbol{\nabla}} \boldsymbol{u}^{(1,0)}\big) = \hat{\boldsymbol{\nabla}} \cdot \big(\mathbb{C}_{\mathrm{Si}} : \gamma_{\mathrm{Si}} c_{\mathrm{Si}}^{(0,0)} \mathbf{1}\big) \qquad \text{in } \Omega_{\mathrm{Si}}, \tag{3.22a}$$

$$\big(\mathbb{C}_{\mathrm{Si}} : \hat{\boldsymbol{\nabla}} \boldsymbol{u}^{(1,0)}\big)\mathbf{n} = -\Big(\mathbb{C}_{\mathrm{Si}} : \big(\boldsymbol{\nabla} \boldsymbol{u}^{(0)} - \gamma_{\mathrm{Si}} c_{\mathrm{Si}}^{(0,0)} \mathbf{1}\big)\Big)\mathbf{n} \qquad \text{on } \Gamma_e, \tag{3.22b}$$

at leading order. Substituting the expansion (3.20b) into (3.10c) yields

$$\mu_{\mathrm{Si}}^{\mathrm{SF}}\big(c_{\mathrm{Si}}^{(0,0)}\big) = \mu, \tag{3.23}$$

at leading order in S_{Si}^{d}, showing that $c_{\mathrm{Si}}^{(0,0)}$ is independent of the microscale. This results in the right-hand side of (3.22a) being zero.

Now the macroscale displacement gradient $\boldsymbol{\nabla} \boldsymbol{u}^{(0)}$ and $\hat{\boldsymbol{\nabla}} \boldsymbol{u}^{(1,0)}$ appear linearly in (3.22). We also note that we can add a term that is independent of $\hat{\mathbf{x}}$ to $\boldsymbol{u}^{(1,0)}$ and still satisfy (3.22). Therefore, $\boldsymbol{u}^{(1,0)}$ is only unique up to an additive constant, independent of $\hat{\mathbf{x}}$. We write the microscale displacement $\boldsymbol{u}^{(1,0)}$ as a general linear function of $\boldsymbol{\nabla} \boldsymbol{u}^{(0)}$, given by

$$\boldsymbol{u}^{(1,0)} = \boldsymbol{\mathcal{A}}^{(0)} : \boldsymbol{\nabla} \boldsymbol{u}^{(0)} + \gamma_{\mathrm{Si}} c_{\mathrm{Si}}^{(0,0)} \boldsymbol{\xi}^{(0)} + \bar{\boldsymbol{u}}^{(1,0)}, \tag{3.24a}$$

where $\boldsymbol{\mathcal{A}}^{(0)}$ is a rank-3 tensor, $\mathbf{v}^{(0)}$ is a vector of length three and $\bar{\boldsymbol{u}}^{(1,0)}$ is a vector of length three which is independent of $\hat{\mathbf{x}}$. In suffix notation,

$$u_i^{(1,0)} = \mathcal{A}_{ijk}^{(0)} \frac{\partial u_j^{(0)}}{\partial x_k} + \gamma_{\mathrm{Si}} c_{\mathrm{Si}}^{(0,0)} \xi_i^{(0)} + \bar{u}_i^{(1,0)}. \tag{3.24b}$$

We require the microscale displacement, $\boldsymbol{u}^{(1)}$, to be periodic in the microscale variable $\hat{\mathbf{x}}$ and so $\boldsymbol{\mathcal{A}}^{(0)}$ and $\boldsymbol{\xi}^{(0)}$ must also be periodic in $\hat{\mathbf{x}}$. This periodicity is already satisfied by $\bar{\boldsymbol{u}}^{(1,0)}$ as it is uniform in $\hat{\mathbf{x}}$.

Substituting (3.24a) into (3.22) yields

$$\hat{\boldsymbol{\nabla}} \cdot \Big(\mathbb{C}_{\mathrm{Si}} : \Big\{\hat{\boldsymbol{\nabla}}\big(\boldsymbol{\mathcal{A}}^{(0)} : \boldsymbol{\nabla} \boldsymbol{u}^{(0)} + \gamma_{\mathrm{Si}} c_{\mathrm{Si}}^{(0,0)} \boldsymbol{\xi}^{(0)}\big)\Big\}\Big) = 0 \qquad \text{in } \hat{\Omega}_{\mathrm{Si}}, \tag{3.25a}$$

$$\begin{aligned} &\Big(\mathbb{C}_{\mathrm{Si}} : \Big\{\hat{\boldsymbol{\nabla}}\big(\boldsymbol{\mathcal{A}}^{(0)} : \boldsymbol{\nabla} \boldsymbol{u}^{(0)} + \gamma_{\mathrm{Si}} c_{\mathrm{Si}}^{(0,0)} \boldsymbol{\xi}^{(0)}\big)\Big\}\Big)\mathbf{n} \\ &\qquad = -\Big[\mathbb{C}_{\mathrm{Si}} : \Big(\boldsymbol{\nabla} \boldsymbol{u}^{(0)} - \gamma_{\mathrm{Si}} c_{\mathrm{Si}}^{(0,0)} \mathbf{1}\Big)\Big]\mathbf{n} \end{aligned} \qquad \text{on } \hat{\Gamma}_e. \tag{3.25b}$$

We then need to solve (3.25) for $\boldsymbol{\mathcal{A}}^{(0)}$ and $\boldsymbol{\xi}^{(0)}$ to find the leading-order microscale displacement, $\boldsymbol{u}^{(1,0)}$ in terms of the macroscale displacement $\boldsymbol{u}^{(0)}$. Since the system (3.25) must be valid for any $\boldsymbol{u}^{(0)}$ and is linear in $\boldsymbol{u}^{(0)}$, we can separate (3.25) into the parts which depend on $\boldsymbol{u}^{(0)}$ and those which do not. The $\boldsymbol{u}^{(0)}$-dependent terms form a problem for $\mathcal{A}^{(0)}$ given by

$$\hat{\boldsymbol{\nabla}} \cdot \left(\mathbb{C}_{\mathrm{Si}} : \hat{\boldsymbol{\nabla}} \mathcal{A}^{(0)}\right) = \mathbf{0} \qquad \text{in } \hat{\Omega}_{\mathrm{Si}}, \tag{3.26a}$$

$$\left(\mathbb{C}_{\mathrm{Si}} : \hat{\boldsymbol{\nabla}} \mathcal{A}^{(0)}\right)\mathbf{n} = -\mathbb{C}_{\mathrm{Si}} \cdot \mathbf{n} \qquad \text{on } \hat{\Gamma}_e. \tag{3.26b}$$

This problem for $\mathcal{A}^{(0)}$ is also only solveable up to an arbitrary additional constant rank-3 tensor. Although there is non-uniqueness to the problem for $\boldsymbol{u}^{(1,0)}$, we allow all arbitrary functions of $\mathbf{x}$ in $\boldsymbol{u}^{(1,0)}$ to be a part of $\bar{u}_i^{(1,0)}$, and thus the integral of $\mathcal{A}^{(0)}$ across the unit cell must be zero. This is helpful in numerically solving for $\mathcal{A}^{(0)}$ as it is now unique. We impose this integral condition along with the periodicity constraints to give

$$\int_{\hat{\Omega}_{\mathrm{Si}}} \mathcal{A}^{(0)} \; \mathrm{d}V = 0, \tag{3.26c}$$

$$\mathcal{A}^{(0)} \text{ is periodic in } \hat{\mathbf{x}}, \tag{3.26d}$$

respectively. For ease of understanding, we write (3.26a)-(3.26b) in suffix notation as

$$\frac{\partial}{\partial \hat{x}_j} c^{\mathrm{Si}}_{ijkl} \frac{\partial \mathcal{A}^{(0)}_{krs}}{\partial \hat{x}_l} = 0 \qquad \text{in } \hat{\Omega}_{\mathrm{Si}}, \tag{3.27a}$$

$$\mathrm{n}_j \left(c^{\mathrm{Si}}_{ijkl} \frac{\partial \mathcal{A}^{(0)}_{krs}}{\partial \hat{x}_l} \right) = -\mathrm{n}_j c^{\mathrm{Si}}_{ijrs} \qquad \text{on } \hat{\Gamma}_e. \tag{3.27b}$$

Now we consider the parts of the system (3.25) that do not depend on $\boldsymbol{u}^{(0)}$ and these form a problem for the vector $\boldsymbol{\xi}^{(0)}$ given by

$$\hat{\boldsymbol{\nabla}} \cdot \left(\mathbb{C}_{\mathrm{Si}} : \hat{\boldsymbol{\nabla}} \boldsymbol{\xi}^{(0)}\right) = 0, \qquad \text{in } \hat{\Omega}_{\mathrm{Si}}, \tag{3.28a}$$

$$\left(\mathbb{C}_{\mathrm{Si}} : \hat{\boldsymbol{\nabla}} \boldsymbol{\xi}^{(0)}\right)\mathbf{n} = \left(\mathbb{C}_{\mathrm{Si}} : \mathbf{1}\right)\mathbf{n}, \qquad \text{on } \hat{\Gamma}_e. \tag{3.28b}$$

For the same reasons as for $\mathcal{A}^{(0)}$, we impose integral and periodicity constraints for $\boldsymbol{\xi}^{(0)}$ so that

$$\int_{\hat{\Omega}_{\mathrm{Si}}} \boldsymbol{\xi}^{(0)} \; \mathrm{d}V = 0, \tag{3.28c}$$

$$\boldsymbol{\xi} \text{ is periodic in } \hat{\mathbf{x}}. \tag{3.28d}$$

The problem for $\boldsymbol{\xi}^{(0)}$ can be written in suffix notation as

$$\frac{\partial}{\partial \hat{x}_j} c^{\mathrm{Si}}_{ijkl} \frac{\partial \xi^{(0)}_{k}}{\partial \hat{x}_l} = 0 \qquad \text{in } \hat{\Omega}_{\mathrm{Si}}, \tag{3.29a}$$

$$\mathrm{n}_j \left(c^{\mathrm{Si}}_{ijkl} \frac{\partial \xi^{(0)}_{k}}{\partial \hat{x}_l} \right) = \mathrm{n}_j c^{\mathrm{Si}}_{ijkl} \delta_{kl} \qquad \text{on } \hat{\Gamma}_e. \tag{3.29b}$$

As we have (3.26c) and (3.28c), we now know the integral of $\boldsymbol{u}^{(1,0)}$ is equal to the integral of $\bar{\boldsymbol{u}}^{(1,0)}$ over the unit cell.

The systems of equations, (3.26) and (3.28), are called the cell problems for $\boldsymbol{\mathcal{A}}^{(0)}$ and $\boldsymbol{\xi}^{(0)}$, respectively. These are solved numerically over the unit cell shown in Figure 3.4 to find $\boldsymbol{\mathcal{A}}^{(0)}$ and $\boldsymbol{\xi}^{(0)}$, typically by the finite element method. These solutions are then substituted into (3.24a) to find the leading-order microscale displacement, $\boldsymbol{u}^{(1,0)}$.

3.2.2.2 $\boldsymbol{F_1}$ Problem

Assuming a lithiation-independent stiffness tensor, the first-order system in S_{Si}^{d} from substituting (3.20) into (3.12), is given by

$$\hat{\boldsymbol{\nabla}} \cdot \left(\mathbb{C}_{\mathrm{Si}} : \hat{\boldsymbol{\nabla}} \boldsymbol{u}^{(1,1)}\right) = \hat{\boldsymbol{\nabla}} \cdot \left(\mathbb{C}_{\mathrm{Si}} : \gamma_{\mathrm{Si}} c_{\mathrm{Si}}^{(0,1)} \mathbf{1}\right) \qquad \text{in } \Omega_{\mathrm{Si}}, \tag{3.30a}$$

$$\left[\mathbb{C}_{\mathrm{Si}} : \left\{\hat{\boldsymbol{\nabla}} \boldsymbol{u}^{(1,1)} - \gamma_{\mathrm{Si}} c_{\mathrm{Si}}^{(0,1)} \mathbf{1}\right\}\right] \mathbf{n} = 0 \qquad \text{on } \Gamma_e. \tag{3.30b}$$

Substituting (3.21b) for $c_{\mathrm{Si}}^{(0,1)}$ yields

$$\hat{\boldsymbol{\nabla}} \cdot \left[\mathbb{C}_{\mathrm{Si}} : \left\{\hat{\boldsymbol{\nabla}} \boldsymbol{u}^{(1,1)} - \tilde{\gamma}_{\mathrm{Si}} \operatorname{tr}\Big(\mathbb{C}_{\mathrm{Si}} : \big\{\hat{\boldsymbol{\nabla}} \boldsymbol{u}^{(1,0)}\big\}\Big) \mathbf{1}\right\}\right] = 0 \qquad \text{in } \hat{\Omega}_{\mathrm{Si}}, \tag{3.31a}$$

$$\left[\mathbb{C}_{\mathrm{Si}} : \left\{\hat{\boldsymbol{\nabla}} \boldsymbol{u}^{(1,1)} - \tilde{\gamma}_{\mathrm{Si}} \operatorname{tr}\Big(\mathbb{C}_{\mathrm{Si}} : \big\{\hat{\boldsymbol{\nabla}} \boldsymbol{u}^{(1,0)} + \boldsymbol{\nabla} \boldsymbol{u}^{(0)} - \gamma_{\mathrm{Si}} c_{\mathrm{Si}}^{(0,0)} \mathbf{1}\big\}\Big) \mathbf{1}\right\}\right] \mathbf{n} = 0 \text{ on } \hat{\Gamma}_e, \tag{3.31b}$$

where, using the inverse function theorem,

$$\tilde{\gamma}_{\mathrm{Si}} = \gamma_{\mathrm{Si}} \left.\frac{\partial \mu_{\mathrm{SF}}^{-1}}{\partial \mu_{\mathrm{Si}}^{\mathrm{SF}}}\right|_{\mu_{\mathrm{Si}}^{\mathrm{SF}} = \mu} = \frac{\gamma_{\mathrm{Si}}}{\left.\frac{\partial \mu_{\mathrm{Si}}^{\mathrm{SF}}}{\partial c_{\mathrm{Si}}}\right|_{c_{\mathrm{Si}} = c_{\mathrm{Si}}^{(0,0)}}}. \tag{3.32}$$

We assume $\tilde{\gamma}_{\mathrm{Si}} = o(1/S_{\mathrm{Si}}^{d})$. However, for chemical potentials with plateaus, for example graphite, this quantity may be very large or even singular if γ_a is not small, and so this term must be treated with care in practice. Note, the $\boldsymbol{u}^{(0)}$ and $c_{\mathrm{Si}}^{(0,0)}$ terms from $c_{\mathrm{Si}}^{(0,1)}$ do not appear in the PDE (3.31a) as they are independent of $\hat{\mathbf{x}}$.

As (3.31) is linear in $\boldsymbol{\nabla} \boldsymbol{u}^{(0)}$, we make a similar ansatz for the relationship to between $\boldsymbol{u}^{(1,1)}$ and $\boldsymbol{u}^{(0)}$, similar to (3.24a), given by

$$\boldsymbol{u}^{(1,1)} = \tilde{\gamma}_{\mathrm{Si}} \boldsymbol{\mathcal{A}}^{(1)} : \boldsymbol{\nabla} \boldsymbol{u}^{(0)} + \gamma_{\mathrm{Si}} \tilde{\gamma}_{\mathrm{Si}} c_{\mathrm{Si}}^{(0,0)} \boldsymbol{\xi}^{(1)} + \bar{\boldsymbol{u}}^{(1,1)}, \tag{3.33}$$

where $\bar{\boldsymbol{u}}^{(1,1)}$ is independent of $\hat{\mathbf{x}}$. When substituting (3.33) into (3.31), it useful to note that for a rank-2 tensor, $\mathbf{Z}$, we have

$$\operatorname{tr}(\mathbb{C}_{\mathrm{Si}} : \mathbf{Z}) = \delta_{ij} c_{ijkl}^{\mathrm{Si}} Z_{kl} = c_{iikl}^{\mathrm{Si}} Z_{kl} = \operatorname{Tr}(\mathbb{C}_{\mathrm{Si}}) : \mathbf{Z}, \tag{3.34a}$$

where

$$\mathrm{Tr}(\mathbb{C}_{\mathrm{Si}}) = \sum_{i=1}^{3} c^{\mathrm{Si}}_{iikl}. \tag{3.34b}$$

This changes (3.31) to

$$\hat{\boldsymbol{\nabla}} \cdot \left[\mathbb{C}_{\mathrm{Si}} : \left\{\hat{\boldsymbol{\nabla}} \boldsymbol{u}^{(1,1)} - \tilde{\gamma}_{\mathrm{Si}} \mathrm{Tr}(\mathbb{C}_{\mathrm{Si}}) : \{\hat{\boldsymbol{\nabla}} \boldsymbol{u}^{(1,0)}\}\mathbf{1}\right\}\right] = 0 \quad \text{in } \hat{\Omega}_{\mathrm{Si}}, \tag{3.35a}$$

$$\left[\mathbb{C}_{\mathrm{Si}} : \left\{\hat{\boldsymbol{\nabla}} \boldsymbol{u}^{(1,1)} - \tilde{\gamma}_{\mathrm{Si}} \mathrm{Tr}(\mathbb{C}_{\mathrm{Si}}) : \{\hat{\boldsymbol{\nabla}} \boldsymbol{u}^{(1,0)} + \boldsymbol{\nabla} \boldsymbol{u}^{(0)} - \gamma_{\mathrm{Si}} c_{\mathrm{Si}}^{(0,0)} \mathbf{1}\}\mathbf{1}\right\}\right]\mathbf{n} = 0 \quad \text{on } \hat{\Gamma}_e. \tag{3.35b}$$

Substituting (3.24a) and (3.33) into (3.35) yields

$$\begin{aligned}
&\hat{\boldsymbol{\nabla}} \cdot \Bigg[\mathbb{C}_{\mathrm{Si}} : \Bigg\{\hat{\boldsymbol{\nabla}} \mathcal{A}^{(1)} : \boldsymbol{\nabla} \boldsymbol{u}^{(0)} + \gamma_{\mathrm{Si}} c_{\mathrm{Si}}^{(0,0)} \hat{\boldsymbol{\nabla}} \boldsymbol{\xi}^{(1)} \\
&- \mathrm{Tr}\big(\mathbb{C}_{\mathrm{Si}}\big) : \{\hat{\boldsymbol{\nabla}} \mathcal{A}^{(0)} : \boldsymbol{\nabla} \boldsymbol{u}^{(0)}\}\mathbf{1} - \gamma_{\mathrm{Si}} c_{\mathrm{Si}}^{(0,0)} \mathrm{Tr}\big(\mathbb{C}_{\mathrm{Si}}\big) : \{\hat{\boldsymbol{\nabla}} \boldsymbol{\xi}^{(0)}\}\mathbf{1}\Bigg\}\Bigg] = 0 \;\; \text{in } \hat{\Omega}_{\mathrm{Si}},
\end{aligned} \tag{3.36a}$$

$$\begin{aligned}
&\Bigg[\mathbb{C}_{\mathrm{Si}} : \Bigg\{\hat{\boldsymbol{\nabla}} \mathcal{A}^{(1)} : \boldsymbol{\nabla} \boldsymbol{u}^{(0)} + \gamma_{\mathrm{Si}} c_{\mathrm{Si}}^{(0,0)} \hat{\boldsymbol{\nabla}} \boldsymbol{\xi}^{(1)} - \mathrm{Tr}\big(\mathbb{C}_{\mathrm{Si}}\big) : \{\hat{\boldsymbol{\nabla}} \mathcal{A}^{(0)} : \boldsymbol{\nabla} \boldsymbol{u}^{(0)}\}\mathbf{1} \\
&\qquad - \gamma_{\mathrm{Si}} c_{\mathrm{Si}}^{(0,0)} \mathrm{Tr}\big(\mathbb{C}_{\mathrm{Si}}\big) : \{\hat{\boldsymbol{\nabla}} \boldsymbol{\xi}^{(0)}\}\mathbf{1} - \mathrm{Tr}\big(\mathbb{C}_{\mathrm{Si}}\big) : \{\boldsymbol{\nabla} \boldsymbol{u}^{(0)}\}\mathbf{1} \\
&\qquad\qquad - \gamma_{\mathrm{Si}} c_{\mathrm{Si}}^{(0,0)} \Big(\mathrm{Tr}\big(\mathbb{C}_{\mathrm{Si}}\big) : \mathbf{1}\Big)\mathbf{1}\Bigg\}\Bigg]\mathbf{n} = 0 \qquad \text{on } \hat{\Gamma}_e.
\end{aligned} \tag{3.36b}$$

Taking the terms proportional to $\boldsymbol{\nabla} \boldsymbol{u}^{(0)}$, we form a problem for $\mathcal{A}^{(1)}$, given by

$$\hat{\boldsymbol{\nabla}} \cdot \left[\mathbb{C}_{\mathrm{Si}} : \left\{\hat{\boldsymbol{\nabla}} \mathcal{A}^{(1)}\right\}\right] = \hat{\boldsymbol{\nabla}} \cdot \left[\mathbb{C}_{\mathrm{Si}} : \left\{\mathrm{Tr}\big(\mathbb{C}_{\mathrm{Si}}\big) : \{\hat{\boldsymbol{\nabla}} \mathcal{A}^{(0)}\}\mathbf{1}\right\}\right] \text{ in } \hat{\Omega}_{\mathrm{Si}}, \tag{3.37a}$$

$$\left[\mathbb{C}_{\mathrm{Si}} : \left\{\hat{\boldsymbol{\nabla}} \mathcal{A}^{(1)}\right\}\right]\mathbf{n} = \left[\mathbb{C}_{\mathrm{Si}} : \left\{\left[\mathrm{Tr}\big(\mathbb{C}_{\mathrm{Si}}\big) : \{\hat{\boldsymbol{\nabla}} \mathcal{A}^{(0)}\} + \mathrm{Tr}\big(\mathbb{C}_{\mathrm{Si}}\big)\right]\mathbf{1}\right\}\right]\mathbf{n} \text{ on } \hat{\Gamma}_e. \tag{3.37b}$$

The remaining terms form a problem for $\boldsymbol{\xi}^{(1)}$, given by

$$\hat{\boldsymbol{\nabla}} \cdot \left[\mathbb{C}_{\mathrm{Si}} : \left\{\hat{\boldsymbol{\nabla}} \boldsymbol{\xi}^{(1)}\right\}\right] = \hat{\boldsymbol{\nabla}} \cdot \left[\mathbb{C}_{\mathrm{Si}} : \left\{\left[\mathrm{Tr}\big(\mathbb{C}_{\mathrm{Si}}\big) : \{\hat{\boldsymbol{\nabla}} \boldsymbol{\xi}^{(0)}\}\right]\mathbf{1}\right\}\right] \text{ in } \hat{\Omega}_{\mathrm{Si}}, \tag{3.38a}$$

$$\begin{aligned}
&\left[\mathbb{C}_{\mathrm{Si}} : \left\{\hat{\boldsymbol{\nabla}} \boldsymbol{\xi}^{(1)}\right\}\right]\mathbf{n} \\
&\qquad = \left[\mathbb{C}_{\mathrm{Si}} : \left\{\left[\mathrm{Tr}\big(\mathbb{C}_{\mathrm{Si}}\big) : \{\hat{\boldsymbol{\nabla}} \boldsymbol{\xi}^{(0)}\} - \mathrm{Tr}\big(\mathbb{C}_{\mathrm{Si}}\big) : \mathbf{1}\right]\mathbf{1}\right\}\right]\mathbf{n} \text{ in } \hat{\Gamma}_e,
\end{aligned} \tag{3.38b}$$

We also have the usual periodicity and integral conditions on $\mathcal{A}^{(1)}$ and $\boldsymbol{\xi}^{(1)}$.

The cell problems for $\mathcal{A}^{(0)}$, $\boldsymbol{\xi}^{(0)}$, $\mathcal{A}^{(1)}$ and $\boldsymbol{\xi}^{(1)}$, given by (3.26), (3.28), (3.37) and (3.38), respectively, do not depend on any macroscale variables. Therefore, they only need to be solved once for a given unit cell geometry, saving a huge amount of computational cost.

3.2.2.3 Homogenised Equation

We have now derived problems for $\mathcal{A}^{(0)}$, $\mathcal{A}^{(1)}$, $\boldsymbol{\xi}^{(0)}$ and $\boldsymbol{\xi}^{(1)}$. To find the effective parameters for the porous silicon, we now substitute (3.24a) and (3.33) into (3.17) to give

$$\begin{aligned}
&\boldsymbol{\nabla}\cdot\Bigg[\int_{\hat{\Omega}_{\mathrm{Si}}}\mathbb{C}_{\mathrm{Si}}:\Big\{\hat{\boldsymbol{\nabla}}\Big(\boldsymbol{u}^{(1,0)}+S^d_{\mathrm{Si}}\boldsymbol{u}^{(1,1)}+\mathcal{O}\big((S^d_{\mathrm{Si}})^2\big)\Big)+\boldsymbol{\nabla}\boldsymbol{u}^{(0)}-\gamma_{\mathrm{Si}}c^{(0)}_{\mathrm{Si}}\mathbf{1}\Big\}\ \mathrm{d}V\Bigg]\\
&=\boldsymbol{\nabla}\cdot\Bigg[\int_{\hat{\Omega}_{\mathrm{Si}}}\mathbb{C}_{\mathrm{Si}}:\Big\{\hat{\boldsymbol{\nabla}}\Big[\mathcal{A}^{(0)}:\boldsymbol{\nabla}\boldsymbol{u}^{(0)}+\gamma_{\mathrm{Si}}c^{(0,0)}_{\mathrm{Si}}\boldsymbol{\xi}^{(0)}\\
&\qquad\qquad\qquad\qquad+S^d_{\mathrm{Si}}\tilde{\gamma}_{\mathrm{Si}}\big(\mathcal{A}^{(1)}:\boldsymbol{\nabla}\boldsymbol{u}^{(0)}+\gamma_{\mathrm{Si}}c^{(0,0)}_{\mathrm{Si}}\boldsymbol{\xi}^{(1)}\big)\Big]\\
&\quad-S^d_{\mathrm{Si}}\tilde{\gamma}_{\mathrm{Si}}\mathrm{Tr}(\mathbb{C}_{\mathrm{Si}}):\Big\{\hat{\boldsymbol{\nabla}}\big[\mathcal{A}^{(0)}:\boldsymbol{\nabla}\boldsymbol{u}^{(0)}+\gamma_{\mathrm{Si}}c^{(0,0)}_{\mathrm{Si}}\boldsymbol{\xi}^{(0)}\big]+\boldsymbol{\nabla}\boldsymbol{u}^{(0)}-\gamma_{\mathrm{Si}}c^{(0,0)}_{\mathrm{Si}}\mathbf{1}\Big\}\mathbf{1}\\
&\qquad\qquad+\boldsymbol{\nabla}\boldsymbol{u}^{(0)}-\gamma_{\mathrm{Si}}c^{(0,0)}_{\mathrm{Si}}\mathbf{1}\Big\}+\mathcal{O}\big((S^d_{\mathrm{Si}})^2\big)\ \mathrm{d}V\Bigg]=0.
\end{aligned}\tag{3.39}$$

We write this mechanical equilibrium equation for the porous silicon as $\boldsymbol{\nabla}\cdot\boldsymbol{\sigma}_\phi=0$, where

$$\boldsymbol{\sigma}_\phi=\Big(\mathbb{C}^{(0)}_\phi+S^d_{\mathrm{Si}}\tilde{\gamma}_{\mathrm{Si}}\mathbb{C}^{(1)}_\phi\Big):\boldsymbol{\nabla}\boldsymbol{u}^{(0)}-\gamma_{\mathrm{Si}}c^{(0,0)}_{\mathrm{Si}}\Big(\boldsymbol{\Psi}^{(0)}_\phi+S^d_{\mathrm{Si}}\tilde{\gamma}_{\mathrm{Si}}\boldsymbol{\Psi}^{(1)}_\phi\Big).\tag{3.40}$$

The tensors $\mathbb{C}^{(0)}_\phi$ and $\boldsymbol{\Psi}^{(0)}_\phi$ are the leading-order effective stiffness and effective expansion coefficient, respectively, given by

$$\mathbb{C}^{(0)}_\phi=\frac{1}{|\hat{\Omega}|}\int_{\hat{\Omega}_{\mathrm{Si}}}\mathbb{C}_{\mathrm{Si}}:\hat{\boldsymbol{\nabla}}\mathcal{A}^{(0)}+\mathbb{C}_{\mathrm{Si}}\ \mathrm{d}V,\tag{3.41a}$$

$$\boldsymbol{\Psi}^{(0)}_\psi=\frac{1}{|\hat{\Omega}|}\int_{\hat{\Omega}_{\mathrm{Si}}}\mathbb{C}_{\mathrm{Si}}:\Big\{\mathbf{1}-\hat{\boldsymbol{\nabla}}\boldsymbol{\xi}^{(0)}\Big\}\ \mathrm{d}V,\tag{3.41b}$$

where we normalise by the volume of the unit cell, $|\hat{\Omega}|$, including the pore and the silicon scaffold. The first-order corrections to the effective stiffness and expansion coefficient, given by $\mathbb{C}_{\phi}^{(1)}$ and $\boldsymbol{\Psi}_{\phi}^{(1)}$, are given by

$$\mathbb{C}_{\phi}^{(1)} = \frac{1}{|\hat{\Omega}|}\int_{\hat{\Omega}_{\mathrm{Si}}} \mathbb{C}_{\mathrm{Si}} : \left\{ \hat{\boldsymbol{\nabla}}\mathcal{A}^{(1)} - \Big[\mathrm{Tr}\big(\mathbb{C}_{\mathrm{Si}}\big) : \big\{\hat{\boldsymbol{\nabla}}\mathcal{A}^{(0)}\big\} + \mathrm{Tr}\big(\mathbb{C}_{\mathrm{Si}}\big)\Big]\mathbf{1} \right\} \, \mathrm{d}V, \tag{3.41c}$$

$$\boldsymbol{\Psi}_{\phi}^{(1)} = \frac{1}{|\hat{\Omega}|}\int_{\hat{\Omega}_{\mathrm{Si}}} \mathbb{C}_{\mathrm{Si}} : \left\{ \Big[\mathrm{Tr}\big(\mathbb{C}_{\mathrm{Si}}\big) : \big\{\hat{\boldsymbol{\nabla}}\boldsymbol{\xi}^{(0)} - \mathbf{1}\big\}\Big]\mathbf{1} - \hat{\boldsymbol{\nabla}}\boldsymbol{\xi}^{(1)} \right\} \, \mathrm{d}V. \tag{3.41d}$$

We have now derived approximate effective parameters, $\mathbb{C}_{\phi}$ and $\boldsymbol{\Psi}_{\phi}$, for porous silicon consisting of a periodic lattice of pores for materials with a small stress-assisted diffusion parameter, S_{Si}^{d}. These are given by

$$\mathbb{C}_{\phi} = \mathbb{C}_{\phi}^{(0)} + S_{\mathrm{Si}}^{d}\tilde{\gamma}_{\mathrm{Si}}\mathbb{C}_{\phi}^{(1)}, \tag{3.42a}$$

$$\boldsymbol{\Psi}_{\phi} = \gamma_{\mathrm{Si}}\big(\boldsymbol{\Psi}_{\phi}^{(0)} + S_{\mathrm{Si}}^{d}\tilde{\gamma}_{\mathrm{Si}}\boldsymbol{\Psi}_{\phi}^{(1)}\big). \tag{3.42b}$$

As $\mathcal{A}^{(0)}$, $\boldsymbol{\xi}^{(0)}$, $\mathcal{A}^{(1)}$ and $\boldsymbol{\xi}^{(1)}$ need only be solved for once for a given unit cell geometry, these effective parameters can be calculated much more efficiently than the full nonlinear problem (3.12).

3.2.3 Large S_{Si}^{d} Limit

We now consider the limit of large S_{Si}^{d} in the multiple-scales formulation (3.12)-(3.13). The leading order equation for the lithium concentration is given by (3.10c), reading

$$\mu_{\mathrm{Si}}^{\mathrm{SF}}\big(c_{\mathrm{Si}}^{(0)}\big) - S_{\mathrm{Si}}^{d}\mathrm{tr}\big(\boldsymbol{\sigma}^{(0)}\big) = \mu. \tag{3.43}$$

We assume $\mu = \mathcal{O}(1)$ throughout this section. From nondimensionalising the stress-free chemical potentials shown in Figure 2.2, we have that $\mu_{\mathrm{Si}}^{\mathrm{SF}}(c_{\mathrm{Si}}^{(0)}) \sim \mathcal{O}(1)$ for $0 < c_{\mathrm{Si}}^{(0)} < 1$. Therefore, for $0 < c_{\mathrm{Si}}^{(0)} < 1$, in the limit of large S_{Si}^{d}, (3.43) becomes $\mathrm{tr}\big(\boldsymbol{\sigma}^{(0)}\big) = 0$ at leading order. In this case, substituting (3.11b) into $\mathrm{tr}\big(\boldsymbol{\sigma}^{(0)}\big) = 0$, yields

$$\mathrm{Tr}\big(\mathbb{C}_{\mathrm{Si}}\big) : \left\{\hat{\boldsymbol{\nabla}}\boldsymbol{u}^{(1)} + \boldsymbol{\nabla}\boldsymbol{u}^{(0)} - \gamma_{\mathrm{Si}}c_{\mathrm{Si}}^{(0)}\mathbf{1}\right\} = 0. \tag{3.44}$$

Writing this expression in suffix notation and rearranging, yields

$$c_{iikl}^{\mathrm{Si}}\left(\frac{\partial u_k^{(1)}}{\partial \hat{x}_l} + \frac{\partial u_k^{(0)}}{\partial x_l}\right) = \gamma_{\mathrm{Si}}c_{\mathrm{Si}}^{(0)}c_{iikl}^{\mathrm{Si}}\delta_{kl} = \gamma_{\mathrm{Si}}c_{\mathrm{Si}}^{(0)}c_{iikk}^{\mathrm{Si}}, \tag{3.45}$$

$$\implies c_{\mathrm{Si}}^{(0)} = \frac{c_{iikl}^{\mathrm{Si}}}{\gamma_{\mathrm{Si}}c_{ppnn}^{\mathrm{Si}}}\left(\frac{\partial u_k^{(1)}}{\partial \hat{x}_l} + \frac{\partial u_k^{(0)}}{\partial x_l}\right). \tag{3.46}$$

As c^{Si}_{ppnn} is a scalar combination of the components of $\mathbb{C}_{\mathrm{Si}}$, the prefactor to the $\boldsymbol{u}^{(0)}$ and $\boldsymbol{u}^{(1)}$ terms can be written as a modified stiffness tensor, $\tilde{\mathbb{C}}_{\mathrm{Si}}$, which is rank-2. This gives the expression for the leading-order concentration as

$$c^{(0)}_{\mathrm{Si}} = \mathrm{tr}\Big[\tilde{\mathbb{C}}_{\mathrm{Si}}\big(\hat{\boldsymbol{\nabla}}\boldsymbol{u}^{(1)} + \boldsymbol{\nabla}\boldsymbol{u}^{(0)}\big)\Big]. \tag{3.47}$$

Therefore, if $0 < c^{(0)}_{\mathrm{Si}} < 1$, the leading-order concentration, $c^{(0)}_{\mathrm{Si}}$, has periodic variations within each unit cell due to the dependence on $\boldsymbol{u}^{(1)}$, and aperiodic variation across the macroscale geometry due to the dependence on $\boldsymbol{u}^{(0)}$.

However, if $c^{(0)}_{\mathrm{Si}} = 0$ or $c^{(0)}_{\mathrm{Si}} = 1$, we must address (3.43) more carefully. As explained in Section 2.5.1.1, as $c^{(0)}_{\mathrm{Si}} \to 0$, $\mu^{\mathrm{SF}}_{\mathrm{Si}}\big(c^{(0)}_{\mathrm{Si}}\big) \to -\infty$ and as $c^{(0)}_{\mathrm{Si}} \to 1$, $\mu^{\mathrm{SF}}_{\mathrm{Si}}\big(c^{(0)}_{\mathrm{Si}}\big) \to \infty$. Therefore, for $c^{(0)}_{\mathrm{Si}} = 0$ or 1, the S^{d}_{Si} term may balance with $\mu^{\mathrm{SF}}_{\mathrm{Si}}$, giving

$$\mu^{\mathrm{SF}}_{\mathrm{Si}}\big(c^{(0)}_{\mathrm{Si}}\big) = S^{d}_{\mathrm{Si}}\mathrm{tr}\big(\boldsymbol{\sigma}^{(0)}\big), \tag{3.48}$$

at leading order. The sign of $\mathrm{tr}\big(\boldsymbol{\sigma}^{(0)}\big)$ will change to satisfy (3.48), depending on whether $c^{(0)}_{\mathrm{Si}} = 0$ or $c^{(0)}_{\mathrm{Si}} = 1$.

Therefore there are three cases for terms to balance in (3.43), given by

$$\begin{aligned}
&\mathrm{tr}\big(\boldsymbol{\sigma}^{(0)}\big) < 0 \qquad \text{for} \quad c^{(0)}_{\mathrm{Si}} = 0, && \text{(3.49a)}\\
&\mathrm{tr}\big(\boldsymbol{\sigma}^{(0)}\big) = 0 \qquad \text{for} \quad 0 < c^{(0)}_{\mathrm{Si}} < 1, && \text{(3.49b)}\\
&\mathrm{tr}\big(\boldsymbol{\sigma}^{(0)}\big) > 0 \qquad \text{for} \quad c^{(0)}_{\mathrm{Si}} = 1. && \text{(3.49c)}
\end{aligned}$$

This can be written as a nonlinear complementarity problem (NCP), given by

$$\begin{aligned}
c^{(0)}_{\mathrm{Si}}\big(1 - c^{(0)}_{\mathrm{Si}}\big)\mathrm{tr}\big(\boldsymbol{\sigma}^{(0)}\big) &= 0, && \text{(3.50a)}\\
c^{(0)}_{\mathrm{Si}} \geq 0, \quad 1 - c^{(0)}_{\mathrm{Si}} &\geq 0, && \text{(3.50b)}\\
\text{if } c^{(0)}_{\mathrm{Si}} = 0, \mathrm{tr}\big(\boldsymbol{\sigma}^{(0)}\big) < 0, &\text{ and if } c^{(0)}_{\mathrm{Si}} = 1, \mathrm{tr}\big(\boldsymbol{\sigma}^{(0)}\big) > 0. && \text{(3.50c)}
\end{aligned}$$

NCPs are often solved by constructing a complementarity function Φ such that

$$\Phi(a,b) = 0 \Longleftrightarrow a \geq 0,\ b \geq 0,\ ab = 0, \tag{3.51}$$

for example, in [10, 122]. Two examples of complementarity functions are the max-plus function [16] and the Fischer-Burmeister function [36], given by

$$\begin{aligned}
\Phi(a,b) &= a - \max(0, a-b), && \text{(3.52a)}\\
\Phi(a,b) &= \sqrt{a^2 + b^2} - a - b, && \text{(3.52b)}
\end{aligned}$$

respectively. The complementarity problem in (3.50) has two conditions but can be written as

$$\Phi\left(\Phi\left(\mathrm{tr}\left(\boldsymbol{\sigma}^{(0)}\right), 1 - c_{\mathrm{Si}}^{(0)}\right), c_{\mathrm{Si}}^{(0)}\right) = 0. \tag{3.53}$$

From (3.11b), we have

$$\mathrm{tr}\left(\boldsymbol{\sigma}\right) = \mathrm{Tr}\left(\mathbb{C}_{\mathrm{Si}}\left(c_{\mathrm{Si}}^{(0)}\right)\right) : \left\{\hat{\boldsymbol{\nabla}}\boldsymbol{u}^{(1)} + \boldsymbol{\nabla}\boldsymbol{u}^{(0)} - \gamma_{\mathrm{Si}} c_{\mathrm{Si}}^{(0)} \mathbf{1}\right\}. \tag{3.54}$$

Substituting (3.54) into (3.53) yields a nonlinear equation in $c_{\mathrm{Si}}^{(0)}$ and $\boldsymbol{\nabla}\boldsymbol{u}^{(0)}$ for either of the complementarity functions in (3.52). Therefore, to find how the microscale displacement, $\boldsymbol{u}^{(1)}$, relates to the macroscale displacement, $\boldsymbol{u}^{(0)}$, would require solving the NCP along with the PDE system (3.12) at every macroscale point, as the NCP is nonlinear in $\boldsymbol{\nabla}\boldsymbol{u}^{(0)}$ and $c_{\mathrm{Si}}^{(0)}$. Unlike the nonlinear terms that arise in the small S_{Si}^{d} case, the nonlinearities in the large S_{Si}^{d} case cannot be removed by assuming a lithiation-independent stiffness tensor.

3.2.4 Reductions in Spherical Symmetry

Here, we briefly discuss the reductions to the computational cost of solving both the fully nonlinear multiple-scales problem and the large S_{Si}^{d} problem by interpolating between different solutions and exploiting the spherical symmetry in the macroscale problem. Firstly, as the macroscale lithium concentration, $c_{\mathrm{Si}}^{(0)}$, is bounded by zero and one, the cell problems can be solved for a sample of $c_{\mathrm{Si}}^{(0)} \in [0,1]$. We can then approximate the dependence of $\boldsymbol{u}^{(1)}$ on $c_{\mathrm{Si}}^{(0,0)}$ by interpolating between these solutions. These solutions can then be used to find the $c_{\mathrm{Si}}^{(0)}$-dependence of the effective parameters, $\mathbb{C}_{\phi}$ and Ψ_{ϕ}, also. Thus, when solving the macroscale problem, the effective parameters can be quickly calculated from this interpolation function. This causes a large initial computational cost to create the interpolation function, but keeping the additional cost to solve the macroscale problem lower. Reducing the computational cost this way applies to any anode particle geometry.

For a general anode particle geometry, calculating $\boldsymbol{u}^{(1)}$ for each $\boldsymbol{\nabla}\boldsymbol{u}^{(0)}$ value is particularly computationally expensive because $\boldsymbol{\nabla}\boldsymbol{u}^{(0)}$ has six independent components. However, if the macroscale problem is simplified such that the number of independent components of $\boldsymbol{\nabla}\boldsymbol{u}^{(0)}$ is reduced, solving for each value of $\boldsymbol{\nabla}\boldsymbol{u}^{(0)}$ becomes more computationally achievable. For example, the radial symmetry in the nano-particle geometry allows us to write

$$\boldsymbol{\nabla}\boldsymbol{u}^{(0)} = \mathrm{diag}\left(\frac{\mathrm{d}u^{(0)}}{\mathrm{d}r}, \frac{u^{(0)}}{r}, \frac{u^{(0)}}{r}\right), \tag{3.55}$$

yielding the general solution (2.55), with two integration constants, A_{Si} and B_{Si}. This reduces the number of independent components of $\boldsymbol{\nabla}\boldsymbol{u}^{(0)}$ to two. Furthermore, if the porous silicon is in the centre of the nano-particle, without a central void, $B_{\mathrm{Si}} = 0$ due to the zero displacement condition at $r = 0$, giving $\mathrm{d}u^{(0)}/\mathrm{d}r = u^{(0)}/r = A_{\mathrm{Si}}$. In this case, the number of independent components of $\boldsymbol{\nabla}\boldsymbol{u}^{(0)}$ is reduced to just one. Similar to the interpolation function for solutions at different macroscale concentrations, this can now be achieved fairly cheaply for the nonlinearities in $\boldsymbol{\nabla}\boldsymbol{u}^{(0)}$ as well. Therefore, for simplified macroscale problems such as the spherical nano-particle, the large S^d_{Si} case, or even the full nonlinear multiple-scales problem can be solved with a large reduction in computational cost compared to solving the macroscale equations on the full porous domain. We do not, however, explore the nonlinear multiple-scales formulation any further and instead simplify the multiple-scales problem by considering the porous silicon to be fully lithiated.

3.2.5 Fully Lithiated Case

We now consider the case in which the anode is at its maximum theoretical lithiation state. In this case, $c_a = 1$ in each material, thus we prescribe $c^{(0)}_{\mathrm{Si}} = 1$. The governing equation for $c^{(0)}_{\mathrm{Si}}$, (3.10c), is now dominated by the $\mu^{\mathrm{SF}}_{\mathrm{Si}}$ term because $\mu^{\mathrm{SF}}_{\mathrm{Si}} \to \infty$ at $c^{(0)}_{\mathrm{Si}} = 1$. This removes the the coupling between the stress and the concentration, greatly simplifying our multiple-scales analysis. Additionally, prescribing $c^{(0)}_{\mathrm{Si}} = 1$ removes the lithiation-dependence of the stiffness tensor as we have $\mathbb{C}_{\mathrm{Si}} = \mathbb{C}_{\mathrm{Si}}|_{c_{\mathrm{Si}}=1}$.

The microscale displacement is therefore given by

$$\boldsymbol{u}^{(1)} = \boldsymbol{\mathcal{A}} : \boldsymbol{\nabla}\boldsymbol{u}^{(0)} + \gamma_{\mathrm{Si}}\boldsymbol{\xi} + \bar{\boldsymbol{u}}^{(1)} \tag{3.56}$$

and the cell problems are given by

$$\begin{aligned} \hat{\boldsymbol{\nabla}} \cdot \left(\mathbb{C}_{\mathrm{Si}} : \hat{\boldsymbol{\nabla}}\boldsymbol{\mathcal{A}}\right) &= \mathbf{0} && \text{in } \hat{\Omega}_{\mathrm{Si}}, && (3.57\text{a}) \\ \left(\mathbb{C}_{\mathrm{Si}} : \hat{\boldsymbol{\nabla}}\boldsymbol{\mathcal{A}}\right)\mathbf{n} &= -\mathbb{C}_{\mathrm{Si}} \cdot \mathbf{n} && \text{on } \hat{\Gamma}_e, && (3.57\text{b}) \end{aligned}$$

and

$$\begin{aligned} \hat{\boldsymbol{\nabla}} \cdot \left(\mathbb{C}_{\mathrm{Si}} : \hat{\boldsymbol{\nabla}}\boldsymbol{\xi}\right) &= 0, && \text{in } \hat{\Omega}_{\mathrm{Si}}, && (3.58\text{a}) \\ \left(\mathbb{C}_{\mathrm{Si}} : \hat{\boldsymbol{\nabla}}\boldsymbol{\xi}\right)\mathbf{n} &= \left(\mathbb{C}_{\mathrm{Si}} : \mathbf{1}\right)\mathbf{n}, && \text{on } \hat{\Gamma}_e, && (3.58\text{b}) \end{aligned}$$

along with the periodicity and integral conditions on $\boldsymbol{\mathcal{A}}$ and $\boldsymbol{\xi}$. We assume the silicon is amorphous as in Chapter 2 allowing us to write $\mathbb{C}_{\mathrm{Si}}$ as (2.17). Therefore, we can write the cell problems as

$$\frac{\partial}{\partial \hat{x}_j}\left[\lambda_{\mathrm{Si}}\delta_{ij}\frac{\partial \mathcal{A}_{krs}}{\partial \hat{x}_k}+G_{\mathrm{Si}}\left(\frac{\partial \mathcal{A}_{irs}}{\partial \hat{x}_j}+\frac{\partial \mathcal{A}_{jrs}}{\partial \hat{x}_i}\right)\right]=0_i, \tag{3.59a}$$

$$\left[\lambda_{\mathrm{Si}}\delta_{ij}\frac{\partial \mathcal{A}_{krs}}{\partial \hat{x}_k}+G_{\mathrm{Si}}\left(\frac{\partial \mathcal{A}_{irs}}{\partial \hat{x}_j}+\frac{\partial \mathcal{A}_{jrs}}{\partial \hat{x}_i}\right)\right]\mathrm{n}_j=-\lambda_{\mathrm{Si}}\delta_{rs}\mathrm{n}_i-G_{\mathrm{Si}}(\delta_{ir}\mathrm{n}_s+\delta_{is}\mathrm{n}_r), \tag{3.59b}$$

and

$$\frac{\partial}{\partial \hat{x}_j}\left[\lambda_{\mathrm{Si}}\delta_{ij}\frac{\partial \xi_k}{\partial \hat{x}_k}+G_{\mathrm{Si}}\left(\frac{\partial \xi_i}{\partial \hat{x}_j}+\frac{\partial \xi_j}{\partial \hat{x}_i}\right)\right]=0_i, \tag{3.60a}$$

$$\left[\lambda_{\mathrm{Si}}\delta_{ij}\frac{\partial \xi_k}{\partial \hat{x}_k}+G_{\mathrm{Si}}\left(\frac{\partial \xi_i}{\partial \hat{x}_j}+\frac{\partial \xi_j}{\partial \hat{x}_i}\right)\right]\mathrm{n}_j=(3\lambda_{\mathrm{Si}}+2G_{\mathrm{Si}})\mathrm{n}_i, \tag{3.60b}$$

where λ_{Si} and G_{Si} are the Lamé parameters of silicon, evaluated at $c_{\mathrm{Si}}=1$.

The effective stress in the fully lithiated case is given by $\boldsymbol{\sigma}_\phi=\mathbb{C}_\phi:\boldsymbol{\nabla}\boldsymbol{u}^{(0)}-\gamma_{\mathrm{Si}}\boldsymbol{\Psi}_\phi$, written in suffix notation as

$$\sigma^\phi_{ij}=c^\phi_{ijrs}\frac{\partial u^{(0)}_r}{\partial x_s}-\gamma_{\mathrm{Si}}\Psi_{ij}. \tag{3.61}$$

The stiffness tensor and effective expansion coefficient are given by

$$\mathbb{C}_\phi=\frac{1}{|\hat{\Omega}|}\int_{\hat{\Omega}_{\mathrm{Si}}}\mathbb{C}_{\mathrm{Si}}:\hat{\boldsymbol{\nabla}}\mathcal{A}+\mathbb{C}_{\mathrm{Si}}\ \mathrm{d}V, \tag{3.62a}$$

$$\boldsymbol{\Psi}_\phi=\frac{1}{|\hat{\Omega}|}\int_{\hat{\Omega}_{\mathrm{Si}}}\mathbb{C}_{\mathrm{Si}}:\left\{\mathbf{1}-\hat{\boldsymbol{\nabla}}\boldsymbol{\xi}\right\}\ \mathrm{d}V, \tag{3.62b}$$

respectively. We substitute the isotropic stiffness tensor (2.17) for silicon to find, in suffix notation,

$$\begin{aligned}c^\phi_{ijrs}=\frac{1}{|\hat{\Omega}|}\Bigg[\int_{\hat{\Omega}_{\mathrm{Si}}}&\lambda_{\mathrm{Si}}\delta_{ij}\frac{\partial A_{krs}}{\partial \hat{x}_k}+G_{\mathrm{Si}}\left(\frac{\partial A_{irs}}{\partial \hat{x}_j}+\frac{\partial A_{jrs}}{\partial \hat{x}_i}\right)\\&+\lambda_{\mathrm{Si}}\delta_{ij}\delta_{rs}+G_{\mathrm{Si}}(\delta_{ir}\delta_{js}+\delta_{is}\delta_{jr})\ \mathrm{d}V\Bigg],\end{aligned} \tag{3.63a}$$

$$\Psi^\phi_{ij}=\frac{1}{|\hat{\Omega}|}\left[\int_{\hat{\Omega}_{\mathrm{Si}}}(3\lambda_{\mathrm{Si}}+2G_{\mathrm{Si}})\delta_{ij}-\left(\lambda_{\mathrm{Si}}\delta_{ij}\frac{\partial \xi_k}{\partial \hat{x}_k}+G_{\mathrm{Si}}\left(\frac{\partial \xi_i}{\partial \hat{x}_j}+\frac{\partial \xi_j}{\partial \hat{x}_i}\right)\right)\ \mathrm{d}V\right]. \tag{3.63b}$$

3.2.5.1 Reductions Due to Symmetry

To solve for all components of $\mathbb{C}_\phi$ and $\boldsymbol{\Psi}_\phi$, we would need to solve the cell problem for each subvector of $\mathcal{A}$, $\mathcal{A}_{irs}=(\mathcal{A}_{1rs},\mathcal{A}_{2rs},\mathcal{A}_{3rs})$, and the cell problem for $\boldsymbol{\xi}$, totalling ten 3-dimensional finite element solves of vector functions. Additionally, there are 81 components of $\mathbb{C}_\phi$ and nine components of $\boldsymbol{\Psi}_\phi$ and thus 90 integrals would need to be calculated. We now discuss the symmetries of this problem and how we can reduce the number of finite element solutions we require and how many integrals we need to calculate.

Using similar symmetry arguments to those in [18], we can find which derivatives of the components $\mathcal{A}$ and ξ are even and odd with respect to which microscale coordinates, $\hat{x}_i$. This method uses the boundary conditions (3.57b) and (3.60b), noting that each component of the normal vector n_i is odd in $\hat{x}_i$ and even in $\hat{x}_j$ where $j \neq i$. Those derivatives which are odd will not contribute to the integrals in each component of $\mathbb{C}_\phi$ and $\boldsymbol{\Psi}_\phi$, whereas those which are even will. Following this method, it can be shown that non-zero elements of $\mathbb{C}_\phi = c^\phi_{ijrs}$ only occur if

$$i = j = r = s, \quad i = j \text{ and } r = s, \quad i = r \text{ and } j = s, \text{ or } i = s \text{ and } j = r. \tag{3.64}$$

This does not reduce the number of subvectors of $\mathcal{A}$ that need to be calculated but reduces the number of non-zero components of $\mathbb{C}_\phi$ to 21. Additionally, if $i \neq j$, the only terms in (3.63b) are $\partial\xi_i/\partial\hat{x}_j$ and $\partial\xi_j/\partial\hat{x}_i$ which, from the boundary condition (3.60b), are odd when $i \neq j$. Therefore, the off-diagonal entries of $\boldsymbol{\Psi}_\phi$ are zero, reducing the number of non-zero components of $\boldsymbol{\Psi}_\phi$ to three. There is r, s and i, j symmetry in (3.59b) and (3.63a), reducing the number of unique components of $\mathbb{C}_\phi$ to 12 and reducing the number of subvectors of $\mathcal{A}$ which need to be solved for to six. All these symmetry arguments are independent of the unit cell geometry and occur due to the isotropy of the stiffness tensor.

The unit cell geometry we use here has symmetry in the different components of $\hat{\mathbf{x}}$, such that the solution remains the same for $\hat{x}_i \leftrightarrow \hat{x}_j$ for $i \neq j$. Therefore, we have $c^\phi_{1111} = c^\phi_{2222} = c^\phi_{3333}$ and $c^\phi_{1122} = c^\phi_{1133} = c^\phi_{2211} = c^\phi_{2233} = c^\phi_{3311} = c^\phi_{3322}$ for the components of $\mathbb{C}_\phi$ and $\Psi_{11} = \Psi_{22} = \Psi_{33}$. Lastly, by calculating the non-zero contributions to the integrals, one finds by inspection that $c^\phi_{1111} = c^\phi_{1122} + 2c^\phi_{1212}$.

Due to the symmetries outlined here, the stiffness and expansion of the porous silicon are also isotropic, meaning we can write the components of $\mathbb{C}_\phi$ and $\boldsymbol{\Psi}_\phi$ as

$$c^\phi_{ijkl} = \lambda_\phi \delta_{ij}\delta_{kl} + G_\phi \delta_{ik}\delta_{jl} + G_\phi \delta_{il}\delta_{jk} \quad \text{and} \quad \Psi^\phi_{ij} = \psi_\phi \delta_{ij}, \tag{3.65}$$

where λ_ϕ and G_ϕ are the effective Lamé parameters and ψ_ϕ is the scalar effective expansion parameter. Therefore, we can calculate just 2 integrals of $\mathbb{C}_\phi$ involving λ_ϕ and G_ϕ to calculate these constants: c^ϕ_{1111} ($=\lambda_\phi + 2G_\phi$) and c^ϕ_{2211} ($= \lambda_\phi$), for example, which only require us to solve for the subvector $\mathcal{A}_{i11}$. We also only need to calculate one integral to obtain ψ_ϕ, for example Ψ^ϕ_{11}. Substituting (3.65) into (3.61) yields

$$\sigma^\phi_{ij} = \lambda_\phi \delta_{ij} \frac{\partial u^{(0)}_k}{\partial x_k} + G_\phi \left(\frac{\partial u^{(0)}_i}{\partial x_j} + \frac{\partial u^{(0)}_j}{\partial x_i} \right) - \gamma_{\mathrm{Si}} \psi_\phi \delta_{ij}, \tag{3.66}$$

and comparing this with (2.23), we define $\gamma_\phi = (\gamma_{\mathrm{Si}}\psi_\phi)/(3\lambda_\phi + 2G_\phi)$. This allows us to write $\boldsymbol{\sigma}_\phi$ in the form of the stress used in (2.20)

$$\boldsymbol{\sigma}_\phi = \mathbb{C}_\phi : \left[\boldsymbol{\nabla} \boldsymbol{u}^{(0)} - \gamma_\phi \mathbf{1} \right]. \tag{3.67}$$

In summary, to find the Lamé parameters, λ_ϕ and G_ϕ, and expansion coefficient, γ_ϕ, of the porous silicon, the cell problems that need to be solved numerically are given by (3.59) with $r = s = 1$ and (3.60). Using these solutions we then calculate (3.63a) with $i = j = r = s = 1$, (3.63a) with $i = j = 2$, $r = s = 1$ and (3.63b) with $i = j = 1$. Then, we have $\lambda_\phi = c^\phi_{2211}$, $G_\phi = (c^\phi_{1111} - c^\phi_{2211})/2$ and $\psi_\phi = \Psi^\phi_{11}$.

3.2.5.2 Numerical Solution to Cell Problems

We now briefly outline the details of solving the cell problems (3.57) and (3.58) numerically. The PDE systems for $\mathcal{A}_{i11}$ and $\boldsymbol{\xi}$ are solved using the FEniCS finite element package [1]. This requires writing the cell problems in weak form. Using the isotropic stiffness tensor (2.17), we rewrite (3.57) as

$$\hat{\boldsymbol{\nabla}} \cdot \left[\lambda_{\mathrm{Si}} \big(\hat{\boldsymbol{\nabla}} \cdot \mathcal{A}_{i11} \big) \mathbf{1} + G_{\mathrm{Si}} \Big(\hat{\boldsymbol{\nabla}} \mathcal{A}_{i11} + \big(\hat{\boldsymbol{\nabla}} \mathcal{A}_{i11} \big)^{\mathrm{T}} \Big) \right] = \mathbf{0}, \tag{3.68a}$$

$$\begin{aligned} &\left[\lambda_{\mathrm{Si}} \big(\hat{\boldsymbol{\nabla}} \cdot \mathcal{A}_{i11} \big) \mathbf{1} + G_{\mathrm{Si}} \Big(\hat{\boldsymbol{\nabla}} \mathcal{A}_{i11} + \big(\hat{\boldsymbol{\nabla}} \mathcal{A}_{i11} \big)^{\mathrm{T}} \Big) \right] \mathbf{n} \\ &\qquad = \begin{bmatrix} -\lambda_{\mathrm{Si}} - 2G_{\mathrm{Si}} & 0 & 0 \\ 0 & -\lambda_{\mathrm{Si}} & 0 \\ 0 & 0 & -\lambda_{\mathrm{Si}} \end{bmatrix} \mathbf{n}. \end{aligned} \tag{3.68b}$$

Similarly for $\boldsymbol{\xi}$ we have

$$\hat{\boldsymbol{\nabla}} \cdot \left[\lambda_{\mathrm{Si}} \big(\hat{\boldsymbol{\nabla}} \cdot \boldsymbol{\xi} \big) \mathbf{1} + G_{\mathrm{Si}} \Big(\hat{\boldsymbol{\nabla}} \boldsymbol{\xi} + \big(\hat{\boldsymbol{\nabla}} \boldsymbol{\xi} \big)^{\mathrm{T}} \Big) \right] = \mathbf{0}, \tag{3.69a}$$

$$\left[\lambda_{\mathrm{Si}} \big(\hat{\boldsymbol{\nabla}} \cdot \boldsymbol{\xi} \big) \mathbf{1} + G_{\mathrm{Si}} \Big(\hat{\boldsymbol{\nabla}} \boldsymbol{\xi} + \big(\hat{\boldsymbol{\nabla}} \boldsymbol{\xi} \big)^{\mathrm{T}} \Big) \right] \mathbf{n} = (3\lambda_{\mathrm{Si}} + 2G_{\mathrm{Si}}) \mathbf{n}. \tag{3.69b}$$

By multiplying (3.68a) and (3.69a) by a test function, $\mathbf{w}$, and integrating by parts over the silicon domain in the unit cell, we obtain

$$\begin{aligned}\int_{\hat{\Omega}_{\mathrm{Si}}} \hat{\boldsymbol{\nabla}}\mathbf{w} : \Big[\lambda_{\mathrm{Si}}\big(\hat{\boldsymbol{\nabla}}\cdot\boldsymbol{\mathcal{A}}_{i11}\big)\mathbf{1} + G_{\mathrm{Si}}\Big(\hat{\boldsymbol{\nabla}}\boldsymbol{\mathcal{A}}_{i11} + \big(\hat{\boldsymbol{\nabla}}\boldsymbol{\mathcal{A}}_{i11}\big)^{\mathrm{T}}\Big)\Big]\,\mathrm{d}V \\ = \int_{\hat{\Gamma}_e}\Big[\lambda_{\mathrm{Si}}\big(\hat{\boldsymbol{\nabla}}\cdot\boldsymbol{\mathcal{A}}_{i11}\big)\mathbf{1} + G_{\mathrm{Si}}\Big(\hat{\boldsymbol{\nabla}}\boldsymbol{\mathcal{A}}_{i11} + \big(\hat{\boldsymbol{\nabla}}\boldsymbol{\mathcal{A}}_{i11}\big)^{\mathrm{T}}\Big)\Big]\mathbf{n}\cdot\mathbf{w}\,\mathrm{d}S,\end{aligned} \tag{3.70a}$$

$$\begin{aligned}\int_{\hat{\Omega}_{\mathrm{Si}}} \hat{\boldsymbol{\nabla}}\mathbf{w} : \Big[\lambda_{\mathrm{Si}}\big(\hat{\boldsymbol{\nabla}}\cdot\boldsymbol{\xi}\big)\mathbf{1} + G_{\mathrm{Si}}\Big(\hat{\boldsymbol{\nabla}}\boldsymbol{\xi} + \big(\hat{\boldsymbol{\nabla}}\boldsymbol{\xi}\big)^{\mathrm{T}}\Big)\Big]\,\mathrm{d}V \\ = \int_{\hat{\Gamma}_e}\Big[\lambda_{\mathrm{Si}}\big(\hat{\boldsymbol{\nabla}}\cdot\boldsymbol{\xi}\big)\mathbf{1} + G_{\mathrm{Si}}\Big(\hat{\boldsymbol{\nabla}}\boldsymbol{\xi} + \big(\hat{\boldsymbol{\nabla}}\boldsymbol{\xi}\big)^{\mathrm{T}}\Big)\Big]\mathbf{n}\cdot\mathbf{w}\,\mathrm{d}S.\end{aligned} \tag{3.70b}$$

Substituting the boundary conditions (3.68b) and (3.69b) into (3.70a) and (3.70b), and noting $\hat{\boldsymbol{\nabla}}\mathbf{w} : \mathbf{1} = \hat{\boldsymbol{\nabla}}\cdot\mathbf{w}$, yields the weak forms

$$\begin{aligned}\int_{\hat{\Omega}_{\mathrm{Si}}} \lambda_{\mathrm{Si}}\big(\hat{\boldsymbol{\nabla}}\cdot\boldsymbol{\mathcal{A}}_{i11}\big)\big(\hat{\boldsymbol{\nabla}}\cdot\mathbf{w}\big) + G_{\mathrm{Si}}\hat{\boldsymbol{\nabla}}\mathbf{w} : \Big(\hat{\boldsymbol{\nabla}}\boldsymbol{\mathcal{A}}_{i11} + \big(\hat{\boldsymbol{\nabla}}\boldsymbol{\mathcal{A}}_{i11}\big)^{\mathrm{T}}\Big)\,\mathrm{d}V \\ = \int_{\hat{\Gamma}_e}\begin{bmatrix} -\lambda_{\mathrm{Si}} - 2G_{\mathrm{Si}} & 0 & 0 \\ 0 & -\lambda_{\mathrm{Si}} & 0 \\ 0 & 0 & -\lambda_{\mathrm{Si}}\end{bmatrix}\mathbf{n}\cdot\mathbf{w}\,\mathrm{d}S,\end{aligned} \tag{3.71a}$$

$$\begin{aligned}\int_{\hat{\Omega}_{\mathrm{Si}}} \lambda_{\mathrm{Si}}\big(\hat{\boldsymbol{\nabla}}\cdot\boldsymbol{\xi}\big)\big(\hat{\boldsymbol{\nabla}}\cdot\mathbf{w}\big) + G_{\mathrm{Si}}\hat{\boldsymbol{\nabla}}\mathbf{w} : \Big(\hat{\boldsymbol{\nabla}}\boldsymbol{\xi} + \big(\hat{\boldsymbol{\nabla}}\boldsymbol{\xi}\big)^{\mathrm{T}}\Big)\,\mathrm{d}V \\ = (3\lambda_{\mathrm{Si}} + 2G_{\mathrm{Si}})\int_{\hat{\Gamma}_e}\mathbf{n}\cdot\mathbf{w}\,\mathrm{d}S.\end{aligned} \tag{3.71b}$$

The domain of the unit cell is given by $-0.5 \leq \hat{x}_i \leq 0.5$ for $i = 1, 2, 3$. The mesh of the silicon domain inside the unit cell is constructed using gmsh [43] for a given volume fraction of silicon. The solutions for $\boldsymbol{\mathcal{A}}_{i11}$ and $\boldsymbol{\xi}$ are not unique for the same reasons as discussed in (3.24a) so we choose to make the solution unique by requiring that the integral of $\boldsymbol{\mathcal{A}}_{i11}$ is zero. The periodic boundary conditions on $\hat{\Gamma}_{\mathrm{Si}}$ are enforced by having nodes at corresponding positions on opposite sides of the mesh and enforcing that the solution on the $\hat{x}_i = 0.5$ side is equal to that at the corresponding position on the $\hat{x}_i = -0.5$ side. The finite element solver uses the Flexible Generalized Minimal Residual (FGMRES) method [93] along with an algebraic multigrid preconditioner developed by hypre [33].

3.2.6 Varying Porosity

We now wish to see how the scalar effective parameters λ_ϕ, G_ϕ and ψ_ϕ depend on the porosity of the porous silicon at full lithiation. We define the volume fraction of silicon as $\phi = |\hat{\Omega}_{\mathrm{Si}}|/|\hat{\Omega}|$ where $|\hat{\Omega}_{\mathrm{Si}}|$ is the volume of silicon in the unit cell. The porosity is then defined as $1-\phi$. We vary the volume fraction by varying the width of the pillars that make up the silicon in the unit cell, denoted by $\hat{l}$, and calculate the volume fraction ϕ for a given $\hat{l}$ by

$$\phi = \frac{(4\hat{L}+8\big(\hat{L}-\hat{l})\big)\big(\frac{\hat{l}}{2}\big)^2}{(\hat{L})^3} = \frac{(3\hat{L}-2\hat{l})\hat{l}^2}{\hat{L}^3}. \tag{3.72}$$

We calculate the effective parameters for a range of ϕ values and plot the mechanical parameters, λ_ϕ and G_ϕ, and the expansion parameter ψ_ϕ against the volume fraction ϕ in Figures 3.5 and 3.6, respectively. It can be seen in Figure 3.6 that the value of ψ_ϕ for each ϕ value is equal to $3\lambda_\phi + 2G_\phi$. This is because the anode material in the unit cell is a single anode material with a uniform lithium concentration. Therefore, we expect the porous silicon to expand the same amount as the non-porous material if unstressed, giving $\gamma_\phi = \gamma_{\mathrm{Si}}$ and thus $\psi_\phi = 3\lambda_\phi + 2G_\phi$. Therefore, as our effective stress is given by (3.66), we only need to calculate λ_ϕ and G_ϕ.

Instead of solving the cell problem for $\mathcal{A}_{i11}$ every time we use the porous silicon in the macroscale problem, we wish to be able to calculate λ_ϕ and G_ϕ quickly. Therefore, we find the effective parameters for a discrete set of ϕ values, shown by the points in Figures 3.5 and 3.6 and fit a polynomial function to these points, shown by the solid lines in Figures 3.5 and 3.6. The polynomials for λ_ϕ and G_ϕ calculated from the least-squares minimisation of the data points are

$$\lambda_\phi = 1.3215\phi^5 - 1.8471\phi^4 + 1.2315\phi^3 - 0.1562\phi^2 + 0.0429\phi - 0.0009, \tag{3.73a}$$

$$G_\phi = 0.0784\phi^5 - 0.0673\phi^4 + 0.1021\phi^3 + 0.1083\phi^2 + 0.2058\phi - 0.0003. \tag{3.73b}$$

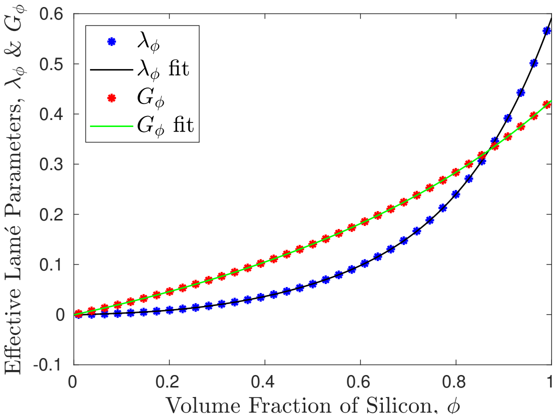

Figure 3.5: Effective Lamé parameters λ_ϕ and G_ϕ for fully lithiated porous silicon against the volume fraction of silicon in the unit cell ϕ, alongside the polynomial fits for each parameter.

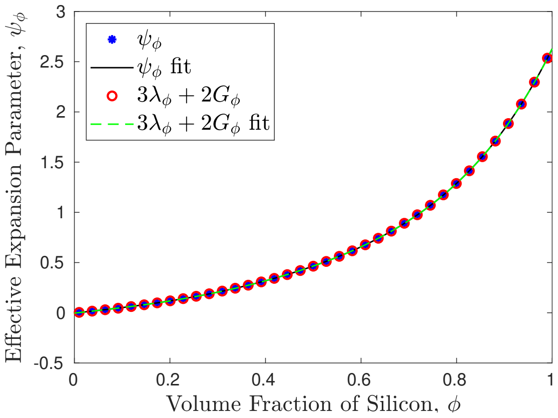

Figure 3.6: Effective expansion parameter ψ_ϕ for fully lithiated porous silicon against the volume fraction of silicon in the unit cell ϕ alongside the polynomial fit. The quantity $3\lambda_\phi + 2G_\phi$ is also plotted.

We use (3.73) to calculate the effective material parameters of the porous silicon in the following macroscale problems.

3.3 Numerical Experiments

In this section we apply the linear elasticity model presented in Chapter 2 to nano-particle designs which incorporate the porous silicon introduced in the last section. The first design is identical to the core–shell geometry in Figure 2.1 with the non-porous silicon core replaced by a porous one. The second design incorporates a porous silicon layer between the non-porous silicon core and the graphite shell. We investigate how the porosity of the silicon and the geometry of these designs affect the expanded volume at full lithiation and the maximum capacity.

3.3.1 Porous Silicon Core

For the case in which we replace the silicon core with a porous silicon core, we label the outer radius of the porous silicon core as R_ϕ^*, nondimensionalised by $R_\phi = R_\phi^*/R_\mathrm{C}^*$. The radially-symmetric solution for this geometry is identical to that given in Section 2.4 with λ_Si, G_Si, γ_Si and R_Si replaced with λ_ϕ, G_ϕ, 1 and R_ϕ, respectively. Additionally, as we are considering the fully lithiated case, we have $c_\mathrm{Si} = c_\mathrm{C} = 1$. The relative expanded volume of the nano-particle at full lithiation, V_1, is calculated using (2.83). The maximum capacity for this case is given by

$$Q_1 = \phi R_\phi^3 + \frac{c_\mathrm{C}^\mathrm{max}}{c_\mathrm{Si}^\mathrm{max}}(1 - R_\phi^3), \tag{3.74}$$

where we have taken the porosity ϕ into account as only the silicon within each unit cell of the porous silicon can accommodate lithium.

Similar to the central void geometry, we compare the nano-particle designs which have the same capacity and investigate whether the use of porous silicon reduces the expansion. We calculate the fully lithiated expanded volume, V_1, and the maximum capacity, Q_1, for different volume fractions of silicon in the porous silicon core and for different sizes of core, R_ϕ^3. In Figure 3.7, we plot V_1 against Q_1 for different values of ϕ. The maximum capacities of nano-particles with very porous silicon cores is much lower than that of the non-porous silicon case, but with a comparable expanded volumes, shown by the maximum values for each value of ϕ. Therefore, a large porous silicon core has a much higher expansion than a nano-particle with a medium-sized non-porous core with the same capacity. However, for nano-particles with lower capacities around $Q_1 = 0.15$-0.35, nano-particles with a porous silicon core have a smaller expanded volume than a nano-particle with a non-porous silicon core with the same capacity. This is seen more clearly in Figure 3.8 where it can clearly be seen that in this range of Q_1, the nano-particles with $\phi < 1$ have a lower expanded volume. These results can also be used to approximate the porosity of silicon core which maximises the capacity, Q_1, for a given fully lithiated expanded volume, V_1. For example, for $V_1 = 1.3$, a nano-particle with a core of volume fraction $\phi \approx 0.6$ will have the greatest capacity of around $Q_1 \approx 0.225$, as seen in Figure 3.8.

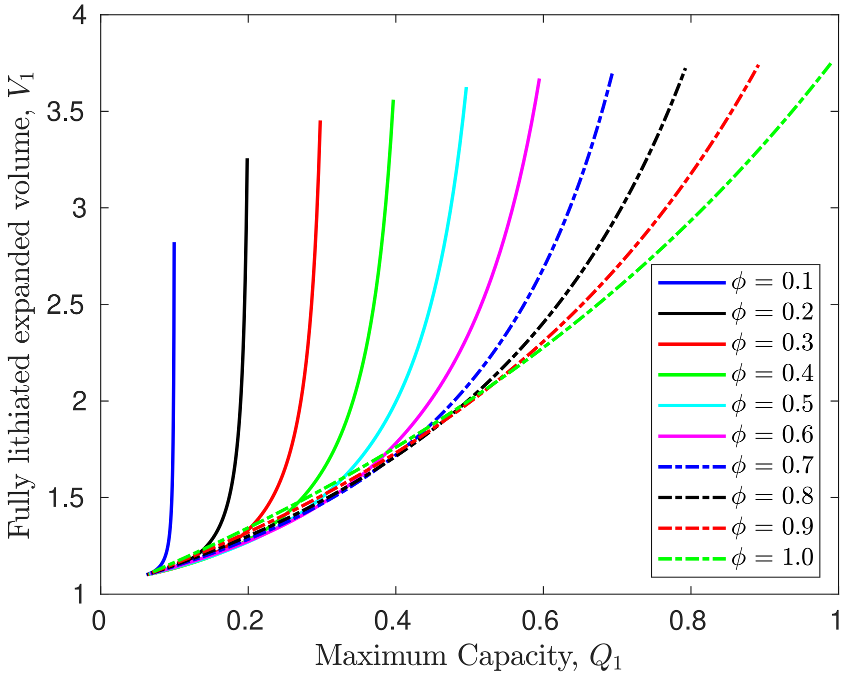

Figure 3.7: Expanded volume at full lithiation, V_1, against the maximum capacity, Q_1, for different volume fractions of silicon in the porous core, ϕ.

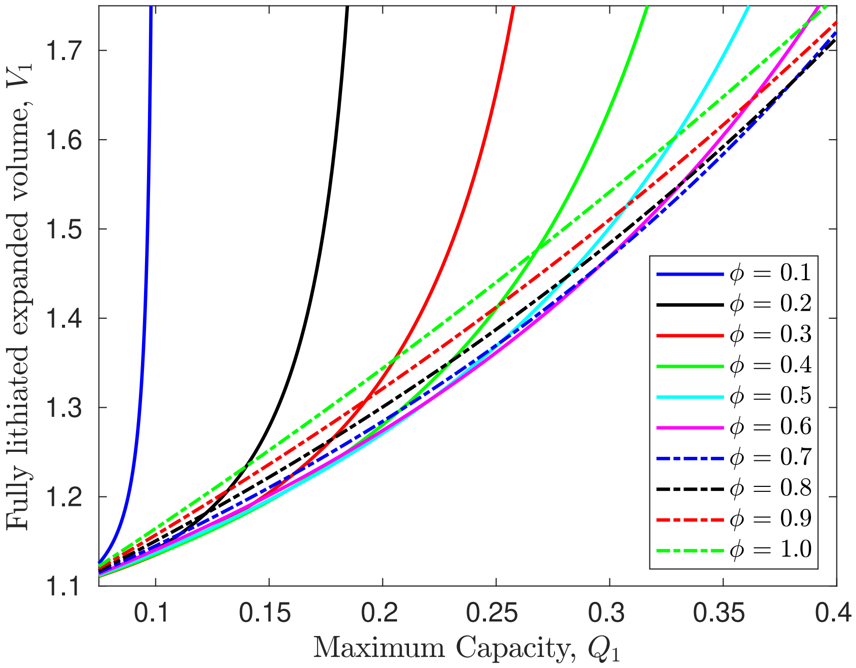

Figure 3.8: Figure 3.7 focussed on $Q_1 \in [0.075, 0.4]$ and $V_1 \in [1.1, 1.75]$.

3.3.2 Porous Silicon Layer

We now analyse a nano-particle comprising a non-porous silicon core, surrounded by a porous silicon layer, surrounded by a graphite shell, as shown in Figure 3.9. This design is of particular interest as it tends to the yolk–shell nano-particle design as $\phi \to 0$. As this geometry still has radial symmetry, the displacement and radial stress in the porous silicon layer are given by (2.55) and (2.56a), respectively. We label the integration constants in the porous silicon layer as A_ϕ and B_ϕ, i.e. $a = \phi$. Prescribing continuity of displacement and radial stress between the porous silicon layer and the adjacent materials, the boundary conditions for this geometry are given by

$$B_{\mathrm{Si}} = 0, \tag{3.75a}$$

$$A_{\mathrm{Si}} R_{\mathrm{Si}} = A_\phi R_{\mathrm{Si}} + \frac{B_\phi}{R_{\mathrm{Si}}^2}, \tag{3.75b}$$

$$(3\lambda_{\mathrm{Si}} + 2G_{\mathrm{Si}})(A_{\mathrm{Si}} - \gamma_{\mathrm{Si}} c_{\mathrm{Si}}) = (3\lambda_\phi + 2G_\phi)(A_\phi - \gamma_\phi c_\phi) - \frac{4G_\phi B_\phi}{R_{\mathrm{Si}}^3}, \tag{3.75c}$$

$$A_\phi R_\phi + \frac{B_\phi}{R_\phi^2} = A_{\mathrm{C}} R_\phi + \frac{B_{\mathrm{C}}}{R_\phi^2}, \tag{3.75d}$$

$$(3\lambda_\phi + 2G_\phi)(A_\phi - \gamma_\phi c_\phi) - \frac{4G_\phi B_\phi}{R_\phi^3} = (3\lambda_{\mathrm{C}} + 2G_{\mathrm{C}})(A_{\mathrm{C}} - \gamma_{\mathrm{C}} c_{\mathrm{C}}) - \frac{4G_{\mathrm{C}} B_{\mathrm{C}}}{R_\phi^3}, \tag{3.75e}$$

$$(3\lambda_{\mathrm{C}} + 2G_{\mathrm{C}})(A_{\mathrm{C}} - \gamma_{\mathrm{C}} c_{\mathrm{C}}) = 4G_{\mathrm{C}} B_{\mathrm{C}}, \tag{3.75f}$$

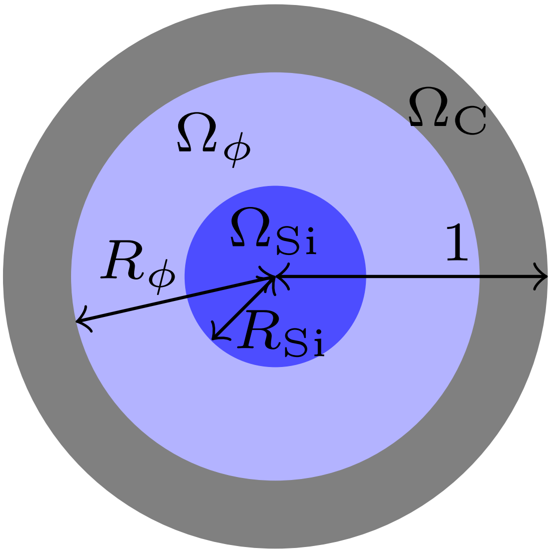

Figure 3.9: Schematic of a slice through the spherical nano-particle design with a spherical core of non-porous silicon (Ω_{Si}), a porous silicon layer (Ω_ϕ) and a graphite shell (Ω_{C}). The outer radii of each region are labelled as R_{Si}, R_ϕ and 1, respectively.

where $R_\phi = R^*_\phi / R^*_{\mathrm{C}}$ is the outer radius of the porous silicon layer, nondimensionalised by the outer radius of the graphite shell.

To find whether this design of nano-particle improves on the previous designs we have analysed, we again calculate V_1 and Q_1 for different initial volumes of each region and for different volume fractions of silicon in the porous silicon layer, ϕ. We calculate the expanded volume of the nano-particle at maximum lithiation using the linearised equation (2.83). The introduction of a porous silicon layer means that the maximum capacity, Q_1, is now given by

$$Q_1 = R^3_{\mathrm{Si}} + \phi(R^3_\phi - R^3_{\mathrm{Si}}) + \frac{c^{\max}_{\mathrm{C}}}{c^{\max}_{\mathrm{Si}}}(1 - R^3_\phi). \tag{3.76}$$

In Figure 3.10, we plot the fully lithiated expansion, V_1, against maximum capacity, Q_1, for several different geometries of the nano-particle with a porous silicon layer. In each subfigure, we keep the ratio between the outer radii of the non-porous silicon core, R_{Si}, and the porous silicon layer, R_ϕ fixed. We vary R^3_ϕ from 0.01 to 0.99 in each subfigure, which also increases $R^3_{\mathrm{Si}} = V_{\mathrm{Si}}$ and the maximum capacity, Q_1. The different plots within each subfigure are for different volume fractions of the porous silicon, ϕ, within the porous silicon layer. The case of $\phi = 1.0$ is therefore the same in each subfigure because the porous and non-porous silicon are indistinct thus the non-porous silicon core has initial volume R^3_ϕ. As in the porous core design, the maximum capacities decrease for a more porous silicon in the porous layer, but the maximum expansions remain similar.

We can see that for low capacity designs, the nano-particles containing a porous layer have a lower expanded volume in all four subfigures. For those designs with $\phi < 1.0$, at some capacity the expanded volume begins to increase rapidly with Q_1. These designs become worse than for the solely non-porous core design at some capacity due to this rapid increase in expansion. This rapid increase occurs at lower capacities for silicon layers with a lower value of ϕ. The Q_1 value at which the designs with a porous silicon layer have a larger expansion than the non-porous core design increases as the ratio between R_{Si} and R_ϕ increases. For example, for $R^3_{\mathrm{Si}} = 0.75R^3_\phi$, a porous silicon layer with $\phi = 0.1$ can cause a reduction in the expanded volume up to $Q_1 \approx 0.7$, whereas for $R^3_{\mathrm{Si}} = 0.1R^3_\phi$, the designs with porous layers only achieve a lower expansion for $Q_1 < 0.55$. The size of the reduction also increases as the $R_{\mathrm{Si}} : R_\phi$ ratio increases. This implies the inclusion of a very porous and thin silicon layer can greatly reduce the expansion of the nano-particle without sacrificing too much lithium capacity, and this effect increases with porosity and size of non-porous core.

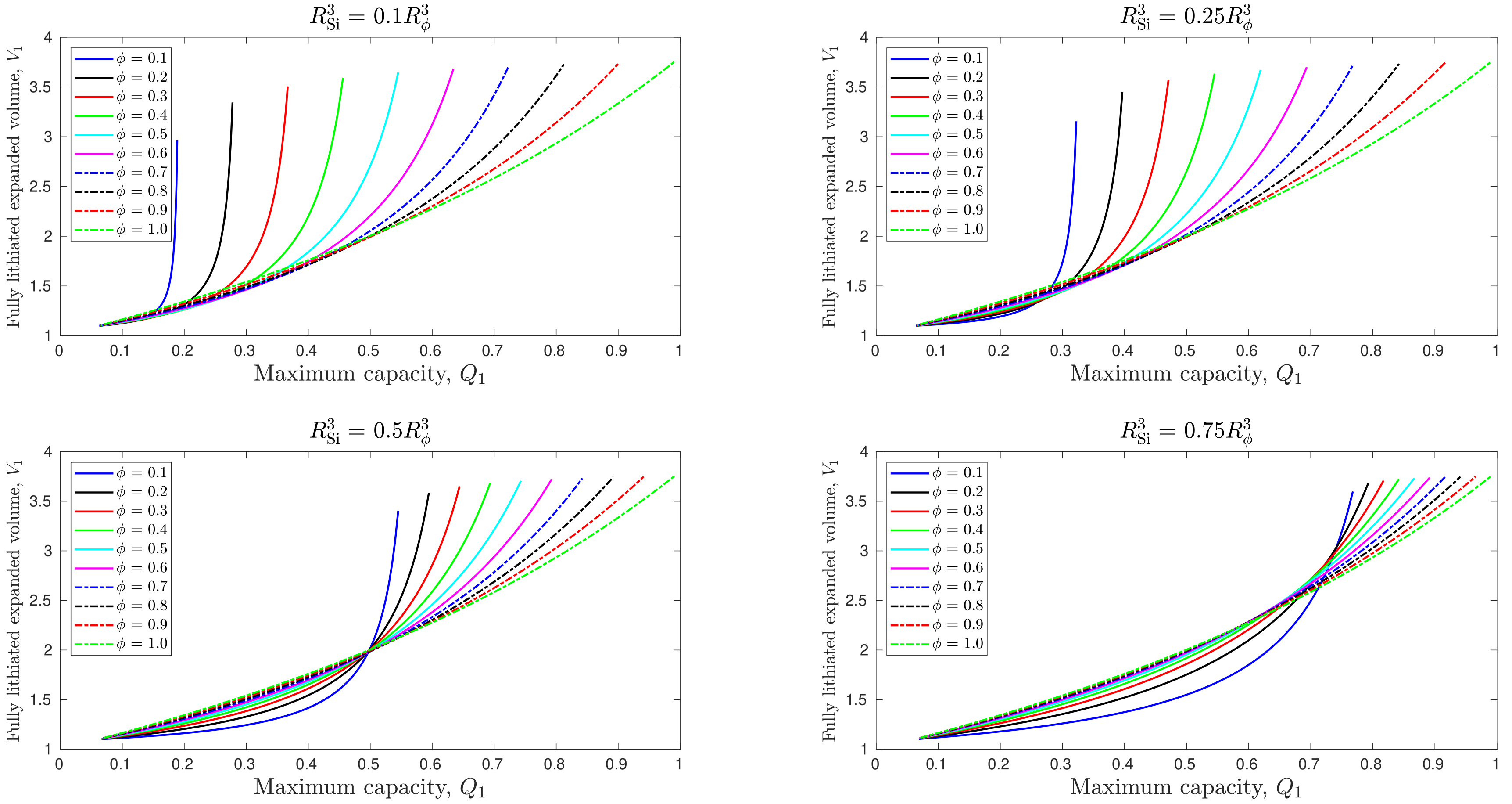

Figure 3.10: Fully lithiated expanded volume, V_1, against maximum capacity, Q_1 for the nano-particle design shown in Figure 3.9. In each subfigure, the ratio of R_{Si} to R_ϕ is fixed. The maximum capacity in each subfigure is varied by increasing the initial outer radius of the porous silicon layer and thus the initial volume of the silicon core. This is done for a range of volume fractions of silicon in the porous silicon layer, ϕ, in each subfigure.

If we analyse the displacement within one of the nano-particle designs for which there is a large reduction in V_1 in detail, we can see that there is a problem. In Figure 3.11, we plot $u + r$ against r for $R_\phi^3 = 0.5$, $R_{\text{Si}}^3 = 0.375 = 0.75R_\phi^3$ and $\phi = 0.1$. We plot $u+r$ against r because each point starting at r in the unstressed configuration has a final position $u + r$ after being displaced. It can be seen that the derivative of $u + r$ is negative in the porous silicon layer. This implies that points in the anode with different initial unstressed positions have the same final position, thus this model predicts overlap of the materials within the nano-particle after expanding, which is clearly unphysical. This is the origin of the greatly reduced expanded volume in these cases. The overlap is a consequence of using linear elasticity in which the Eulerian and Lagrangian coordinate systems are assumed to be the same.

This behaviour does not occur in all the cases in which a porous layer decreases the expansion of the nano-particle, however. In Figure 3.12, we plot $u + r$ against r for $R_\phi^3 = 0.01$, $R_{\text{Si}}^3 = 0.001$ and $\phi = 0.7$. In this case, the capacity of the nano-particle is 0.0687, given by substituting R_{Si} and R_ϕ into (3.76). We can find the geometry of the nano-particle without a porous layer that has the same maximum capacity by

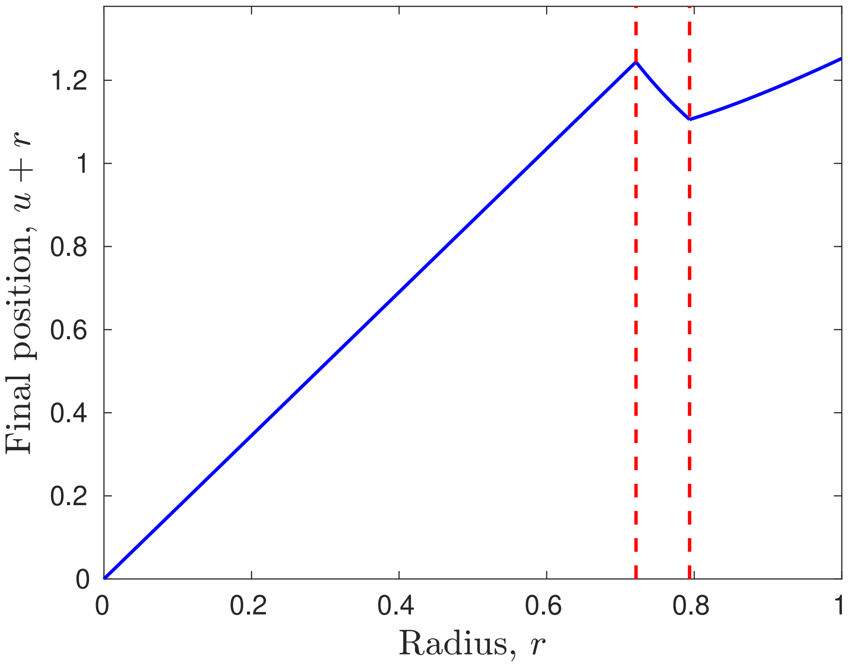

Figure 3.11: Final position after displacement, $u + r$, against initial position, r. The different regions are separated with dashed red lines with $R_{\text{Si}}^3 = 0.375$, $R_\phi^3 = 0.5$ and $\phi = 0.1$.

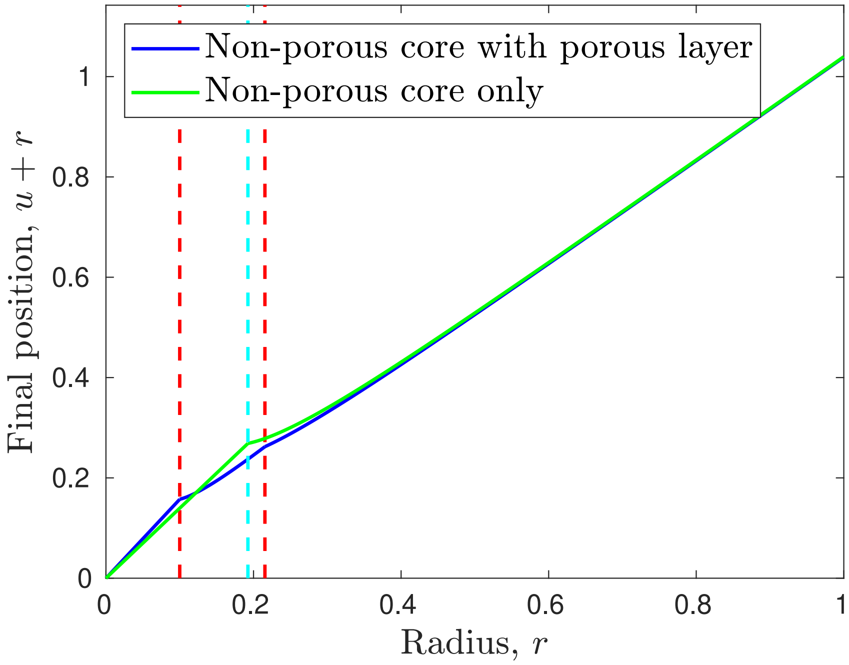

Figure 3.12: Final position after displacement, $u + r$, against initial position, r for a nano-particle with a porous silicon layer and for one without with the same capacity. The former design has a core of initial volume $V_{\text{Si}} = R_{\text{Si}}^3 = 0.001$, and a porous layer with outer radius such that $R_\phi^3 = 0.01$, shown by red dashed lines at $r = \sqrt[3]{0.001}$ and $r = \sqrt[3]{0.01}$. The non-porous core has initial volume $R_{\text{Si}}^3 = R_{\text{N-P}}^3 = 0.1924$, calculated from (3.79), shown by the cyan dashed line at $r = \sqrt[3]{0.1924}$.

equating (3.76) and

$$Q_1 = R_{\text{N-P}}^3 + \frac{c_{\text{C}}^{\max}}{c_{\text{Si}}^{\max}}(1 - R_{\text{N-P}}^3), \tag{3.77}$$

giving

$$R_{\text{N-P}}^3 + \frac{c_{\text{C}}^{\max}}{c_{\text{Si}}^{\max}}(1 - R_{\text{N-P}}^3) = R_{\text{Si}}^3 + \phi(R_\phi^3 - R_{\text{Si}}^3) + \frac{c_{\text{C}}^{\max}}{c_{\text{Si}}^{\max}}(1 - R_\phi^3), \tag{3.78}$$

where $R_{\text{N-P}}$ is the outer radius of the non-porous silicon core in the nano-particle without a porous layer. We can solve (3.78) to find

$$R_{\text{N-P}} = \left[\frac{c_{\text{Si}}^{\max}\left(R_{\text{Si}}^3 + \phi(R_\phi^3 - R_{\text{Si}}^3)\right) - c_{\text{C}}^{\max} R_\phi^3}{c_{\text{Si}}^{\max} - c_{\text{C}}^{\max}}\right]^{\frac{1}{3}}, \tag{3.79}$$

yielding $R_{\text{N-P}}$ for the parameters listed above. We also plot $u+r$ for the nano-particle with the non-porous core of initial volume $R_{\text{Si}} = R_{\text{N-P}}$ in Figure 3.12. We can see that there is no overlap of materials in either $u + r$ profile but the expanded volume of the nano-particle with $R_{\text{Si}} = R_{\text{N-P}}$ is 1.1190 whereas for that with the porous layer, $V_1 = 1.1155$. Both nano-particles have the same capacity. Therefore, there are still some geometries for which this linear model suggests that including a porous layer is beneficial for anode nano-particle design in this case, without predicting unphysical overlap of materials. However, as the linear elasticity assumption is only valid for $|u/r| \ll 1$ and $|\mathrm{d}u/\mathrm{d}r| \ll 1$, this must be considered when assessing the validity of these results as well. For example, the displacement gradient in Ω_{Si} for the nano-particle with a porous silicon layer in Figure 3.12 is $\mathrm{d}u/\mathrm{d}r \approx 0.5$.

3.4 Conclusions

In this chapter, we have focussed on two aspects of including voids into nano-particles. We analysed the multiple-scales formulation of the chemo-mechanical model presented in Chapter 2 and compared the expansions of nano-particle designs utilising central voids and porous silicon.

Applying the method of multiple scales to the linear model from Chapter 2 yielded a nonlinear relationship between the microscale displacement and the macroscale displacement. This is due to the stress and lithium concentration being coupled through stress-assisted diffusion. We considered the limits of large and small stress-assisted diffusion based on the parameter, S^d_{Si}. For the small S^d_{Si} limit, we found that if the lithiation-dependent stiffness is used, the resulting cell problems are nonlinear in both the macroscale concentration and the macroscale displacement gradient, $\boldsymbol{\nabla}\boldsymbol{u}^{(0)}$. Removing the lithiation-dependence of the stiffness in the small S^d_{Si} limit removes the nonlinearity and the resulting leading order cell problems and the first-order corrections only need to be solved once for a given unit cell geometry. However, this is not true for the large S^d_{Si} case and this is nonlinear in both the macroscale lithium concentration and the macroscale displacement gradient with or without lithiation-dependence in the stiffness tensor. We have briefly demonstrated how simple macroscale problems could be exploited to simplify the mechanical modelling of the porous silicon using the method of multiple scales in this case.

We have analysed the effectiveness of including void spaces and porosity into the nano-particle by comparing structures of equal capacity and calculating the expanded volume at full lithiation. This measure was used here as the initial volume of silicon, V_{Si}, is no longer the only independent variable in the nano-particle geometries in this chapter. Additionally, restricting the lithiation of anodes is difficult in practice and so analysing nano-particle designs at full lithiation is of particular interest. However, as we have seen in Chapter 2, the linearised model breaks down at large silicon cores and high lithiation states.

We have found that all three structures studied in this chapter can achieve lower expansion than their analogous designs with a non-porous silicon core. These mainly occur for low-capacity designs but these capacities are still greater than solely graphite nano-particles. One consideration that should be taken into account when incorporating porosity that is not discussed here is the power reduction that would occur. This is due to the diffusion through the anode material being slowed because the lithium must travel around the pores when moving towards the anode–electrolyte interface, increasing the diffusion time, decreasing the power. We do not consider this in our model as we have analysed the equilibrium case but it is an important consideration in practice. Extensions to this work would be to investigate the cases in which the nano-particles are not fully lithiated. This would require more computational cost for the designs containing porous silicon, but would be simple for the central void design. The model used in this chapter will be quantitatively more accurate for anode materials with lower expansions than silicon, but the conclusions drawn from the numerical experiments may differ for such materials.

Finally, we have seen that the linear model predicts overlap of materials for the nano-particles with a very porous silicon layer between the non-porous core and the graphite shell. This is a consequence of the linear elasticity assumption that the Eulerian and Lagrangian coordinate systems are indistinguishable. Even in cases where this overlap is not observed, the displacement gradient is large enough due to the expansion of silicon that the linear elasticity assumption may not be valid. Motivated by these results, in the next chapter we derive a geometrically nonlinear mechanical model for a spherical anode particle. This model keeps the Eulerian and Lagrangian coordinate systems distinct throughout and hopefully will produce physically viable results for the porous silicon layer geometry.

Chapter 4

Nonlinear Elastic Model

In this chapter, we present a geometrically nonlinear mechanical model of the lithiation of a spherical nano-particle, consisting of a silicon core and a graphite shell, as shown in Figure 2.1. The motivation for considering this nonlinear model is the prediction from the linear model of the overlap of materials when applied to a nano-particle with a non-porous silicon core and a porous silicon layer, seen in Figure 3.11. This geometrically nonlinear model differentiates between the Lagrangian (reference) and Eulerian (current) coordinate systems, meaning the overlap should be avoided. Moreover, the nonlinear model does not make the assumption that the value $\eta_a V_a^m c_a^{\max}$ is small for $a = 1, \ldots, n$. Therefore, the model in this chapter should provide more physically accurate displacement results than the linear model in Chapter 2 for silicon at high states of charge.

We derive the geometrically nonlinear model following the same approach as Cui *et al.* [25] but make some simplifications in order to make the analysis of the model easier. These include neglecting plastic flow and stress-assisted diffusion, and considering quasi-static lithium diffusion. We derive a nonlinear ODE for the displacement u in terms of the radius r describing mechanical equilibrium. We solve the boundary value problem for u numerically for the core–shell geometry in Chapter 2 and show that solutions appear to cease to exist above a certain state of charge (SOC). We analyse the nonlinear ODE further, searching for a bifurcation at the critical SOC at which the solution suddenly changes, but find that solutions cease to exist altogether. We linearise the nonlinear ODE about this bifurcation point to confirm this finding. Suspecting that solutions do not exist due to the high compression in the graphite at the surface between the silicon core and graphite shell, we adapt Cui's model [25] by using compressive nonlinear constitutive laws to describe the silicon and graphite. We are able to solve the model using these constitutive laws for all states of charge. Finally, we apply this geometrically and constitutively nonlinear model to the porous silicon layer example in Section 3.3.2 and this permits solutions without overlap of materials.

Thus we find the geometrically nonlinear model removes the overlap of materials seen when extremely weak materials are used with silicon, but only when using nonlinear constitutive laws. We conclude the chapter by showing that in fact plasticity or other yielding mechanisms will take effect before the strains become large enough for the nonlinearities to become significant.

4.1 Geometrically Nonlinear Elastic Model

We begin this chapter by deriving the geometrically nonlinear elasticity model from [25], highlighting the differences we make here.

4.1.1 General Geometry

We derive the governing equations for this model for a general multi-material anode geometry, given formally in Section 2.1.1. As we are now using geometrically nonlinear elasticity, we differentiate between the coordinate frame of the stress-free configuration, $\boldsymbol{X}^*$, and the coordinate frame of the current, deformed configuration, $\boldsymbol{x}^*$. We define the displacement gradient, $\mathbf{F}$, as in (2.2), and also have the displacement gradient in terms of the current configuration

$$\mathbf{f} := \frac{\partial \boldsymbol{X}^*}{\partial \boldsymbol{x}^*} = \mathbf{1} - \frac{\partial \boldsymbol{u}^*}{\partial \boldsymbol{x}^*}. \tag{4.1}$$

We therefore have $\mathbf{f} = \mathbf{F}^{-1}$ and as the strains are no longer assumed small, the approximation (2.14) is no longer accurate. As in [25], we multiplicatively decompose the deformation gradient, $\mathbf{F}$, into $\mathbf{F} = \mathbf{F}^e\mathbf{F}^{\mathrm{SF}}$, neglecting plastic displacement, where $\mathbf{F}^e$ and $\mathbf{F}^{\mathrm{SF}}$ are both defined in Section 2.1.2. We use the same form of $\mathbf{F}^{\mathrm{SF}}$ as in (2.3) and therefore, we have the same elastic strain given by

$$\mathbf{E}^e = \frac{1}{2}\left[(J_a^c)^{-2/3}\left\{\mathbf{1} + \left(\frac{\partial \boldsymbol{u}^*}{\partial \boldsymbol{X}^*}\right)^{\mathrm{T}} + \frac{\partial \boldsymbol{u}^*}{\partial \boldsymbol{X}^*} + \left(\frac{\partial \boldsymbol{u}^*}{\partial \boldsymbol{X}^*}\right)^{\mathrm{T}} \frac{\partial \boldsymbol{u}^*}{\partial \boldsymbol{X}^*}\right\} - \mathbf{1}\right] \quad \text{in } \Omega_a. \tag{4.2}$$

As we differentiate between $\boldsymbol{X}^*$ and $\boldsymbol{x}^*$, we now must define different stress measures depending on the coordinate frame being used. The Cauchy stress tensor, $\boldsymbol{\sigma}^*$, used in the previous chapter is the force per area in the current configuration. The first Piola-Kirchhoff (P-K) stress, $\boldsymbol{\sigma}^{0*}$, is defined as the force in the current configuration per area in the reference frame. Finally, the second P-K stress, $\tilde{\boldsymbol{\sigma}}^*$, is defined as the force that would have acted on an area in the reference configuration given a force in the current frame, per area in the current frame. These are related to the Cauchy stress by

$$\boldsymbol{\sigma}^{0*} = J\boldsymbol{\sigma}^{*}\mathbf{f}^{\mathrm{T}}, \quad \tilde{\boldsymbol{\sigma}}^{*} = J\mathbf{f}\boldsymbol{\sigma}^{*}\mathbf{f}^{\mathrm{T}}, \tag{4.3}$$

where $J = \det(\mathbf{F})$ is the Jacobian of the deformation gradient, $\mathbf{F}$.

We relate the stress and the elastic strain by describing the anode materials as hyperelastic, thus we write the 1st P-K stress as

$$\sigma^{0*}_{ij} = \frac{\partial \mathcal{W}}{\partial F_{ij}} \qquad \text{in } \Omega, \tag{4.4}$$

where $\mathcal{W}$ is the elastic strain energy per unit volume in the reference configuration. Using the chain rule and the decomposition of the displacement gradient $\mathbf{F} = \mathbf{F}^{e}\mathbf{F}^{\mathrm{SF}}$, we write

$$F^{\mathrm{SF}}_{ik}\sigma^{0*}_{kj} = \frac{\partial \mathcal{W}}{\partial F^{e}_{ij}} \qquad \text{in } \Omega. \tag{4.5}$$

In our analysis we will take the materials to have the special properties of being isotropic and constitutively linear. Thus the elastic strain energy density is given by

$$\mathcal{W} = \frac{J^{c}_{a}}{2}\frac{E^{*}_{a}}{(1+\nu_a)}\left(\frac{\nu_a}{1-2\nu_a}(E^{e}_{kk})^2 + E^{e}_{jk}E^{e}_{kj}\right) \qquad \text{in } \Omega_a, \tag{4.6}$$

where ν_a is the Poisson ratio of the anode material a, $J^{c}_{a} = \det(\mathbf{F}^{\mathrm{SF}})$ is the Jacobian of the stress-free deformation gradient in material a defined in (2.4), $\mathbf{E}^{e} = E^{e}_{ij}$ is the elastic strain defined in (4.2) and E^{*}_{a} is the dimensional lithiation-dependent Young's modulus as a function of c_a, the relative lithium concentration in material a. We use the same linear lithiation-dependence of the Young's modulus of each anode material as in Chapter 2 and write the Young's modulus as $E^{*}_{a}(c_a) = E^{0*}_{a}(1 + \eta^{E}_{a}x^{\max}_{a}c_a)$. Here, E^{0*}_{a} is the dimensional Young's modulus of the unlithiated material, η^{E}_{a} is the variation of the Young's modulus with respect to the lithium concentration and $x^{\max}_{a}$ is the maximum stoichiometric ratio of material a to lithium at the fully lithiated state (3.8 for silicon and 1/6 for graphite). As in Chapter 2, we assume the Poisson's ratio is independent of lithiation.

We model the anode material to be in mechanical equilibrium. This can be expressed in terms of both the 1st P-K stress and the Cauchy stress by

$$\frac{\partial \sigma^{0*}_{ij}}{\partial X^{*}_{i}} = 0 \qquad \text{in } \Omega, \qquad \text{and} \qquad \frac{\partial \sigma^{*}_{ij}}{\partial x^{*}_{i}} = 0 \qquad \text{in } \bar{\Omega}, \tag{4.7}$$

respectively, where $\bar{\Omega}$ is the current domain of the anode particle.

4.1.2 Radially-Symmetric Case

The geometrically nonlinear model derived in the previous section is now applied to the radially-symmetric spherical geometry in Figure 2.1. The displacement and concentration can be written as (2.43) and the displacement gradient $\mathbf{F}$ is written as

$$\mathbf{F} = \mathrm{diag}[1 + \mathrm{d}u^*/\mathrm{d}r^*, 1 + u^*/r^*, 1 + u^*/r^*], \tag{4.8}$$

where r^* is the dimensional radial variable in the reference frame. From the multiplicative decomposition, we can write

$$\begin{aligned}\mathbf{F}^e &= \mathrm{diag}[F^e_{rr}, F^e_{\theta\theta}, F^e_{\phi\phi}]\\ &= (J^c_a)^{-1/3}\mathrm{diag}[1 + \mathrm{d}u^*/\mathrm{d}r^*, 1 + u^*/r^*, 1 + u^*/r^*] \quad \text{in } \Omega_a.\end{aligned} \tag{4.9}$$

and from (2.6), we have

$$E^e_{rr} = \frac{1}{2}\left[(J^c_a)^{-2/3}\left(1 + \frac{\mathrm{d}u^*}{\mathrm{d}r^*}\right)^2 - 1\right] \qquad \text{in } \Omega_a, \tag{4.10a}$$

$$E^e_{\theta\theta} = E^e_{\phi\phi} = \frac{1}{2}\left[(J^c_a)^{-2/3}\left(1 + \frac{u^*}{r^*}\right)^2 - 1\right] \qquad \text{in } \Omega_a. \tag{4.10b}$$

We substitute these elastic strains into the elastic strain energy density (4.6), giving

$$\begin{aligned}\mathcal{W}(\mathbf{F}, c) = \frac{J^c_a}{2}\frac{E^*_a}{(1+\nu_a)(1-2\nu_a)}\Big((1-\nu_a)\big[(E^e_{rr})^2 + (E^e_{\theta\theta})^2 + (E^e_{\phi\phi})^2\big]\\ + 2\nu_a\big[E^e_{rr}E^e_{\theta\theta} + E^e_{rr}E^e_{\phi\phi} + E^e_{\theta\theta}E^e_{\phi\phi}\big]\Big) \quad \text{in } \Omega_a.\end{aligned} \tag{4.11}$$

Note that we retain the distinction between $E^e_{\theta\theta}$ and $E^e_{\phi\phi}$ to make the derivation of the P-K stresses clear. We calculate the three non-zero elements of the 1st P-K stress σ^{0*}_{rr}, $\sigma^{0*}_{\theta\theta}$ and $\sigma^{0*}_{\phi\phi}$ using (4.5), giving

$$\begin{aligned}\sigma^{0*}_{rr} &= \frac{1}{(J^c_a)^{1/3}}\frac{\partial\mathcal{W}}{\partial E^e_{rr}}\frac{\partial E^e_{rr}}{\partial F^e_{rr}}\\ &= \frac{(J^c_a)^{2/3}E^*_a}{2(1+\nu_a)(1-2\nu_a)}\left[2(1-\nu_a)E^e_{rr} + 2\nu_a(E^e_{\theta\theta} + E^e_{\phi\phi})\right]F^e_{rr}\\ &= \frac{J^c_a E^*_a}{(1+\nu_a)(1-2\nu_a)}\left[(1-\nu_a)E^e_{rr} + 2\nu_a E^e_{\theta\theta}\right]\frac{2E^e_{rr}+1}{1+\mathrm{d}u^*/\mathrm{d}r^*} \qquad \text{in } \Omega_a,\end{aligned} \tag{4.12}$$

where we have applied $E^e_{\theta\theta} = E^e_{\phi\phi}$ in the final equality. Similarly,

$$\sigma^{0*}_{\theta\theta} = \sigma^{0*}_{\phi\phi} = \frac{J^c_a E^*_a}{(1+\nu_a)(1-2\nu_a)}\left[E^e_{\theta\theta} + \nu_a E^e_{rr}\right]\frac{2E^e_{\theta\theta}+1}{1+u^*/r^*} \qquad \text{in } \Omega_a. \tag{4.13}$$

We can then derive the non-zero elements of the Cauchy stress σ^*_{rr}, $\sigma^*_{\theta\theta}$ and $\sigma^*_{\phi\phi}$ using (4.3), giving

$$\begin{aligned}\sigma^*_{rr} &= \frac{1}{J}F_{rr}\sigma^{0*}_{rr}\\ &= \frac{1}{(1+u^*/r^*)^2}\frac{J^c_aE^*_a}{(1+\nu_a)(1-2\nu_a)}\left[(1-\nu_a)E^e_{rr}+2\nu_aE^e_{\theta\theta}\right]\frac{2E^e_{rr}+1}{1+\mathrm{d}u^*/\mathrm{d}r^*}\\ &= \frac{J^c_aE^*_a}{(1+\nu_a)(1-2\nu_a)}\left[(1-\nu_a)E^e_{rr}+2\nu_aE^e_{\theta\theta}\right]\frac{(J^c_a)^{-2/3}(1+\mathrm{d}u^*/\mathrm{d}r^*)^2}{(1+\mathrm{d}u^*/\mathrm{d}r^*)(1+u^*/r^*)^2}\\ &= \frac{E^*_a}{(1+\nu_a)(1-2\nu_a)}\left[(1-\nu_a)E^e_{rr}+2\nu_aE^e_{\theta\theta}\right]\frac{\sqrt{2E^e_{rr}+1}}{2E^e_{\theta\theta}+1}\qquad \text{in } \Omega_a, \end{aligned}\tag{4.14}$$

and

$$\sigma^*_{\theta\theta}=\sigma^*_{\phi\phi}=\frac{E^*_a}{(1+\nu_a)(1-2\nu_a)}\left[\nu_aE^e_{rr}+E^e_{\theta\theta}\right]\frac{1}{\sqrt{1+2E^e_{rr}}}\qquad \text{in } \Omega_a.\tag{4.15}$$

The equilibrium condition in terms of the 1st P-K stress, (4.7), is written in spherical coordinates as

$$\frac{\mathrm{d}\sigma^{0*}_{rr}}{\mathrm{d}r^*}+2\frac{\sigma^{0*}_{rr}-\sigma^{0*}_{\theta\theta}}{r^*}=0\qquad \text{in } \Omega.\tag{4.16}$$

Hence (4.10), (4.12) and (4.13) allow us to write (4.16) in terms of u^* and r^*, giving

$$\begin{aligned} r^{*2}&\left[\frac{3}{2}(1-\nu_a)r^{*2}\left(1+\frac{\mathrm{d}u^*}{\mathrm{d}r^*}\right)^2+\nu_a(r^*+u^*)^2-\frac{\nu_a+1}{2}(J^c_a)^{2/3}r^{*2}\right]\frac{\mathrm{d}^2u^*}{\mathrm{d}r^{*2}}\\ &= (r^*+u^*)^3-(1-\nu_a)r^{*3}\left(1+\frac{\mathrm{d}u^*}{\mathrm{d}r^*}\right)^3-\nu_ar^{*2}(r^*+u^*)\left(1+\frac{\mathrm{d}u^*}{\mathrm{d}r^*}\right)^2\\ &\qquad +(\nu_a+1)(J^c_a)^{2/3}r^{*2}\left(r^*\frac{\mathrm{d}u^*}{\mathrm{d}r^*}-u^*\right)\qquad \text{in } \Omega_a. \end{aligned}\tag{4.17}$$

This is the ODE that we solve to find the deformation in each material, a, inside the nano-particle. Lastly, it is useful to write the radial Cauchy stress σ^*_{rr}, given in (4.14), in terms of u^* and r^* as

$$\begin{aligned}\sigma^*_{rr}=\frac{(J^c_a)^{-1/3}E^*_a}{(1+\nu_a)(1-2\nu_a)}&\left\{\frac{(1-\nu_a)}{2}\left(1+\frac{\mathrm{d}u^*}{\mathrm{d}r^*}\right)^2+\nu_a\left(1+\frac{u^*}{r^*}\right)^2\right.\\ &\left.-\frac{1+\nu_a}{2}(J^c_a)^{2/3}\right\}\frac{1+\mathrm{d}u^*/\mathrm{d}r^*}{(1+u^*/r^*)^2}\qquad \text{in } \Omega_a.\end{aligned}\tag{4.18}$$

To complete the mechanical model, we need to prescribe boundary conditions. Here, we assume i) zero displacement at the centre of the nano-particle, ii) continuity of displacement between materials, iii) continuity of radial stress between materials, and iv) zero traction at the outer radius of the nano-particle.

To determine the lithium concentration at each radial point, Cui *et al.* [25] use a time-dependent diffusion model and couple the lithium flux to the mechanical model through stress-assisted diffusion using the Eshelby tensor [31]. We simplify the model by again taking the quasi-static case, resulting in the chemical potential being uniform across the nano-particle as derived in Section 2.2. We also neglect stress-assisted diffusion in this nonlinear model to keep the mechanical model uncoupled from the lithium transport model. The lithium concentrations are found by solving

$$\mu_a^{\mathrm{SF},*}(c_a) = \mu^*, \qquad \text{in } \Omega_a, \tag{4.19}$$

implying c_a is uniform in each material a. After c_a are determined for a given SOC, c_0, using the SOC condition (2.59), we calculate J_a^c and E_a^* for each material. These are then substituted into (4.17) and the corresponding boundary conditions to obtain a boundary value problem for the displacement which must then be solved numerically.

We now apply this radially-symmetric model to the nano-particle with a silicon core of radius R_{Si}^* and a graphite shell of outer radius R_{C}^*. As we no longer use the assumption that $\eta_a V_a^m c_a^{\max} \ll 1$, we do not need to scale the displacement and stresses using this quantity. Instead, we nondimensionalise the displacement and radius using the outer radius of the nano-particle, R_{C}^*, giving $r^* = R_{\mathrm{C}}^* r$, $u^* = R_{\mathrm{C}}^* u$ as in Section 2.4. The nondimensional radius of the silicon core is given by $R_{\mathrm{Si}} = R_{\mathrm{Si}}^*/R_{\mathrm{C}}^*$ and the nano-particle has a nondimensional outer radius of one, as in Figure 2.1. We nondimensionalise the Young's moduli of each material, the 1st P-K stress and the Cauchy stress using the dimensional shear modulus of silicon as in Chapter 2, giving $E_a^* = G_{\mathrm{Si}}^*(0) E_a$, $\boldsymbol{\sigma}^{0*} = G_{\mathrm{Si}}^*(0)\boldsymbol{\sigma}^0$ and $\boldsymbol{\sigma}^* = G_{\mathrm{Si}}^*(0)\boldsymbol{\sigma}$, respectively. Substituting these expressions into the ODE (4.17) and the Cauchy stress (4.18) means we simply remove the asterisks from these variables. We nondimensionalise the stress free chemical potentials of the silicon and graphite according to (2.38). The concentrations, c_{Si} and c_{C}, are therefore determined by $\mu_{\mathrm{Si}}^{\mathrm{SF}}(c_{\mathrm{Si}}) = \mu_{\mathrm{C}}^{\mathrm{SF}}(c_{\mathrm{C}})$, along with the SOC condition

(2.68). The full boundary value problem to be solved is given by

$$
\begin{aligned}
r^2\left[\frac{3}{2}(1-\nu_a)r^2\left(1+\frac{\mathrm{d}u}{\mathrm{d}r}\right)^2+\nu_a(r+u)^2-\frac{\nu_a+1}{2}(J_a^c)^{2/3}r^2\right]\frac{\mathrm{d}^2u}{\mathrm{d}r^2}& \\
=(r+u)^3-(1-\nu_a)r^3\left(1+\frac{\mathrm{d}u}{\mathrm{d}r}\right)^3-\nu_a r^2(r+u)\left(1+\frac{\mathrm{d}u}{\mathrm{d}r}\right)^2& \qquad (4.20a)\\
+(\nu_a+1)(J_a^c)^{2/3}r^2\left(r\frac{\mathrm{d}u}{\mathrm{d}r}-u\right) \quad \text{in } \Omega_a,&
\end{aligned}
$$

$$u=0 \qquad \text{at } r=0, \tag{4.20b}$$

$$[u]_-^+=0 \qquad \text{at } r=R_{\mathrm{Si}}, \tag{4.20c}$$

$$[\sigma_{rr}]_-^+=0 \qquad \text{at } r=R_{\mathrm{Si}}, \tag{4.20d}$$

$$\sigma_{rr}=0 \qquad \text{at } r=1, \tag{4.20e}$$

where

$$
\begin{aligned}
\sigma_{rr}=\frac{(J_a^c)^{-1/3}E_a}{(1+\nu_a)(1-2\nu_a)}\Bigg\{\frac{(1-\nu_a)}{2}\left(1+\frac{\mathrm{d}u}{\mathrm{d}r}\right)^2+\nu_a\left(1+\frac{u}{r}\right)^2& \\
-\frac{1+\nu_a}{2}(J_a^c)^{2/3}\Bigg\}\frac{1+\mathrm{d}u/\mathrm{d}r}{(1+u/r)^2} \quad \text{in } \Omega_a,&
\end{aligned}
\tag{4.21}
$$

and E_a and J_a^c are functions of the lithium concentration in material a, c_a, but are independent of r because the lithium concentration is uniform in each material.

4.2 Numerical Solution

In this section, we describe the numerical method used to solve the system (4.20) and present the displacements and radial stresses that are obtained for low states of charge.

4.2.1 Double Shooting Method

We first describe the numerical method we use to solve (4.20). We use a multi-point shooting method [74] by integrating the ODE (4.20a) for $a = \mathrm{Si}$ forwards from $r = 0$ to $r = R_{\mathrm{Si}}$ and backwards from $r = 1$ to $r = R_{\mathrm{Si}}$ for $a = \mathrm{C}$. We use guesses for the displacement gradient, u', at $r = 0$ and $r = 1$, and calculate $u(0)$ and $u(1)$ from these guesses. The $u'(0)$ and $u'(1)$ values are then explored to find solutions which satisfy the continuity conditions at R_{Si}: (4.20c) and (4.20d).

As the ODE (4.20a) is singular at $r = 0$, we solve the ODE in Ω_{Si} on the interval $[\epsilon, R_{\mathrm{Si}}]$ with $0 < \epsilon \ll 1$ to avoid numerical complications at this singularity. We use a Taylor series to replace (4.20b) by the approximation

$$u(\epsilon) - \epsilon \left.\frac{\mathrm{d}u}{\mathrm{d}r}\right|_{r=\epsilon} = 0, \tag{4.22}$$

and use this as the condition for $u'(\epsilon)$, which we write as $u(\epsilon) = \epsilon u'(\epsilon)$. To accurately derive the boundary condition at $r = 0$, we should look at the asymptotic behaviour of (4.20a) as $r \to 0$. However, we use this approximation for simplicity, and will assume that the profile in Ω_{Si} is linear in Section 4.3, making (4.22) exact.

To find the displacement in the graphite region, we rearrange the zero traction conditions at $r = 1$ given by substituting $r = 1$ and $\sigma_{rr} = 0$ into (4.21). This obtains the three roots

$$u(1) = \pm\sqrt{\frac{1+\nu_{\mathrm{C}}}{2\nu_{\mathrm{C}}}(J_{\mathrm{C}}^{\mathrm{c}})^{2/3} - \frac{1-\nu_{\mathrm{C}}}{2\nu_{\mathrm{C}}}\big(1+u'(1)\big)^2} - 1, \tag{4.23a}$$

$$u'(1) = -1. \tag{4.23b}$$

The negative square root solution causes the displacement at $r = 1$ to be negative and we must have $u' > -1$ to avoid a singularity in the 1st P–K stress (4.12). We therefore disregard the negative square root and $u'(1) = -1$ solutions as these are both unphysical. We therefore have

$$u(1) = \sqrt{\frac{1+\nu_{\mathrm{C}}}{2\nu_{\mathrm{C}}}(J_{\mathrm{C}}^{\mathrm{c}})^{2/3} - \frac{1-\nu_{\mathrm{C}}}{2\nu_{\mathrm{C}}}\big(1+u'(1)\big)^2} - 1, \tag{4.24}$$

as the condition for $u(1)$ in terms of $u'(1)$.

Starting from an initial guesses for $u'(\epsilon)$, we now numerically integrate the ODE (4.20a) from $r = \epsilon$ to $r = R_{\mathrm{Si}}$, using (4.22) to find $u(\epsilon)$. Similarly, we start from an initial guess for $u'(1)$ and numerically integrate (4.20a) from $r = 1$ to $r = R_{\mathrm{Si}}$ using (4.24) to find $u(1)$. We then vary $u'(\epsilon)$ and $u'(1)$ to find the pair $(u'(\epsilon), u'(1))$ which minimises the objective function

$$f_{\mathrm{obj}}(u'(\epsilon), u'(1)) = \sqrt{\left(\frac{[u(R_{\mathrm{Si}})]_-^+}{u(R_{\mathrm{Si}}^-)}\right)^2 + \left(\frac{[\sigma_{rr}(R_{\mathrm{Si}})]_-^+}{\sigma_{rr}(R_{\mathrm{Si}}^-)}\right)^2}. \tag{4.25}$$

The initial guess for $(u'(\epsilon), u'(1))$ must be sufficiently close to the solution to converge quickly. We initially solve for a low SOC, c_0, with an initial guess of $u'(\epsilon) = u'(1) = 0$, as we know that, for $c_0 = 0$, $u = u' = 0$ $\forall r \in [\epsilon, 1]$. We then solve for increasing c_0 values, using the solution for the previous c_0 value as the initial guess for the subsequent value.

4.2.2 Results

We use the parameter values given in Table 2.1 to produce the following results. In Figure 4.1, we plot the numerical solutions to the BVP (4.20) for $R_{\text{Si}} = 0.5$ and $c_0 \in [0.025, 0.15]$. We can see that the displacement and radial stress profiles for this model are qualitatively the same as for the linear case in Figures 2.8 and 2.9. We can also see that $u''(r)$, at the right-hand side of the interface, $r = R_{\text{Si}}$, is very large for $c_0 = 0.15$. The numerical solver does not find a solution for $c_0 = 0.175$ or greater, including for much smaller intervals between c_0 values so that the initial guesses at each c_0 are closer to the solution.

Due to the large second derivative of u at R_{Si}, we investigate the radial stress continuity condition at the interface to investigate why the solver is unable to solve for large c_0 values. Given a radial stress and displacement in the silicon at R_{Si}, $\sigma_{rr}(R_{\text{Si}}^-)$ and $u(R_{\text{Si}}^-)$, respectively, the continuity condition is given by

$$\begin{aligned}\sigma_{rr}(R_{\text{Si}}^-) =& \frac{(J_{\text{C}}^c)^{-1/3} E_{\text{C}}(c_{\text{C}})}{(1+\nu_{\text{C}})(1-2\nu_{\text{C}})} \Bigg\{ \frac{(1-\nu_{\text{C}})}{2} \left(1 + u'(R_{\text{Si}}^+)\right)^2 \\ & + \nu_{\text{C}} \left(1 + \frac{u(R_{\text{Si}}^-)}{R_{\text{Si}}} \right)^2 - \frac{1+\nu_{\text{C}}}{2} (J_{\text{C}}^c)^{2/3} \Bigg\} \frac{1 + u'(R_{\text{Si}}^+)}{(1 + u(R_{\text{Si}}^-)/R_{\text{Si}})^2},\end{aligned} \tag{4.26}$$

where $u(R_{\text{Si}}^+)$ and $u'(R_{\text{Si}}^+)$ are the displacement and displacement gradient in the graphite at $r = R_{\text{Si}}$, respectively, and we have used $u(R_{\text{Si}}^+) = u(R_{\text{Si}}^-)$. Equation (4.26) shows that $\sigma_{rr}(R_{\text{Si}}^-)$ is a cubic function of $u'(R_{\text{Si}}^+)$ which we plot against $u'(R_{\text{Si}}^+)$ for $c_0 = 0.025, \ldots, 0.15$ in Figure 4.2. We also plot $\sigma_{rr}(R_{\text{Si}}^-)$ using dotted lines in Figure 4.2, calculated by solving the BVP (4.20) for these c_0 values. The values of $u'(R_{\text{Si}}^+)$ that satisfy the continuity of stress condition are the points where the dotted lines cross the cubic function. The solutions shown in Figure 4.1 have a $u'(R_{\text{Si}}^+)$ value corresponding to the least negative solution to the continuity equation, represented by the circles in Figure 4.2.

It can be seen that for $c_0 = 0.15$, the two right-most roots of (4.26) have almost converged to a single root. If c_0 is increased further, it is reasonable to expect these solutions to cease to exist, leaving only one real root of (4.26) which is much greater in magnitude. We expect a bifurcation of the solution at $c_0 = 0.15$ such that $u'(R_{\text{Si}}^+)$ decreases by a large amount. This would appear to explain why the numerical solver is unable to solve the BVP for $c_0 > 0.15$, as the initial guess from the solution for $c_0 = 0.15$ will be significantly different to the solution for $c_0 = 0.175$.

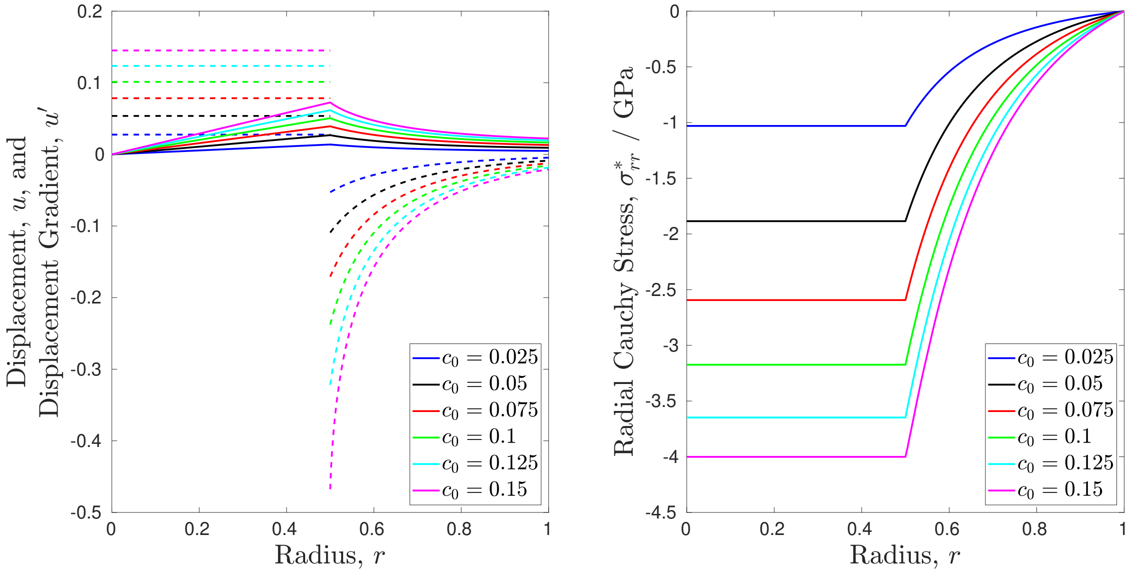

Figure 4.1: Left: Displacement, u (solid lines), and displacement gradient, $u'(r)$ (dashed lines), against radius, r. Right: Radial stress, σ^*_{rr}, against radius, r. Results obtained using the double shooting method described in Section 4.2.1 with $R_{\mathrm{Si}} = 0.5$.

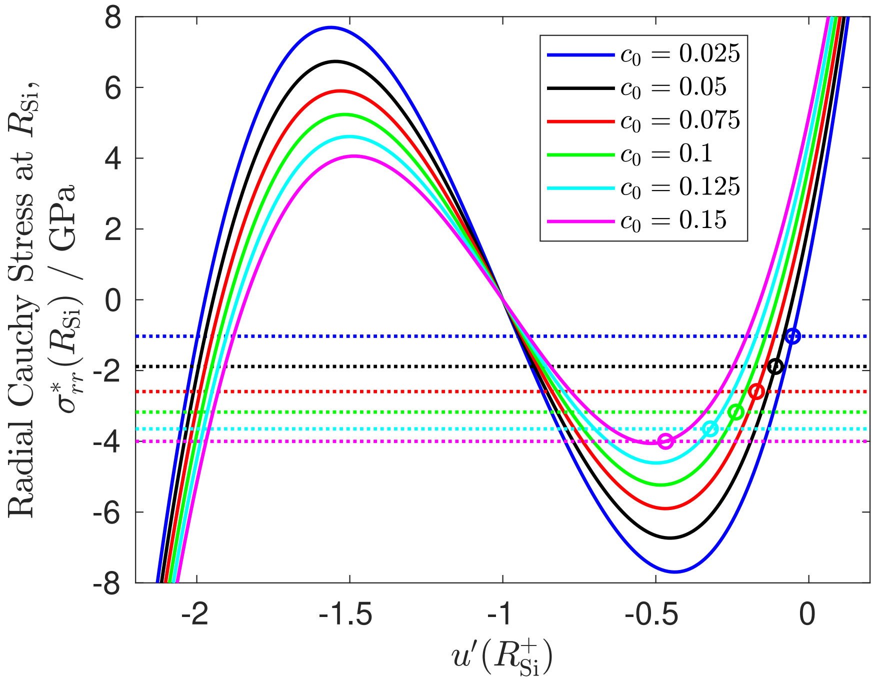

Figure 4.2: Solid lines: Radial Cauchy stress at R_{Si} for graphite, $\sigma^*_{rr}(R^+_{\mathrm{Si}})$, as a function of $u'(R^+_{\mathrm{Si}})$ using (4.26). Dotted lines: Radial Cauchy stress at R_{Si} for silicon, $\sigma^*_{rr}(R^-_{\mathrm{Si}})$, from the numerical solution shown in Figure 4.1. The roots of the cubic that produce the σ^*_{rr} profiles in Ω_{C} in Figure 4.1 are circled.

4.3 Bifurcation of Solution

In the previous section we found that the numerical scheme to solve the BVP system (4.20) fails for $c_0 > 0.15$ due to a suspected bifurcation caused by the continuity of stress condition (4.26). In this section, we analyse this bifurcation by assuming that the displacement in Ω_{Si} is linear and numerically integrating the ODE (4.20a) from $r = R_{\mathrm{Si}}$ to $r = 1$, using each of the three roots of (4.26) as the value for $u'(R_{\mathrm{Si}}^+)$. We then check if any of these solutions satisfy the boundary condition (4.20e) for σ_{rr} at $r = 1$. Throughout this section, we only consider the geometry $R_{\mathrm{Si}} = 0.5$.

We define $u = \alpha r$ for $\epsilon < r < R_{\mathrm{Si}}$ and some constant α, as yet to be determined. Using the boundary condition (4.20c), $u(R_{\mathrm{Si}}^-) = u(R_{\mathrm{Si}}^+) = \alpha R_{\mathrm{Si}}$, and we also have $u'(R_{\mathrm{Si}}^-) = \alpha$. We label $u'(R_{\mathrm{Si}}^+) = \beta$, for some constant β, as yet to be determined and substitute α and β into the stress continuity condition (4.26), giving

$$\begin{aligned}
&\frac{(J_{\mathrm{Si}}^c)^{-1/3}E_{\mathrm{Si}}(c_{\mathrm{Si}})}{(1+\nu_{\mathrm{Si}})(1-2\nu_{\mathrm{Si}})}\left\{\frac{(1+\nu_{\mathrm{Si}})}{2}(1+\alpha)^2 - \frac{1+\nu_{\mathrm{Si}}}{2}(J_{\mathrm{Si}}^c)^{2/3}\right\}\frac{1}{1+\alpha} \\
&\qquad = \frac{(J_{\mathrm{C}}^c)^{-1/3}E_{\mathrm{C}}(c_{\mathrm{C}})}{(1+\nu_{\mathrm{C}})(1-2\nu_{\mathrm{C}})}\left\{\frac{(1-\nu_{\mathrm{C}})}{2}(1+\beta)^2 + \nu_{\mathrm{C}}(1+\alpha)^2\right. \\
&\qquad\qquad\qquad\qquad \left. - \frac{1+\nu_{\mathrm{C}}}{2}(J_{\mathrm{C}}^c)^{2/3}\right\}\frac{1+\beta}{(1+\alpha)^2}.
\end{aligned} \tag{4.27}$$

At a given SOC, c_0, a given R_{Si}, and a given gradient of the linear displacement in Ω_{Si}, α, there are one, two or three real solutions for β, which we label as β_1, β_2 and β_3, and which can be calculated analytically. In Figure 4.3 we plot the bifurcation diagram for the solutions, β, of (4.27) against α for two particular values of c_0: $c_0 = 0.1$ and $c_0 = 0.2$. We note here that for large values of c_0 (for $R_{\mathrm{Si}} = 0.5$), there is only one root of (4.27) for all α, and so this diagram qualitatively changes based on the parameters in the problem.

For each of these solutions, β_1, β_2, and β_3, we numerically integrate (4.20a) from $r = R_{\mathrm{Si}}$ to $r = 1$ using $u(R_{\mathrm{Si}}) = \alpha R_{\mathrm{Si}}$ and $u'(R_{\mathrm{Si}}) = \beta_i$, for $i = 1, 2, 3$. From the resulting solutions, we calculate $\sigma_{rr}(1)$ for each set of α and β_i values and plot $\sigma_{rr}(1)$ against α, for $c_0 = 0.1$ and $c_0 = 0.2$, in Figure 4.4. The points where the plots in Figure 4.4 cross $\sigma_{rr}(1) = 0$ correspond to α values which produce solutions to the BVP (4.20). In the lower row of plots, we focus on the region around $\sigma_{rr}(1) = 0$ and can see that for $c_0 = 0.1$, there is exactly one root at around $\alpha = 0.1$, denoted by the star. We expect that as c_0 is increased, the value of α which satisfies $\sigma_{rr}(1) = 0$ to vary continuously. However, we see that for $c_0 = 0.2$, there are no values of α which

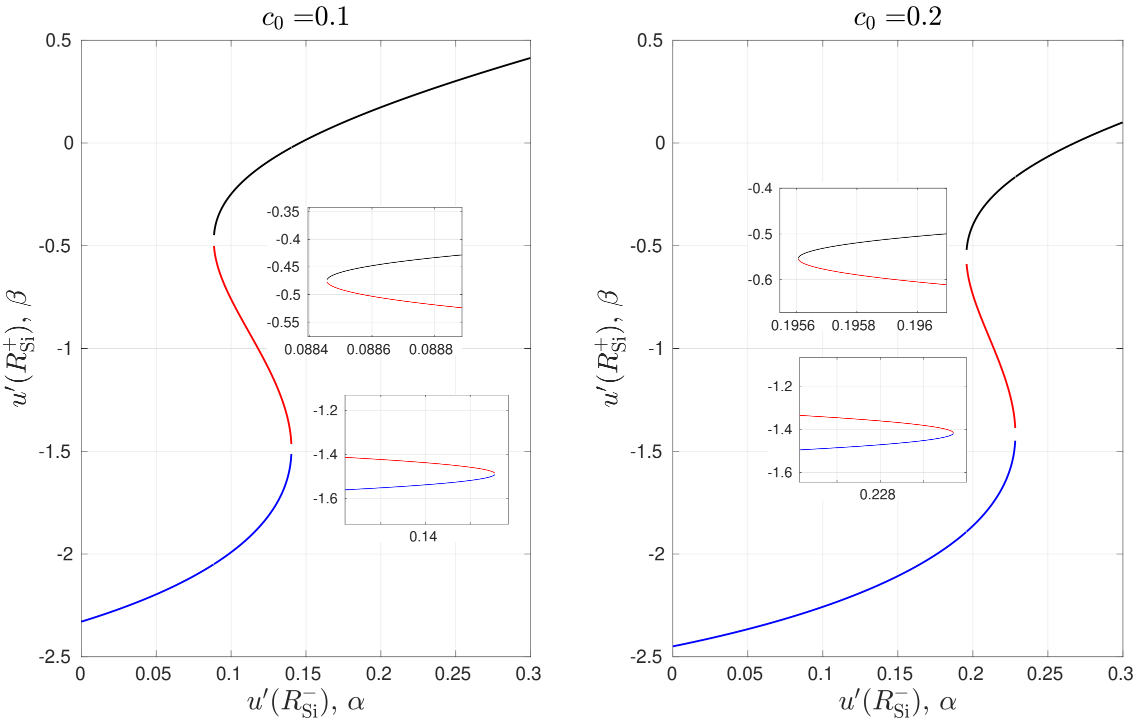

Figure 4.3: Bifurcation diagram of the roots, β, of (4.27) against the u' in Ω_{Si}, α, for $c_0 = 0.1$ (left) and $c_0 = 0.2$ (right). The inset plots have smaller intervals between α values around the bifurcation points.

satisfy the zero traction condition (4.20e). This is because the red and black plots in Figure 4.4 are discontinuous, so for $c_0 = 0.2$, $\sigma_{rr}^* = 0$ is between both of these plots. The inset plots in Figure 4.4 show that this is not due to the discretisation of α. It is unusual for branches in bifurcation diagrams to be discontinuous, especially considering the bifurcation diagram for the roots to (4.27), β, is continuous, as shown in the inset plots of Figure 4.3.

To investigate the discontinuities in Figure 4.4, we calculate the displacements, u, and radial stresses, σ_{rr}, for the α value at the discontinuity between the red and black branches for $c_0 = 0.2$, approximately $\alpha = 0.2$. In Figure 4.5 we plot u, u' and σ_{rr}^* for $c_0 = 0.2$, $\alpha = 0.1926$ and for both the red and black solutions for β: $\beta = -0.55329$ and $\beta = -0.55441$. Although the values for β are very similar, as shown by the $\mathrm{d}u/\mathrm{d}r$ values at R_{Si}^+, the two displacement and stress profiles are very different for $r > R_{\text{Si}}$. This is because the bracket multiplying the second derivative in (4.20a), which we

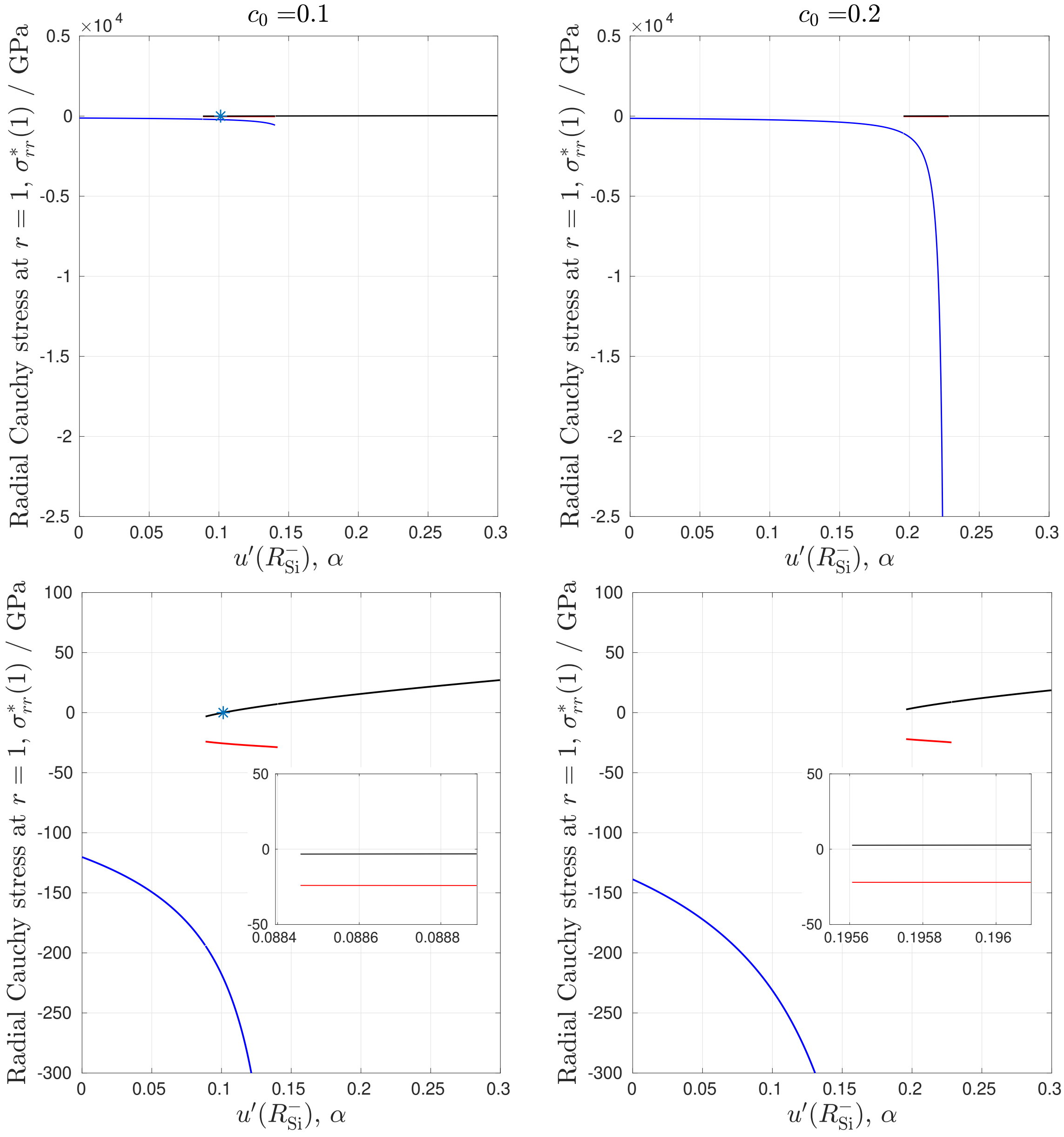

Figure 4.4: Radial Cauchy stress at $r = 1$, $\sigma^*_{rr}(1)$, calculated by integrating (4.20a) from $r = R^+_{\text{Si}}$ to $r = 1$, the roots of (4.27), denoted β_1, β_2, and β_3, as the value for $u'(R^+_{\text{Si}})$, against α. Plotted for $c_0 = 0.1$ (left) and $c_0 = 0.2$ (right). On the lower row of plots, we focus around $\sigma^*_{rr}(1) = 0$. The inset plots have a higher resolution of α values nearby the points where the red and black branches begin.

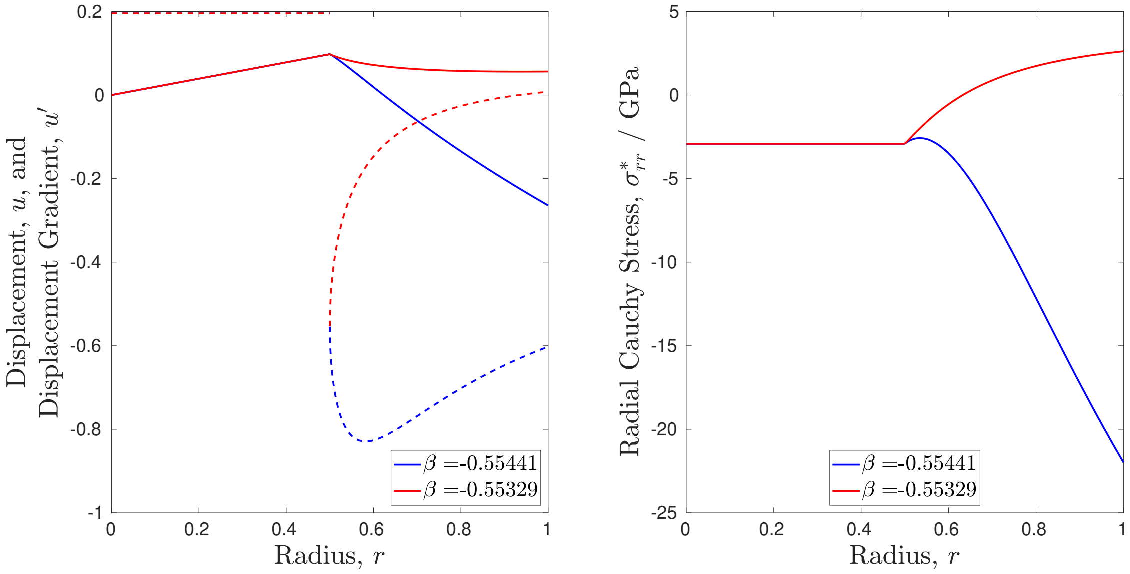

Figure 4.5: Left: Displacement, u (solid lines), and displacement gradient, u' (dashed lines), against radius, r. Right: Radial stress, σ^*_{rr}, against radius, r. Calculated by solving the ODE (4.17) for graphite using $\alpha = 0.1956$, the β values in the legend, $c_0 = 0.2$, and $R_{\text{Si}} = 0.5$.

label LHS, given by

$$\begin{aligned}\text{LHS} &= R_{\text{Si}}^2\left[\frac{3}{2}(1-\nu_{\text{C}})R_{\text{Si}}^2(1+\beta)^2 + \nu_{\text{C}}(R_{\text{Si}}+\alpha R_{\text{Si}})^2 - \frac{\nu_{\text{C}}+1}{2}(J_{\text{C}}^{\text{c}})^{2/3}R_{\text{Si}}^2\right]\\ &= R_{\text{Si}}^4\left[\frac{3}{2}(1-\nu_{\text{C}})(1+\beta)^2 + \nu_{\text{C}}(1+\alpha)^2 - \frac{\nu_{\text{C}}+1}{2}(J_{\text{C}}^{\text{c}})^{2/3}\right],\end{aligned} \tag{4.28}$$

is zero for some critical values of α and β which we label $\hat{\alpha}$ and $\hat{\beta}$. At LHS $= 0$, $u''(R_{\text{Si}}^+)$ is unbounded for a finite right-hand side of (4.20a).

We can show that LHS $= 0$ at the values of α and β where the red and black branches in Figure 4.3 join. The α value at which this occurs is that at which (4.27) has a repeated real root greater than the third root. We write (4.27) as

$$\beta^3 + p_2\beta^2 + p_1\beta + p_0 = 0, \tag{4.29a}$$

where

$$p_2 = 3, \tag{4.29b}$$

$$p_1 = 3 - \frac{1+\nu_{\text{C}}}{1-\nu_{\text{C}}}(J_{\text{C}}^{\text{c}})^{2/3} + \frac{2\nu_{\text{C}}}{1-\nu_{\text{C}}}(1+\alpha)^2, \tag{4.29c}$$

$$p_0 = 1 - \frac{1+\nu_{\text{C}}}{1-\nu_{\text{C}}}(J_{\text{C}}^{\text{c}})^{2/3} + \frac{2\nu_{\text{C}}}{1-\nu_{\text{C}}}(1+\alpha)^2 - \frac{2\sigma_{rr}(R_{\text{Si}}^-)(1+\nu_{\text{C}})(1-2\nu_{\text{C}})(1+\alpha)^2}{(1-\nu_{\text{C}})(J_{\text{C}}^{\text{c}})^{-1/3}E_{\text{C}}(c_{\text{C}})}, \tag{4.29d}$$

and

$$\sigma_{rr}(R_{\mathrm{Si}}^{-}) = \frac{(J_{\mathrm{Si}}^{c})^{-1/3}E_{\mathrm{Si}}(c_{\mathrm{Si}})}{(1+\nu_{\mathrm{Si}})(1-2\nu_{\mathrm{Si}})}\left\{\frac{(1+\nu_{\mathrm{Si}})}{2}(1+\alpha)^2 - \frac{1+\nu_{\mathrm{Si}}}{2}(J_{\mathrm{Si}}^{c})^{2/3}\right\}\frac{1}{1+\alpha}. \tag{4.29e}$$

There is a repeated root of the cubic equations (4.29a) when the discriminant, given by

$$\Delta = \frac{1}{4(27^2)}(2p_2^3 - 9p_1p_2 + 27p_0)^2 + \frac{1}{27^2}(3p_1 - p_2^2)^3, \tag{4.30}$$

is equal to zero. The roots of (4.29a) when $\Delta = 0$ are dependent on the sign of $2p_2^3 - 9p_1p_2 + 27p_0$. If $2p_2^3 - 9p_1p_2 + 27p_0 > 0$, the repeated root is greater than the other root, which is the case for the α and β values at which the red and black branches join. The roots β_i, $i = 1, 2, 3$ are then given by

$$\beta_1 = -2\sqrt{\frac{p_2^2 - 3p_1}{9}} - 1, \quad \beta_2 = \beta_3 = \sqrt{\frac{p_2^2 - 3p_1}{9}} - 1. \tag{4.31}$$

Substituting (4.29b) and (4.29c) into (4.31) yields

$$\beta_2 = \beta_3 = \frac{1}{3}\sqrt{\frac{3(1+\nu_{\mathrm{C}})}{1-\nu_{\mathrm{C}}}(J_{\mathrm{C}}^{c})^{\frac{2}{3}} - \frac{6\nu_{\mathrm{C}}}{1-\nu_{\mathrm{C}}}(1+\alpha)^2} - 1. \tag{4.32}$$

Substituting (4.32) into (4.28) yields

$$\begin{aligned}\mathrm{LHS} &= R_{\mathrm{Si}}^2\left[\frac{3}{2}(1-\nu_{\mathrm{C}})R_{\mathrm{Si}}^2\left(\frac{1}{3}\sqrt{\frac{3(1+\nu_{\mathrm{C}})}{1-\nu_{\mathrm{C}}}(J_{\mathrm{C}}^{c})^{2/3} - \frac{6\nu_{\mathrm{C}}}{1-\nu_{\mathrm{C}}}(1+\alpha)^2}\right)^2\right. \\ &\qquad \left. + \nu_{\mathrm{C}}R_{\mathrm{Si}}^2(1+\alpha)^2 - \frac{\nu_{\mathrm{C}}+1}{2}(J_{\mathrm{C}}^{c})^{2/3}R_{\mathrm{Si}}^2\right] \\ &= R_{\mathrm{Si}}^4\left(\frac{1}{2}(1+\nu_{\mathrm{C}})(J_{\mathrm{C}}^{c})^{2/3} - \nu_{\mathrm{C}}(1+\alpha)^2 + \nu_{\mathrm{C}}(1+\alpha)^2 - \frac{\nu_{\mathrm{C}}+1}{2}(J_{\mathrm{C}}^{c})^{2/3}\right) \\ &= 0.\end{aligned} \tag{4.33}$$

Therefore, the values of α and β at which the bifurcation in Figure 4.3 occurs are the same as the critical values, $\hat{\alpha}$ and $\hat{\beta}$, at which LHS = 0.

Therefore, $u''(R_{\mathrm{Si}}^{+})$ will be unbounded for $\alpha = \hat{\alpha}$ and $\beta = \hat{\beta}$ because LHS is exactly zero and the right-hand side of the ODE (4.20a) is finite. Perturbing α away from $\hat{\alpha}$, such that β_2 is slightly less than $\hat{\beta}$ and β_3 is slightly greater than $\hat{\beta}$, causes $u''(R_{\mathrm{Si}}^{+})$ to be large and negative or large and positive. This has a large effect on the radial stress at $r = 1$, due to the very different displacement profiles for $r \in [R_{\mathrm{Si}}, 1]$ between a positive perturbation and a negative perturbation. This is the reason the red and black branches in Figure 4.4 are discontinuous.

4.4 Linearisation Around Bifurcation

In this section, we seek to analytically confirm the behaviour of the displacement at $r = R_{\text{Si}}$ for the critical values $\alpha = \hat{\alpha}$ and $\beta = \hat{\beta}$ by linearising the ODE (4.20a) around $r = R_{\text{Si}}$. We then analyse the effect of a small perturbation to α about $\hat{\alpha}$ to confirm that the red and black branches in $\sigma_{rr}(1)$ in Figure 4.4 are two discontinuous branches as opposed to a connected curve, which might have been expected.

4.4.1 Linearisation Around $\boldsymbol{R_{\text{Si}}}$

To linearise the ODE (4.20a) about R_{Si}, we introduce a new spatial variable $\tilde{r}$ by defining

$$r = R_{\text{Si}} + \delta\tilde{r}, \tag{4.34}$$

where $\delta \ll 1$. We also assume that the displacement, u, near R_{Si} can be written as

$$u = \hat{\alpha}R_{\text{Si}} + \hat{\beta}(r - R_{\text{Si}}) + \varepsilon\tilde{u} = \hat{\alpha}R_{\text{Si}} + \delta\hat{\beta}\tilde{r} + \varepsilon\tilde{u}, \tag{4.35}$$

where we have introduced a new displacement, $\tilde{u}$, used (4.34) in the second equality, and we will assume $\varepsilon \ll 1$. By differentiating (4.35) and using the chain rule, we can write the first and second derivatives of u with respect to r as

$$\frac{\mathrm{d}u}{\mathrm{d}r} = \hat{\beta} + \frac{\epsilon}{\delta}\frac{\mathrm{d}\tilde{u}}{\mathrm{d}\tilde{r}}, \tag{4.36a}$$

$$\frac{\mathrm{d}^2u}{\mathrm{d}r^2} = \frac{\epsilon}{\delta^2}\frac{\mathrm{d}^2\tilde{u}}{\mathrm{d}\tilde{r}^2}. \tag{4.36b}$$

The conditions for the displacement u at $r = R_{\text{Si}}^+$ are $u(R_{\text{Si}}^+) = \hat{\alpha}R_{\text{Si}}$ and $u'(R_{\text{Si}}^+) = \hat{\beta}$, which corresponds to the following conditions on $\tilde{u}(\tilde{r})$,

$$\tilde{u}(\tilde{r} = 0) = 0, \tag{4.37a}$$

$$\frac{\mathrm{d}\tilde{u}}{\mathrm{d}\tilde{r}}(\tilde{r} = 0) = 0. \tag{4.37b}$$

The condition on $\tilde{u}$ (4.37a), suggests the solution $\tilde{u}$ has the form $\tilde{u} = \tilde{r}^a$ close to $\tilde{r} = 0$, for some constant, a. Under this assumption, (4.37b) suggests that $a > 1$. The variations in u are therefore much smaller than the variations in r as $\tilde{r} \to 0$, and from (4.36a), we therefore have $\varepsilon \ll \delta$ so the $\mathrm{d}\tilde{u}/\mathrm{d}\tilde{r}$ term balances this small variation in u with r.

We now substitute (4.34)-(4.36) into the ODE (4.20a), giving

$$\begin{aligned}
&(R_{\mathrm{Si}}+\delta\tilde{r})^2\Bigg[\frac{3}{2}(1-\nu_{\mathrm{C}})(R_{\mathrm{Si}}+\delta\tilde{r})^2\left(1+\hat{\beta}+\frac{\varepsilon}{\delta}\frac{\mathrm{d}\tilde{u}}{\mathrm{d}\tilde{r}}\right)^2 \\
&\qquad+\nu_{\mathrm{C}}\big((1+\hat{\alpha})R_{\mathrm{Si}}+(1+\hat{\beta})\delta\tilde{r}+\varepsilon\tilde{u}\big)^2-\frac{\nu_{\mathrm{C}}+1}{2}(J_{\mathrm{C}}^{\mathrm{c}})^{2/3}(R_{\mathrm{Si}}+\delta\tilde{r})^2\Bigg]\frac{\varepsilon}{\delta^2}\frac{\mathrm{d}^2\tilde{u}}{\mathrm{d}\tilde{r}^2} \\
&=\big((1+\hat{\alpha})R_{\mathrm{Si}}+(1+\hat{\beta})\delta\tilde{r}+\varepsilon\tilde{u}\big)^3-(1-\nu_{\mathrm{C}})(R_{\mathrm{Si}}+\delta\tilde{r})^3\left(1+\hat{\beta}+\frac{\varepsilon}{\delta}\frac{\mathrm{d}\tilde{u}}{\mathrm{d}\tilde{r}}\right)^3 \\
&\qquad-\nu_{\mathrm{C}}(R_{\mathrm{Si}}+\delta\tilde{r})^2\big((1+\hat{\alpha})R_{\mathrm{Si}}+(1+\hat{\beta})\delta\tilde{r}+\varepsilon\tilde{u}\big)\left(1+\hat{\beta}+\frac{\varepsilon}{\delta}\frac{\mathrm{d}\tilde{u}}{\mathrm{d}\tilde{r}}\right)^2 \\
&\qquad\qquad+(\nu_{\mathrm{C}}+1)(J_{\mathrm{C}}^{\mathrm{c}})^{2/3}(R_{\mathrm{Si}}+\delta\tilde{r})^2\left[R_{\mathrm{Si}}(\hat{\beta}-\hat{\alpha})+(R_{\mathrm{Si}}+\delta\tilde{r})\frac{\varepsilon}{\delta}\frac{\mathrm{d}\tilde{u}}{\mathrm{d}\tilde{r}}-\varepsilon\tilde{u}\right].
\end{aligned}\tag{4.38}$$

For ease of understanding, we label the left-hand and right-hand sides of (4.38) as L and R, respectively.

The leading-order terms of L (of size $\mathcal{O}(\varepsilon/\delta^2)$) are

$$\begin{aligned}
\mathrm{L}(\mathcal{O}(\varepsilon/\delta^2))=R_{\mathrm{Si}}^2\Bigg[&\frac{3}{2}(1-\nu_{\mathrm{C}})R_{\mathrm{Si}}^2(1+\hat{\beta})^2+\nu_{\mathrm{C}}(1+\hat{\alpha})R_{\mathrm{Si}}^2 \\
&-\frac{\nu_{\mathrm{C}}+1}{2}(J_{\mathrm{C}}^{\mathrm{c}})^{2/3}R_{\mathrm{Si}}^2\Bigg]\frac{\mathrm{d}^2\tilde{u}}{\mathrm{d}\tilde{r}^2}.
\end{aligned}\tag{4.39}$$

The terms in brackets of (4.39) are equal to LHS in (4.28) with $\alpha=\hat{\alpha}$ and $\beta=\hat{\beta}$. We showed in Section 4.3 that LHS $=0$ for $\alpha=\hat{\alpha}$ and $\beta=\hat{\beta}$ and so we must therefore match the next-order terms of L to the $\mathcal{O}(1)$ terms of R.

The next-order terms of L are $\mathcal{O}(\varepsilon^3/\delta^2)$ and $\mathcal{O}(\varepsilon/\delta)$ terms. If we were to match the $\mathcal{O}(\varepsilon/\delta)$ terms to the $\mathcal{O}(1)$ terms in R, this would imply $\epsilon\sim\delta$ which violates the relative orders found earlier from (4.36)-(4.37). Therefore, we must have $\varepsilon^3/\delta^2\sim 1$ so we take $\varepsilon=\delta^{3/2}$. Hence, (4.38) is given at leading order by

$$\begin{aligned}
3R_{\mathrm{Si}}(1-\nu_{\mathrm{C}})(1+\hat{\beta})\frac{\mathrm{d}\tilde{u}}{\mathrm{d}\tilde{r}}\frac{\mathrm{d}^2\tilde{u}}{\mathrm{d}\tilde{r}^2}&=(1+\hat{\alpha})^3-(1-\nu_{\mathrm{C}})(1+\hat{\beta})^3 \\
&\quad-\nu_{\mathrm{C}}(1+\hat{\alpha})(1+\hat{\beta})^2+(\nu_{\mathrm{C}}+1)(J_{\mathrm{C}}^{\mathrm{c}})^{2/3}(\hat{\beta}-\hat{\alpha}).
\end{aligned}\tag{4.40}$$

The ODE (4.40) can easily be solved to yield the general solution

$$\tilde{u}=\pm\frac{2}{3C}(C\tilde{r}+A)^{\frac{3}{2}}+B,\tag{4.41}$$

where

$$C=\frac{2\big[(1+\hat{\alpha})^3-(1-\nu_{\mathrm{C}})(1+\hat{\beta})^3-\nu_{\mathrm{C}}(1+\hat{\alpha})(1+\hat{\beta})^2+(\nu_{\mathrm{C}}+1)(J_{\mathrm{C}}^{\mathrm{c}})^{2/3}(\hat{\beta}-\hat{\alpha})\big]}{3R_{\mathrm{Si}}(1-\nu_{\mathrm{C}})(1+\hat{\beta})},\tag{4.42}$$

and A and B are integration constants. Applying the conditions (4.37), reveals $A = B = 0$, giving the solution

$$\tilde{u} = \pm\frac{2}{3}\sqrt{C}\tilde{r}^{\frac{3}{2}}. \tag{4.43}$$

In Figure 4.6 we plot the solution (4.43) for $\tilde{r} \in [0, 10]$ for $\hat{\alpha} = 0.1956$ and $\hat{\beta} = -0.5538$ which are the $\hat{\alpha}$ and $\hat{\beta}$ values for $c_0 = 0.2$ and $R_{\text{Si}} = 0.5$. It can be seen that the two solutions of this equation diverge from $\tilde{r} = 0$ which is the behaviour we observe in Figure 4.5. By considering the expression for the radial Cauchy stress (4.21), we can see that the two σ_{rr} profiles calculated from the positive and negative solutions in (4.43) also diverge from $\tilde{r} = 0$. This leads to the distinct values of $\sigma_{rr}(1)$ seen in Figure 4.4 for $\alpha = \hat{\alpha}$ and $\beta = \hat{\beta}$. Additionally, from the solution (4.43) we see that $\tilde{u}''(\tilde{r} = 0)$ is unbounded, supporting our finding that the second derivative of u is infinite at $(\hat{\alpha}, \hat{\beta})$.

4.4.2 Linearisation Around $\hat{\alpha}$

We now wish to investigate how the solution close to $r = R_{\text{Si}}$ varies when we perturb the value of α away from $\hat{\alpha}$. We perturb α by some small amount, $f(\delta)$, and write the resulting small amount that β is perturbed as $g(\delta)$, giving

$$\alpha = \hat{\alpha} + f(\delta)\alpha^{(1)} + \ldots, \qquad \beta = \hat{\beta} + g(\delta)\beta^{(1)} + \ldots, \tag{4.44}$$

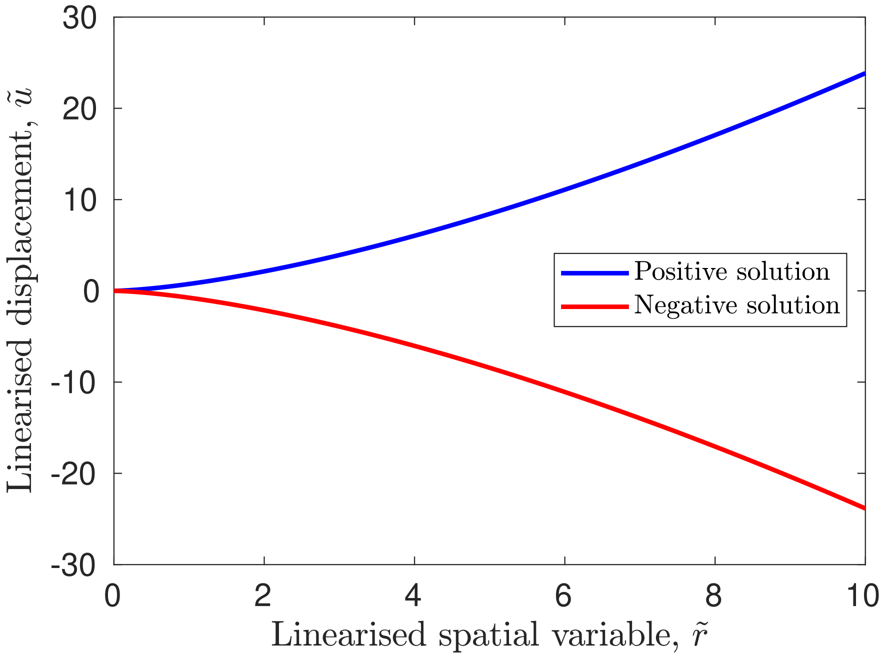

Figure 4.6: Solution (4.43) to the leading-order non-trivial ODE (4.38). Here, $R_{\text{Si}} = 0.5$, $c_0 = 0.2$, $\hat{\alpha} = 0.1956$ and $\hat{\beta} = -0.5538$.

where the size of $f(\delta)$ and $g(\delta)$ are to be found. Using the expressions (4.35) and (4.36), along with $\varepsilon \sim \delta^{3/2}$, found in the last section, we have

$$\begin{aligned} u &= (\hat{\alpha} + f(\delta)\alpha^{(1)})R_{\mathrm{Si}} + \delta(\hat{\beta} + g(\delta)\beta^{(1)})\tilde{r} + \delta^{3/2}\tilde{u}, && \text{(4.45a)}\\ \frac{\mathrm{d}u}{\mathrm{d}r} &= \hat{\beta}g(\delta)\beta^{(1)} + \delta^{1/2}\frac{\mathrm{d}\tilde{u}}{\mathrm{d}\tilde{r}}, && \text{(4.45b)}\\ \frac{\mathrm{d}^2u}{\mathrm{d}r^2} &= \delta^{-1/2}\frac{\mathrm{d}^2\tilde{u}}{\mathrm{d}\tilde{r}^2}. && \text{(4.45c)} \end{aligned}$$

Additionally, substituting (4.44) into the stress-continuity condition in terms of α and β, given by (4.27), yields the continuity of stress boundary condition at $r = R_{\mathrm{Si}}$,

$$\begin{aligned} &\mathcal{J}_{\mathrm{Si}}\left\{\frac{(1+\nu_{\mathrm{Si}})}{2}\big(1+\hat{\alpha}+f(\delta)\alpha^{(1)}\big)^2 - \frac{1+\nu_{\mathrm{Si}}}{2}(J^c_{\mathrm{Si}})^{2/3}\right\}\big(1+\hat{\alpha}+f(\delta)\alpha^{(1)}\big)\\ &\qquad = \mathcal{J}_{\mathrm{C}}\left\{\frac{(1-\nu_{\mathrm{C}})}{2}\big(1+\hat{\beta}+g(\delta)\beta^{(1)}\big)^2 + \nu_{\mathrm{C}}\big(1+\hat{\alpha}+f(\delta)\alpha^{(1)}\big)^2\right. \qquad \text{(4.46a)}\\ &\qquad\qquad\qquad \left. - \frac{1+\nu_{\mathrm{C}}}{2}(J^c_{\mathrm{C}})^{2/3}\right\}\big(1+\hat{\beta}+g(\delta)\beta^{(1)}\big), \end{aligned}$$

where

$$\mathcal{J}_a = \frac{(J^c_a)^{-1/3}E_a(c_a)}{(1+\nu_a)(1-2\nu_a)}, \qquad \text{(4.46b)}$$

for $a = \mathrm{Si}, \mathrm{C}$.

The leading-order terms of (4.46a) recover (4.27). Matching the $\mathcal{O}\big(g(\delta)\big)$ and $\mathcal{O}\big(f(\delta)\big)$ terms yields

$$\begin{aligned} &\mathcal{J}_{\mathrm{Si}}\left\{\frac{3(1+\nu_{\mathrm{Si}})}{2}(1+\hat{\alpha})^2 - \frac{1+\nu_{\mathrm{Si}}}{2}(J^c_{\mathrm{Si}})^{2/3}\right\}\alpha^{(1)} - 2\nu_{\mathrm{C}}\mathcal{J}_{\mathrm{C}}(1+\hat{\alpha})(1+\hat{\beta})\alpha^{(1)}\\ &\qquad = \mathcal{J}_{\mathrm{C}}\left\{\frac{3(1-\nu_{\mathrm{C}})}{2}(1+\hat{\beta})^2 + \nu_{\mathrm{C}}(1+\hat{\alpha})^2 - \frac{1+\nu_{\mathrm{C}}}{2}(J^c_{\mathrm{C}})^{2/3}\right\}\beta^{(1)}. \end{aligned} \qquad \text{(4.47)}$$

Comparing the right-hand side of (4.47) to LHS in (4.28), we see that the $\mathcal{O}\big(g(\delta)\big)$ terms are zero because LHS $= 0$ for $\alpha = \hat{\alpha}$ and $\beta = \hat{\beta}$. Therefore, the $\mathcal{O}\big(f(\delta)\big)$ terms must balance with the $\mathcal{O}\big(g(\delta)^2\big)$ terms instead, implying $g(\delta) \sim \big(f(\delta)\big)^{1/2}$. This matching yields

$$\begin{aligned} &\mathcal{J}_{\mathrm{Si}}\left\{\frac{3(1+\nu_{\mathrm{Si}})}{2}(1+\hat{\alpha})^2 - \frac{1+\nu_{\mathrm{Si}}}{2}(J^c_{\mathrm{Si}})^{2/3}\right\}\alpha^{(1)} - 2\nu_{\mathrm{C}}\mathcal{J}_{\mathrm{C}}(1+\hat{\alpha})(1+\hat{\beta})\alpha^{(1)}\\ &\qquad = \mathcal{J}_{\mathrm{C}}\left\{\frac{3(1-\nu_{\mathrm{C}})}{2}(1+\hat{\beta})\right\}\big(\beta^{(1)}\big)^2, \end{aligned} \qquad \text{(4.48)}$$

which we rearrange to give

$$\beta^{(1)} = \pm\left[\frac{\mathcal{J}_{\mathrm{Si}}(1+\nu_{\mathrm{Si}})\big(3(1+\hat{\alpha})^2 - (J_{\mathrm{Si}}^{c})^{2/3}\big) - 4\nu_{\mathrm{C}}\mathcal{J}_{\mathrm{C}}(1+\hat{\alpha})(1+\hat{\beta})}{3\mathcal{J}_{C}(1-\nu_{\mathrm{C}})(1+\hat{\beta})}\alpha^{(1)}\right]^{\frac{1}{2}} \tag{4.49}$$

As in Section 4.4.1, substituting (4.45) into the governing ODE (4.20a) recovers (4.39) at leading order ($\mathcal{O}(\delta^{-1/2})$), and thus we analyse the next-order terms. From the scaling found above, we have that $g(\delta) \gg f(\delta)$, and thus we match the $\mathcal{O}\big(g(\delta)\delta^{-1/2}\big)$ and $\mathcal{O}(1)$ terms of L to the $\mathcal{O}(1)$ terms of R. This yields

$$\begin{aligned} R_{\mathrm{Si}}\left[3(1-\nu_{\mathrm{C}})(1+\hat{\beta})\left(\beta^{(1)}g(\delta) + \frac{\mathrm{d}\tilde{u}}{\mathrm{d}\tilde{r}}\delta^{\frac{1}{2}}\right)\right]\delta^{-\frac{1}{2}}\frac{\mathrm{d}^2\tilde{u}}{\mathrm{d}\tilde{r}^2} \\ = (1+\hat{\alpha})^3 - (1-\nu_{\mathrm{C}})(1+\hat{\beta})^3 - \nu_{\mathrm{C}}(1+\hat{\alpha})(1+\hat{\beta})^2 \\ + (\nu_{\mathrm{C}}+1)(J_{\mathrm{C}}^{c})^{2/3}(\hat{\beta}-\hat{\alpha}). \end{aligned} \tag{4.50}$$

Therefore, we must have $g(\delta) = \delta^{1/2}$ and $f(\delta) = \delta$. By substituting $g(\delta) = \delta^{1/2}$ into (4.50), the ODE at leading order is given by

$$\left(\beta^{(1)} + \frac{\mathrm{d}\tilde{u}}{\mathrm{d}\tilde{r}}\right)\frac{\mathrm{d}^2\tilde{u}}{\mathrm{d}\tilde{r}^2} = \frac{C}{2}, \tag{4.51}$$

where C is given by (4.42) and $\beta^{(1)}$ is given by (4.49).

The ODE (4.51) can be integrated to give

$$2\beta^{(1)}\frac{\mathrm{d}\tilde{u}}{\mathrm{d}\tilde{r}} + \left(\frac{\mathrm{d}\tilde{u}}{\mathrm{d}\tilde{r}}\right)^2 = C\tilde{r} + A, \tag{4.52}$$

where A is an integration constant. Applying the condition (4.37b) yields $A = 0$. Substituting $A = 0$ and rearranging gives

$$\left(\beta^{(1)} + \frac{\mathrm{d}\tilde{u}}{\mathrm{d}\tilde{r}}\right)^2 = C\tilde{r} + \big(\beta^{(1)}\big)^2 \implies \frac{\mathrm{d}\tilde{u}}{\mathrm{d}\tilde{r}} = \pm\Big(C\tilde{r} + \big(\beta^{(1)}\big)^2\Big)^{\frac{1}{2}} - \beta^{(1)}, \tag{4.53}$$

which is integrated again, giving

$$\tilde{u} = \pm\frac{2}{3C}\Big(C\tilde{r} + \big(\beta^{(1)}\big)^2\Big)^{\frac{3}{2}} - \beta^{(1)}\tilde{r} + B. \tag{4.54}$$

Applying the condition (4.37b) again to (4.54) yields

$$\beta^{(1)} = \pm\Big(\big(\beta^{(1)}\big)^2\Big)^{\frac{1}{2}} \implies \beta^{(1)} = \pm\big|\beta^{(1)}\big|. \tag{4.55}$$

This implies that the boundary condition (4.37b) is only satisfied by the positive solution in (4.54) if $\beta^{(1)} > 0$ and by the negative solution if $\beta^{(1)} < 0$. Therefore, we write the solution as

$$\tilde{u} = \operatorname{sgn}\big(\beta^{(1)}\big)\frac{2}{3C}\Big(C\tilde{r} + \big(\beta^{(1)}\big)^2\Big)^{\frac{3}{2}} - \beta^{(1)}\tilde{r} + B. \tag{4.56}$$

Applying the initial condition (4.37a) to (4.56) yields

$$0 = \operatorname{sgn}\big(\beta^{(1)}\big)\frac{2}{3C}\Big(\big(\beta^{(1)}\big)^2\Big)^{\frac{3}{2}} + B \implies B = -\operatorname{sgn}\big(\beta^{(1)}\big)\frac{2}{3C}\big|\beta^{(1)}\big|^3, \tag{4.57}$$

yielding the exact solution

$$\tilde{u} = \operatorname{sgn}\big(\beta^{(1)}\big)\frac{2}{3C}\left[\Big(C\tilde{r} + \big(\beta^{(1)}\big)^2\Big)^{\frac{3}{2}} - \big|\beta^{(1)}\big|^3\right] - \beta^{(1)}\tilde{r}. \tag{4.58}$$

For the parameters we use here ($R_{\mathrm{Si}} = 0.5, c_0 = 0.2$), the prefactor for $\alpha^{(1)}$ in (4.49) is positive. Therefore, the solution (4.58) to the linearised ODE (4.51) is only real if $\alpha^{(1)} > 0$ due to the quadratic relationship between $\beta^{(1)}$ and $\alpha^{(1)}$ in (4.49). This can be seen in the bifurcation diagram for β in Figure 4.3. If α is increased slightly from $\alpha = \hat{\alpha}$, such that $\alpha^{(1)} > 0$, the roots represented by the black and red branches come into existence, whereas if $\alpha^{(1)} < 0$, these solutions cease to exist. As seen in Section 4.4.1, at the bifurcation point, $\alpha = \hat{\alpha}$, there are only two distinct roots of (4.27), β_1 and $\hat{\beta}$. For the $\beta = \hat{\beta}$ case, there are two solutions for the linearised displacement, $\tilde{u}$, given by (4.43). As there are three roots, β_i, $i = 1, 2, 3$, for $\alpha = \hat{\alpha} + \delta\alpha^{(1)}$, it could be expected that there are four solutions to $\tilde{u}$ for the two greater β values: two for $\beta = \hat{\beta} + \beta^{(1)}$ and two for $\beta = \hat{\beta} - \beta^{(1)}$. However, the condition (4.37b) results in the choice of solution in (4.54) being dependent on $\operatorname{sgn}\big(\beta^{(1)}\big)$. Therefore, there is only one solution for positive $\beta^{(1)}$ and one for negative $\beta^{(1)}$.

Therefore, as α is increased, the number of roots, β, of (4.3) increases from one, to two at $\alpha = \hat{\alpha}$, then to three, before reducing to two at the other bifurcation point and eventually reducing to one for larger α. Conversely, the number of values of $\sigma_{rr}(1)$ that result from these roots, β, increases from one, immediately to three at $\alpha = \hat{\alpha}$, and remains at three until the other bifurcation in α occurs, which we do not study here. In terms of the solution to the BVP (4.20), the discontinuity in $\sigma_{rr}(1)$ causes the solution to not exist for c_0 and R_{Si} values in which $\sigma_{rr}(1) = 0$ is within this gap caused by the discontinuity. This analysis is only valid for R_{Si} and c_0 values in which the bifurcation in the roots of (4.3) occurs. As previously discussed, the bifurcation does not occur for large values of c_0, however we do not study the behaviour of the solution in these cases here.

So far in this chapter, we have shown both numerically and analytically that the nonlinear elasticity model derived in Section 4.1 does not permit solutions for states of charge above a certain value. The reason that the solutions cease to exist is because the strain energy density (4.6) does not penalise strongly enough the large values of

u'', which are caused by the high compression of the graphite at $r = R_{\mathrm{Si}}$. In the next section we account for this by using a different constitutive law to describe the mechanics of each material.

4.5 Compressible Constitutive Laws

In this section, we present a geometrically *and constitutively* nonlinear model for the mechanical behaviour of both the silicon and the graphite, and solve the model applied to the spherical core–shell geometry in Figure 2.1. We then apply the model to the nano-particle with a porous silicon layer between the silicon core and graphite shell, shown in Figure 3.9. We find that the fully nonlinear model no longer predicts overlap of materials for this geometry. Lastly, we reproduce Figure 3.10 using this nonlinear model to show that this nano-particle design can reduce the expansion of the nano-particle but only by a small amount and for a small range of geometric parameters.

4.5.1 Silicon Core and Graphite Shell

We extend the model in Section 4.1 by considering nonlinear constitutive laws which penalise high compression. In particular, we consider strain energy densities which include terms that tend to infinity as the determinant of the elastic deformation gradient $\det(\mathbf{F}^e) \to 0$. The two constitutive laws we consider are compressible neo-Hookean (NH) and Blatz–Ko (BK) [8] whose strain energy densities are given by

$$\mathcal{W}^{\mathrm{NH}} = J_a^c \left[\frac{\lambda_a}{2} (\ln J^e)^2 - G_a \ln J^e + \frac{G_a}{2}(I_1 - 3) \right], \tag{4.59a}$$

$$\mathcal{W}^{\mathrm{BK}} = \frac{J_a^c G_a}{2} \left[f\left((I_1 - 3) + \frac{1}{\beta_a}\left(I_3^{-\beta_a} - 1\right) \right) + (1 - f)\left(\frac{I_2}{I_3} - 3 + \frac{1}{\beta_a}\left(I_3^{\beta_a} - 1\right) \right) \right], \tag{4.59b}$$

respectively, where λ_a and G_a are the Lamé parameters of material a and $\beta_a = \lambda_a/(2G_a)$, and $f \in [0.0, 1.0]$ is an additional parameter. Throughout the remainder of this chapter, we take $f = 0.5$. The terms I_1, I_2 and I_3 are known as the three invariants of the Left Cauchy–Green tensor, $\mathbf{F}^e\left(\mathbf{F}^e\right)^{\mathrm{T}}$, and J^e is the Jacobian of the elastic deformation tensor, $\mathbf{F}^e$. These are written as functions of $\mathbf{F}^e$ as

$$J^e = \det(\mathbf{F}^e), \tag{4.60a}$$

$$I_1 = \mathrm{tr}\big(\mathbf{F}^e(\mathbf{F}^e)^{\mathrm{T}}\big), \tag{4.60b}$$

$$I_2 = \frac{1}{2}\Big[\Big(\mathrm{tr}\big(\mathbf{F}^e(\mathbf{F}^e)^{\mathrm{T}}\big)\Big)^2 - \mathrm{tr}\Big(\big(\mathbf{F}^e(\mathbf{F}^e)^{\mathrm{T}}\big)^2\Big)\Big], \tag{4.60c}$$

$$I_3 = \det\big(\mathbf{F}^e(\mathbf{F}^e)^{\mathrm{T}}\big). \tag{4.60d}$$

Therefore, it can be seen that in (4.59a), as $J^e \to 0$, $\ln J^e \to -\infty \implies [\lambda_a/2(\ln J^e)^2 - G_a \ln J^e] \to \infty$. Similarly, in (4.59b), as $I_3 = \det(\mathbf{F}^e)\det\big((\mathbf{F}^e)^{\mathrm{T}}\big) \to 0$, $I_3^{-\beta_a} \to \infty$ and $I_2/I_3 \to \infty$. Thus, these strain energy densities provide the desired properties.

Following the same procedure as in Section 4.1.2, we can derive the 1st P-K stresses, Cauchy stresses, ODE and boundary conditions that result from applying (4.59) to the model in Section 4.1. These are presented in Appendix D for both the NH and BK constitutive laws. Using the same double shooting method as in Section 4.2.1, we solve the two boundary value problems that arise from using these nonlinear constitutive laws for $R_{\mathrm{Si}} = 0.5$ and $c_0 = 0.1, 0.2, \ldots 1.0$. In Figures 4.7 and 4.8, we plot the displacements, u, the displacement gradients, u', and the radial Cauchy stresses, $\boldsymbol{\sigma}^*_{rr}$, for the NH and BK constitutive laws, respectively.

We now obtain solutions for all c_0 values from 0 to 1. In both cases, while σ_{rr} is monotonic with increasing c_0 in Ω_{Si}, u' is not. For example, in Figure 4.7, $\mathrm{d}u/\mathrm{d}r$ for $c_0 = 0.7$ is greater than that for $c_0 = 0.8$ in the silicon region. This is due to the dependence of the Young's modulus of graphite with c_{C} in the model. In Figure 4.9, we plot the Young's modulus of the graphite and u' in Ω_{Si} against c_0, using the solution from the NH constitutive law. We can see that for increases in c_0 in which the Young's modulus of the graphite increases rapidly, u' in Ω_{C} either only increases slightly or decreases, such as between $c_0 \approx 0.7$ and $c_0 \approx 0.85$. The opposite effect is observed when E^*_{C} increases slowly with c_0. Referring to Figure 2.6 of c_{Si} and c_{C} against c_0, the large increases in E^*_{C} occur at the same c_0 values as the large increases in c_{C}. This is expected given the linear variation of E_{C} with c_{C}. At the c_0 values that c_{C} greatly increases, c_{Si}, and thus u', does not increase very much. However, if stress-assisted diffusion is included into the model, as it is in the displacement profiles in Figure 2.8, c_{C} increases very rapidly at low c_0 values due to the tensile stress caused by the expanding silicon. This masks the effects of the lithiation-dependent stiffness of the graphite, meaning u' in Ω_{Si} is monotonic if stress-assisted diffusion is included in the model.

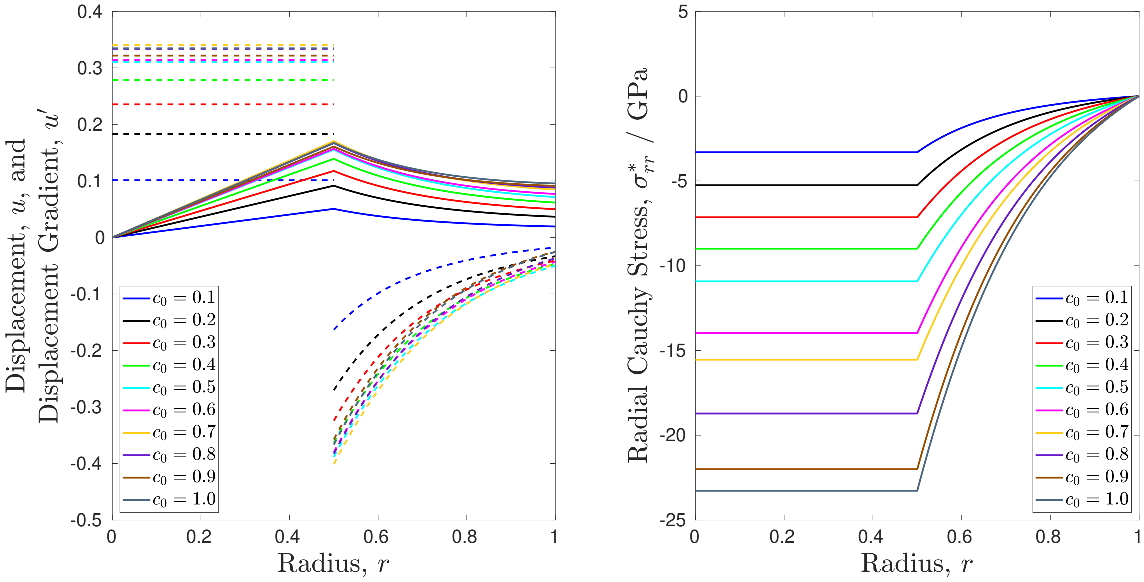

Figure 4.7: Displacement, u (left, solid lines), displacement gradient, u' (left, dashed lines), and radial Cauchy stress, σ^*_{rr} (right), obtained using the compressible NH constitutive law.

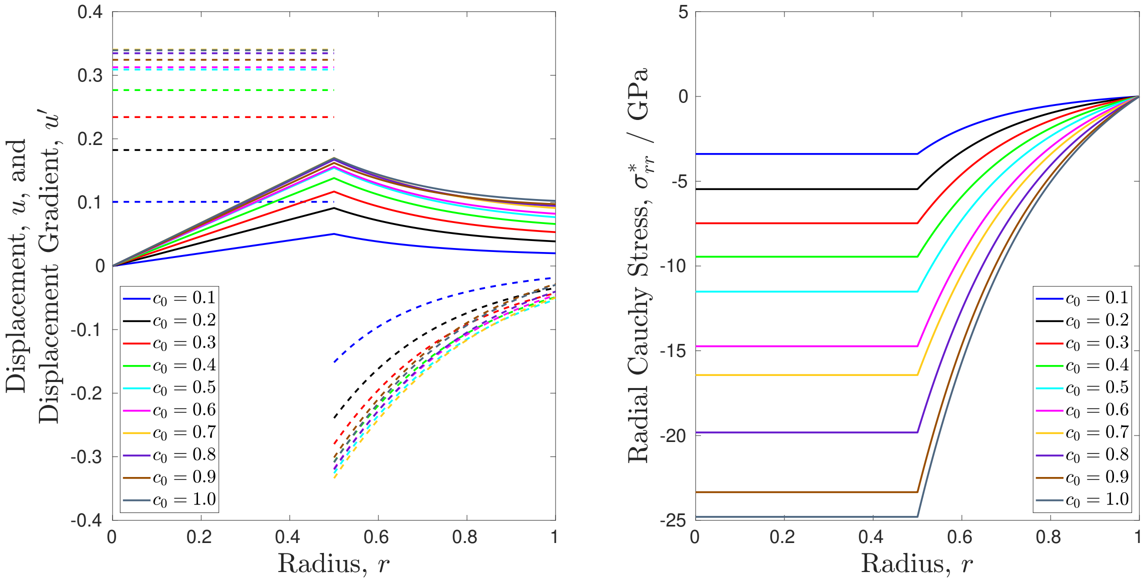

Figure 4.8: Displacement, u (left, solid lines), displacement gradient, u' (left, dashed lines), and radial Cauchy stress, σ^*_{rr} (right), obtained using the compressible BK constitutive law.

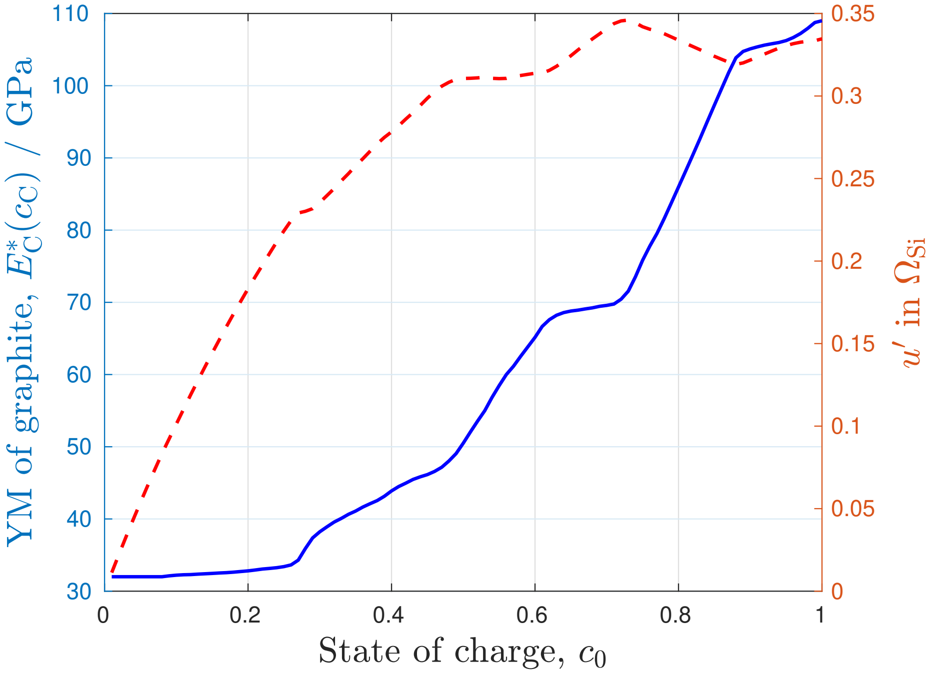

Figure 4.9: Young's modulus (YM) of graphite, $E^*_{\mathrm{C}}(c_{\mathrm{C}})$, (solid blue line) and u' in Ω_{Si} (dashed red line), against SOC, c_0. The compressible NH constitutive law was used to calculate u' in Ω_{Si}.

4.5.2 Porous Silicon Layer

We have now discussed two geometrically nonlinear constitutive laws which yield solutions to the silicon and graphite core–shell geometry for all c_0 values. We now revisit the results that motivated this chapter, and in particular those in Figure 3.11. We wish to find the displacement of the nano-particle with a non-porous silicon core, a porous silicon layer and a graphite shell, as shown in Figure 3.9, when fully lithiated ($c_0 = 1$). We must solve the nonlinear mechanical equilibrium equation (4.16) in each region, Ω_{Si}, Ω_ϕ, and Ω_{C}, and apply the boundary conditions

$$u = 0 \text{ at } r = 0, \tag{4.61a}$$

$$[u(R_{\mathrm{Si}})]^+_- = [\sigma_{rr}(R_{\mathrm{Si}})]^+_- = 0, \tag{4.61b}$$

$$[u(R_\phi)]^+_- = [\sigma_{rr}(R_\phi)]^+_- = 0, \tag{4.61c}$$

$$\sigma_{rr}(1) = 0, \tag{4.61d}$$

where σ_{rr} can be derived from the constitutive laws (4.59), as shown in Appendix D, and R_ϕ and R_{Si} are shown in Figure 3.9. We note that the effective parameters of the porous silicon were calculated using the linear elasticity model and we are assuming here that silicon and graphite behave according to a nonlinear constitutive law. However, we assume that the Lamé parameters vary with the porosity in a similar way to that using the linear model, shown in Figures 3.5 and 3.6, and thus still use the fitted function (3.73) to calculate λ_ϕ and G_ϕ.

We wish to compare the numerical solution to the nonlinear BVP in this chapter to the solution to the linear BVP in Figure 3.11. We therefore take the same geometric parameter values: $R_{\mathrm{Si}}^3 = 0.375$, $R_\phi^3 = 0.5$ and $\phi = 0.1$, and consider the fully lithiated state, $c_0 = 1$. However, as we have nondimensionalised the displacement differently in the linear and nonlinear models, we compare the dimensional final position, relative to the outer radius of the nano-particle, given by $(u^* + r^*)/R_{\mathrm{C}}^*$. This is opposed to nondimensional $u + r$ plotted in Figure 3.11.

As we have two internal boundaries in this geometry, the double-shooting method in Section 4.2.1 is no longer appropriate. Instead, we solve the BVP system for the nonlinear constitutive laws using the MATLAB BVP solver `bvp5c` [54]. As the nonlinear ODE arising from (4.16) has multiple solutions, we first solve the BVP ignoring the porous silicon core, such that $R_{\mathrm{Si}}^3 = 0.5$, and incrementally increase the porosity of the porous silicon layer until $\phi = 0.1$. This ensures the solver converges to the desired solution.

In Figure 4.10, we plot $(u^* + r^*)/R_{\mathrm{C}}^*$ against r, using solutions obtained using the three mechanical models: the linear elasticity model, the NH constitutive law and the BK constitutive law. It can be seen that the results from the nonlinear model, using either constitutive law, do not exhibit overlap of materials as $(u^* + r^*)/R_{\mathrm{C}}^*$ is monotonically increasing in r. This means every initial radial point in the nano-particle has a unique final position after the lithiation-induced displacement. This is confirmed in the inset plots focussed on the porous silicon region $r \in [R_{\mathrm{Si}}, R_\phi]$ which show the nonlinear solutions have a positive gradient. We can see that the linear solution gives a smaller displacement at $r = 1$, yielding a smaller expanded volume, as expected due to the unphysical overlap.

We can now return to Figure 3.10, where we saw that including a porous silicon layer into the nano-particle design could greatly reduce the expansion without decreasing the capacity. We reproduce Figure 3.10 using the nonlinear elasticity model with the NH constitutive law in Figure 4.11, and with the BK constitutive law in Figure 4.12. Analysing Figures 4.11-4.12 the same way as Figures 3.7-3.10, we see that the nonlinear model predicts that there are still nano-particle geometries with a porous silicon layer which cause a lower expanded volume than a nano-particle of the same capacity but without a porous silicon layer. The geometric parameters for

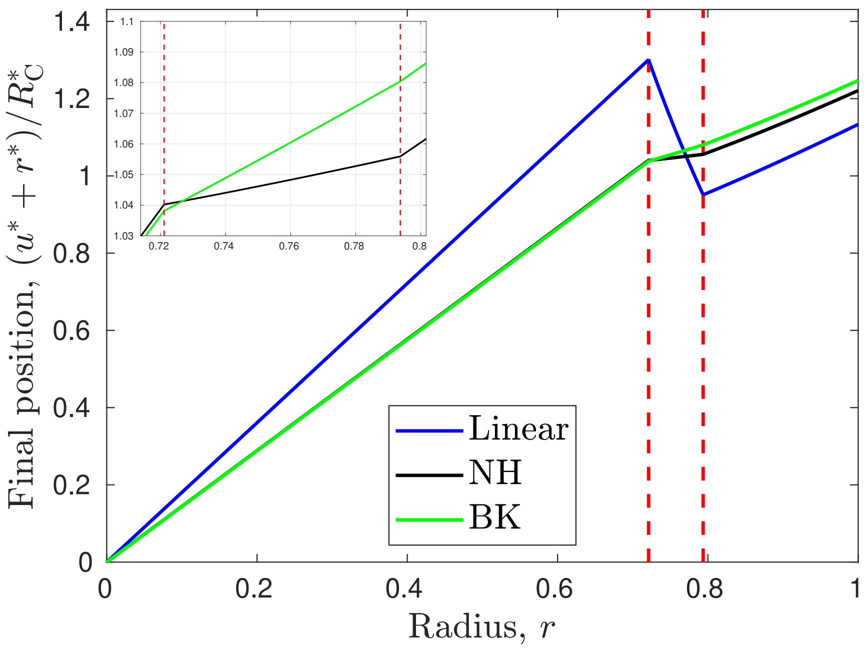

Figure 4.10: Final position $(u^*+r^*)/R_{\mathrm{C}}^*$ against initial position r, for the linear model and the nonlinear model using the NH and BK constitutive laws. Red dashed lines separate the different regions at $r = R_{\mathrm{Si}} = \sqrt[3]{0.375}$ and $r = R_\phi = \sqrt[3]{0.5}$. The porous layer has $\phi = 0.1$, and the inset plot shows the nonlinear results focussed on the porous silicon region, Ω_ϕ.

which this occurs are different for the two constitutive laws, showing that this result depends on the law used to describe each material.

We now demonstrate a case in which the nano-particle with a porous layer reduces the expansion according to the nonlinear model in Figure 4.13. We plot the displacement of a nano-particle with a silicon core, a porous silicon layer and a graphite shell alongside the displacement of a nano-particle with just a silicon core and graphite shell. We choose the geometric parameters, R_{Si}, R_ϕ and the radius of the non-porous core without a porous layer, $R_{\text{N-P}}$, such that both designs of nano-particles have the same maximum capacity, Q_1. This is achieved by rearranging (3.76) with $R_{\mathrm{Si}}^3 = V_{\mathrm{Si}:\phi} R_\phi^3$ and (3.78), yielding

$$R_\phi^3 = \frac{c_{\mathrm{Si}}^{\max} Q_1 - c_{\mathrm{C}}^{\max}}{c_{\mathrm{Si}}^{\max}(V_{\mathrm{Si}:\phi}(1-\phi)+\phi) - c_{\mathrm{C}}^{\max}}, \tag{4.62a}$$

$$R_{\text{N-P}}^3 = \frac{c_{\mathrm{Si}}^{\max} Q_1 - c_{\mathrm{C}}^{\max}}{c_{\mathrm{Si}}^{\max} - c_{\mathrm{C}}^{\max}}, \tag{4.62b}$$

respectively, where $V_{\mathrm{Si}:\phi}$ is the ratio between R_{Si}^3 to R_ϕ^3. In Figure 4.13, we choose $Q_1 = 0.2$, $\phi = 0.1$ and $V_{\mathrm{Si}:\phi} = 0.5$. We see that the displacement for the nano-particle

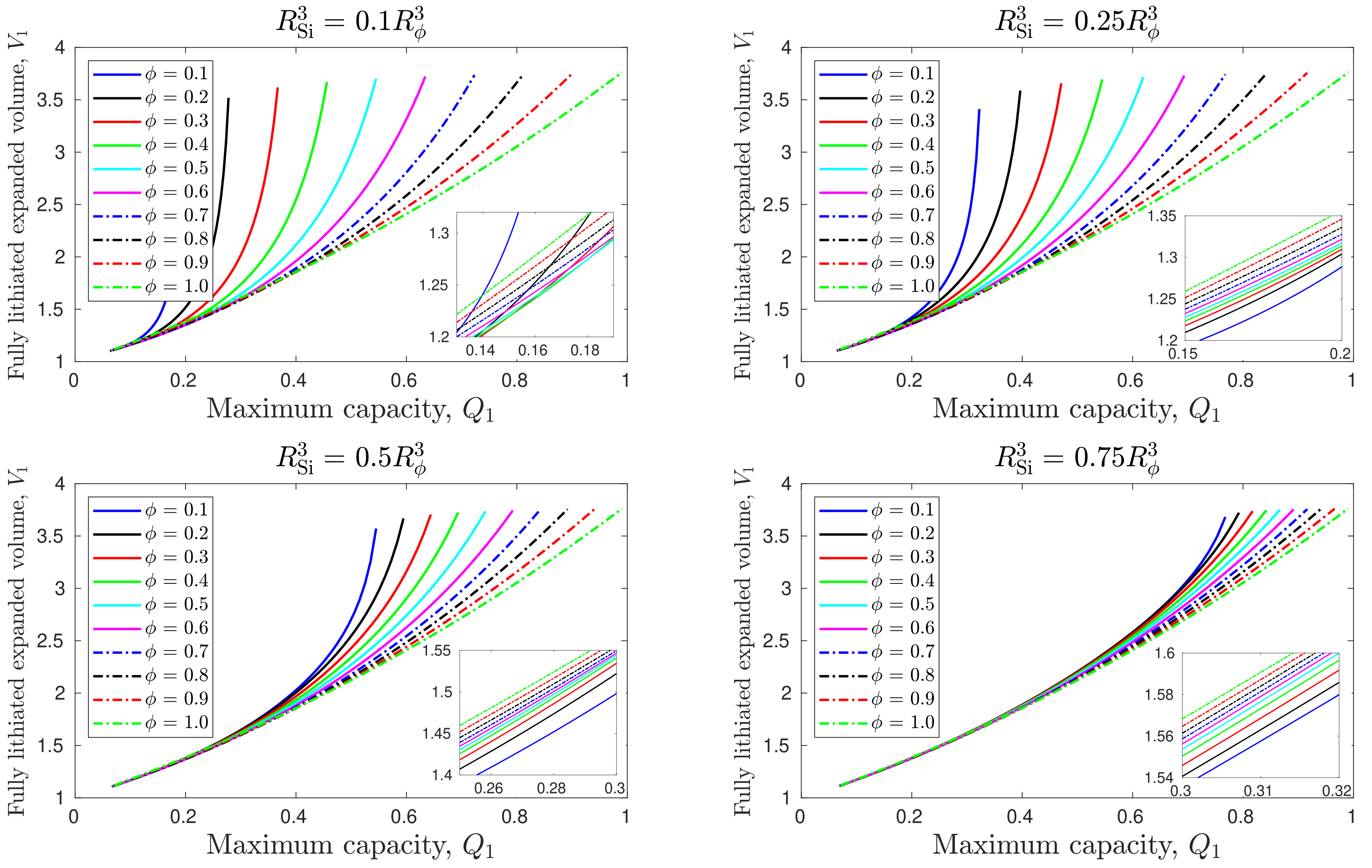

Figure 4.11: Fully lithiated expanded volume, V_1, against maximum capacity, Q_1, for the nano-particle design shown in Figure 3.9 using the nonlinear model with the NH constitutive law. In each subfigure, the ratio of R_{Si} to R_ϕ is fixed and the maximum capacity is varied by increasing the initial outer radius of the porous silicon layer (and thus the initial volume of the silicon core). This is plotted for several volume fractions of silicon in the porous silicon layer, ϕ. The inset plots show the regions in which a porous layer reduces the expanded volume.

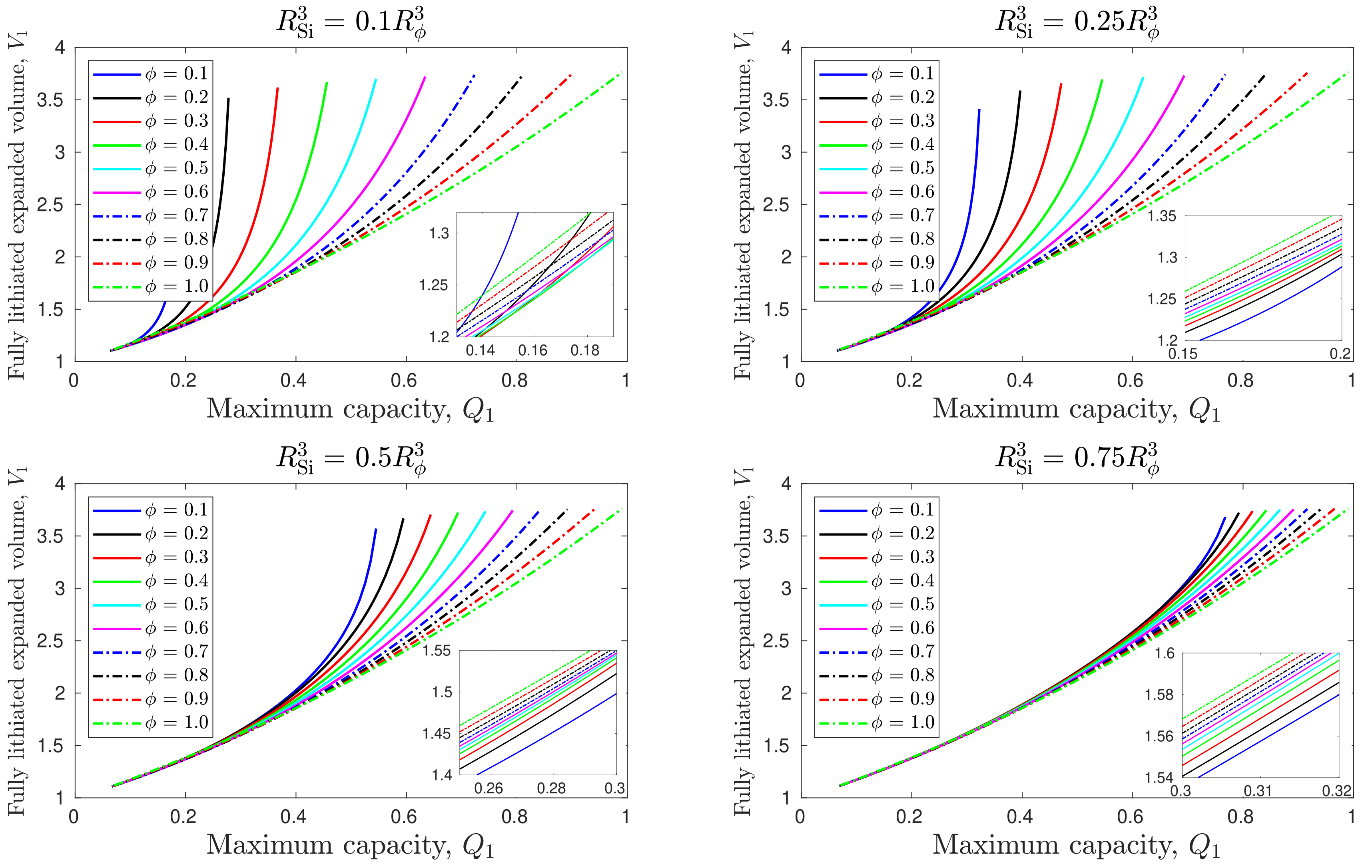

Figure 4.12: Fully lithiated expanded volume, V_1, against maximum capacity, Q_1, for the nano-particle design shown in Figure 3.9 using the nonlinear model with the BK constitutive law. In each subfigure, the ratio of R_{Si} to R_ϕ is fixed and the maximum capacity is varied by increasing the initial outer radius of the porous silicon layer (and thus the initial volume of the silicon core). This is plotted for several volume fractions of silicon in the porous silicon layer, ϕ. The inset plots show the regions in which a porous layer reduces the expanded volume.

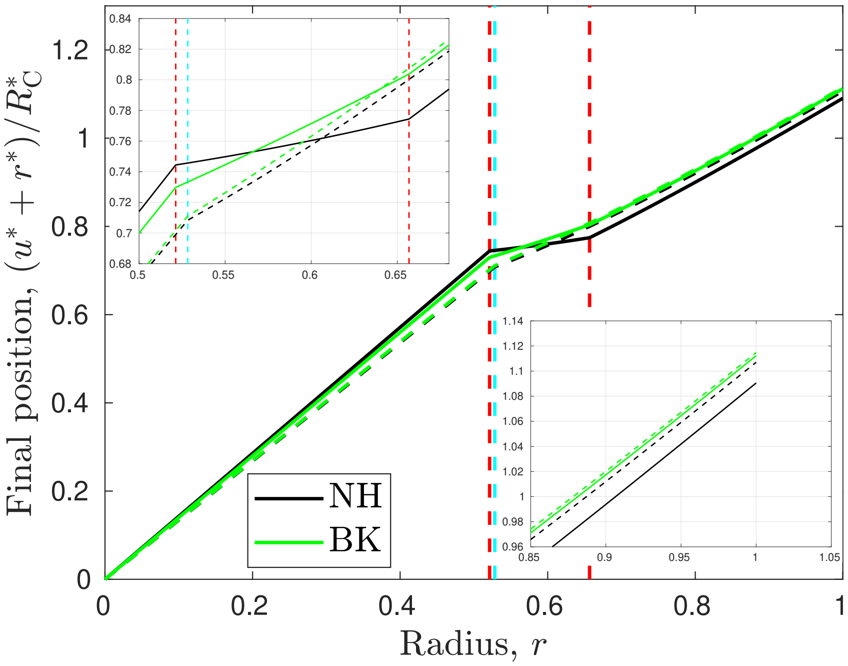

Figure 4.13: Final position $(u^* + r^*)/R^*_\mathrm{C}$ against initial position r, for the nonlinear model using the NH and BK constitutive laws. Solid green and black lines show the final position of each material point in the nano-particle with the porous layer and red dashed lines separate the different regions at $r = R_\mathrm{Si} = \sqrt[3]{0.5}R_\phi$ and $r = R_\phi$. The porous layer has $\phi = 0.1$. Dashed green and black lines show the final position of each material point in the nano-particle without the porous layer and the cyan dashed line separates the silicon and graphite at $r = R_\text{N-P}$. The upper-left inset plot focusses around R_Si, R_ϕ and $R_\text{N-P}$, and the lower-right inset plot focusses on $r = 1$.

with the porous layer at $r = 1$ is less than that for the nano-particle without for the solution of both the NH and BK constitutive laws in the lower-right inset plot of Figure 4.13. This is without overlap, as seen in the upper-left inset plot of Figure 4.13. Therefore, this nonlinear elastic model predicts the nano-particles with a porous layer can reduce the expansion of the nano-particle with the same capacity but no porous layer.

4.6 Conclusions

This chapter has been motivated by the unphysical results obtained when using the linear model from Chapter 2 to model a porous silicon layer within the nano-particle. We presented a model using geometric nonlinear elasticity, a linear constitutive law but neglecting stress-assisted diffusion, plasticity, cracking, and delamination. We then applied this model to the nano-particle of a silicon core and graphite shell, showing that this model does not have solutions for lithiation states above a certain value. This is due to the linear constitutive law not penalising the high compression that occurs at the interface between the silicon and the graphite. We confirmed this by using two nonlinear constitutive laws which included penalisation of high compression due to the terms dependent on the determinant of the elastic deformation gradient, $\mathbf{F}^e$. We then produced solutions for all lithiation states using these nonlinear constitutive laws and solved the model for a nano-particle geometry with a porous silicon layer between the core and the shell. The results do not exhibit the unphysical overlap observed in Figure 3.11 or the non-existence of solutions seen for the linear constitutive law.

While this confirmed our concerns about the linear model in Chapter 2, it is not clear that it is appropriate to model silicon and graphite using nonlinear constitutive laws. There may be other physical processes that need to be considered in practice. We conclude the chapter by showing that yielding mechanisms will come into effect before the nonlinearity of the stress-strain relationship becomes significant, motivating the next chapter. To do this, we critically consider the solution to the nonlinear elasticity model for a silicon core of radius $R_{\mathrm{Si}} = 0.5$, using the NH constitutive law for $c_0 = 0.1, 0.2, \dots, 1$.

The nonlinearity in the stress-strain relationship becomes non-negligible when large elastic strains occur. In Figure 4.14, we plot the elastic strains in the radial and hoop directions, E^e_{rr} and $E_{\theta\theta}$, respectively, given by (4.10), against the radius, r, for different amounts of lithium, c_0. We can see that both elastic strains are uniform in the silicon region, Ω_{Si}, and $E^e_{rr} = E^e_{\theta\theta}$ reach a magnitude of around 13%. The elastic strain in the graphite region is caused by compression in the radial direction and tension in the hoop direction. The elastic strains are greatest at $r = R_{\mathrm{Si}}$ for the graphite region and decrease as r increases because the stretching caused by the expanding silicon decreases away from the silicon core. However, as observed for the maximum displacement at $r = R_{\mathrm{Si}}$ in section 4.5, the maximum elastic strain is observed at $c_0 = 0.7$, not $c_0 = 1.0$, and reaches a strain of around 38%. These strains are considered to be large and thus, if the materials did behave according to a nonlinear constitutive law, at these lithium concentrations, it would be important to include the nonlinearities in the model.

Other effects, known as yielding mechanisms, often take effect if materials are put under sufficient elastic strain. These effects include cracking and plasticity. One model of such yielding is to assume a material yields if an effective stress measure is

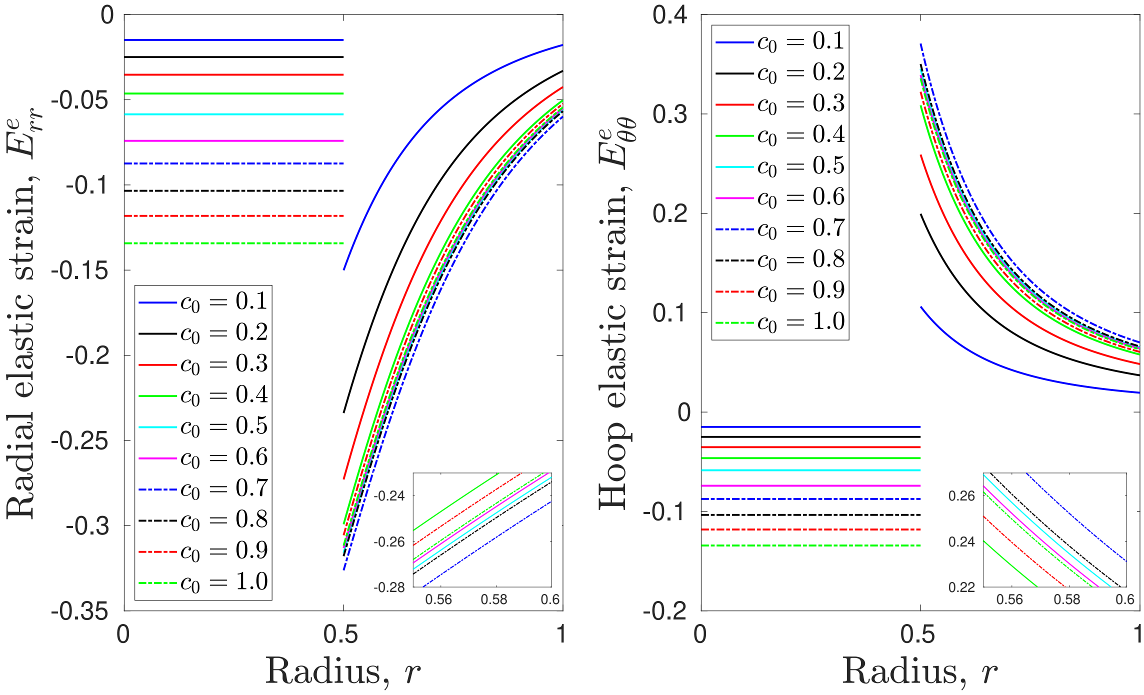

Figure 4.14: Elastic strains in radial (left) and hoop (right) directions against radius for different states of charge, c_0. Calculated using the NH constitutive law. Inset plots show the strains at high states of charge more clearly.

exceeded at a point in the material. At the points which the material has yielded, it stops behaving elastically and other physical effects occur instead. The von Mises yield function, which we denote by $f^{\mathrm{VM}}(\boldsymbol{\sigma})$, is an effective stress measure often used to determine whether a material has yielded [48]. It is calculated for a material in simple tension by

$$f^{\mathrm{VM}}(\boldsymbol{\sigma}) = \left(\frac{(\sigma_{11}-\sigma_{22})^2 + (\sigma_{22}-\sigma_{33})^2 + (\sigma_{33}-\sigma_{11})^2 + 6(\sigma_{12}^2+\sigma_{23}^2+\sigma_{31}^2)}{2}\right)^{\frac{1}{2}}, \tag{4.63}$$

where σ_{ij} is the Cauchy stress. While $f^{\mathrm{VM}}(\boldsymbol{\sigma})$ is less than some yield stress, which is obtained from experiments, the material behaves elastically; if the Cauchy stress is such that $f^{\mathrm{VM}}(\boldsymbol{\sigma})$ exceeds the yield stress, the material is said to have yielded at that point. The von Mises function (4.63) can be written for the radially-symmetric nano-particle as

$$f^{\mathrm{VM}}(\sigma_{rr}, \sigma_{\theta\theta}) = |\sigma_{rr} - \sigma_{\theta\theta}|. \tag{4.64}$$

In Figure 4.15, we plot $f^{\mathrm{VM}}(\sigma_{rr}, \sigma_{\theta\theta})$, calculated using the Cauchy stress from the nonlinear elastic model with the NH constitutive law, against the radial position

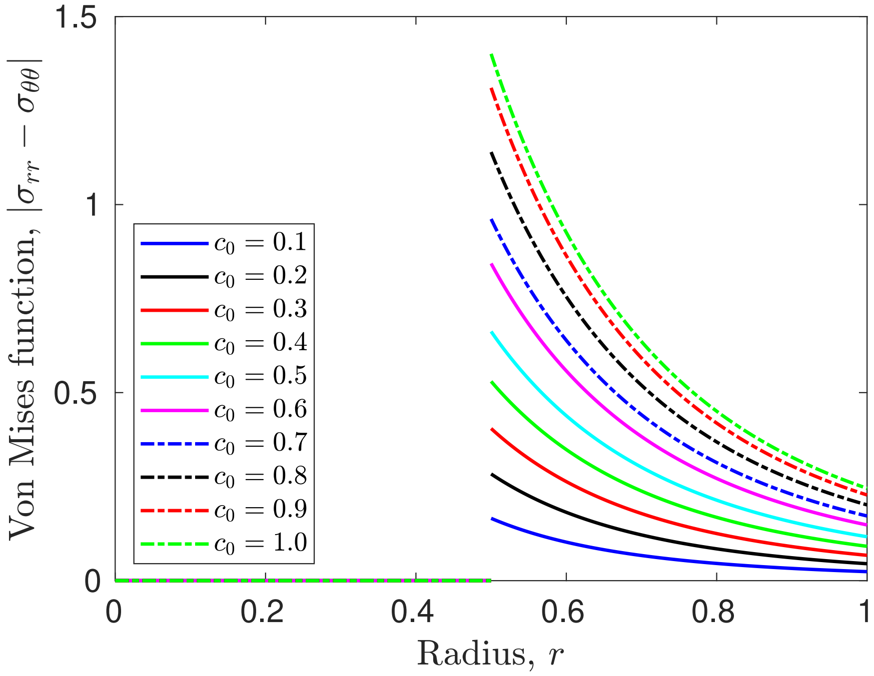

Figure 4.15: Von Mises function against radius. It can be seen the von Mises function is zero in the entire silicon region.

in the core–shell nano-particle with $R_{\text{Si}} = 0.5$. It can be seen that f^{VM} is zero in the silicon region, as $\sigma_{rr} = \sigma_{\theta\theta}$. This can be explained by the linear displacement, $u = Ar$, giving constant elastic deformation gradients $\mathbf{F}^e$, according to (4.9). The components of the Cauchy stress, σ_{rr} and $\sigma_{\theta\theta}$, are given as functions of F^e_{rr}, $F^e_{\theta\theta}$ and gradients of F^e_{rr} and $F^e_{\theta\theta}$. Therefore, the stress in the silicon core is independent of r. In the graphite region, however, f^{VM} is non-zero, as u is nonlinear. The von Mises yield function is greatest at the interface $r = R_{\text{Si}}$ and decreases as r increases.

Lastly, we wish to see whether the elastic strains, E^e_{rr} and $E_{\theta\theta}$, become large enough such that nonlinearities cannot be neglected before the materials have mechanically yielded. In Figure 4.16, we plot the maximum radial and hoop elastic strains for the silicon and the graphite against $c_0 \in [0.001, 0.05]$ using the blue axes. We plot the maximum of f^{VM}, which is in the graphite at $r = R_{\text{Si}}$, against c_0 alongside elastic strains, using the red axes. As the von Mises yield function is zero for all $r \in [0, R_{\text{Si}}]$, we focus on the graphite yielding, plotting $f^{\text{VM}}(\boldsymbol{\sigma})$ in the graphite region, $\sigma^{\text{VM}}_{\text{C}}(R_{\text{Si}})$, as the solid red line. As graphite is a ceramic, it is not expected to plastically deform when yielding but instead cracks when the effective stress exceeds the tensile strength of the graphite. The tensile strength of graphite, σ^Y_{C}, is on the order of 10 MPa and is plotted in Figure 4.16 using a dashed red line at $\sigma^Y_{\text{C}} = 11.7$

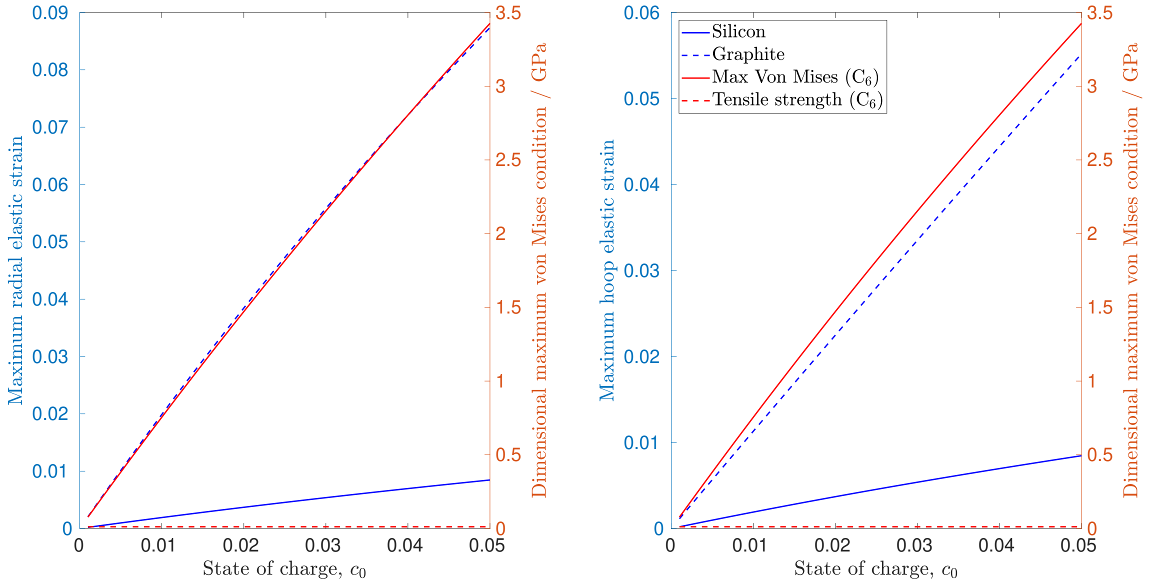

Figure 4.16: Blue axes: maximum elastic strains in both radial (left) and hoop (right) directions for both silicon (solid line) and graphite (dashed line) against SOC ($c_0 < 0.05$). Red axis: maximum value of the von Mises function in the graphite shell (at $r = R_{\text{Si}}$). The tensile strength of graphite is also plotted as the dashed red line at the bottom of each subfigure.

MPa, the value of which is taken from [70]. It is clear that stresses in the graphite at $r = R_{\text{Si}}$ will exceed the yield function of graphite for any reasonable SOC. At these low states of charge, the elastic strains are less than 0.5%, showing that the nonlinearities in the stress-strain relationship will be negligible.

The observations suggest that graphite does not need to be modelled using a nonlinear constitutive law as the stresses caused by the silicon will cause it to crack before the nonlinearities become significant. Instead, cracking should be incorporated into the model once the stresses become sufficiently high. Therefore, the geometrically nonlinear but constitutively linear model is not necessarily an inaccurate way to model the mechanics of the anode materials although solutions cease to exist at high states of charge. We expect that before the solution ceases to exist, the graphite will most likely have yielded at a lower c_0 value. A different model is needed to account for yielding which will lead to changes in the stress distribution and displacement profile from those predicted by the elastic model.

As seen in Figure 4.15, the von Mises function in the silicon is zero because the radial and hoop stresses are equal due to the displacement being linear with respect to the radius in this region. Therefore, for geometries with a silicon core, such that there is no central void, the silicon never yields and can be solely modelled elastically. However, if central voids are incorporated into the nano-particle design, deviatoric stresses will be induced into the silicon. If the deviatoric stresses cause the yield function of the silicon to be exceeded, it will begin to act plastically. In the next chapter, we incorporate both the yielding of silicon and graphite into the linear elasticity model in Chapter 2.

Chapter 5

Yielding Mechanisms

In Chapter 4, we found that the elastic models predict that the stress induced in the graphite shell of a silicon and graphite core–shell nano-particle exceeds the tensile strength even at low states of charge. The graphite shell will therefore yield at low states of charge and crack. In this chapter, we incorporate the cracking behaviour of the graphite shell into the quasi-static linear chemo-mechanical model from Chapter 2. This model retains the assumptions from Chapter 2 that $\eta_a x_a^{\max} \ll 1$, that the Young's modulus of each material is linearly dependent on their respective lithium concentrations and that the nano-particle is at its equilibrium state. These assumptions allow us to make a lot of analytical progress with this yielding model and obtain insight into how the geometry of the nano-particle affects the mechanical failure of the materials.

Cracking of materials is often modelled using stress intensity factors (SIFs) which characterise how likely it is that existing cracks will grow [48]. This model has been applied to single-material cylindrical anode particles [32, 120] and spherical nano-particles [15, 95, 118] based on a phase-field model for lithiation. Instead, here we model the cracking of graphite by supposing it cracks at a point where a yield condition, for example the von Mises condition in (4.63), exceeds some yield stress of graphite, σ_{C}^{Y}. After the graphite has cracked, we model it as 'pulverised' graphite which can only withstand some maximum deviatoric stress, denoted by $\sigma_p^{\max}$. This model is very similar to an elastic–perfect plastic model when $\sigma_p^{\max} = \sigma_{\mathrm{C}}^{Y}$. However, we present the model for a general $\sigma_p^{\max}$ and also briefly consider the special case, $\sigma_p^{\max} = 0$, when the pulverised graphite has no shear strength. For simplicity here, we only consider the effect of the first lithiation of the nano-particle, and do not consider the effects to the pulverised graphite during delithiation or subsequent cycles.

We first investigate, using the previous linear elastic model of the silicon and graphite, how the state of charge (SOC) at which the graphite first cracks is related to the initial volume of the silicon core in the nano-particle design depicted in Figure 2.1. We then model the nano-particle at higher SOC values using the maximum deviatoric stress condition for the pulverised graphite while modelling the silicon and unyielded graphite as linearly elastic. Using this model, we calculate the size of the pulverised graphite region as a function of both the SOC and the initial silicon core volume. We then make several analytic approximations to the model to find analytic expressions which relate the size of the pulverised graphite region at full lithiation to the initial volume of the silicon core. Of particular interest is the maximum initial volume of the silicon core (and thus the maximum amount of lithium that can be intercalated) such that the graphite is not fully pulverised when the nano-particle is fully lithiated. If the pulverised graphite is contained within a layer of undamaged graphite, the elastic graphite can give the nano-particle some structural support. However, if the graphite at the surface of the nano-particle is pulverised, the nano-particle can begin to disintegrate and electrolyte can flow into the nano-particle, causing the growth of SEI layers. Therefore, we aim to find the geometries of the nano-particle which avoid the graphite fully pulverising, and maximise the capacity subject to this constraint.

We then consider a nano-particle consisting of a spherical void in the centre with a surrounding silicon layer, as in Figure 3.1. As the von Mises stress in the silicon is now non-zero, we incorporate the possibility of the silicon yielding, and model the yielded silicon as perfectly plastic. We also only model this for the initial lithiation of the nano-particle, not considering the plastic flow during delithiation. We define different regimes of the nano-particle according to which materials have yielded and whether they have fully yielded or not. We then find how the thickness of the silicon layer and the radius of the central void affects which regimes the nano-particle will be in during a single charge. Lastly, we use this model to find whether including a central void allows the fully-lithiated nano-particle to have a greater capacity before the graphite fully pulverises.

5.1 Yield Condition

We begin by defining the criterion we use to determine where each material has yielded. As in Section 4.6, we use the von Mises yield function, $f^{\mathrm{VM}}(\boldsymbol{\sigma})$, defined in (4.63). We describe the material as yielded at a point $\mathbf{x}$ if $f^{\mathrm{VM}}\big(\boldsymbol{\sigma}(\mathbf{x})\big) \geq \sigma_a^Y$, where σ_a^Y is the yield stress of material a.

All geometries in this chapter are radially symmetric and thus we can write the von Mises function in radially-symmetric spherical coordinates, given by (4.64). Before the materials yield, we consider them to be linearly elastic, isotropic solids. We have solved the linear elasticity problem for a general spherical radially-symmetric geometry in Section 2.3 and the expressions for σ_{rr} and $\sigma_{\theta\theta}$ in each material are given in (2.56a) and (2.56b). The radially-symmetric yield condition is therefore given by

$$f^{\mathrm{VM}}(\sigma_{rr}, \sigma_{\theta\theta}) = \frac{6G_a|B_a|}{r^3}, \tag{5.1}$$

where B_a is the integration constant for the r^{-2} term in the displacement solution (2.55) and G_a is the shear modulus of the material a.

5.2 Core–Shell Geometry

We first consider the geometry in Figure 2.1 of a spherical nano-particle with a silicon core and a graphite shell. We have solved the linear elasticity problem in this geometry in Section 2.3, giving the integration constants (2.71) for the general solution (2.55). For this geometry, $B_{\mathrm{Si}} = 0$ as the displacement is zero at $r = 0$. Therefore, the von Mises yield condition is zero for the silicon at all states of charge. The expression for B_{C} in (2.71c) is given by

$$B_{\mathrm{C}} = \frac{\Lambda_{\mathrm{Si}}\Lambda_{\mathrm{C}}(\gamma_{\mathrm{Si}}c_{\mathrm{Si}} - \gamma_{\mathrm{C}}c_{\mathrm{C}})R_{\mathrm{Si}}^3}{\Lambda_{\mathrm{Si}}\Lambda_C + 4G_{\mathrm{C}}\big(\Lambda_{\mathrm{C}}(1 - R_{\mathrm{Si}}^3) + \Lambda_{\mathrm{Si}}R_{\mathrm{Si}}^3\big)}, \tag{5.2}$$

where $\Lambda_a = 3\lambda_a + 2G_a$ for $a = \mathrm{Si}, \mathrm{C}$. As the Lamé parameters are all greater than zero and $R_{\mathrm{Si}} < 1$, we can calculate the von Mises yield function (5.1) for the graphite as

$$f^{\mathrm{VM}}(\sigma_{rr}, \sigma_{\theta\theta}) = \frac{6G_{\mathrm{C}}\Lambda_{\mathrm{Si}}\Lambda_{\mathrm{C}}|\gamma_{\mathrm{Si}}c_{\mathrm{Si}} - \gamma_{\mathrm{C}}c_{\mathrm{C}}|R_{\mathrm{Si}}^3}{\big[\Lambda_{\mathrm{Si}}\Lambda_{\mathrm{C}} + 4G_{\mathrm{C}}\big(\Lambda_{\mathrm{C}}(1 - R_{\mathrm{Si}}^3) + \Lambda_{\mathrm{Si}}R_{\mathrm{Si}}^3\big)\big]r^3}. \tag{5.3}$$

5.2.1 The SOC at which Graphite Cracks

We first investigate the SOC at which the graphite cracks for this geometry, as a function of the initial volume of the silicon core, V_{Si}. We start by finding the SOC, c_0, for which $f^{\mathrm{VM}}(\sigma_{rr}, \sigma_{\theta\theta}) = \sigma_{\mathrm{C}}^Y$, where σ_{C}^Y is the yield stress of graphite. We choose the tensile strength as the yield stress of graphite because the graphite shell is in tension, as seen by the positive $\mathrm{tr}(\boldsymbol{\sigma})$ in Figure 2.4. We take the dimensional value of the tensile stress, $\sigma_{\mathrm{C}}^{Y,*}$, from [70] giving $\sigma_{\mathrm{C}}^{Y,*} = 1.17 \times 10^{-2}$ GPa. This is then nondimensionalised by the same value as the Cauchy stress in (2.19), giving

$$\sigma_{\mathrm{C}}^{Y,*} = G_1^*(0)\eta_1 V_1^m c_1^{\max}\sigma_{\mathrm{C}}^Y, \tag{5.4}$$

so that $\sigma_{\mathrm{C}}^Y = 3.369 \times 10^{-4}$.

It can be seen from (5.3) that $f^{\mathrm{VM}}(\sigma_{rr}, \sigma_{\theta\theta})$ will be greatest in the graphite at the smallest value of r, i.e. $r = R_{\mathrm{Si}}$. Therefore, the graphite first cracks when the SOC is such that

$$|\gamma_{\mathrm{Si}} c_{\mathrm{Si}} - \gamma_{\mathrm{C}} c_{\mathrm{C}}| = \frac{\sigma_{\mathrm{C}}^{Y}\left[\Lambda_{\mathrm{Si}}\Lambda_{\mathrm{C}} + 4G_{\mathrm{C}}\big(\Lambda_{\mathrm{C}}(1 - R_{\mathrm{Si}}^3) + \Lambda_{\mathrm{Si}} R_{\mathrm{Si}}^3\big)\right]}{6G_{\mathrm{C}}\Lambda_{\mathrm{Si}}\Lambda_{\mathrm{C}}}, \tag{5.5}$$

which can be simplified to give

$$|\gamma_{\mathrm{Si}} c_{\mathrm{Si}} - \gamma_{\mathrm{C}} c_{\mathrm{C}}| = \frac{\sigma_{\mathrm{C}}^{Y}}{6}\left[\frac{1}{G_{\mathrm{C}}} + \frac{4(1 - R_{\mathrm{Si}}^3)}{\Lambda_{\mathrm{Si}}} + \frac{4R_{\mathrm{Si}}^3}{\Lambda_{\mathrm{C}}}\right]. \tag{5.6}$$

We denote the SOC at which the graphite first cracks at $r = R_{\mathrm{Si}}$ as c_0^{crack}.

We plot c_0^{crack} against the initial volume of the silicon core, $V_{\mathrm{Si}} \in [0.01, 0.99]$, in Figure 5.1. We can see that the c_0^{crack} is very low, around 1×10^{-4}. This is due to the tensile stress of graphite, 1.17×10^{-2} GPa, being very small compared to the magnitude of the stresses induced in the graphite by the silicon, around 30 GPa, as seen in Figures 2.9 and 2.10. For small values of V_{Si}, c_0^{crack} increases rapidly with V_{Si} but plateaus for larger V_{Si} values. This increase of c_0^{crack} with V_{Si} is because $f^{\mathrm{VM}}(R_{\mathrm{Si}})$ decreases with V_{Si} for small states of charge, as seen in Figure 5.2. This is in contrast to higher states of charge shown in Figure 2.13 where the yield function increases

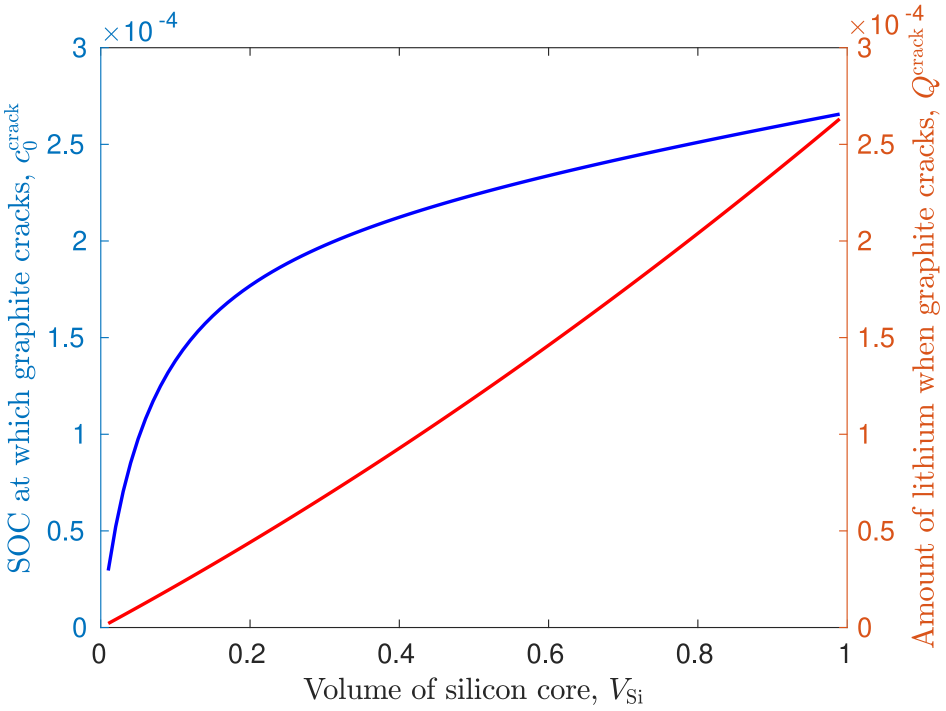

Figure 5.1: SOC, c_0^{crack} and amount of intercalated lithium, Q^{crack}, when the graphite shell first cracks against the initial volume of the silicon core, V_{Si}.

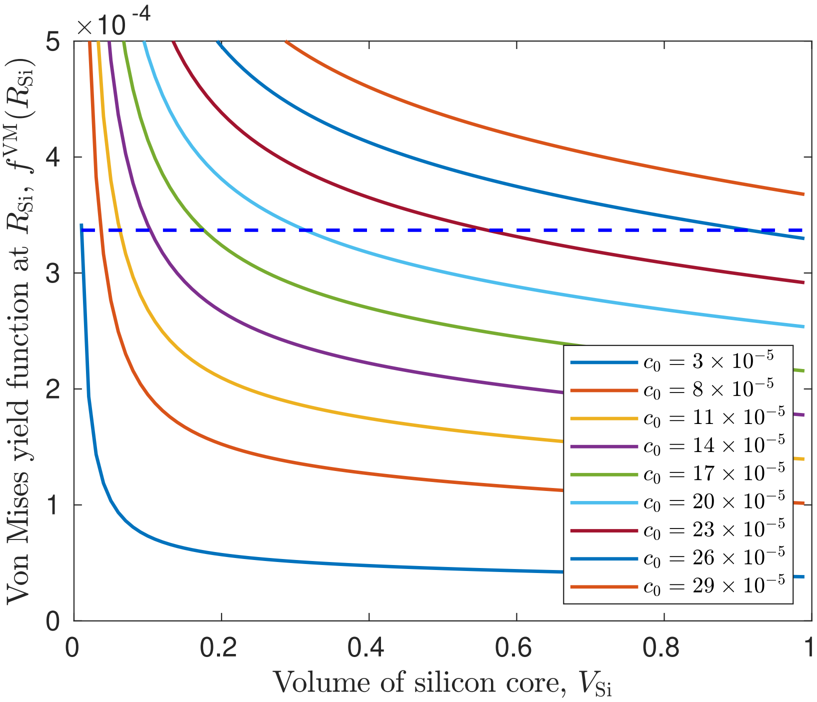

Figure 5.2: Yield function, $f^{\rm VM}$, in the graphite shell, given by (5.3), at $r = R_{\rm Si}$, against the initial volume of the silicon core, $V_{\rm Si}$, for low states of charge. The non-dimensional yield stress for graphite, $\sigma_{\rm C}^Y$, is also plotted using a horizontal blue dashed line.

with $V_{\rm Si}$ for $c_0 = 0.1, \ldots, 1.0$. We also plot the relative amount of lithium that is intercalated into the nano-particle at $c_0 = c_0^{\rm max}$, denoted by $Q^{\rm crack}$. This is calculated using the $c_{\rm Si}$ and $c_{\rm C}$ values at $c_0^{\rm crack}$ and substituting these into (2.81). The relationship between $Q^{\rm crack}$ and $V_{\rm Si}$ is close to linear.

At such low states of charge, all the lithium is lithiated into the silicon so that $c_{\rm C} = 0$. We can write analytical expressions for $c_{\rm Si}$ at $c_0 = c_0^{\rm crack}$, which we denote as $c_{\rm Si}^{\rm crack}$, by substituting $c_{\rm C} = 0$ into (5.6), to see that $c_{\rm Si}^{\rm crack}$ is linear in $V_{\rm Si} = R_{\rm Si}^3$, given by

$$c_{\rm Si}^{\rm crack} = \frac{\sigma_{\rm C}^Y}{6\gamma_{\rm Si}}\left[\frac{1}{G_{\rm C}} + \frac{4(1-V_{\rm Si})}{\Lambda_{\rm Si}} + \frac{4V_{\rm Si}}{\Lambda_{\rm C}}\right]. \tag{5.7}$$

We can then substitute this relationship into (2.68) to find $c_0^{\rm crack}$ is given as

$$c_0^{\rm crack} = \frac{\sigma_{\rm C}^Y c_{\rm Si}^{\rm max} V_{\rm Si}}{6\gamma_{\rm Si}\left(c_{\rm Si}^{\rm max}V_{\rm Si} + c_{\rm C}^{\rm max}(1-V_{\rm Si})\right)}\left[\frac{1}{G_{\rm C}} + \frac{4(1-V_{\rm Si})}{\Lambda_{\rm Si}} + \frac{4V_{\rm Si}}{\Lambda_{\rm C}}\right]. \tag{5.8}$$

Finally, we can write an expression for $Q^{\rm crack}$ by substituting (5.7) and $c_{\rm C} = 0$ into (2.81), yielding

$$Q^{\rm crack} = \frac{\sigma_{\rm C}^Y}{6\gamma_{\rm Si}}\left[\frac{1}{G_{\rm C}} + \frac{4(1-V_{\rm Si})}{\Lambda_{\rm Si}} + \frac{4V_{\rm Si}}{\Lambda_{\rm C}}\right]V_{\rm Si}. \tag{5.9}$$

5.2.2 Post-cracking Model

We now model the expansion and lithium distribution after the graphite yields. We assume that for all $c_0 > c_0^{\text{crack}}$, there is a region of the graphite shell which is pulverised, where the yield condition, $f^{\text{VM}}(\sigma_{rr}, \sigma_{\theta\theta})$, has reached the yield stress, σ_{C}^{Y}, and cracked, changing its mechanical behaviour. We model the pulverised graphite by supposing that it can only hold a maximum deviatoric stress, $\sigma_p^{\max}$. In this section, we present the model for the nano-particle with a layer of pulverised graphite and derive the equations that need to be solved to find the displacement, stresses and lithium concentration in each region.

5.2.2.1 Geometry

Using the results of Section 5.2.1, the graphite initially cracks at $r = R_{\text{Si}}$. Therefore, once the graphite has initially pulverised, we assume we have three distinct regions. The silicon region is defined by $\Omega_{\text{Si}} = \{r : 0 < r \leq R_{\text{Si}}\}$, the pulverised graphite region by $\Omega_{\text{C}}^{p} = \{r : R_{\text{Si}} < r \leq s_{\text{C}}(c_0)\}$ and the elastic graphite region by $\Omega_{\text{C}}^{e} = \{r : s_{\text{C}}(c_0) < r \leq 1\}$, where r is the radial position nondimensionalised by the outer radius of the nano-particle and s_{C} is the outer radius of the pulverised region, known as the position of the pulverised front. We also denote the entire graphite region as $\Omega_{\text{C}} = \Omega_{\text{C}}^{e} \cup \Omega_{\text{C}}^{p}$. A schematic of a two-dimensional slice of this geometry is shown in Figure 5.3. The position of the pulverised front, s_{C}, is dependent on the SOC, c_0, because the stress in the elastic graphite will increase as the SOC increases, causing more of the graphite to exceed the yield criterion, increasing the amount of pulverised graphite.

5.2.2.2 Governing Mechanical Equations

The governing equation for the entire nano-particle is given by the mechanical equilibrium equation

$$\frac{\mathrm{d}\sigma_{rr}}{\mathrm{d}r} + \frac{2(\sigma_{rr} - \sigma_{\theta\theta})}{r} = 0 \qquad \text{in } \Omega. \tag{5.10}$$

The silicon behaves elastically for all SOC values in this geometry because it never exceeds the yield criterion. The graphite that has not yielded will also behave elastically. For the elastic regions, this results in the general solution for the displacement given by (2.65), and the stresses given by (2.66).

For the pulverised graphite, we prescribe the maximum deviatoric stress that the material can accommodate. The deviatoric stress $\boldsymbol{\sigma}'$ is given by

$$\sigma'_{ij} = \sigma_{ij} - \frac{1}{3}\delta_{ij}\sigma_{kk} \quad \text{in } \Omega. \tag{5.11}$$

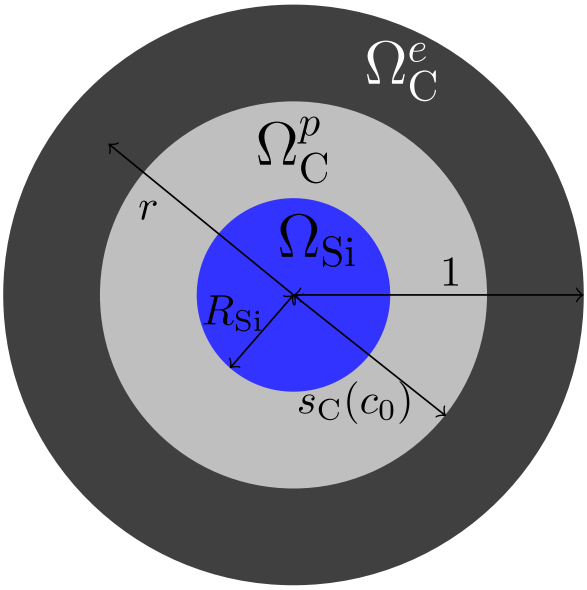

Figure 5.3: Schematic of a slice through a nano-particle consisting of a silicon core of radius R_{Si} and a graphite shell with outer radius 1. The graphite has been pulverised up to a radius, s_{C}, which depends on the SOC, c_0. The elastic graphite region is denoted by Ω_{C}^{e}, the region of pulverised graphite is denoted by Ω_{C}^{p} and the silicon region is denoted by Ω_{Si}.

In radially-symmetric spherical coordinates, we have $\boldsymbol{\sigma} = \mathrm{diag}(\sigma_{rr}, \sigma_{\theta\theta}, \sigma_{\theta\theta})$ so σ' is given by

$$\boldsymbol{\sigma}' = \frac{1}{3}(\sigma_{rr} - \sigma_{\theta\theta})\mathrm{diag}[2, -1, -1] \quad \text{in } \Omega. \tag{5.12}$$

The magnitude of $\boldsymbol{\sigma}'$ is dictated by the magnitude of $\sigma_{rr} - \sigma_{\theta\theta}$. We prescribe a maximum deviatoric stress, $\sigma_p^{\max}$, that the pulverised graphite can accommodate, giving

$$|\sigma_{rr} - \sigma_{\theta\theta}| \leq \sigma_p^{\max} \quad \text{in } \Omega_{\mathrm{C}}^{p}. \tag{5.13}$$

We only consider the first lithiation of the nano-particle, and we know that $\sigma_{rr} < 0$ and $\sigma_{\theta\theta} > 0$ in the graphite during lithiation due to the large expansion of the silicon core. In this case, we expect the graphite to experience stress such that $\sigma_{rr} - \sigma_{\theta\theta} < 0$. Therefore, we choose to write

$$\sigma_{rr} - \sigma_{\theta\theta} \geq -\sigma_p^{\max} \quad \text{in } \Omega_{\mathrm{C}}^{p}. \tag{5.14}$$

During delithiation, we might expect $\sigma_{rr} - \sigma_{\theta\theta} > 0$, in which we would change (5.14) to be $\sigma_{rr} - \sigma_{\theta\theta} \leq \sigma_p^{\max}$, assuming the graphite can accommodate the same magnitude of deviatoric stress in each direction. Furthermore, as we are considering the first lithiation, and the graphite is elastic before being pulverised, we expect that the deviatoric stress in the pulverised graphite is equal to this maximum, $\sigma_p^{\max}$, as long as $\sigma_p^{\max} \leq \sigma_{\mathrm{C}}^{Y}$. If $\sigma_p^{\max} > \sigma_{\mathrm{C}}^{Y}$, it is unclear whether the resulting problem from this model will be well-posed. In this thesis, we only consider cases such that $\sigma_p^{\max} \leq \sigma_{\mathrm{C}}^{Y}$. Therefore, we take the deviatoric stress in the pulverised graphite to be governed by

$$\sigma_{rr} - \sigma_{\theta\theta} = -\sigma_p^{\max} \quad \text{in } \Omega_{\mathrm{C}}^{p}. \tag{5.15}$$

From these assumptions, it is clear here how the model is similar to a perfectly plastic model in the case of $\sigma_p^{\max} = \sigma_{\mathrm{C}}^{Y}$.

Substituting (5.15) into the governing equation (5.10) yields

$$\frac{\mathrm{d}\sigma_{rr}}{\mathrm{d}r} = \frac{2\sigma_p^{\max}}{r} \quad \text{in } \Omega_{\mathrm{C}}^{p}, \tag{5.16}$$

which can be integrated to give

$$\sigma_{rr} = C_{\mathrm{C}} + 2\sigma_p^{\max}\log(r) \quad \text{in } \Omega_{\mathrm{C}}^{p}, \tag{5.17}$$

where C_{C} is an integration constant. This is substituted into (5.15) to give

$$\sigma_{\theta\theta} = C_{\mathrm{C}} + 2\sigma_p^{\max}\log(r) + \sigma_p^{\max} \quad \text{in } \Omega_{\mathrm{C}}^{p}. \tag{5.18}$$

5.2.2.3 Concentration in Each Region

The lithium concentration in each region, c_a, is determined by the chemical potential, μ, being uniform throughout the nano-particle. The nondimensional chemical potential is given by

$$\mu = \mu_a^{\mathrm{SF}}(c_a) - S_a^{d}\mathrm{tr}(\boldsymbol{\sigma}) \quad \text{in } \Omega_a, \quad a = \mathrm{Si}, \mathrm{C}, \tag{5.19}$$

where

$$S_a^{d} = \frac{\eta_a \eta_{\mathrm{Si}} V_a^{m} V_{\mathrm{Si}}^{m} c_{\mathrm{Si}}^{\max} G_{\mathrm{Si}}^{*}(0)}{R_g T}. \tag{5.20}$$

We assume that the molar volume, V_a^m, the maximum lithium concentration, $c_a^{\max}$, the coefficient of compositional expansion, η_a and the stress-free chemical potential, μ_a^{SF}, are the same in the pulverised graphite and the elastic graphite. Using (2.67) and (5.17)-(5.18) the chemical potential is given by

$$\mu = \mu_{\mathrm{Si}}^{\mathrm{SF}}(c_{\mathrm{Si}}) - 3S_{\mathrm{Si}}^{d}\Lambda_{\mathrm{Si}}(A_{\mathrm{Si}} - \gamma_{\mathrm{Si}}c_{\mathrm{Si}}) \quad \text{in } \Omega_{\mathrm{Si}}, \tag{5.21a}$$

$$\mu = \mu_{\mathrm{C}}^{\mathrm{SF}}\big(c_{\mathrm{C}}^{p}(r)\big) - S_{\mathrm{C}}^{d}\big[3C_{\mathrm{C}} + 6\sigma_p^{\max}\log(r) + 2\sigma_p^{\max}\big] \quad \text{in } \Omega_{\mathrm{C}}^{p}, \tag{5.21b}$$

$$\mu = \mu_{\mathrm{C}}^{\mathrm{SF}}(c_{\mathrm{C}}) - 3S_{\mathrm{C}}^{d}\Lambda_{\mathrm{C}}(A_{\mathrm{C}} - \gamma_{\mathrm{C}}c_{\mathrm{C}}) \quad \text{in } \Omega_{\mathrm{C}}^{e}, \tag{5.21c}$$

where A_{Si} and A_{C} are the integration constants that arise in the displacement in the elastic regions (2.65). Here, c_{C}^{p} is the lithium concentration in the pulverised graphite which is a function of r due to the $\log(r)$ term in the trace of the stress.

5.2.2.4 Yielding Criterion

The graphite first cracks when the yield condition at $r = R_{\mathrm{Si}}$ is equal to the yield stress, σ_{C}^{Y}. This occurs when

$$(\sigma_{rr} - \sigma_{\theta\theta})^2 = (\sigma_{\mathrm{C}}^{Y})^2. \tag{5.22}$$

As $\sigma_{\mathrm{C}}^{Y} > 0$, we must determine the sign of $\sigma_{rr} - \sigma_{\theta\theta}$ at the SOC at which the graphite yields to determine which root of this quadratic to take. From (2.56a) and (2.56b) we have that, for elastic graphite,

$$\sigma_{rr} - \sigma_{\theta\theta} = \frac{-6G_{\mathrm{C}}B_{\mathrm{C}}}{r^3} \qquad \text{in } \Omega_{\mathrm{C}}^{e}. \tag{5.23}$$

and we know from Section 5.2.1 that the yield condition is first met at $r = R_{\mathrm{Si}}$. From (5.2), we have that

$$\sigma_{rr} - \sigma_{\theta\theta} = \frac{6G_{\mathrm{C}}\Lambda_{\mathrm{Si}}\Lambda_{\mathrm{C}}(\gamma_{\mathrm{C}}c_{\mathrm{C}} - \gamma_{\mathrm{Si}}c_{\mathrm{Si}})}{\Lambda_{\mathrm{Si}}\Lambda_{\mathrm{C}} + 4G_{\mathrm{C}}\big(\Lambda_{\mathrm{C}}(1 - R_{\mathrm{Si}}^3) + \Lambda_{\mathrm{Si}}R_{\mathrm{Si}}^3\big)}, \tag{5.24}$$

at $r = R_{\mathrm{Si}}$. Each term in (5.24) is greater than zero other than $(\gamma_{\mathrm{C}}c_{\mathrm{C}} - \gamma_{\mathrm{Si}}c_{\mathrm{Si}})$, whose sign may depend on the SOC. Therefore, the sign of $\gamma_{\mathrm{Si}}c_{\mathrm{Si}} - \gamma_{\mathrm{C}}c_{\mathrm{C}}$ determines which root of (5.22) we must take. Therefore,

$$\sigma_{rr} - \sigma_{\theta\theta} = \begin{cases} -\sigma_{\mathrm{C}}^{Y} & \gamma_{\mathrm{Si}}c_{\mathrm{Si}} > \gamma_{\mathrm{C}}c_{\mathrm{C}}, \\ \sigma_{\mathrm{C}}^{Y} & \gamma_{\mathrm{Si}}c_{\mathrm{Si}} < \gamma_{\mathrm{C}}c_{\mathrm{C}}, \end{cases} \qquad \text{at } r = s_{\mathrm{C}}. \tag{5.25}$$

As we have that $c_{\mathrm{C}} = 0$ at $c_{\mathrm{Si}} = c_0^{\mathrm{crack}}$ $\forall$ $V_{\mathrm{Si}} \in [0, 1]$ in this geometry, as discussed in Section 5.2.1, we can conclude that $\sigma_{rr} - \sigma_{\theta\theta} = -\sigma_{\mathrm{C}}^{Y}$ when the graphite yields.

5.2.2.5 Displacement in the Pulverised Graphite

We assume that the displacement in Ω_{C}^{p} due to the mechanical response after expansion is incompressible, similar to plastic flow in perfect plasticity theory. A full derivation for the displacement in a plastic material can be found in [48].

As we are assuming the incremental displacements are small, the displacement, $\boldsymbol{u}$, can be decomposed additively into a stress-free expansion, $\boldsymbol{u}_{\mathrm{SF}}$, caused by lithiation, and a mechanical response, $\boldsymbol{u}_p$, such that $\boldsymbol{u} = \boldsymbol{u}_{\mathrm{SF}} + \boldsymbol{u}_p$. In perfectly plastic materials, $\boldsymbol{u}_p$ would be the plastic displacement; here, $\boldsymbol{u}_p$ is the mechanical response of the pulverised graphite to the displacement due to lithiation. We assume $\boldsymbol{u}_p$ is incompressible, such that

$$\frac{\partial(\boldsymbol{\nabla} \cdot \boldsymbol{u}_p)}{\partial t} = 0. \tag{5.26}$$

To find the total displacement, $\boldsymbol{u}$, we substitute $\boldsymbol{u}_p = \boldsymbol{u} - \boldsymbol{u}_{\mathrm{SF}}$ into (5.26) giving

$$\frac{\partial(\boldsymbol{\nabla}\cdot\boldsymbol{u})}{\partial t} = \frac{\partial(\boldsymbol{\nabla}\cdot\boldsymbol{u}_{\mathrm{SF}})}{\partial t}. \tag{5.27}$$

Using the definition of the stress-free deformation gradient, given by (2.3), and J_a^c, given by (2.4), we have

$$\begin{aligned} \mathbf{F}^{\mathrm{SF}} &= (1 + 3\eta_{\mathrm{C}} V_{\mathrm{C}}^m c_{\mathrm{C}}^{p*})^{1/3}\mathbf{1} = \mathbf{1} + \boldsymbol{\nabla}^* \boldsymbol{u}_{\mathrm{SF}}^* && \text{in } \Omega_{\mathrm{C}}^p, \\ \implies \boldsymbol{\nabla}^* \boldsymbol{u}_{\mathrm{SF}}^* &= [(1 + 3\eta_{\mathrm{C}} V_{\mathrm{C}}^m c_{\mathrm{C}}^{p*})^{1/3} - 1]\mathbf{1} && \text{in } \Omega_{\mathrm{C}}^p, \end{aligned} \tag{5.28}$$

where we have assumed that V_{C}^m, $c_{\mathrm{C}}^{\max}$ and η_{C} are the same for the elastic and pulverised graphite. Taking the trace of either side of (5.28) yields

$$\boldsymbol{\nabla}^* \cdot \boldsymbol{u}_{\mathrm{SF}}^* = 3\big((1 + 3\eta_{\mathrm{C}} V_{\mathrm{C}}^m c_{\mathrm{C}}^{p*})^{1/3} - 1\big) \qquad \text{in } \Omega_{\mathrm{C}}^p. \tag{5.29}$$

Nondimensionalising using (2.8) and employing the assumption that $\eta_a V_a^m c_a^{\max}$ is small for all materials, a, yields

$$\begin{aligned} \eta_{\mathrm{Si}} V_{\mathrm{Si}}^m c_{\mathrm{Si}}^{\max} \boldsymbol{\nabla}\cdot\boldsymbol{u}_{\mathrm{SF}} &= 3\eta_{\mathrm{C}} V_{\mathrm{C}}^m c_{\mathrm{C}}^{\max} c_{\mathrm{C}}^p + \mathcal{O}\big((\eta_a V_a^m c_a^*)^2\big) && \text{in } \Omega_{\mathrm{C}}^p, \\ \implies \boldsymbol{\nabla}\cdot\boldsymbol{u}_{\mathrm{SF}} &\approx 3\gamma_{\mathrm{C}} c_{\mathrm{C}}^p && \text{in } \Omega_{\mathrm{C}}^p, \end{aligned} \tag{5.30}$$

where γ_{C} is defined in (2.13).

Substituting (5.30) into (5.27) yields

$$\frac{\partial(\boldsymbol{\nabla}\cdot\boldsymbol{u})}{\partial t} = 3\gamma_{\mathrm{C}} \frac{\partial c_{\mathrm{C}}^p(r,t)}{\partial t} \qquad \text{in } \Omega_{\mathrm{C}}^p. \tag{5.31}$$

We integrate (5.31) with respect to time to yield

$$\boldsymbol{\nabla}\cdot\boldsymbol{u} = 3\gamma_{\mathrm{C}} c_{\mathrm{C}}^p(r,t) + D_{\mathrm{C}}(r) \quad \text{in } \Omega_{\mathrm{C}}^p, \tag{5.32}$$

where $D_{\mathrm{C}}(r)$ is an integration function dependent on r but constant with respect to time. Substituting the expression for $\boldsymbol{\nabla}\cdot\boldsymbol{u}$ in radially-symmetric spherical coordinates yields

$$\frac{1}{r^2}\frac{\mathrm{d}}{\mathrm{d}r}(r^2 u) = 3\gamma_{\mathrm{C}} c_{\mathrm{C}}^p(r,t) + D_{\mathrm{C}}(r) \qquad \text{in } \Omega_{\mathrm{C}}^p. \tag{5.33}$$

We rearrange and integrate once to give the displacement in the pulverised graphite, given by

$$u = \frac{1}{r^2}\int_{R_{\mathrm{Si}}}^{r} \big(3\gamma_{\mathrm{C}} c_{\mathrm{C}}^p(\tilde{r},t) + D_{\mathrm{C}}(\tilde{r})\big)\tilde{r}^2 \ \mathrm{d}\tilde{r} + \frac{E_{\mathrm{C}}}{r^2} \qquad \text{in } \Omega_{\mathrm{C}}^p, \tag{5.34}$$

where we choose the lower bound of the integration interval to be R_{Si} to simplify the boundary conditions, and E_{C} is an integration constant. Note that (5.32) is sufficient to find u in radially-symmetric coordinates, but in general coordinates, a flow rule would be needed to determine $\boldsymbol{u}$.

As in Chapter 2, we focus on a time-scale much slower than any of the dynamics in the system, leading to the quasi-static case of the diffusion equation (2.27). Time is now a parameter and we assume that the SOC of the anode is being increased at a constant rate allowing us to replace the time parameter by c_0 and we drop the t-dependence in c^p_{C}. We can calculate $D(r)$ by considering the value of $\boldsymbol{u}$ and c^p_{C} at s_{C} for $s_{\mathrm{C}} \in [R_{\mathrm{Si}}, 1]$, writing it as

$$D_{\mathrm{C}}(r) = \big(\boldsymbol{\nabla} \cdot \boldsymbol{u}(r)\big)|_{c_0(s_{\mathrm{C}}=r)} - 3\gamma_{\mathrm{C}} c^p_{\mathrm{C}}(r)|_{c_0(s_{\mathrm{C}}=r)}, \tag{5.35}$$

where $\boldsymbol{u}(r)|_{c_0(s_{\mathrm{C}}=r)}$ and $c^p_{\mathrm{C}}(r)|_{c_0(s_{\mathrm{C}}=r)}$ are the displacement and lithium concentration at r, respectively, when c_0 is such that $s_{\mathrm{C}} = r$.

5.2.2.6 Boundary Conditions

We now outline the boundary conditions for the chemo-mechanical problem for the geometry in this section, shown in Figure 5.3. We have $u = 0$ at $r = 0$ as we do not account for cavitation. The displacement, u, and normal stress, σ_{rr}, are continuous on boundaries between the three domains and we prescribe zero traction on the outer radius of the nano-particle. Additionally, we have that the graphite will be at the yield stress at the boundary between the elastic and pulverised graphite, such that $f^{\mathrm{VM}}(\sigma_{ij}) = \sigma_{rr} - \sigma_{\theta\theta} = -\sigma^Y_{\mathrm{C}}$ at $s_{\mathrm{C}}(c_0)$. Using (2.65), (2.66), (5.17), (5.18), (5.23), (5.25) and (5.34), the boundary conditions are thus given mathematically by

$$B_{\mathrm{Si}} = 0, \tag{5.36a}$$

$$A_{\mathrm{Si}} R_{\mathrm{Si}} = \frac{E_{\mathrm{C}}}{R^2_{\mathrm{Si}}}, \tag{5.36b}$$

$$\Lambda_{\mathrm{Si}}(A_{\mathrm{Si}} - \gamma_{\mathrm{Si}} c_{\mathrm{Si}}) = C_{\mathrm{C}} + 2\sigma^{\max}_p \log(R_{\mathrm{Si}}), \tag{5.36c}$$

$$\int_{R_{\mathrm{Si}}}^{s_{\mathrm{C}}} \big(3\gamma_{\mathrm{C}} c^p_{\mathrm{C}}(\tilde{r}) + D_{\mathrm{C}}(\tilde{r})\big)\tilde{r}^2 \;\mathrm{d}\tilde{r} = A_{\mathrm{C}} s^3_{\mathrm{C}} + B_{\mathrm{C}} - E_{\mathrm{C}}, \tag{5.36d}$$

$$C_{\mathrm{C}} + 2\sigma^{\max}_p \log(s_{\mathrm{C}}) = \Lambda_{\mathrm{C}}(A_{\mathrm{C}} - \gamma_{\mathrm{C}} c_{\mathrm{C}}) - \frac{4G_{\mathrm{C}} B_{\mathrm{C}}}{s^3_{\mathrm{C}}}, \tag{5.36e}$$

$$\frac{6G_{\mathrm{C}} B_{\mathrm{C}}}{s^3_{\mathrm{C}}} = \sigma^Y_{\mathrm{C}}, \tag{5.36f}$$

$$\Lambda_{\mathrm{C}}(A_{\mathrm{C}} - \gamma_{\mathrm{C}} c_{\mathrm{C}}) = 4G_{\mathrm{C}} B_{\mathrm{C}}, \tag{5.36g}$$

respectively, where (5.36a) has been already been used in (5.36b)-(5.36c).

5.2.2.7 Lithium Concentration Conditions

As we are assuming the nano-particle is in chemical equilibrium, the chemical potential in each region, given by (5.21), must be equal. As in Chapter 2, the relationship between the lithium concentration and the chemical potential in Ω_{Si} and Ω_{C}^{e} is independent in r but this is not true for Ω_{C}^{p} as $\mathrm{tr}(\boldsymbol{\sigma})$ is a function of r in this region. Therefore, the lithium concentration in Ω_{C}^{p} is also a function of r, but is uniform in Ω_{Si} and Ω_{C}^{e}. We can write the uniform chemical potential condition as

$$\begin{aligned}
&\mu_{\mathrm{Si}}^{\mathrm{SF}}(c_{\mathrm{Si}}) - 3S_{\mathrm{Si}}^{d}\Lambda_{\mathrm{Si}}(A_{\mathrm{Si}} - \gamma_{\mathrm{Si}}c_{\mathrm{Si}}) \\
&\qquad = \mu_{\mathrm{C}}^{\mathrm{SF}}\big(c_{\mathrm{C}}^{p}(r)\big) - S_{\mathrm{C}}^{d}\big[3C_{\mathrm{C}} + 6\sigma_{p}^{\max}\log(r) + 2\sigma_{p}^{\max}\big] \\
&\qquad\qquad = \mu_{\mathrm{C}}^{\mathrm{SF}}(c_{\mathrm{C}}) - 3S_{\mathrm{C}}^{d}\Lambda_{\mathrm{C}}(A_{\mathrm{C}} - \gamma_{\mathrm{C}}c_{\mathrm{C}}) \qquad \forall\, r \in \Omega_{\mathrm{C}}^{p}.
\end{aligned} \tag{5.37}$$

Finally, we have the SOC condition given for a general geometry in (2.41). In the case of the geometry in Figure 5.3, (2.41) is given by

$$\begin{aligned}
c_0\left[R_{\mathrm{Si}}^3 + \frac{c_{\mathrm{C}}^{\max}}{c_{\mathrm{Si}}^{\max}}\big(1 - R_{\mathrm{Si}}^3\big)\right] &= c_{\mathrm{Si}}R_{\mathrm{Si}}^3 + \frac{c_{\mathrm{C}}^{\max}}{c_{\mathrm{Si}}^{\max}}c_{\mathrm{C}}(1 - s_{\mathrm{C}}^3) + \frac{3}{4\pi}\frac{c_{\mathrm{C}}^{\max}}{c_{\mathrm{Si}}^{\max}}\int_{\Omega_{\mathrm{C}}^{p}} c_{\mathrm{C}}^{p}\ \mathrm{d}V \\
&= c_{\mathrm{Si}}R_{\mathrm{Si}}^3 + \frac{c_{\mathrm{C}}^{\max}}{c_{\mathrm{Si}}^{\max}}c_{\mathrm{C}}(1 - s_{\mathrm{C}}^3) + 3\frac{c_{\mathrm{C}}^{\max}}{c_{\mathrm{Si}}^{\max}}\int_{R_{\mathrm{Si}}}^{s_{\mathrm{C}}} c_{\mathrm{C}}^{p}(r)r^2\ \mathrm{d}r.
\end{aligned} \tag{5.38}$$

In summary, for a given SOC, c_0, and initial radius of the silicon core, R_{Si}, we have A_{Si}, B_{Si}, A_{C}, B_{C}, C_{C}, D_{C}, E_{C}, s_{C}, c_{Si}, c_{C}, c_{C}^{p} as unknowns in our problem and we have conditions (5.35)-(5.38). Therefore, the system of equations can be solved to find the displacement, stresses and lithium concentrations.

5.2.2.8 Numerical Solution

Instead of finding the position of the pulverised front, s_{C}, for a given SOC, c_0, it is more convenient to calculate c_0 for a given s_{C}. This is due to the calculation of D_{C} given by (5.35) which requires $\boldsymbol{\nabla}\cdot\boldsymbol{u}$ and c_{C}^{p} to be calculated at $r = s_{\mathrm{C}}$ for each value of c_0. It is unclear how the values of c_0 should be chosen to ensure the discretisation of Ω_{C}^{p} provides good approximations to $c_{\mathrm{C}}^{p}(r)$ and $D_{\mathrm{C}}(r)$. Therefore, instead we can control this accuracy by discretising Ω_{C} initially and increasing s_{C} through these discrete points. For each value of $s_{\mathrm{C}} \in [R_{\mathrm{Si}}, 1]$ at the specified discretisation points in Ω_{C}, we solve (5.35)-(5.37) for the lithium concentrations and substitute these into (5.38) to obtain c_0.

We use (5.36b), (5.36c), (5.36e), (5.36f) and (5.36g) to find A_{Si}, A_{C}, B_{C}, C_{C} and E_{C} in terms of s_{C}, given by

$$A_{\mathrm{Si}} = \frac{2}{3\Lambda_{\mathrm{Si}}}\left[\sigma_{\mathrm{C}}^{Y}(s_{\mathrm{C}}^{3}-1) + \sigma_{p}^{\max}\log\left(\frac{R_{\mathrm{Si}}^{3}}{s_{\mathrm{C}}^{3}}\right)\right] + \gamma_{\mathrm{Si}}c_{\mathrm{Si}}, \tag{5.39a}$$

$$A_{\mathrm{C}} = \frac{2\sigma_{\mathrm{C}}^{Y}s_{\mathrm{C}}^{3}}{3\Lambda_{\mathrm{C}}} + \gamma_{\mathrm{C}}c_{\mathrm{C}}, \tag{5.39b}$$

$$B_{\mathrm{C}} = \frac{\sigma_{\mathrm{C}}^{Y}s_{\mathrm{C}}^{3}}{6G_{\mathrm{C}}}, \tag{5.39c}$$

$$C_{\mathrm{C}} = \frac{2}{3}\left[\sigma_{\mathrm{C}}^{Y}(s_{\mathrm{C}}^{3}-1) - \sigma_{p}^{\max}\log(s_{\mathrm{C}}^{3})\right], \tag{5.39d}$$

$$E_{\mathrm{C}} = \frac{2R_{\mathrm{Si}}^{3}}{3\Lambda_{\mathrm{Si}}}\left[\sigma_{\mathrm{C}}^{Y}(s_{\mathrm{C}}^{3}-1) + 2\sigma_{p}^{\max}\log\left(\frac{R_{\mathrm{Si}}^{3}}{s_{\mathrm{C}}^{3}}\right)\right] + \gamma_{\mathrm{Si}}c_{\mathrm{Si}}R_{\mathrm{Si}}^{3}. \tag{5.39e}$$

To find $D_{\mathrm{C}}(r)$, we consider that, for a given s_{C}, the displacement at $r = s_{\mathrm{C}}$ is continuous and thus

$$u = A_{\mathrm{C}}s_{\mathrm{C}} + \frac{B_{\mathrm{C}}}{s_{\mathrm{C}}^{2}} \text{ at } r = s_{\mathrm{C}}, \tag{5.40}$$

where A_{C} and B_{C} are the integration constants for the elastic graphite region which depends on the SOC, c_0. The divergence of the displacement at $r = s_{\mathrm{C}}$ is therefore given by

$$\big(\boldsymbol{\nabla}\cdot\boldsymbol{u}\big)|_{c_0(r=s_{\mathrm{C}})} = \frac{1}{r^2}\frac{\mathrm{d}}{\mathrm{d}r}\big(r^2 u(s_{\mathrm{C}})|_{c_0(r=s_{\mathrm{C}})}\big) = 3A_{\mathrm{C}}|_{c_0(r=s_{\mathrm{C}})}. \tag{5.41}$$

Substituting (5.41) into (5.35) for $r = s_{\mathrm{C}}$ yields

$$\begin{aligned} D_{\mathrm{C}}(s_{\mathrm{C}}) &= 3A_{\mathrm{C}}|_{c_0(r=s_{\mathrm{C}})} - 3\gamma_{\mathrm{C}}c_{\mathrm{C}}^{p}(s_{\mathrm{C}}), \\ &= \frac{2\sigma_{\mathrm{C}}^{Y}s_{\mathrm{C}}^{3}}{\Lambda_{\mathrm{C}}} + 3\gamma_{\mathrm{C}}\big(c_{\mathrm{C}} - c_{\mathrm{C}}^{p}(s_{\mathrm{C}})\big). \end{aligned} \tag{5.42}$$

We calculate D_{C} as a function of $r \in [R_{\mathrm{Si}}, 1]$, independent of the SOC. The value of D_{C} at a given r is calculated when $s_{\mathrm{C}} = r$ using (5.42) and remains at this value for larger values of s_{C}, due to D_{C} not being a function of time, shown in (5.33). Therefore, we can write D_{C} as a function of r as

$$D_{\mathrm{C}}(r) = \frac{2\sigma_{\mathrm{C}}^{Y}r^{3}}{\Lambda_{\mathrm{C}}|_{s_{\mathrm{C}}=r}} + 3\gamma_{\mathrm{C}}\big(c_{\mathrm{C}}|_{s_{\mathrm{C}}=r} - c_{\mathrm{C}}^{p}(s_{\mathrm{C}})|_{s_{\mathrm{C}}=r}\big), \tag{5.43}$$

where $\Lambda_{\mathrm{C}}|_{s_{\mathrm{C}}=r} = 3\lambda_{\mathrm{C}}|_{s_{\mathrm{C}}=r} + 2G_{\mathrm{C}}|_{s_{\mathrm{C}}=r}$, and $\lambda_{\mathrm{C}}|_{s_{\mathrm{C}}=r}$ and $G_{\mathrm{C}}|_{s_{\mathrm{C}}=r}$ are the Lamé parameters when $s_{\mathrm{C}} = r$. The Lamé parameters vary with lithium concentration in the lithiation-dependent stiffness case and so these must be calculated at each value of r using the c_{C} value when $s_{\mathrm{C}} = r$.

Substituting (5.39) and (5.43) into (5.36d) yields

$$\begin{aligned}\int_{R_{\mathrm{Si}}}^{s_{\mathrm{C}}} 3\gamma_{\mathrm{C}}\big(c_{\mathrm{C}}^{p}(\tilde{r}) + c_{\mathrm{C}}|_{s_{\mathrm{C}}=\tilde{r}} - c_{\mathrm{C}}^{p}(s_{\mathrm{C}})|_{s_{\mathrm{C}}=\tilde{r}}\big)\tilde{r}^{2} + \frac{2\sigma_{\mathrm{C}}^{Y}\tilde{r}^{5}}{\Lambda_{\mathrm{C}}|_{s_{\mathrm{C}}=\tilde{r}}}\ \mathrm{d}\tilde{r} \\ = \frac{2R_{\mathrm{Si}}^{3}}{3\Lambda_{\mathrm{Si}}}\left[\sigma_{\mathrm{C}}^{Y}(1-s_{\mathrm{C}}^{3}) - \sigma_{p}^{\max}\log\left(\frac{R_{\mathrm{Si}}^{3}}{s_{C}^{3}}\right)\right] + \frac{\sigma_{\mathrm{C}}^{Y}s_{\mathrm{C}}^{3}}{6G_{\mathrm{C}}} \\ + \frac{2\sigma_{\mathrm{C}}^{Y}s_{\mathrm{C}}^{6}}{3\Lambda_{\mathrm{C}}} + \gamma_{\mathrm{C}}c_{\mathrm{C}}s_{\mathrm{C}}^{3} - \gamma_{\mathrm{Si}}c_{\mathrm{Si}}R_{\mathrm{Si}}^{3}.\end{aligned} \tag{5.44}$$

We make substitutions from (5.39) into (5.37) to give

$$\mu_{\mathrm{C}}^{\mathrm{SF}}(c_{\mathrm{C}}^{p}(r)) = \mu_{\mathrm{Si}}^{\mathrm{SF}}(c_{\mathrm{Si}}) + 2\sigma_{\mathrm{C}}^{Y}(1-s_{\mathrm{C}}^{3})(S_{\mathrm{Si}}^{d} - S_{\mathrm{C}}^{d}) + 2S_{\mathrm{C}}^{d}\sigma_{p}^{\max} - 6\sigma_{p}^{\max}\log\left[\frac{s_{\mathrm{C}}^{S_{\mathrm{C}}^{d}}R_{\mathrm{Si}}^{S_{\mathrm{Si}}^{d}}}{s_{\mathrm{C}}^{S_{\mathrm{Si}}^{d}}r^{S_{\mathrm{C}}^{d}}}\right], \tag{5.45a}$$

$$\mu_{\mathrm{C}}^{\mathrm{SF}}(c_{\mathrm{C}}) = \mu_{\mathrm{Si}}^{\mathrm{SF}}(c_{\mathrm{Si}}) + 2\sigma_{\mathrm{C}}^{Y}s_{\mathrm{C}}^{3}(S_{\mathrm{C}}^{d} - S_{\mathrm{Si}}^{d}) + 2S_{\mathrm{Si}}^{d}\sigma_{\mathrm{C}}^{Y} + 6S_{\mathrm{Si}}^{d}\sigma_{p}^{\max}\log\left(\frac{s_{\mathrm{C}}}{R_{\mathrm{Si}}}\right). \tag{5.45b}$$

We can now numerically solve (5.44) for c_{Si} using (5.45). Within the function evaluating (5.44), we have a guess for c_{Si} and use this to find c_{C} by numerically solving (5.45b). Likewise, we find $c_{\mathrm{C}}^{p}(r)$ by numerically solving (5.45a) for each discrete value of r between R_{Si} and s_{C}. These equations (5.45) are solved using a similar scheme as described in Section 2.4.4. At each s_{C} value from R_{Si} to 1, we record c_{C} and $c_{\mathrm{C}}^{p}(s_{\mathrm{C}})$ such that we have the function $D_{\mathrm{C}}(r)$ for $R_{\mathrm{Si}} < r < s_{\mathrm{C}}$ at every value of s_{C}. We then numerically integrate the term on the left side of (5.44) and we can calculate the residual of (5.44), solving for the c_{Si} where the residual is zero.

Once c_{Si} is found from solving (5.44), we calculate c_{C} and $c_{\mathrm{C}}^{p}(r)$ by numerically solving (5.45) again. We then can calculate c_0 from (5.38) to find how the size of the pulverised graphite domain grows with SOC by inverting the calculated values of c_0 as a function of the prescribed s_{C} values. The concentrations are substituted into (5.36) to find the remaining integration constants and therefore to find the displacements and stresses within the nano-particle, fully solving the problem.

5.2.3 Core–Shell Results

We now study the results of the model presented in this section using two different values of $\sigma_{p}^{\max}$. The case where the maximum deviatoric stress is equal to the yield stress, $\sigma_{p}^{\max} = \sigma_{\mathrm{C}}^{Y}$, makes the model for the graphite very similar to an elastic–perfectly plastic model. We analyse the results in this case in detail, and make several analytic approximations to provide expressions for the relationship between s_{C} and

R_{Si}. We also address the case such that the pulverised graphite cannot hold any deviatoric stress, i.e. $\sigma_p^{\max} = 0$. We state how this affects the governing equations, (5.44)-(5.45), and the implications this has on the results, but do not provide numerical results or analytic approximations for this $\sigma_p^{\max}$ value. Throughout this section we use the parameters in Table 2.1 and $\sigma_{\mathrm{C}}^{Y} = 3.369 \times 10^{-4}$.

5.2.3.1 The Case $\boldsymbol{\sigma_p^{\max} = \sigma_{\mathrm{C}}^{Y}}$

We first analyse the case in which the deviatoric stress that the pulverised graphite can accommodate is equal to the yield stress, σ_{C}^{Y}. The model for the behaviour in Ω_{C}^{p} is now perfectly plastic, with the stress in the pulverised plastic remaining on the yield surface after pulverisation. This simplifies the expression for D_{C} in (5.43) by causing the lithium concentration to be continuous across the pulverised front, and we derive this result here.

Firstly, from the continuity of stress condition at $r = s_{\mathrm{C}}$ we have

$$\sigma_{rr}(s_{\mathrm{C}}^{-}) - \sigma_{rr}(s_{\mathrm{C}}^{+}) = 0, \tag{5.46}$$

where $\sigma_{rr}(s_{\mathrm{C}}^{-})$ is the radial stress at s_{C} in terms of the pulverised graphite and $\sigma_{rr}(s_{\mathrm{C}}^{+})$ is that in terms of the elastic graphite. From the maximum deviatoric stress condition (5.15), and the yield condition (5.25), we have

$$\sigma_{rr}(s_{\mathrm{C}}^{-}) = -\sigma_p^{\max} + \sigma_{\theta\theta}(s_{\mathrm{C}}^{-}), \tag{5.47a}$$

$$\sigma_{rr}(s_{\mathrm{C}}^{+}) = -\sigma_{\mathrm{C}}^{Y} + \sigma_{\theta\theta}(s_{\mathrm{C}}^{+}), \tag{5.47b}$$

respectively. Substituting (5.47) into (5.46) yields

$$\sigma_{\theta\theta}(s_{\mathrm{C}}^{-}) - \sigma_{\theta\theta}(s_{\mathrm{C}}^{+}) = \sigma_p^{\max} - \sigma_{\mathrm{C}}^{Y}, \tag{5.48}$$

and in the case $\sigma_p^{\max} = \sigma_{\mathrm{C}}^{Y}$, this implies the hoop stress is also continuous at $r = s_{\mathrm{C}}$. As both the radial and hoop stress are continuous at $r = s_{\mathrm{C}}$, the trace of the Cauchy stress tensor will be continuous also. Using (5.19), we can then see that the stress-free chemical potential in Ω_{C}, $\mu_{\mathrm{C}}^{\mathrm{SF}}$, will be continuous at $r = s_{\mathrm{C}}$. As the $\mu_{\mathrm{C}}^{\mathrm{SF}}$ is a one-to-one function, the lithium concentration must also be continuous at $r = s_{\mathrm{C}}$, i.e. $c_{\mathrm{C}} = c_{\mathrm{C}}^{p}(s_{\mathrm{C}})$. However, if $\mu_{\mathrm{C}}^{\mathrm{SF}}$ is not bijective due to the plateaus in the OCV, the concentration may be multi-valued for a given chemical potential and so this result will not hold. We have approximated these plateaus as having a small gradient, making $\mu_{\mathrm{C}}^{\mathrm{SF}}$ bijective and thus take $c_{\mathrm{C}} = c_{\mathrm{C}}^{p}(s_{\mathrm{C}})$. This simplifies (5.43) as the $c_{\mathrm{C}}|_{s_{\mathrm{C}}=r} - c_{\mathrm{C}}^{p}(s_{\mathrm{C}})|_{s_{\mathrm{C}}=r}$ term is now zero for all r, giving

$$D_{\mathrm{C}}(r) = \frac{2\sigma_{\mathrm{C}}^{Y} r^3}{\Lambda_{\mathrm{C}}|_{s_{\mathrm{C}}=r}}. \tag{5.49}$$

The equations to solve numerically for a given s_{C} and R_{Si} are now

$$\begin{aligned}\int_{R_{\mathrm{Si}}}^{s_{\mathrm{C}}} 3\gamma_{\mathrm{C}} c_{\mathrm{C}}^{p}(\tilde{r})\tilde{r}^2 + \frac{2\sigma_{\mathrm{C}}^{Y}\tilde{r}^5}{\Lambda_{\mathrm{C}}|_{s_{\mathrm{C}}=\tilde{r}}} \,\mathrm{d}\tilde{r} &= \frac{2\sigma_{\mathrm{C}}^{Y} s_{\mathrm{C}}^{6}}{3\Lambda_{\mathrm{C}}} \\ &+ \frac{2\sigma_{\mathrm{C}}^{Y} R_{\mathrm{Si}}^{3}}{3\Lambda_{\mathrm{Si}}}\left[1 - s_{\mathrm{C}}^{3} - \log\left(\frac{R_{\mathrm{Si}}^{3}}{s_{\mathrm{C}}^{3}}\right)\right] + \frac{\sigma_{\mathrm{C}}^{Y} s_{\mathrm{C}}^{3}}{6G_{\mathrm{C}}} + \gamma_{\mathrm{C}} c_{\mathrm{C}} s_{\mathrm{C}}^{3} - \gamma_{\mathrm{Si}} c_{\mathrm{Si}} R_{\mathrm{Si}}^{3}.\end{aligned} \tag{5.50a}$$

$$\mu_{\mathrm{C}}^{\mathrm{SF}}(c_{\mathrm{C}}^{p}(r)) = \mu_{\mathrm{Si}}^{\mathrm{SF}}(c_{\mathrm{Si}}) + 2\sigma_{\mathrm{C}}^{Y}(1 - s_{\mathrm{C}}^{3})(S_{\mathrm{Si}}^{d} - S_{\mathrm{C}}^{d}) + 2S_{\mathrm{C}}^{d}\sigma_{\mathrm{C}}^{Y} - 6\sigma_{\mathrm{C}}^{Y}\log\left[\frac{s_{\mathrm{C}}^{S_{\mathrm{C}}^{d}} R_{\mathrm{Si}}^{S_{\mathrm{Si}}^{d}}}{s_{\mathrm{C}}^{S_{\mathrm{Si}}^{d}} r^{S_{\mathrm{C}}^{d}}}\right], \tag{5.50b}$$

$$\mu_{\mathrm{C}}^{\mathrm{SF}}(c_{\mathrm{C}}) = \mu_{\mathrm{Si}}^{\mathrm{SF}}(c_{\mathrm{Si}}) + 2\sigma_{\mathrm{C}}^{Y} s_{\mathrm{C}}^{3}(S_{\mathrm{C}}^{d} - S_{\mathrm{Si}}^{d}) + 2S_{\mathrm{Si}}^{d}\sigma_{\mathrm{C}}^{Y} + 6S_{\mathrm{Si}}^{d}\sigma_{\mathrm{C}}^{Y}\log\left(\frac{s_{\mathrm{C}}}{R_{\mathrm{Si}}}\right). \tag{5.50c}$$

The history of the nano-particle from the initial crack until the current position of s_{C} must be calculated to obtain the function $D_{\mathrm{C}}(r)$ due to the mechanical parameters, λ_{C} and G_{C}, being dependent on c_{C} at each value of $s_{\mathrm{C}} \in [R_{\mathrm{Si}}, 1]$. However, if λ_{C} and G_{C} are assumed independent of the lithium concentration, or c_{C} remains approximately constant for $s_{\mathrm{C}} \in [R_{\mathrm{Si}}, 1]$, this term can be evaluated exactly to give

$$\int_{R_{\mathrm{Si}}}^{s_{\mathrm{C}}} \frac{2\sigma_{\mathrm{C}}^{Y}\tilde{r}^5}{\Lambda_{\mathrm{C}}} \,\mathrm{d}\tilde{r} = \frac{\sigma_{\mathrm{C}}^{Y}}{3\Lambda_{\mathrm{C}}}(s_{\mathrm{C}}^{6} - R_{\mathrm{Si}}^{6}). \tag{5.51}$$

We can then solve the system for a given R_{Si} and s_{C} without calculating the history of the nano-particle.

5.2.3.2 Numerical Solution for the $\sigma_p^{\max} = \sigma_{\mathrm{C}}^{Y}$ Case

We now solve the system of equations for the case $\sigma_p^{\max} = \sigma_{\mathrm{C}}^{Y}$, given by (5.50), for several different values of the initial volumes of the silicon core, $V_{\mathrm{Si}} = R_{\mathrm{Si}}^{3}$, and for both lithiation-dependent and lithiation-independent Lamé parameters. As explained in Section 5.2.2.8, we increase s_{C} from $s_{\mathrm{C}} = R_{\mathrm{Si}}$ to $s_{\mathrm{C}} = 1$, solving (5.50) using each discrete s_{C} value in Ω_{C}, to find the lithium concentration in each region. We then use c_{Si}, c_{C} and c_{C}^{p} to calculate the resulting value of c_0 using (5.38). We plot s_{C} against c_0 in Figures 5.4 and 5.5 for small values of V_{Si} and large values of V_{Si}, respectively.

In Figure 5.4, we see that the results using lithiation-independent and lithiation-dependent Lamé parameters are very similar at low states of charge, but diverge at

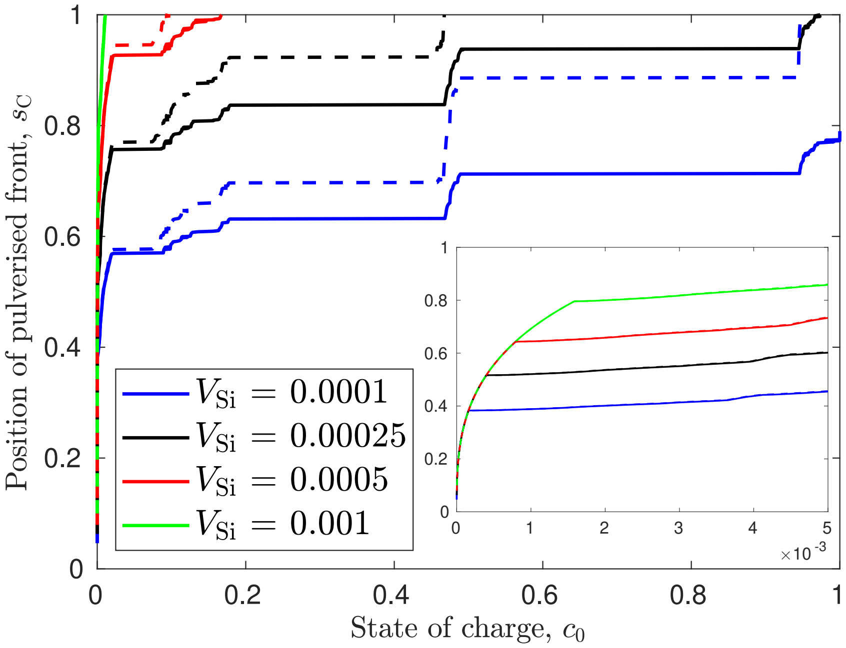

Figure 5.4: Position of pulverised front, s_C, against SOC, c_0, for several small initial volumes of the silicon core, V_{Si}. The inset plot focusses on $c_0 \in [0.0, 0.005]$. Dashed lines are results using the lithiation-dependent Lamé parameters. Solid lines are results using constant Lamé parameters calculated at $c_a = 0$. The discretisation of Ω_C uses grid spacing of $h = 10^{-3}$.

higher states of charge. The value of s_C is consistently greater for the results using the lithiation-dependent Lamé parameters than the lithiation-independent results. This is because the elastic graphite is stronger at high states of charge for lithiation-dependent parameters, causing the integration constant B_C to be less than that for lithiation-independent parameters. From the expressions for the stresses in Ω_C^e given by (2.66b) and (2.66d), this causes σ_{rr} to increase and $\sigma_{\theta\theta}$ to decrease in the graphite. Therefore, more of the graphite will have exceeded the yield stress, causing s_C to be greater. The results in Figure 5.4 appear to not be smooth for all values of c_0. This is due to the interpolation functions of the stress-free chemical potentials causing difficulties when solving the system (5.50), causing there to be multiple, but very similar, solutions for some s_C values.

For very small initial volumes of the silicon core and for very small states of charge, s_C increases very rapidly with SOC as seen in the inset plot of Figure 5.4. This is because the silicon lithiates at lower states of charge to the graphite, causing the silicon to expand, causing stress in the graphite without the graphite being able to expand itself to relieve the stress. At values of SOC at which the graphite is lithiated,

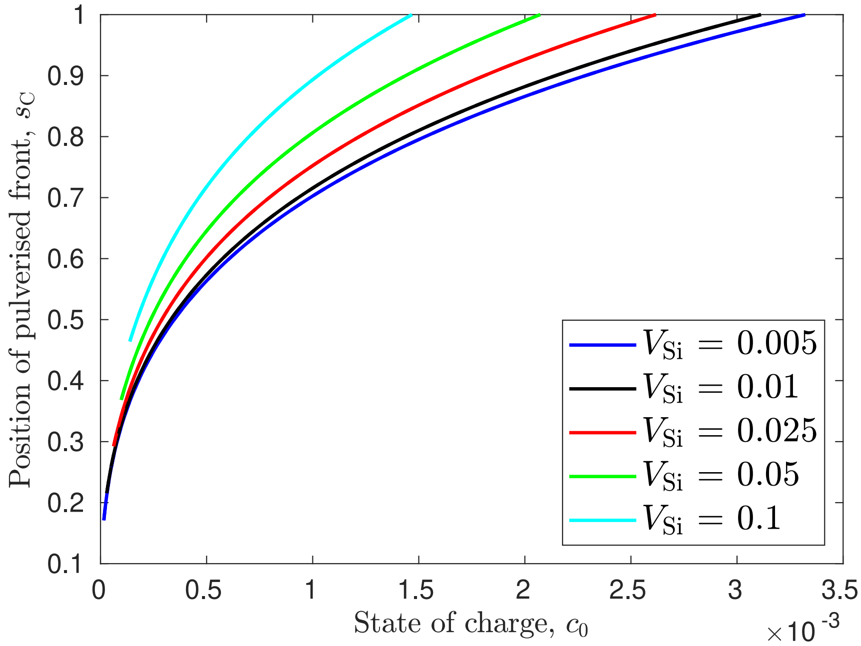

Figure 5.5: Position of pulverised front, s_{C}, against SOC, c_0, for several initial volumes of the silicon core, V_{Si}. Results using both lithiation-dependent and lithiation-independent Lamé parameters are plotted but are approximately equal so that they appear as one curve. The discretisation of Ω_{C} uses grid spacing of $h = 5 \times 10^{-3}$.

the increase in s_{C} with c_0 becomes much less and the steps characteristic of $\mu_{\mathrm{C}}^{\mathrm{SF}}$ (seen in Figure 2.2) are observed in Figure 5.4. For larger V_{Si} values, the graphite fully pulverises without being lithiated, and in this case, s_{C} grows smoothly with c_0, as seen in Figure 5.5.

5.2.3.3 Analytical Approximations to the $\sigma_p^{\max} = \sigma_{\mathrm{C}}^{Y}$ Case

We now consider various limiting cases of the model presented in Section 5.2.2, finding analytical approximations to provide useful results on how the position of the pulverised front is affected by the SOC and the initial volume of the silicon core.

There are two cases we wish to consider: i) the initial volume of the silicon core is large enough to fully pulverise the graphite shell before the nano-particle is fully lithiated, and ii) the initial volume of the silicon core is small enough so that the graphite shell is not fully pulverised at full lithiation. The R_{Si} value which separates these two cases is the one where the pulverised front reaches $s_{\mathrm{C}} = 1$ at full lithiation, $c_0 = 1$, which we denote as $R_{\mathrm{Si}}^{\mathrm{crit}}$. To avoid the need to calculate the history of the lithium concentrations for $s_{\mathrm{C}} < 1$, we approximate the Lamé parameters of the materials to be constant and at the value for $c_{\mathrm{Si}} = c_{\mathrm{C}} = 1$, such that $\lambda_a = \lambda_a|_{c_a=1}$ and $G_a = G_a|_{c_a=1}$ for $a = $ Si and C. This allows us to evaluate the integral in (5.50a) explicitly, and setting $c_{\mathrm{Si}} = c_{\mathrm{C}} = c^p_{\mathrm{C}} = s_{\mathrm{C}} = 1$, we find the expression for $R^{\mathrm{crit}}_{\mathrm{Si}}$, given by the solution of

$$\begin{aligned} 3\gamma_{\mathrm{C}} \int_{R_{\mathrm{Si}}}^{1} \tilde{r}^2 \,\mathrm{d}\tilde{r} &= \frac{\sigma^Y_{\mathrm{C}}}{6G_{\mathrm{C}}} - \frac{2\sigma^Y_{\mathrm{C}} R^3_{\mathrm{Si}}}{\Lambda_{\mathrm{Si}}} \log(R_{\mathrm{Si}}) + \frac{\sigma^Y_{\mathrm{C}}\left(1 + R^6_{\mathrm{Si}}\right)}{3\Lambda_{\mathrm{C}}} + \gamma_{\mathrm{C}} - \gamma_{\mathrm{Si}} R^3_{\mathrm{Si}}, \\ \implies \frac{\sigma^Y_{\mathrm{C}}}{6G_{\mathrm{C}}} + \frac{\sigma^Y_{\mathrm{C}}(1 + R^6_{\mathrm{Si}})}{3\Lambda_{\mathrm{C}}} - \frac{2\sigma^Y_{\mathrm{C}} R^3_{\mathrm{Si}}}{3\Lambda_{\mathrm{Si}}} \log(R_{\mathrm{Si}}) &= (\gamma_{\mathrm{Si}} - \gamma_{\mathrm{C}}) R^3_{\mathrm{Si}}. \end{aligned} \tag{5.52}$$

Solving (5.52) numerically for R_{Si} yields $R^{\mathrm{crit}}_{\mathrm{Si}} = 0.0406$ and $V^{\mathrm{crit}}_{\mathrm{Si}} = (R^{\mathrm{crit}}_{\mathrm{Si}})^3 = 6.6846 \times 10^{-5}$. We expect that for all initial silicon core volumes such that $V_{\mathrm{Si}} > V^{\mathrm{crit}}_{\mathrm{Si}}$, the graphite shell fully pulverises with $c_0 < 1$ and for all initial silicon core volumes such that $V_{\mathrm{Si}} < V^{\mathrm{crit}}_{\mathrm{Si}}$, the graphite shell does not fully pulverise when the nano-particle is fully lithiated.

We now examine in more detail the two cases, $V_{\mathrm{Si}} > V^{\mathrm{crit}}_{\mathrm{Si}}$ and $V_{\mathrm{Si}} < V^{\mathrm{crit}}_{\mathrm{Si}}$. In the former case, the graphite shell will reach $s_{\mathrm{C}} = 1$ before the nano-particle is fully lithiated. If the pulverised front does not reach $s_{\mathrm{C}} = 1$, there is a shell of elastic graphite surrounding the pulverised graphite, which would retain the integrity of the nano-particle by keeping the pulverised graphite in place. If the pulverised front reaches $s_{\mathrm{C}} = 1$, the anode particles may begin to mechanically fail and the networks of cracks in the pulverised graphite may allow electrolyte to come into contact with the silicon, causing an SEI layer to grow. Therefore, analysing this case is very important to avoid the degradation of the nano-particle. For small values of V_{Si}, as in Figure 5.4, we find that $c_{\mathrm{C}}, c^p_{\mathrm{C}} > 0$ when $s_{\mathrm{C}} = 1$. This makes finding the SOC at which $s_{\mathrm{C}} = 1$ difficult because the c^p_{C} term in the integral would need to be solved for. However, in Figure 5.5, we see that for silicon cores with fairly large silicon cores ($V_{\mathrm{Si}} > 0.005$), the graphite is not lithiated at all before the graphite fully pulverises. We can use this to simplify (5.50a), and find how the SOC at which $s_{\mathrm{C}} = 1$ varies with V_{Si}. As $c_{\mathrm{C}} = 0$, we have $\lambda_{\mathrm{C}} = \lambda_{\mathrm{C}}|_{c_{\mathrm{C}}=0}$, $G_{\mathrm{C}} = G_{\mathrm{C}}|_{c_{\mathrm{C}}=0}$ for $s_{\mathrm{C}} \in [R_{\mathrm{Si}}, 1]$ and $c_{\mathrm{C}} = c^p_{\mathrm{C}} = 0$ allowing us to calculate the integral term explicitly. Additionally, we have

$$c_{\mathrm{Si}} = \left[1 + \frac{c^{\max}_{\mathrm{C}}}{c^{\max}_{\mathrm{Si}}}\left(\frac{1 - V_{\mathrm{Si}}}{V_{\mathrm{Si}}}\right)\right] c_0. \tag{5.53}$$

Therefore, (5.50a) and (5.53) give

$$\begin{aligned} \frac{\sigma^Y_{\mathrm{C}}(s^6_{\mathrm{C}} + V^2_{\mathrm{Si}})}{3\Lambda_{\mathrm{C}}} + \frac{2\sigma^Y_{\mathrm{C}} R^3_{\mathrm{Si}}}{3\Lambda_{\mathrm{Si}}(c_{\mathrm{Si}})}\left[1 - s^3_{\mathrm{C}} - \log\left(\frac{V_{\mathrm{Si}}}{s^3_{\mathrm{C}}}\right)\right] + \frac{\sigma^Y_{\mathrm{C}} s^3_{\mathrm{C}}}{6G_{\mathrm{C}}} \\ = \gamma_{\mathrm{Si}}\left(V_{\mathrm{Si}} + \frac{c^{\max}_{\mathrm{C}}}{c^{\max}_{\mathrm{Si}}}(1 - V_{\mathrm{Si}})\right) c_0. \end{aligned} \tag{5.54}$$

Before finding the behaviour of c_0 at which $s_\mathrm{C} = 1$, we verify that this approximation of $c_\mathrm{C} = 0$ is valid for $V_\mathrm{Si} > 0.005$. We solve (5.54) numerically for $s_\mathrm{C} = [R_\mathrm{Si}, 1]$, for the values of V_Si used in Figure 5.5. We plot the solutions to the approximation (5.54) alongside the numerical results for the same V_Si values in Figure 5.6. We can see there is very good agreement between the approximate and numerical solutions, showing that c_C is zero for these values of V_Si and showing that the simplification in (5.54) is accurate in this case.

To find the maximum SOC such that the graphite is not fully pulverised, which we denote as c_0^pulv, we set $s_\mathrm{C} = 1$ in (5.54), giving

$$\frac{\sigma_\mathrm{C}^Y(1+V_\mathrm{Si}^2)}{3\Lambda_\mathrm{C}} - \frac{2\sigma_\mathrm{C}^Y V_\mathrm{Si}}{3\Lambda_\mathrm{Si}(c_\mathrm{Si})}\log(V_\mathrm{Si}) + \frac{\sigma_\mathrm{C}^Y}{6G_\mathrm{C}} = \gamma_\mathrm{Si}\left(V_\mathrm{Si} + \frac{c_\mathrm{C}^\mathrm{max}}{c_\mathrm{Si}^\mathrm{max}}(1-V_\mathrm{Si})\right)c_0. \tag{5.55}$$

This is solved numerically to find c_0 as a function of $V_\mathrm{Si} = R_\mathrm{Si}^3$. Additionally, we use (2.81) to find the relative amount of lithium able to be intercalated into the nano-particle before the graphite fully pulverises, which we denote Q^pulv. As we have

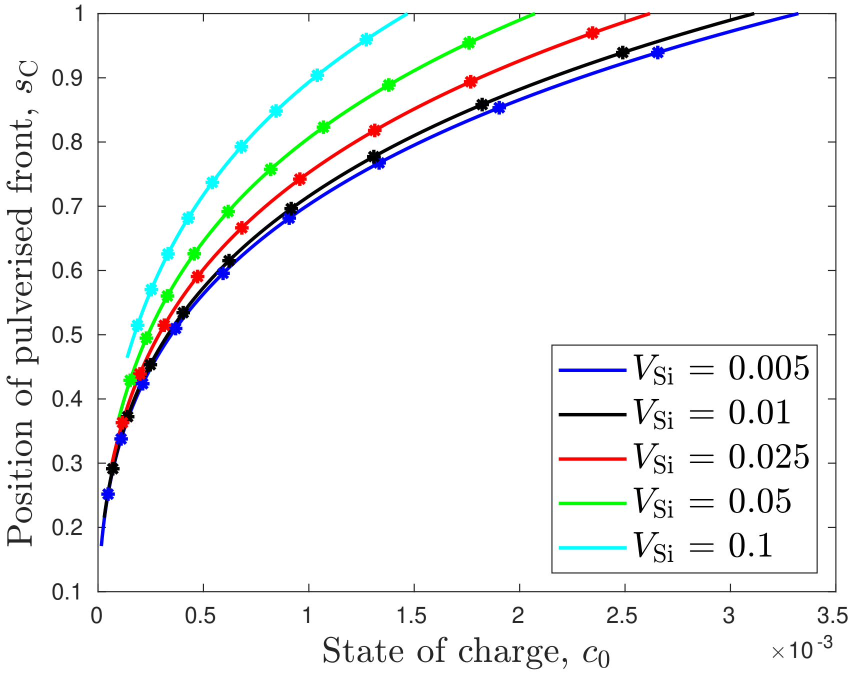

Figure 5.6: Position of the pulverised front, s_C, against the SOC, c_0, for several initial volumes of silicon core, V_Si. The solid lines are the $c_\mathrm{C} = 0$ approximation in (5.54) and the asterisks are numerical results taken from the data used to plot Figure 5.5.

$c_{\mathrm{C}} = 0$ for these plots, (2.81) reduces to

$$Q^{\mathrm{pulv}} = c_{\mathrm{Si}} V_{\mathrm{Si}} = \left[V_{\mathrm{Si}} + \frac{c_{\mathrm{C}}^{\max}}{c_{\mathrm{Si}}^{\max}} (1 - V_{\mathrm{Si}}) \right] c_0, \tag{5.56a}$$

$$\implies Q^{\mathrm{pulv}} = \frac{1}{\gamma_{\mathrm{Si}}} \left[\frac{\sigma_{\mathrm{C}}^{Y} (1 + V_{\mathrm{Si}}^2)}{3\Lambda_{\mathrm{C}}} - \frac{2\sigma_{\mathrm{C}}^{Y} V_{\mathrm{Si}}}{3\Lambda_{\mathrm{Si}}(c_{\mathrm{Si}})} \log(V_{\mathrm{Si}}) + \frac{\sigma_{\mathrm{C}}^{Y}}{6G_{\mathrm{C}}} \right], \tag{5.56b}$$

where (5.56b) comes from substituting (5.56a) into (5.55). We plot c_0^{pulv} against V_{Si} in Figure 5.7 for $V_{\mathrm{Si}} \in [0.005, 1.0]$. We see that the SOC at $s_{\mathrm{C}} = 1$ rapidly decreases before reaching the SOC of approximately 2.5×10^{-4}, at which the graphite first cracks for $V_{\mathrm{Si}} = 1$. Conversely, Q^{pulv} increases nonlinearly as V_{Si} increases, dominated by the $V_{\mathrm{Si}} \log(V_{\mathrm{Si}})$ term for small V_{Si} and by the V_{Si}^2 term for $V_{\mathrm{Si}} \approx 1$.

We now consider the case $V_{\mathrm{Si}} < V_{\mathrm{Si}}^{\mathrm{crit}}$ in which the graphite has not fully pulverised at full lithiation. By prescribing $c_0 = 1$, we obtain a relationship between the position of the plastic front, at full lithiation, denoted by $s_{\mathrm{C},1}$, and the initial volume of the silicon core, V_{Si}. We again make the approximation that $\lambda_a = \lambda_a|_{c_a=1}$ and $G_a = G_a|_{c_a=1}$ for $a = \mathrm{Si}, \mathrm{C}$ so we can explicitly calculate the integral in (5.50a). Substituting

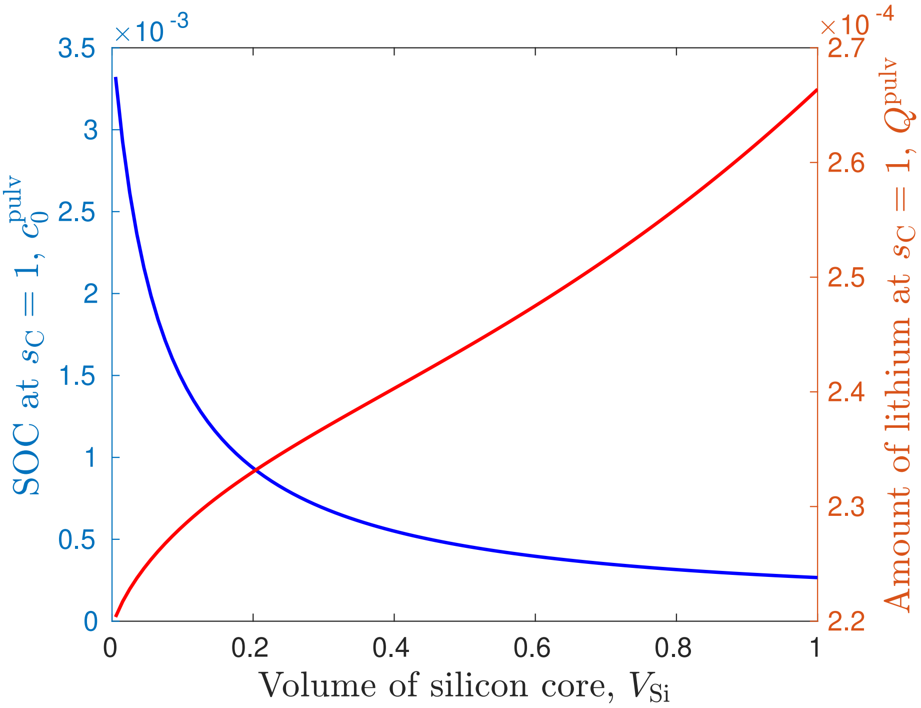

Figure 5.7: Left axis: SOC at which the graphite fully pulverises, c_0^{pulv}. Right axis: Relative amount of lithium intercalated at $c_0 = c_0^{\mathrm{pulv}}$, Q^{pulv}. Both plotted against the initial volume of the silicon core, V_{Si}, for $V_{\mathrm{Si}} \in [0.005, 1.0]$.

$c_{\mathrm{Si}} = c_{\mathrm{C}} = c^{p}_{\mathrm{C}} = 1$ and the lithiation-dependent Lamé parameters into (5.50a) yields

$$\frac{\sigma^{Y}_{\mathrm{C}}(s^{6}_{\mathrm{C}} + V^{2}_{\mathrm{Si}})}{3\Lambda_{\mathrm{C}}} + \frac{\sigma^{Y}_{\mathrm{C}} s^{3}_{\mathrm{C}}}{6G_{\mathrm{C}}} + \frac{2\sigma^{Y}_{\mathrm{C}} V_{\mathrm{Si}}}{3\Lambda_{\mathrm{Si}}}\left[1 - s^{3}_{\mathrm{C}} - \log\left(\frac{V_{\mathrm{Si}}}{s^{3}_{\mathrm{C}}}\right)\right] = (\gamma_{\mathrm{Si}} - \gamma_{\mathrm{C}})V_{\mathrm{Si}}. \tag{5.57}$$

We solve (5.57) for s_{C} numerically to find $s_{\mathrm{C},1}$ and plot both $s_{\mathrm{C},1}$ and $s^{3}_{\mathrm{C},1}$ against V_{Si} in Figure 5.8. We can see that $s^{3}_{\mathrm{C},1}$ is approximately linear in V_{Si}, showing that $s_{\mathrm{C},1}$ is approximately linear in R_{Si}, because $R^{3}_{\mathrm{Si}} = V_{\mathrm{Si}}$.

Lastly, we consider the limit of small silicon cores. The motivation for this simplification is to consider a regular array of silicon cores in a large matrix of graphite, a schematic of which is depicted in Figure 5.9. As we have only considered single silicon particles in the model, applying this pulverisation model to this geometry requires us to ignore any interaction between the silicon particles in the matrix. We also no longer consider the outer radius of the nano-particle, and this is equivalent to taking the limit $R_{\mathrm{Si}} \to 0$. If the pulverised graphite regions caused by the expansion of adjacent silicon particles interact, this may cause the whole graphite matrix to fail. However, if some of the graphite is still elastic after fully lithiating, these elastic regions would be able to provide structural support to the matrix. We aim to find the minimum distance the silicon cores can be apart such that the pulverised regions will not interact. We use an ansatz that the maximum outer radius of the pulverised

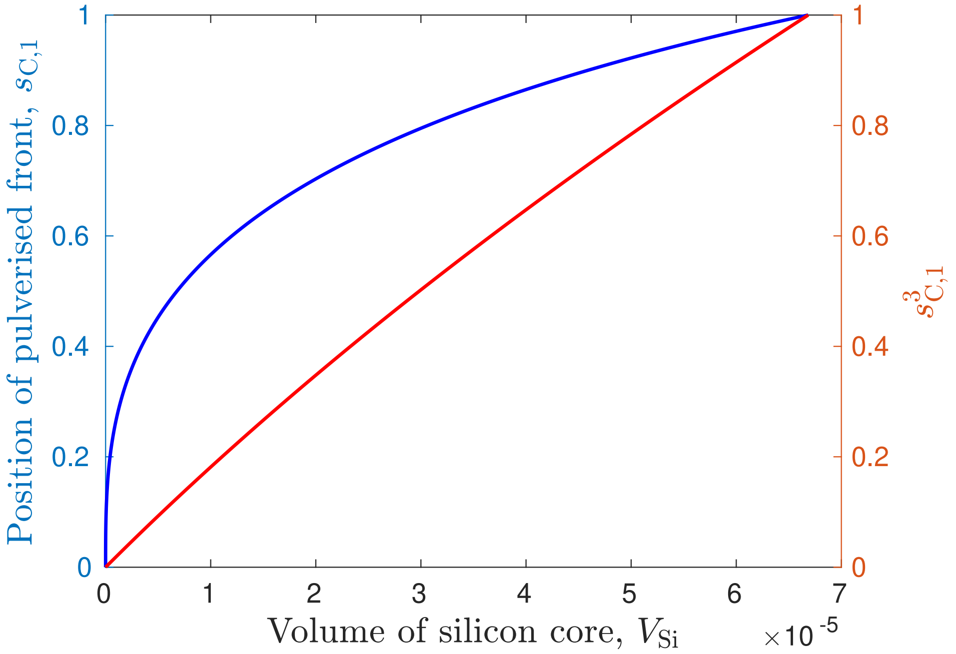

Figure 5.8: Left axis: Position of pulverised front at full lithiation, $s_{\mathrm{C},1}$. Right axis: $s^{3}_{\mathrm{C},1}$. Both quantities are plotted against the initial volume of the silicon core, V_{Si}, for $V_{\mathrm{Si}} \in [0.0, V^{\mathrm{crit}}_{\mathrm{Si}}]$.

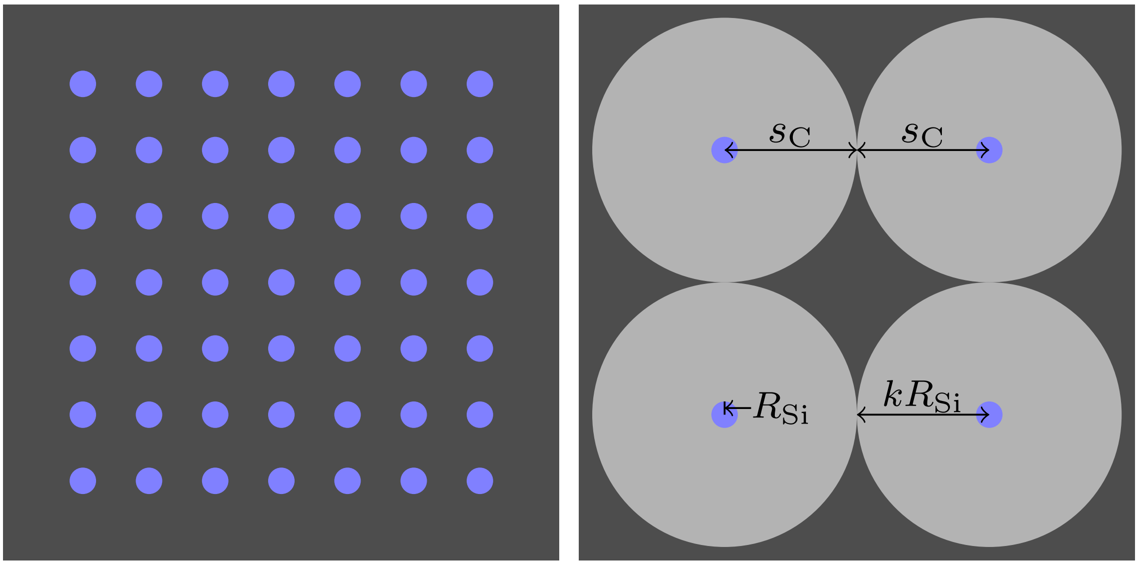

Figure 5.9: Left: Schematic of a periodic array of silicon inclusions (blue) in a graphite matrix (black). Right: Schematic showing the minimum distance the silicon inclusions can be for the pulverised graphite regions (light grey) to not be touching.

region is proportional to the radius of the silicon core and substitute $s_{\mathrm{C}} = kR_{\mathrm{Si}}$ into (5.57). We then take the limit $R_{\mathrm{Si}} \to 0$, yielding

$$\gamma_{\mathrm{Si}} - \gamma_{\mathrm{C}} = \frac{\sigma_{\mathrm{C}}^{Y} k^3}{6G_{\mathrm{C}}} + \frac{2\sigma_{\mathrm{C}}^{Y}}{3\Lambda_{\mathrm{Si}}}\big(1 + \log(k^3)\big), \tag{5.58}$$

giving us a transcendental equation for k. The minimum distance between adjacent silicon cores in the graphite matrix such that the pulverised regions caused by their expansion will just touch is therefore given by kR_{Si}, as shown in Figure 5.9. Therefore, the maximum volume fraction of silicon that is able to be included in this graphite matrix is proportional to $1/k^3$ where the constant of proportionality depends on the packing efficiency of the silicon inclusions. For the parameters used in this problem and $\lambda_a = \lambda_a|_{c_a=1}$ and $G_a = G_a|_{c_a=1}$, we obtain $k = 26.7016$, yielding a maximum volume fraction of 5.2528×10^{-5}. This estimated value shows that due to the low yield stress of graphite and the high expansion of the silicon, only a tiny amount of silicon can be doped into a graphite matrix in this example.

5.2.3.4 The Case $\boldsymbol{\sigma_p^{\max} = 0}$

We now briefly address another special case for the maximum deviatoric stress: $\sigma_p^{\max} = 0$, and outline some of the features of the model in this case. If $\sigma_p^{\max} = 0$, (5.15) simplifies to

$$\sigma_{rr} - \sigma_{\theta\theta} = 0 \qquad \text{in } \Omega_{\mathrm{C}}^{p}, \tag{5.59}$$

and after solving the ODE (5.10), we have

$$\sigma_{rr} = \sigma_{\theta\theta} = C_{\mathrm{C}}, \qquad \text{in } \Omega_{\mathrm{C}}^{p}. \tag{5.60}$$

Therefore, the stress in the pulverised graphite is now uniform in r. The integration constants arising from the boundary conditions (5.36) are now given by

$$A_{\mathrm{Si}} = \frac{2\sigma_{\mathrm{C}}^{Y}(s_{\mathrm{C}}^{3}-1)}{3\Lambda_{\mathrm{Si}}} + \gamma_{\mathrm{Si}} c_{\mathrm{Si}}, \tag{5.61a}$$

$$C_{\mathrm{C}} = \frac{2\sigma_{\mathrm{C}}^{Y}}{3}(s_{\mathrm{C}}^{3}-1), \tag{5.61b}$$

$$E_{\mathrm{C}} = \frac{2\sigma_{\mathrm{C}}^{Y}(s_{\mathrm{C}}^{3}-1)R_{\mathrm{Si}}^{3}}{3\Lambda_{\mathrm{Si}}} + \gamma_{\mathrm{Si}} c_{\mathrm{Si}} R_{\mathrm{Si}}^{3}, \tag{5.61c}$$

and A_{C} and B_{C}, which are given in (5.39b) and (5.39c), respectively.

Using (2.67), (5.19), (5.39b), (5.60) and (5.61), we write the chemical potential of the lithium within each region as

$$\mu = \mu_{\mathrm{Si}}^{\mathrm{SF}}(c_{\mathrm{Si}}) - 2S_{\mathrm{Si}}^{d}\sigma_{\mathrm{C}}^{Y}(s_{\mathrm{C}}^{3}-1) \quad \text{in } \Omega_{\mathrm{Si}}, \tag{5.62a}$$

$$\mu = \mu_{\mathrm{C}}^{\mathrm{SF}}\left(c_{\mathrm{C}}^{p}\right) - 2S_{\mathrm{C}}^{d}\sigma_{\mathrm{C}}^{Y}(s_{\mathrm{C}}^{3}-1) \quad \text{in } \Omega_{\mathrm{C}}^{p}, \tag{5.62b}$$

$$\mu = \mu_{\mathrm{C}}^{\mathrm{SF}}(c_{\mathrm{C}}) - 2S_{\mathrm{C}}^{d}\sigma_{\mathrm{C}}^{Y}s_{\mathrm{C}}^{3} \quad \text{in } \Omega_{\mathrm{C}}^{e}, \tag{5.62c}$$

Therefore, the lithium concentration in the pulverised graphite is uniform in r. As c_{C}^{p} is now independent of r, we can evaluate the integral of c_{C}^{p} in the governing equation for the general case (5.44), yielding $\gamma_{\mathrm{C}} c_{\mathrm{C}}^{p}(s_{\mathrm{C}}^{3} - R_{\mathrm{Si}}^{3})$. As the hoop stresses in the elastic and pulverised graphite regions are no longer equal, the concentrations, c_{C} and c_{C}^{p}, are not equal and thus the expression for D_{C} is given in (5.43).

Substituting the integration constants in (5.61), (5.39b) and (5.39c) into (5.36d) and equating the chemical potentials of the lithium in each region yields the governing equations

$$\begin{aligned} 3\gamma_{\mathrm{C}} \int_{R_{\mathrm{Si}}}^{s_{\mathrm{C}}} \frac{2\sigma_{\mathrm{C}}^{Y}\tilde{r}^{5}}{\Lambda_{\mathrm{C}}|_{s_{\mathrm{C}}=r}} + \left(c_{\mathrm{C}}|_{s_{\mathrm{C}}=\tilde{r}} - c_{\mathrm{C}}^{p}|_{s_{\mathrm{C}}=\tilde{r}}\right)\tilde{r}^{2} \,\mathrm{d}\tilde{r} &= \frac{2\sigma_{\mathrm{C}}^{Y}R_{\mathrm{Si}}^{3}(1-s_{\mathrm{C}}^{3})}{3\Lambda_{\mathrm{Si}}} + \frac{\sigma_{\mathrm{C}}^{Y}s_{\mathrm{C}}^{3}}{6G_{\mathrm{C}}} \\ &\quad + \frac{2\sigma_{\mathrm{C}}^{Y}s_{\mathrm{C}}^{6}}{3\Lambda_{\mathrm{C}}} + \gamma_{\mathrm{C}}c_{\mathrm{C}}s_{\mathrm{C}}^{3} - \gamma_{\mathrm{C}}c_{\mathrm{C}}^{p}(s_{\mathrm{C}}^{3} - R_{\mathrm{Si}}^{3}) - \gamma_{\mathrm{Si}}c_{\mathrm{Si}}R_{\mathrm{Si}}^{3}, \end{aligned} \tag{5.63a}$$

$$\mu_{\mathrm{C}}^{\mathrm{SF}}(c_{\mathrm{C}}^{p}) = \mu_{\mathrm{Si}}^{\mathrm{SF}}(c_{\mathrm{Si}}) + 2\sigma_{\mathrm{C}}^{Y}(1-s_{\mathrm{C}}^{3})(S_{\mathrm{Si}}^{d} - S_{\mathrm{C}}^{d}), \tag{5.63b}$$

$$\mu_{\mathrm{C}}^{\mathrm{SF}}(c_{\mathrm{C}}) = \mu_{\mathrm{Si}}^{\mathrm{SF}}(c_{\mathrm{Si}}) + 2\sigma_{\mathrm{C}}^{Y}s_{\mathrm{C}}^{3}(S_{\mathrm{C}}^{d} - S_{\mathrm{Si}}^{d}) + 2S_{\mathrm{Si}}^{d}\sigma_{\mathrm{C}}^{Y}. \tag{5.63c}$$

Solving (5.63) requires knowledge of the history of the concentrations c_{C} and c_{C}^{p} at all values of s_{C}, even if the Lamé parameters are assumed independent of the lithiation state. We do not solve this set of equations, and instead introduce a new geometry of nano-particle to apply this yielding model to.

5.3 Central Void and Silicon Layer

We now study the case where the silicon also yields but by plasticising. Sethuraman *et al.* showed experimentally that silicon exhibits plastic flow at sufficiently large deviatoric stress [98]. However, more recently the plastic behaviour of silicon has been debated in the literature due to evidence that the plastic flow has been observed under hydrostatic compressive stress [37]. This is due to the yielding occurring by a phase transition from amorphous silicon to a denser structure of silicon, as opposed to more traditional dislocation-based plastic deformation. However, standard elastic-plastic models based on yielding according to the von Mises yield condition are frequently used to describe silicon yielding and this is the approach we take here.

For the deviatoric stress to be non-zero in the silicon, we require a change in the geometry of the nano-particle from that in Figure 5.3. We incorporate a central void into the geometry as shown in Figure 3.1. The main aim of applying this model to this geometry is to investigate whether allowing the silicon to plastically flow into the central void can allow more lithium to be intercalated into the nano-particle without the graphite fully pulverising. We focus on discussing the different regimes the nano-particle will go through during lithiation, according to which materials have yielded and whether they have fully yielded or not. Lastly, we calculate the maximum amount of lithium that can be intercalated into the nano-particle when fully lithiated before the graphite fully pulverises, and compare this to the case without a central void in Section 5.2.3.3.

5.3.1 SOC of First Yield

We begin by finding the SOC at which one of the materials first yields, either by the graphite cracking or the silicon plasticising. The yield function for silicon is given by (5.1) with $a = \mathrm{Si}$. The boundary conditions before any yielding occurs are different to that in Section 5.2 due to the central void. In this geometry, the integration constants B_{Si} and B_{C} are given by (3.2c) and (3.2d), respectively. Therefore, from substituting (3.2c) and (3.2d) into (5.1), the von Mises yield functions for the silicon and graphite are

$$f_{\mathrm{Si}}^{\mathrm{VM}} = \frac{6G_{\mathrm{Si}}G_{\mathrm{C}}\Lambda_{\mathrm{Si}}\Lambda_{\mathrm{C}}R_{\mathrm{Si}}^3R_V^3(1-R_{\mathrm{Si}}^3)|\gamma_{\mathrm{Si}}c_{\mathrm{Si}}-\gamma_{\mathrm{C}}c_{\mathrm{C}}|}{\omega_V r^3}, \tag{5.64a}$$

$$f_{\mathrm{C}}^{\mathrm{VM}} = \frac{6G_{\mathrm{Si}}G_{\mathrm{C}}\Lambda_{\mathrm{Si}}\Lambda_{\mathrm{C}}R_{\mathrm{Si}}^3(R_{\mathrm{Si}}^3-R_V^3)|\gamma_{\mathrm{Si}}c_{\mathrm{Si}}-\gamma_{\mathrm{C}}c_{\mathrm{C}}|}{\omega_V r^3}, \tag{5.64b}$$

respectively, where R_V is the radius of the central void, R_{Si} is the outer radius of the silicon layer and ω_V is defined in (3.2e). From (3.2), we can see that $\omega_V > 0$ and it is easily seen that the other terms other than $\gamma_{\mathrm{Si}} c_{\mathrm{Si}} - \gamma_{\mathrm{C}} c_{\mathrm{C}}$ in (5.64) are also positive. Therefore, we only need to take the absolute value of $\gamma_{\mathrm{Si}} c_{\mathrm{Si}} - \gamma_{\mathrm{C}} c_{\mathrm{C}}$ when calculating $|B_a|$.

Now the nano-particle geometry is such that either of the materials can yield, we need to calculate the geometrical parameters for which each material yields at a lower SOC than the other. We can see from (5.64) that both materials' yield functions are maximised at the minimum radial point for that material: R_V for silicon and R_{Si} for graphite. We need to find the SOC at which $f_a^{\mathrm{VM}} = \sigma_a^Y$ where σ_a^Y is the yield stress for material a. Therefore, we rearrange (5.64) to see that the silicon and graphite yield when the SOC is such that

$$|\gamma_{\mathrm{Si}} c_{\mathrm{Si}} - \gamma_{\mathrm{C}} c_{\mathrm{C}}| = \frac{\sigma_{\mathrm{Si}}^Y \omega_V}{6 G_{\mathrm{Si}} G_{\mathrm{C}} \Lambda_{\mathrm{Si}} \Lambda_{\mathrm{C}} R_{\mathrm{Si}}^3 (1 - R_{\mathrm{Si}}^3)}, \tag{5.65a}$$

$$|\gamma_{\mathrm{Si}} c_{\mathrm{Si}} - \gamma_{\mathrm{C}} c_{\mathrm{C}}| = \frac{\sigma_{\mathrm{C}}^Y \omega_V}{6 G_{\mathrm{Si}} G_{\mathrm{C}} \Lambda_{\mathrm{Si}} \Lambda_{\mathrm{C}} (R_{\mathrm{Si}}^3 - R_V^3)}, \tag{5.65b}$$

respectively.

We assume that $|\gamma_{\mathrm{Si}} c_{\mathrm{Si}} - \gamma_{\mathrm{C}} c_{\mathrm{C}}|$ is an increasing function of SOC for all $R_V < R_{\mathrm{Si}}$. Therefore, the silicon will yield at a lower SOC than the graphite if

$$\frac{\sigma_{\mathrm{Si}}^Y}{R_{\mathrm{Si}}^3 (1 - R_{\mathrm{Si}}^3)} < \frac{\sigma_{\mathrm{C}}^Y}{R_{\mathrm{Si}}^3 - R_V^3}, \tag{5.66}$$

which can be rearranged to yield

$$R_V^3 > \frac{\sigma_{\mathrm{C}}^Y}{\sigma_{\mathrm{Si}}^Y} R_{\mathrm{Si}}^3 (1 - R_{\mathrm{Si}}^3) + R_{\mathrm{Si}}^3. \tag{5.67}$$

This provides a condition on the geometrical parameters of the nano-particle and the yield stresses of each material to make the silicon yield before the graphite cracks. The SOC at which the first material yields can be calculated by rearranging (5.65) for each case. Thus, the SOC at which the nano-particle first yields is such that

$$|\gamma_{\mathrm{Si}} c_{\mathrm{Si}} - \gamma_{\mathrm{C}} c_{\mathrm{C}}| = \begin{cases} \frac{\sigma_{\mathrm{Si}}^Y}{6} \left[\left(\frac{1}{G_{\mathrm{C}} R_{\mathrm{Si}}^3} + \frac{4}{\Lambda_{\mathrm{C}}} \right) \left(\frac{R_{\mathrm{Si}}^3 - R_V^3}{1 - R_{\mathrm{Si}}^3} \right) + \frac{R_V^3}{G_{\mathrm{Si}} R_{\mathrm{Si}}^3} + \frac{4}{\Lambda_{\mathrm{Si}}} \right] & \text{if } R_V^3 > R_{\mathrm{Si}}^3 - \frac{\sigma_{\mathrm{C}}^Y}{\sigma_{\mathrm{Si}}^Y} R_{\mathrm{Si}}^3 (1 - R_{\mathrm{Si}}^3), \\ \frac{\sigma_{\mathrm{C}}^Y}{6} \left[\left(\frac{R_V^3}{G_{\mathrm{Si}}} + \frac{4 R_{\mathrm{Si}}^3}{\Lambda_{\mathrm{Si}}} \right) \left(\frac{1 - R_{\mathrm{Si}}^3}{R_{\mathrm{Si}}^3 - R_V^3} \right) + \frac{1}{G_{\mathrm{C}}} + \frac{4 R_{\mathrm{Si}}^3}{\Lambda_{\mathrm{C}}} \right] & \text{if } R_V^3 < R_{\mathrm{Si}}^3 - \frac{\sigma_{\mathrm{C}}^Y}{\sigma_{\mathrm{Si}}^Y} R_{\mathrm{Si}}^3 (1 - R_{\mathrm{Si}}^3). \end{cases} \tag{5.68}$$

The expression for the SOC at which graphite yields can be seen to reduce to (5.6) as $R_V \to 0$.

Several studies have shown that the yield stress, σ_{Si}^{Y}, depends on the lithium concentration of silicon [20, 24, 34, 134], exhibiting plastic softening where the yield stress decreases as c_{Si} increases. However, here we assume that σ_{Si}^{Y} is lithiation-independent for simplicity. Even in studies which assume a constant yield stress, the reported values of σ_{Si}^{Y} from atomistic simulations and experiments differ but are all on the order of 1 GPa [20, 37, 134]. Therefore, for this section, we take $\sigma_{\mathrm{Si}}^{Y*} = 1.0$ GPa, nondimensionalised using (5.4) to give $\sigma_{\mathrm{Si}}^{Y} = 0.0288$. This is significantly greater than the observed tensile strength of graphite, $\sigma_{\mathrm{C}}^{Y} = 3.369 \times 10^{-4}$, meaning that for these yield stress values, the annulus of silicon must be very thin to cause the silicon to yield at a lower SOC than the graphite.

5.3.2 Post-Yield Silicon Model

We now present the perfect plasticity model we use for the plastic silicon after it initially yields at a lower SOC than the graphite. This is very similar to the pulverised graphite model but instead of prescribing a maximum deviatoric stress, we instead prescribe that the yield function of the plastic silicon remains at the yield stress after yielding. We denote the domain of the yielded silicon as $\Omega_{\mathrm{Si}}^{p} = \{r : 0 < R_V \leq r \leq s_{\mathrm{Si}}\}$ and the elastic silicon as $\Omega_{\mathrm{Si}}^{e} = \{r : s_{\mathrm{Si}} \leq r \leq R_{\mathrm{Si}}\}$, where s_{Si} is the plastic front for the silicon. We denote the whole silicon domain as $\Omega_{\mathrm{Si}} = \Omega_{\mathrm{Si}}^{p} \cup \Omega_{\mathrm{Si}}^{e}$. To start this analysis simply, we assume the graphite has not yielded so that we have $\Omega_{\mathrm{C}} = \Omega_{\mathrm{C}}^{e} = \{r : R_{\mathrm{Si}} \leq r \leq 1\}$ and $\Omega_{\mathrm{C}}^{p} = \emptyset$.

The yield condition for the silicon in spherical coordinates is written as

$$(\sigma_{rr} - \sigma_{\theta\theta})^2 = (\sigma_{\mathrm{Si}}^{Y})^2, \tag{5.69}$$

and we determine which root of this quadratic to take based on the sign of $\sigma_{rr} - \sigma_{\theta\theta}$ when the silicon initially yields. From Section 5.3.1 we know elastic silicon will first yield at $r = R_V$ and we have

$$(\sigma_{rr} - \sigma_{\theta\theta})|_{r=R_V} = \frac{-6G_{\mathrm{Si}}B_{\mathrm{Si}}}{R_V^3}. \tag{5.70}$$

As both materials are still completely elastic, B_{Si} is given by (3.2c) and we have

$$\frac{-6G_{\mathrm{Si}}B_{\mathrm{Si}}}{R_V^3} = \frac{6G_{\mathrm{Si}}G_{\mathrm{C}}\Lambda_{\mathrm{Si}}\Lambda_{\mathrm{C}}R_{\mathrm{Si}}^3(1 - R_{\mathrm{Si}}^3)(\gamma_{\mathrm{Si}}c_{\mathrm{Si}} - \gamma_{\mathrm{C}}c_{\mathrm{C}})}{\omega_V}. \tag{5.71}$$

As all the terms other than $\gamma_{\text{Si}}c_{\text{Si}} - \gamma_{\text{C}}c_{\text{C}}$ are positive, the sign of $(\sigma_{rr} - \sigma_{\theta\theta})|_{r=R_V}$ is therefore the same as the sign of $(\gamma_{\text{Si}}c_{\text{Si}} - \gamma_{\text{C}}c_{\text{C}})$. As $\gamma_{\text{C}} \approx 3 \times 10^{-2}$ and $\gamma_{\text{Si}} = 1$, it is reasonable to assume that $\gamma_{\text{Si}}c_{\text{Si}} - \gamma_{\text{C}}c_{\text{C}}$ is positive. Therefore, the yield condition for the silicon is $\sigma_{rr} - \sigma_{\theta\theta} = \sigma^Y_{\text{Si}}$. Through a similar analysis, we find that the yield condition for the graphite once the silicon has already yielded is $\sigma_{rr} - \sigma_{\theta\theta} = -\sigma^Y_{\text{C}}$ for this geometry as well.

We substitute $\sigma_{rr} - \sigma_{\theta\theta} = \sigma^Y_{\text{Si}}$ into the mechanical equilibrium equation (5.10) and integrate to find

$$\sigma_{rr} = C_{\text{Si}} - 2\sigma^Y_{\text{Si}} \log(r) \qquad \text{in } \Omega^p_{\text{Si}}. \tag{5.72}$$

Then, using $\sigma_{rr} - \sigma_{\theta\theta} = \sigma^Y_{\text{Si}}$, we have

$$\sigma_{\theta\theta} = C_{\text{Si}} - 2\sigma^Y_{\text{Si}} \log(r) - \sigma^Y_{\text{Si}} \qquad \text{in } \Omega^p_{\text{Si}}. \tag{5.73}$$

The chemical potential of the lithium in Ω^p_{Si} is therefore given by

$$\mu = \mu^{\text{SF}}_{\text{Si}}\big(c^p_{\text{Si}}(r)\big) - S^d_{\text{Si}}\big(3C_{\text{Si}} - 6\sigma^Y_{\text{Si}}\log(r) - 2\sigma^Y_{\text{Si}}\big) \qquad \text{in } \Omega^p_{\text{Si}}. \tag{5.74}$$

The derivation of the displacement of the plastic silicon is identical to the derivation in Section 5.2.2.5, giving

$$u = \frac{1}{r^2}\int_{R_V}^{r} \big(3\gamma_{\text{Si}}c^p_{\text{Si}}(\tilde{r}) + D_{\text{Si}}(\tilde{r})\big)\tilde{r}^2 \, \mathrm{d}\tilde{r} + \frac{E_{\text{Si}}}{r^2} \qquad \text{in } \Omega^p_{\text{Si}}, \tag{5.75}$$

where we have used R_V as the lower integration limit to simplify the boundary conditions. Similar to Section 5.2.2.8, we have

$$D_{\text{Si}}(r) = \big(\boldsymbol{\nabla} \cdot \boldsymbol{u}(r)\big)|_{c_0(s_{\text{Si}}=r)} - 3\gamma_{\text{Si}}c^p_{\text{Si}}(r)|_{c_0(s_{\text{Si}}=r)}. \tag{5.76}$$

We must now use the traction free boundary condition at $r = R_V$, the yield condition at $r = s_{\text{Si}}$ and the continuity of displacement and normal stress at $r = R_{\text{Si}}$ to solve for the integration constants. However, the continuity conditions, and thus the integration constants, will depend on which materials have yielded and if they have fully yielded. To describe each case, we introduce the different regimes of the nano-particle.

5.3.3 Regimes

At a given SOC, the materials in the nano-particles will either be fully yielded, be partially yielded or not have yielded at all. This will cause the different domains in the nano-particle, Ω^p_{Si}, Ω^e_{Si}, Ω^p_{C} and Ω^e_{C} to be empty or not. We refer to each combination of domains that can be present in the nano-particle as regimes and these are depicted in Figure 5.10. We label each regime by the order of the domains from the centre of the nano-particle to the outer radius, with an ‘e’ representing an elastic domain and a ‘p’ representing a yielded domain, separated by a dot. For example, at zero lithiation, the nano-particle is in the e.e regime, or if both materials have partially yielded such that Ω^p_{Si}, Ω^e_{Si}, Ω^p_{C} and Ω^e_{C} are all non-empty, the nano-particle is in the p.e.p.e regime.

In Figure 5.10, we also include arrows denoting the transitions between regimes that can occur in the nano-particle. From the e.e regime, on the left of Figure 5.10 either the silicon layer yields first, resulting in the p.e.e regime, or the graphite yields first, resulting in the e.p.e regime. For higher states of charge, either the silicon or graphite fully yields before the other yields at all, resulting in the p.e and e.p regimes, respectively, or the other material yields as well, resulting in the p.e.p.e regime. Following the e.p or p.e regimes, if the other material yields, the nano-particle is in the p.e.p or p.p.e regimes, respectively. However, if the nano-particle is in the p.e.p.e regime, one of the materials may fully yield from this regime, resulting in the nano-particle being in the p.e.p or p.p.e regime. Finally, if the nano-particle is in the p.e.p or p.p.e regime, the other material may fully yield such that the entire nano-particle is fully yielded, resulting in the p.p regime.

We have previously derived the general displacements, stresses and lithium chemical potentials for each domain, and these are summarised in Table 5.1. The general boundary conditions we have are that the displacement and radial stress are continuous across domain boundaries, there is zero traction at $r = R_V$ and $r = 1$, and if the material has yielded, the yield condition is met at the yielded front, s_a, for $a = \mathrm{Si}, \mathrm{C}$. Depending on the regime the nano-particle is in, the equations for these boundary conditions will be different and thus the integration constants depend on the regime the nano-particle is in. We present the expressions for the integration constants and chemical potentials in each regime, and how each system of equations can be solved numerically, in Appendix E.

5.3.4 Regime Transitions

Of more interest than the displacements and concentrations in the nano-particle, is the conditions under which the nano-particle transitions from each regime to the next. In this section, we derive the geometrical conditions for each of the regime transitions in Figure 5.10. The conditions all apply to the model with lithiation-dependent elastic

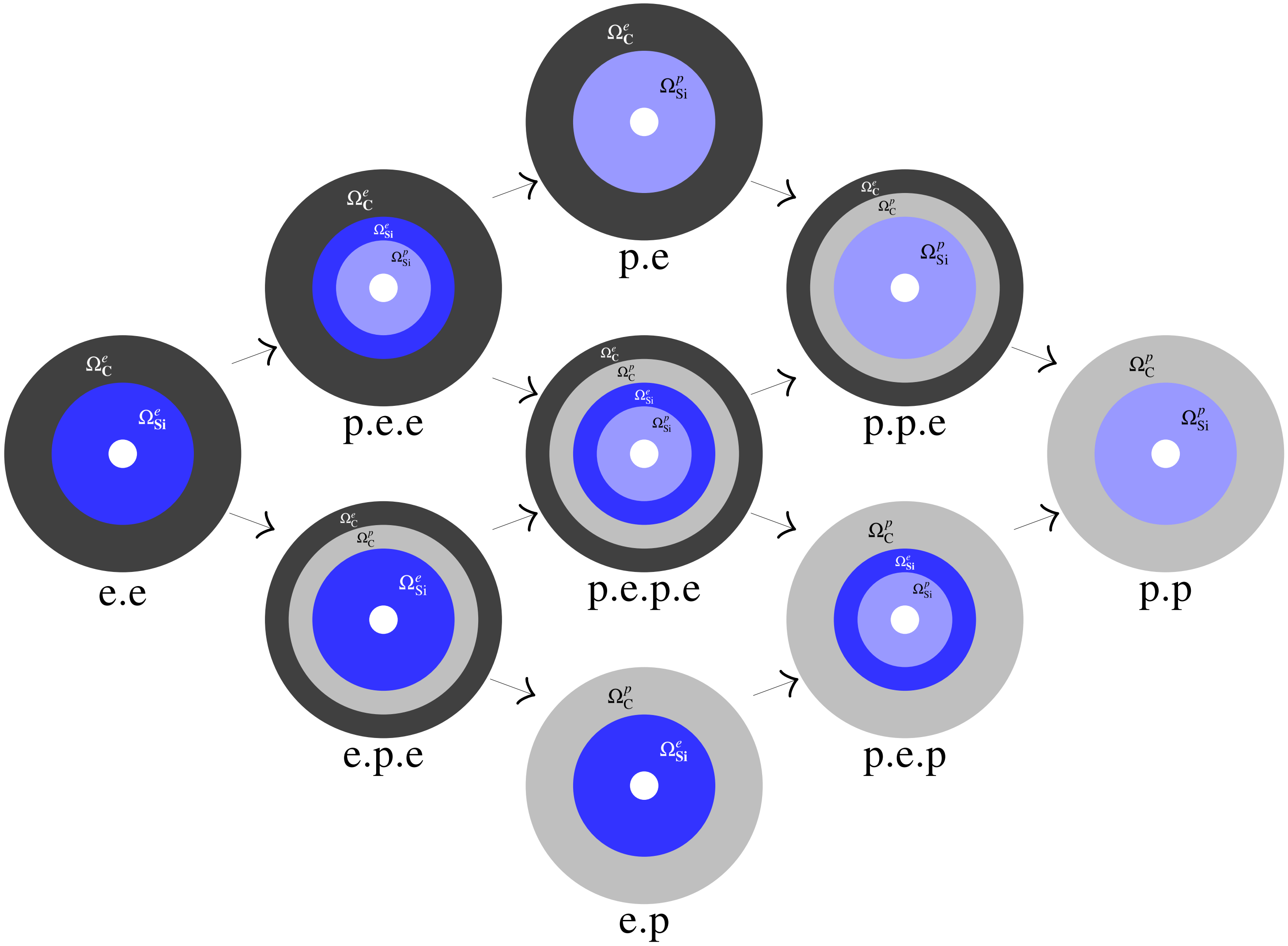

Figure 5.10: The different regimes the nano-particle can be in. The black regions represent Ω^e_C, the dark blue regions represent Ω^e_Si, the light grey regions represent Ω^p_C and the light blue regions repreent Ω^p_Si.

Domain	Displacement	Radial Stress	Li Chemical Potential
Ω^p_{Si}	(5.75)	(5.72)	(5.74)
Ω^e_{Si}	(2.65a)	(2.66a)	(2.67a)
Ω^p_{C}	(5.34)	(5.17)	(5.21b)
Ω^e_{C}	(2.65b)	(2.66b)	(2.67b)

Table 5.1: Equations of the general displacements, radial stresses and lithium chemical potentials for the different domains.

parameters, although we assume that the yield stresses of both materials and the maximum deviatoric stress of the graphite are lithiation-independent.

5.3.4.1 e.e

In Section 5.3.1, we derived the condition determining whether the silicon or the graphite yields at a lower SOC. This same condition determines whether the nano-particle in the e.e regime transitions to the p.e.e regime or the e.p.e regime, thus this transition condition is given by

$$\text{e.e} \rightarrow \begin{cases} \text{p.e.e} & \text{if } R_V^3 > R_{\mathrm{Si}}^3 - \frac{\sigma_{\mathrm{C}}^Y}{\sigma_{\mathrm{Si}}^Y} R_{\mathrm{Si}}^3(1 - R_{\mathrm{Si}}^3), \\ \text{e.p.e} & \text{if } R_V^3 < R_{\mathrm{Si}}^3 - \frac{\sigma_{\mathrm{C}}^Y}{\sigma_{\mathrm{Si}}^Y} R_{\mathrm{Si}}^3(1 - R_{\mathrm{Si}}^3). \end{cases} \tag{5.77}$$

5.3.4.2 p.e.e

We now derive the transition condition between the p.e.e regime to either the p.e regime or the p.e.p.e regime. The nano-particle will transition to the p.e regime if s_{Si} reaches R_{Si} at a lower SOC than that at which the yield condition of the graphite is met. The yield condition for the graphite is given by (5.22) and we need to calculate $\sigma_{rr} - \sigma_{\theta\theta}$ to find which root of this quadratic to take. The maximum yield function of the graphite is given by (5.23) at $r = R_{\mathrm{Si}}$. From the integration constants derived in Section E.2, we have that

$$f_{\mathrm{C}}^{\mathrm{VM}} = \frac{-6G_{\mathrm{C}}B_{\mathrm{C}}}{R_{\mathrm{Si}}^3} = \frac{-\sigma_{\mathrm{Si}}^Y}{1 - R_{\mathrm{Si}}^3}\left[1 - \frac{s_{\mathrm{Si}}^3}{R_{\mathrm{Si}}^3} - \log\left(\frac{R_V^3}{s_{\mathrm{Si}}^3}\right)\right]. \tag{5.78}$$

As $R_V \leq s_{\mathrm{Si}} \leq R_{\mathrm{Si}}$ and $\sigma_{\mathrm{Si}}^Y > 0$, we can conclude that $\sigma_{rr} - \sigma_{\theta\theta} < 0$ for the elastic graphite in the p.e.e regime. Therefore, the graphite yields in the p.e.e regime at $r = R_{\mathrm{Si}}$ when $\sigma_{rr} - \sigma_{\theta\theta} = -\sigma_{\mathrm{C}}^Y$.

As the silicon fully yields, $s_{\mathrm{Si}} \to R_{\mathrm{Si}}$, and

$$f_{\mathrm{C}}^{\mathrm{VM}} \to \frac{\sigma_{\mathrm{Si}}^{Y}}{1 - R_{\mathrm{Si}}^{3}} \log\left(\frac{R_V^3}{R_{\mathrm{Si}}^3}\right). \tag{5.79}$$

Therefore, if the magnitude of (5.79) does not exceed that of the yield stress, σ_{C}^{Y}, the silicon layer will fully yield before the graphite will yield at all. We can summarise this transition condition by rearranging (5.79) to give

$$\text{p.e.e} \to \begin{cases} \text{p.e} & \text{if } R_V^3 > R_{\mathrm{Si}}^3 \exp\left(-\frac{\sigma_{\mathrm{C}}^{Y}}{\sigma_{\mathrm{Si}}^{Y}}(1 - R_{\mathrm{Si}}^3)\right), \\ \text{p.e.p.e} & \text{if } R_V^3 < R_{\mathrm{Si}}^3 \exp\left(-\frac{\sigma_{\mathrm{C}}^{Y}}{\sigma_{\mathrm{Si}}^{Y}}(1 - R_{\mathrm{Si}}^3)\right). \end{cases} \tag{5.80}$$

5.3.4.3 e.p.e

If the graphite yields first, the nano-particle is in the e.p.e regime. Similar to the p.e.e regime, the transition from the e.p.e regime to the e.p or p.e.p.e regimes is determined by whether the pulverised front of the graphite, s_{C}, reaches $r = 1$ at a lower SOC than that at which the yield function of the silicon at $r = R_V$ exceeds σ_{Si}^{Y}. From the boundary conditions in the e.p.e regime in Section E.3, the yield function is given by

$$f_{\mathrm{Si}}^{\mathrm{VM}} = \frac{-6G_{\mathrm{Si}}B_{\mathrm{Si}}}{R_V^3} = \frac{R_{\mathrm{Si}}^3}{R_{\mathrm{Si}}^3 - R_V^3}\left[\sigma_{\mathrm{C}}^{Y}(1 - s_{\mathrm{C}}^3) + \sigma_p^{\max} \log\left(\frac{s_{\mathrm{C}}^3}{R_{\mathrm{Si}}^3}\right)\right]. \tag{5.81}$$

As $R_{\mathrm{Si}} \leq s_{\mathrm{C}} \leq 1$, $R_{\mathrm{Si}} > R_V$ and $\sigma_{\mathrm{C}}^{Y}, \sigma_p^{\max} > 0$, we have $\sigma_{rr} - \sigma_{\theta\theta} > 0$ for the elastic silicon in the e.p.e regime. Therefore, the silicon yields at $r = R_V$ when $\sigma_{rr} - \sigma_{\theta\theta} = \sigma_{\mathrm{Si}}^{Y}$.

As the graphite approaches fully pulverising, $s_{\mathrm{C}} \to 1$ and

$$f_{\mathrm{Si}}^{\mathrm{VM}} \to \frac{-\sigma_p^{\max} R_{\mathrm{Si}}^3}{R_{\mathrm{Si}}^3 - R_V^3} \log(R_{\mathrm{Si}}^3). \tag{5.82}$$

Therefore, if this does not exceed the yield stress for silicon, σ_{Si}^{Y}, the graphite will fully yield before the silicon yields at all. This is summarised as

$$\text{e.p.e} \to \begin{cases} \text{e.p} & \text{if } R_V^3 < \frac{\sigma_p^{\max}}{\sigma_{\mathrm{Si}}^{Y}} R_{\mathrm{Si}}^3 \log(R_{\mathrm{Si}}^3) + R_{\mathrm{Si}}^3, \\ \text{p.e.p.e} & \text{if } R_V^3 > \frac{\sigma_p^{\max}}{\sigma_{\mathrm{Si}}^{Y}} R_{\mathrm{Si}}^3 \log(R_{\mathrm{Si}}^3) + R_{\mathrm{Si}}^3. \end{cases} \tag{5.83}$$

5.3.4.4 p.e and e.p

Using the expressions for B_{C} and B_{Si} in Sections E.5 and E.6, the yield functions for graphite at $r = R_{\mathrm{Si}}$ in the p.e regime and for silicon at $r = R_V$ in the e.p regimes are

$$\frac{-6G_{\mathrm{C}}B_{\mathrm{C}}}{R_{\mathrm{Si}}^3} = \frac{3\sigma_{\mathrm{Si}}^{Y}}{1 - R_{\mathrm{Si}}^3} \log\left(\frac{R_V}{R_{\mathrm{Si}}}\right), \tag{5.84a}$$

$$\frac{-6G_{\mathrm{Si}}B_{\mathrm{Si}}}{R_V^3} = \frac{-3\sigma_p^{\max} R_{\mathrm{Si}}^3}{R_{\mathrm{Si}}^3 - R_V^3}, \tag{5.84b}$$

respectively. Under the current assumptions of the model, these yield functions are both independent of the concentration. Therefore, if one material has fully yielded without the other yielding at all, the unyielded material will not yield at higher states of charge as the yield stress will never be exceeded. Therefore, the nano-particle will not transition from the p.e or e.p regimes.

As discussed, several studies have found that the yield stress of lithiated silicon is a function of lithiation state. If the lithiation-dependence of σ_{Si}^{Y} is included in the model, the yield function for the graphite (5.84a) is therefore a function of the SOC and thus, the graphite could yield at a certain SOC, causing the nano-particle to transition to the p.p.e regime. Likewise, if the maximum deviatoric stress of the pulverised graphite, $\sigma_p^{\max}$, was also modelled as a function of the lithiation state, the nano-particle could transition from the e.p regime to the p.e.p regime.

5.3.4.5 p.e.p.e

If both materials have partially yielded, the nano-particle is in the p.e.p.e regime and will either transition to the p.e.p or p.p.e regime. This is determined by whether s_{Si} reaches R_{Si} at a lower SOC than s_{C} reaches the outer radius of the nano-particle. Using the boundary conditions in the p.e.p.e regime in Section E.4, s_{Si} and s_{C} are related by

$$\sigma_{\mathrm{Si}}^{Y}\left[\log\left(\frac{s_{\mathrm{Si}}^3}{R_V^3}\right)+1-\frac{s_{\mathrm{Si}}^3}{R_{\mathrm{Si}}^3}\right]=\sigma_p^{\max}\log\left(\frac{s_{\mathrm{C}}^3}{R_{\mathrm{Si}}^3}\right)+\sigma_{\mathrm{C}}^{Y}(1-s_{\mathrm{C}}^3). \tag{5.85}$$

The left- and right-hand sides of (5.85) are increasing functions of s_{Si} and s_{C}, respectively, and we expect both s_{Si} and s_{C} to increase with the SOC. Therefore, if the left-hand side of (5.85) as $s_{\mathrm{Si}} \to R_{\mathrm{Si}}$ is greater than the right-hand side as $s_{\mathrm{C}} \to 1$, the plastic front, s_{Si}, will reach $r = R_{\mathrm{Si}}$ at a lower SOC than that at which s_{C} reaches $r = 1$. By setting $s_{\mathrm{Si}} = R_{\mathrm{Si}}$ and $s_{\mathrm{C}} = 1$, we have that if

$$\sigma_{\mathrm{Si}}^{Y}\log\left(\frac{R_{\mathrm{Si}}}{R_V}\right) < -\sigma_p^{\max}\log(R_{\mathrm{Si}}), \tag{5.86}$$

the nano-particle in the p.e.p.e regime will transition to the p.p.e regime and it will transition to the p.e.p regime otherwise. Therefore, we rearrange (5.86) to write the transition condition from the p.e.p.e regime as

$$\text{p.e.p.e} \to \begin{cases} \text{p.e.p} & \text{if } R_V^3 < (R_{\mathrm{Si}}^3)^{1+(\sigma_p^{\max}/\sigma_{\mathrm{Si}}^{Y})} \\ \text{p.p.e} & \text{if } R_V^3 > (R_{\mathrm{Si}}^3)^{1+(\sigma_p^{\max}/\sigma_{\mathrm{Si}}^{Y})}. \end{cases} \tag{5.87}$$

5.3.4.6 p.p.e and p.e.p

From the boundary conditions for the p.p.e and p.e.p regimes in Sections E.7 and E.8, respectively, we find that s_{Si} and s_{C} are given by

$$3\sigma_p^{\max}\log(R_{\text{Si}}) + 3\sigma_{\text{Si}}^Y \log\left(\frac{s_{\text{Si}}}{R_V}\right) = \sigma_{\text{Si}}^Y\left(\frac{s_{\text{Si}}^3}{R_{\text{Si}}^3} - 1\right), \tag{5.88a}$$

$$3\sigma_{\text{Si}}^Y \log\left(\frac{R_V}{R_{\text{Si}}}\right) + 3\sigma_p^{\max}\log\left(\frac{s_{\text{C}}}{R_{\text{Si}}}\right) = \sigma_{\text{C}}^Y(s_{\text{C}}^3 - 1), \tag{5.88b}$$

respectively. As these are both algebraic equations and not functions of lithium concentration, s_{Si} and s_{C} are both constant in the p.e.p and p.p.e regimes, respectively. Therefore, the nano-particle cannot transition from the p.p.e and p.e.p regimes to the p.p regime. Similarly to the transitions from the p.e and e.p regimes in Section 5.3.4.4, if σ_{Si}^Y or σ_{C}^Y are functions of lithiation state, the transition to the p.p regime is possible.

5.3.4.7 p.p

The boundary conditions from the p.p regime, other than the continuity of displacement condition, given by

$$C_{\text{Si}} = 2\sigma_{\text{Si}}^Y \log(R_V), \tag{5.89a}$$

$$C_{\text{Si}} - 2\sigma_{\text{Si}}^Y \log(R_{\text{Si}}) = C_{\text{C}} + 2\sigma_p^{\max}\log(R_{\text{Si}}), \tag{5.89b}$$

$$C_{\text{C}} = -2\sigma_p^{\max}\log(1) = 0, \tag{5.89c}$$

yield the condition

$$R_V^3 = (R_{\text{Si}}^3)^{1+(\sigma_p^{\max}/\sigma_{\text{Si}}^Y)}. \tag{5.90}$$

This is the condition at which neither of (5.87) are satisfied and is a necessary condition for the nano-particle to be in the p.p regime. Therefore, the p.p regime will only occur from the p.e.p.e regime if both the silicon and the graphite fully yield at the same SOC.

5.3.5 Regime Path Phase Diagram

The inequalities determining the regime transitions of the nano-particle in the previous section can be used to produce a phase diagram in (R_{Si}^3, R_V^3) space to identify which regimes the nano-particle will go through during lithiation. We refer to the order of the regimes that the nano-particle goes through during lithiation as the regime path. We use $\sigma_p^{\max} = \sigma_{\text{C}}^Y$ and plot the phase diagram for several different values of $\sigma_{\text{C}}^Y/\sigma_{\text{Si}}^Y$ in Figure 5.11. We present the regime paths of the nano-particle in Figure 5.12

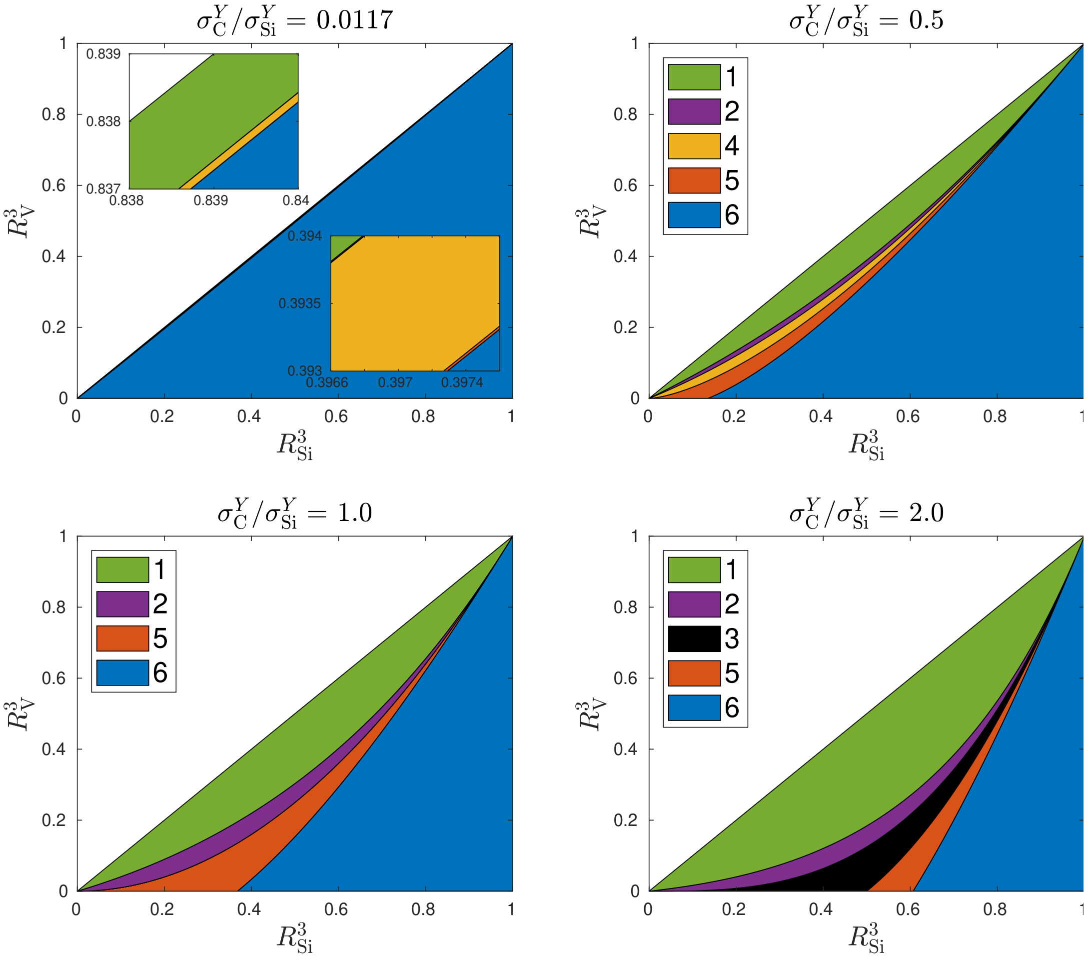

Figure 5.11: Phase diagrams in $(R^3_{\mathrm{Si}}, R^3_V)$ space of the regime paths for different values of $\sigma^Y_{\mathrm{C}}/\sigma^Y_{\mathrm{Si}}$. The phases are labelled 1-6 according to the regime paths displayed in Figure 5.12. The inset plots in the $\sigma^Y_{\mathrm{C}}/\sigma^Y_{\mathrm{Si}} = 0.0117$ plot show the small regions for the regime paths other than 6 in this case.

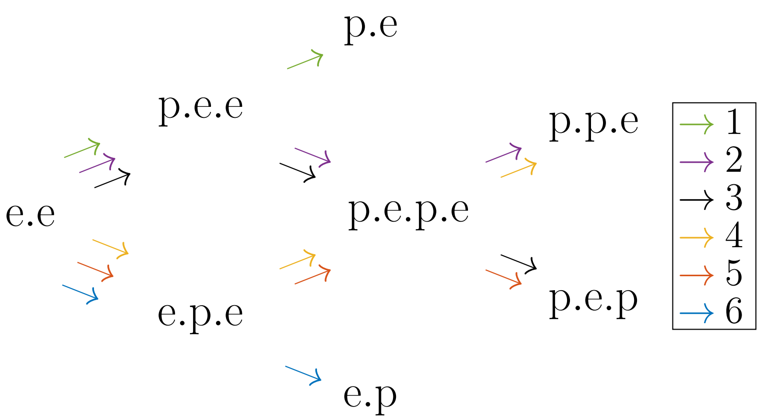

Figure 5.12: Regime paths, corresponding to the phases in Figure 5.11 and labelled one through six.

with the colours of the arrows between regimes corresponding colours of the areas in Figure 5.11.

We see that for the values of σ_{C}^{Y} and σ_{Si}^{Y} from the literature, giving $\sigma_{\mathrm{C}}^{Y}/\sigma_{\mathrm{Si}}^{Y} = 0.0117$, almost all of the viable phase diagram is occupied by regime path 6. This is due to the weak graphite shell yielding much more easily than the silicon, so even for a thin silicon layer, the expansion is great enough to cause the graphite to yield fully before the silicon yields at all, resulting in the nano-particle being in the e.p regime at high states of charge. From the inequalities in Section 5.3.4, we can see that the small value of $\sigma_{\mathrm{C}}^{Y}/\sigma_{\mathrm{Si}}^{Y}$ causes the phase boundaries to be approximately given by $R_V^3 = R_{\mathrm{Si}}^3$, giving the narrow range of viable nano-particle geometries for these regime paths. This is especially apparent for regime paths 2 and 5 shown in the lower-right inset plot of the $\sigma_{\mathrm{C}}^{Y}/\sigma_{\mathrm{Si}}^{Y} = 0.0117$ subplot of Figure 5.11.

The limit as $\sigma_{\mathrm{C}}^{Y}/\sigma_{\mathrm{Si}}^{Y} \to 0$ tends to the case in which the only regime path the nano-particle can have is 6. The $\sigma_p^{\max} = 0$ but $\sigma_{\mathrm{C}}^{Y} > 0$ case considered in Section 5.2.3.4 removes any possibility of regime paths 2, 4 and 5. This is because the inequalities (5.83) and (5.87) reduce to $R_V^3 < R_{\mathrm{Si}}^3$ in this case which is always satisfied in this geometry.

Comparing the diagrams for $\sigma_{\mathrm{C}}^{Y}/\sigma_{\mathrm{Si}}^{Y} = 0.5$ and 2.0, we can see that regime path 3 is not permitted by any geometries for $\sigma_{\mathrm{C}}^{Y}/\sigma_{\mathrm{Si}}^{Y} = 0.5$ and regime path 4 is not permitted for $\sigma_{\mathrm{C}}^{Y}/\sigma_{\mathrm{Si}}^{Y} = 2.0$. We see from the $\sigma_{\mathrm{C}}^{Y}/\sigma_{\mathrm{Si}}^{Y} = 1.0$ case that there is a bifurcation in the phase diagram at this parameter value. For inner layers with higher yield stresses than the shell ($\sigma_{\mathrm{C}}^{Y}/\sigma_{\mathrm{Si}}^{Y} < 1$), regime path 3 is not possible and for shells with higher yield stresses than the inner layer ($\sigma_{\mathrm{C}}^{Y}/\sigma_{\mathrm{Si}}^{Y} > 1$), regime path 4 is not possible. This implies that if the geometry is such that the material with the greater yield stress yields first, it must yield completely before the other material yields completely, as seen in Figure 5.12.

Finally, in the $\sigma_{\mathrm{C}}^{Y}/\sigma_{\mathrm{Si}}^{Y} = 1.0$ case, neither regime paths 3 or 4 are possible for any viable nano-particle geometry. This implies that the first material to yield, whether the shell or the inner layer, will fully yield before the other material. This can be seen analytically by both (5.77) and (5.87) reducing to the same inequality for $\sigma_{\mathrm{C}}^{Y} = \sigma_{\mathrm{Si}}^{Y}$.

This phase diagram can act as a guide to which geometries of nano-particle will cause the desired yielding behaviour of the nano-particle. For example, from Figure 5.12, we can see that to ensure that the shell material does not fully yield, we have a nano-particle which follows the regime paths 1, 2 or 4 assuming the nano-particle transitions through the entire regime path. This is given by the p.e.p.e → p.p.e condition in (5.87). However, to ensure that the shell material does not yield at all the p.e.e → p.e condition in (5.80) must be satisfied and the condition for the inner layer yielding first in (5.77) will automatically be satisfied as well.

5.3.6 Maximum Capacity for $s_{\mathrm{C}} < 1$

We now investigate whether the model presented in this chapter predicts that the inclusion of a central void into the nano-particle will increase the maximum capacity of the nano-particle such that the pulverised front will not reach the outer radius of the nano-particle at full lithiation. For this geometry, the maximum capacity of the nano-particle is given by

$$Q^{\max} = R_{\mathrm{Si}}^3 - R_V^3 + \frac{c_{\mathrm{C}}^{\max}}{c_{\mathrm{Si}}^{\max}}(1 - R_{\mathrm{Si}}^3). \tag{5.91}$$

Therefore, for a given outer radius of the silicon layer, R_{Si}, this will be maximised when we minimise the initial volume of the central void, R_V^3. To find the value of R_V at which the graphite will fully yield as the nano-particle fully lithiates, we take a similar approach to Section 5.2.3.3. We set $c_{\mathrm{Si}} = c_{\mathrm{C}} = c_{\mathrm{Si}}^p = c_{\mathrm{C}}^p = s_{\mathrm{C}} = 1$ in the equation relating the concentrations to the position of the yielded fronts for each regime, take the Lamé parameters at their fully lithiated values, and use $\sigma_p^{\max} = \sigma_{\mathrm{C}}^Y$. We state these equations without derivations in this section, saving the derivations for Appendix E. In this section, we aim to find the minimum R_V such that the graphite does not fully pulverise at full lithiation, denoted by R_V^{crit}, as a function of R_{Si}.

For R_{Si} values less than $R_{\mathrm{Si}}^{\mathrm{crit}}$, as derived in Section 5.2.3.3, a nano-particle without a core will be the optimal design as adding a central void will only decrease the maximum capacity. We assume R_V^{crit} will be a smooth function of R_{Si} and therefore, as R_{Si} increases from $R_{\mathrm{Si}}^{\mathrm{crit}}$, the nano-particle with the optimal geometry will be on regime path 6, as shown by the phase diagrams in Figure 5.11. However, the nano-particle must still be in the e.p.e regime at full lithiation for the graphite to not have fully yielded. The equation relating the lithium concentrations and s_{C} for the e.p.e regime is given by

$$\begin{aligned} 3\gamma_{\mathrm{C}} \int_{R_{\mathrm{Si}}}^{s_{\mathrm{C}}} c_{\mathrm{C}}^p(\tilde{r})\tilde{r}^2 \, \mathrm{d}\tilde{r} = {} & \frac{\sigma_{\mathrm{C}}^Y}{3\Lambda_{\mathrm{C}}}(s_{\mathrm{C}}^6 + R_{\mathrm{Si}}^6) + \frac{\sigma_{\mathrm{C}}^Y s_{\mathrm{C}}^3}{6G_{\mathrm{C}}} + \gamma_{\mathrm{C}} c_{\mathrm{C}} s_{\mathrm{C}}^3 - \gamma_{\mathrm{Si}} c_{\mathrm{Si}} R_{\mathrm{Si}}^3 \\ & + \frac{\sigma_{\mathrm{C}}^Y R_{\mathrm{Si}}^3 (4G_{\mathrm{Si}} R_{\mathrm{Si}}^3 + \Lambda_{\mathrm{Si}} R_V^3)}{6G_{\mathrm{Si}}\Lambda_{\mathrm{Si}}(R_{\mathrm{Si}}^3 - R_V^3)} \left[1 - s_{\mathrm{C}}^3 + \log\left(\frac{s_{\mathrm{C}}^3}{R_{\mathrm{Si}}^3}\right)\right]. \end{aligned} \tag{5.92}$$

Setting $c_{\mathrm{Si}} = c_{\mathrm{C}} = c_{\mathrm{C}}^p = s_{\mathrm{C}} = 1$ gives

$$\frac{\sigma_{\mathrm{C}}^Y}{3\Lambda_{\mathrm{C}}}(1 + R_{\mathrm{Si}}^6) + \frac{\sigma_{\mathrm{C}}^Y}{6G_{\mathrm{C}}} + (\gamma_{\mathrm{C}} - \gamma_{\mathrm{Si}})R_{\mathrm{Si}}^3 - \frac{\sigma_{\mathrm{C}}^Y R_{\mathrm{Si}}^3 (4G_{\mathrm{Si}} R_{\mathrm{Si}}^3 + \Lambda_{\mathrm{Si}} R_V^3)}{6G_{\mathrm{Si}}\Lambda_{\mathrm{Si}}(R_{\mathrm{Si}}^3 - R_V^3)} \log(R_{\mathrm{Si}}^3) = 0. \tag{5.93}$$

We can see that this reduces to the expression we solve to find $R_{\mathrm{Si}}^{\mathrm{crit}}$ in (5.52) as $R_V \to 0$. Rearranging (5.93) gives

$$\left(R_V^{\mathrm{crit}}\right)^3 = \frac{\mathcal{F}_{\mathrm{e.p.e}}}{\mathcal{G}_{\mathrm{e.p.e}}}, \tag{5.94a}$$

where

$$\begin{aligned} \mathcal{F}_{\mathrm{e.p.e}} = {} & 4\sigma_{\mathrm{C}}^Y G_{\mathrm{Si}} G_{\mathrm{C}} \Lambda_{\mathrm{C}} R_{\mathrm{Si}}^3 \log(R_{\mathrm{Si}}^3) \\ & - G_{\mathrm{Si}} \Lambda_{\mathrm{Si}} R_{\mathrm{Si}}^3 (6 G_{\mathrm{C}} \Lambda_{\mathrm{C}} (\gamma_{\mathrm{C}} - \gamma_{\mathrm{Si}}) R_{\mathrm{Si}}^3 + 2\sigma_{\mathrm{C}}^Y G_{\mathrm{C}} (1 + R_{\mathrm{Si}}^6) + \sigma_{\mathrm{C}}^Y \Lambda_{\mathrm{C}}), \end{aligned} \tag{5.94b}$$

$$\begin{aligned} \mathcal{G}_{\mathrm{e.p.e}} = {} & 6 G_{\mathrm{Si}} G_{\mathrm{C}} \Lambda_{\mathrm{Si}} \Lambda_{\mathrm{C}} (\gamma_{\mathrm{Si}} - \gamma_{\mathrm{C}}) R_{\mathrm{Si}}^3 - 2\sigma_{\mathrm{C}}^Y G_{\mathrm{Si}} G_{\mathrm{C}} \Lambda_{\mathrm{Si}} (1 + R_{\mathrm{Si}}^6) \\ & - \sigma_{\mathrm{C}}^Y G_{\mathrm{Si}} \Lambda_{\mathrm{Si}} \Lambda_{\mathrm{C}} - \sigma_{\mathrm{C}}^Y G_{\mathrm{C}} \Lambda_{\mathrm{Si}} \Lambda_{\mathrm{C}} R_{\mathrm{Si}}^3 \log(R_{\mathrm{Si}}^3). \end{aligned} \tag{5.94c}$$

Therefore, (5.94) is the minimum value of R_V^3 such that the graphite will not be fully pulverised at full lithiation if the nano-particle is on regime path 6, the condition for which is given by the bound (5.83).

As R_{Si} increases and R_V^{crit} increases according to (5.94), the nano-particle geometry required for $s_{\mathrm{C}} < 1$ will eventually move out of the feasible region for regime path 6 and into the region for regime path 5. This transition occurs at

$$R_V^3 = R_{\mathrm{Si}}^3 + \frac{\sigma_{\mathrm{C}}^Y}{\sigma_{\mathrm{Si}}^Y} R_{\mathrm{Si}}^3 \log(R_{\mathrm{Si}}^3). \tag{5.95}$$

The R_{Si} value at which the transition occurs is calculated by numerically solving

$$\frac{\mathcal{F}_{\mathrm{e.p.e}}}{\mathcal{G}_{\mathrm{e.p.e}}} = R_{\mathrm{Si}}^3 + \frac{\sigma_{\mathrm{C}}^Y}{\sigma_{\mathrm{Si}}^Y} R_{\mathrm{Si}}^3 \log(R_{\mathrm{Si}}^3), \tag{5.96}$$

for R_{Si}.

For nano-particles on regime path 5, the silicon will yield at a lower SOC than that at which the graphite fully yields. Therefore, as $s_{\mathrm{C}} \to 1$, the nano-particle will be in the p.e.p.e regime. The equation relating the yielded fronts and the concentration in the p.e.p.e regime is given by

$$\begin{aligned} 3\gamma_{\mathrm{C}} \int_{R_{\mathrm{Si}}}^{s_{\mathrm{C}}} c_{\mathrm{C}}^p(\tilde{r}) \tilde{r}^2 \, \mathrm{d}\tilde{r} = {} & \frac{\sigma_{\mathrm{C}}^Y}{3\Lambda_{\mathrm{C}}} (s_{\mathrm{C}}^6 + R_{\mathrm{Si}}^6) + \frac{\sigma_{\mathrm{C}}^Y s_{\mathrm{C}}^3}{6 G_{\mathrm{C}}} + \frac{2\sigma_{\mathrm{Si}}^Y R_{\mathrm{Si}}^3}{3\Lambda_{\mathrm{Si}}} \left[\log\left(\frac{s_{\mathrm{Si}}^3}{R_V^3} \right) + 1 \right] \\ & + \frac{\sigma_{\mathrm{Si}}^Y s_{\mathrm{Si}}^3}{6 G_{\mathrm{Si}}} + \gamma_{\mathrm{C}} c_{\mathrm{C}} s_{\mathrm{C}}^3 - \gamma_{\mathrm{Si}} c_{\mathrm{Si}} R_{\mathrm{Si}}^3, \end{aligned} \tag{5.97a}$$

and the two yielded fronts are related by

$$\sigma_{\mathrm{Si}}^Y \left[\log\left(\frac{s_{\mathrm{Si}}^3}{R_V^3} \right) + 1 - \frac{s_{\mathrm{Si}}^3}{R_{\mathrm{Si}}^3} \right] = \sigma_{\mathrm{C}}^Y \left[\log\left(\frac{s_{\mathrm{C}}^3}{R_{\mathrm{Si}}^3} \right) + 1 - s_{\mathrm{C}}^3 \right]. \tag{5.97b}$$

Setting $c_{\mathrm{Si}} = c_{\mathrm{C}} = c_{\mathrm{C}}^{p} = s_{\mathrm{C}} = 1$ gives

$$\frac{\sigma_{\mathrm{C}}^{Y}}{3\Lambda_{\mathrm{C}}}(1 + R_{\mathrm{Si}}^{6}) + \frac{\sigma_{\mathrm{C}}^{Y}}{6G_{\mathrm{C}}} + \frac{2\sigma_{\mathrm{Si}}^{Y}R_{\mathrm{Si}}^{3}}{3\Lambda_{\mathrm{Si}}}\left[\log\left(\frac{s_{\mathrm{Si}}^{3}|_{s_{\mathrm{C}}=1}}{R_{V}^{3}}\right) + 1\right] + \frac{\sigma_{\mathrm{Si}}^{Y}s_{\mathrm{Si}}^{3}|_{s_{\mathrm{C}}=1}}{6G_{\mathrm{Si}}} + (\gamma_{\mathrm{C}} - \gamma_{\mathrm{Si}})R_{\mathrm{Si}}^{3} = 0, \tag{5.98a}$$

where $s_{\mathrm{Si}}|_{s_{\mathrm{C}}=1}$ is the solution to

$$\sigma_{\mathrm{Si}}^{Y}\left[\log\left(\frac{s_{\mathrm{Si}}^{3}}{R_{V}^{3}}\right) + 1 - \frac{s_{\mathrm{Si}}^{3}}{R_{\mathrm{Si}}^{3}}\right] + \sigma_{\mathrm{C}}^{Y}\log(R_{\mathrm{Si}}^{3}) = 0. \tag{5.98b}$$

Solving (5.98) for R_V at a given R_{Si} produces the value of R_V^{crit} for nano-particles in regime path 5.

For $\sigma_{\mathrm{C}}^{Y} < \sigma_{\mathrm{Si}}^{Y}$, as the value of R_V increases, it eventually moves out of the feasible region for the nano-particle to be on regime path 5 and moves onto regime path 4. This occurs when $s_{\mathrm{Si}}|_{s_{\mathrm{C}}=1} = R_{\mathrm{Si}}$ and also when $R_V = R_{\mathrm{Si}}^{\sigma_{\mathrm{C}}^{Y}/\sigma_{\mathrm{Si}}^{Y}+1}$. Substituting these into (5.98a) yields

$$\frac{\sigma_{\mathrm{C}}^{Y}}{3\Lambda_{\mathrm{C}}}(1+R_{\mathrm{Si}}^{6})+\frac{\sigma_{\mathrm{C}}^{Y}}{6G_{\mathrm{C}}}-\frac{2\sigma_{\mathrm{Si}}^{Y}R_{\mathrm{Si}}^{3}}{3\Lambda_{\mathrm{Si}}}\log(R_{\mathrm{Si}}^{3})+\frac{\sigma_{\mathrm{Si}}^{Y}R_{\mathrm{Si}}^{3}}{6G_{\mathrm{Si}}}+\frac{\sigma_{\mathrm{Si}}^{Y}R_{\mathrm{Si}}^{3}}{3\Lambda_{\mathrm{Si}}}+(\gamma_{\mathrm{C}}-\gamma_{\mathrm{Si}})R_{\mathrm{Si}}^{3} = 0. \tag{5.99}$$

For greater values of R_{Si}, the nano-particle must be on regime path 4 to avoid fully pulverising the graphite. For regime paths 1, 2 and 4, we have shown that the graphite never fully yields as the silicon does so at a lower SOC. Therefore, the R_V^{crit} for R_{Si} values greater than the solution to (5.99) will be the lower bound of the R_V such that the nano-particle is on regime path 4, given by $R_V = R_{\mathrm{Si}}^{\sigma_{\mathrm{C}}^{Y}/\sigma_{\mathrm{Si}}^{Y}+1}$.

In summary, R_V^{crit} is given by

$$(R_V^{\mathrm{crit}})^3 = \begin{cases} \frac{\mathcal{F}_{\mathrm{e.p.e}}}{\mathcal{G}_{\mathrm{e.p.e}}} & \text{if } R_{\mathrm{Si}}^{\mathrm{crit}} \le R_{\mathrm{Si}} \le \text{sol}^{\underline{\text{n}}} \text{ to (5.96)}, \\ \text{sol}^{\underline{\text{n}}} \text{ to (5.98)} & \text{if sol}^{\underline{\text{n}}} \text{ to (5.96)} < R_{\mathrm{Si}} \le \text{sol}^{\underline{\text{n}}} \text{ to (5.99)}, \\ R_{\mathrm{Si}}^{3(\sigma_{\mathrm{C}}^{Y}/\sigma_{\mathrm{Si}}^{Y}+1)} & \text{if sol}^{\underline{\text{n}}} \text{ to (5.99)} < R_{\mathrm{Si}} \le 1, \end{cases} \tag{5.100}$$

where we have used sol$^{\underline{\text{n}}}$ as short-hand for ‘solution’. The solution (5.100) is valid for all nano-particles, regardless of the relative yield stresses of the two materials. However, if $\sigma_{\mathrm{C}}^{Y}/\sigma_{\mathrm{Si}}^{Y}$ becomes too large, the transition from the regime path 6 solution to the regime path 5 solution, given by (5.96), is at a negative value of R_V. The regime path 6 solution (5.94) will therefore not be valid because $R_V^3 < 0$. Thus the solution to (5.98) is valid from $R_{\mathrm{Si}}^3 = 0$. If $\sigma_{\mathrm{C}}^{Y}/\sigma_{\mathrm{Si}}^{Y} \ge 1$, the nano-particle can also be on regime path 3 in which the final regime is p.e.p. Therefore, $(R_V^{\mathrm{crit}})^3$ is given by the solution to (5.98) for the nano-particle geometries on regime path 3 as well. Then, for R_{Si}^3 and $(R_V^{\mathrm{crit}})^3$ values such that the nano-particle is on regime path 2, the solution

$(R_V^{\mathrm{crit}})^3$ follows the minimum R_V^3 for regime path 2. For $\sigma_{\mathrm{C}}^Y/\sigma_{\mathrm{Si}}^Y \geq 1$, the minimum R_V^3 to be on regime path 2 is $R_V = R_{\mathrm{Si}}^{\sigma_{\mathrm{C}}^Y/\sigma_{\mathrm{Si}}^Y+1}$. This shows that the solution still has the form as (5.100) for $\sigma_{\mathrm{C}}^Y \geq \sigma_{\mathrm{Si}}^Y$.

In Figure 5.13, we plot $(R_V^{\mathrm{crit}})^3$ against R_{Si}^3, for the literature value of σ_{C}^Y, and as multiples of the literature value of σ_{C}^Y. These depend not only on the ratio between the yield stresses but also on the yield stresses themselves because the SOC at which the graphite shell yields differs with the yield stress of graphite, not just the ratio between the yield stresses of the core and shell. We also plot $(R_V^{\mathrm{crit}})^3$ for the cases in which the nano-particle is not in the p.p.e regime at full lithiation for the literature value of σ_{C}^Y. We see that for almost all values of R_{Si}^3, the solution is given by $(R_V^{\mathrm{crit}})^3 = R_{\mathrm{Si}}^{3(\sigma_{\mathrm{C}}^Y/\sigma_{\mathrm{Si}}^Y+1)}$ with the fully lithiated nano-particle being in the p.p.e regime. We see that the value of R_{Si}^3 at which $R_V^{\mathrm{crit}} = 0$ agrees with $V_{\mathrm{Si}}^{\mathrm{crit}}$, calculated in Section 5.2.3.3. The value of $(R_V^{\mathrm{crit}})^3$ rapidly increases with R_{Si}^3 for geometries in which the nano-particle is in the e.p.e regime, but this slows down as R_{Si}^3 increases further. As $\sigma_{\mathrm{C}}^Y/\sigma_{\mathrm{Si}}^Y$ is very small for the literature values for σ_{C}^Y and σ_{Si}^Y, $R_{\mathrm{Si}}^{3(\sigma_{\mathrm{C}}^Y/\sigma_{\mathrm{Si}}^Y+1)} \approx R_{\mathrm{Si}}^3$. So for nano-particles in the p.p.e regime at full lithiation, $(R_V^{\mathrm{crit}})^3 \approx R_{\mathrm{Si}}^3$. This is not the case for the other values of σ_{C}^Y and thus the solutions $(R_V^{\mathrm{crit}})^3$ clearly differ from $(R_V^{\mathrm{crit}})^3 = R_{\mathrm{Si}}^3$ for these $\sigma_{\mathrm{C}}^Y/\sigma_{\mathrm{Si}}^Y$ values.

In Figure 5.14, we plot the corresponding maximum capacity, $Q^{\max}$, of the nano-particle with $R_V = R_V^{\mathrm{crit}}$. We see that for the literature value of σ_{C}^Y, $Q^{\max}$ decreases rapidly for geometries for which the nano-particle is in the e.p.e regime at full lithiation but decreases more slowly as R_{Si} increases. For geometries for which the nano-particle is in the p.p.e regime at full lithiation, $Q^{\max}$ still decreases with R_{Si}^3. Therefore, the maximum value for $Q^{\max}$ is given by $R_{\mathrm{Si}} = 0$, showing that adding a void space in the centre of the nano-particle does not improve the capacity of the nano-particle such that the graphite will not fully pulverise. However, if the yield stress of the graphite is able to be increased, for example by the doping of another material, we can obtain a greater value of $Q^{\max}$, as shown by the plots in Figure 5.14 for greater values of σ_{C}^Y. Therefore, for strengthened graphite, there is an optimal initial volume of the central void to maximise the capacity of the nano-particle while ensuring the graphite does not fully pulverise.

5.4 Conclusions

In this chapter we introduced yielding mechanisms into the linear chemo-mechanical model introduced in Chapter 2, applied to two different radially-symmetric geometries

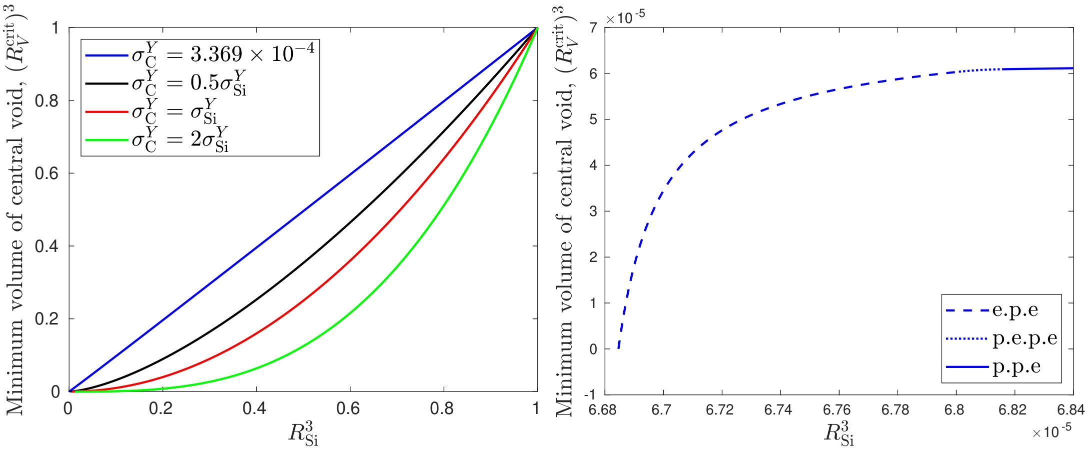

Figure 5.13: Minimum initial volume of the central void such that the graphite shell is not fully pulverised at full lithiation, $(R_V^{\mathrm{crit}})^3$, against $R_{\mathrm{Si}}^3 = V_{\mathrm{Si}}$. Left: Plotted for several values of the yield stress of graphite, σ_{C}^Y for $R_{\mathrm{Si}}^3 \in [V_{\mathrm{Si}}^{\mathrm{crit}}, 1]$. Right: Plotted for the value of σ_{C}^Y from the literature for the cases in which the nano-particle is in the e.p.e, p.e.p.e and p.e.p regimes at full lithiation.

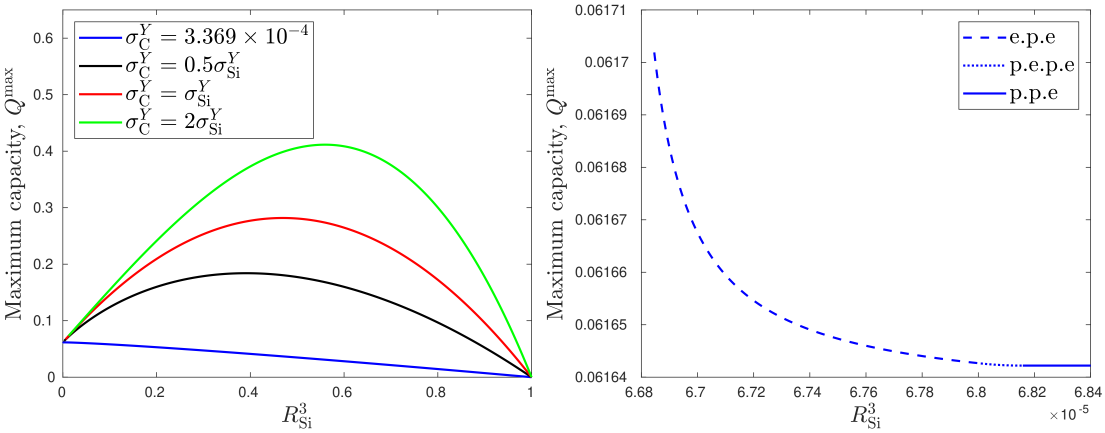

Figure 5.14: Maximum capacity, $Q^{\max}$, such that the graphite shell is not fully pulverised at full lithiation, against R_{Si}^3. Left: Plotted for several values of the yield stress of graphite, σ_{C}^Y, for $R_{\mathrm{Si}}^3 \in [V_{\mathrm{Si}}^{\mathrm{crit}}, 1]$. Right: Plotted for the value of σ_{C}^Y from the literature for the cases in which the nano-particle is in the e.p.e, p.e.p.e and p.e.p regimes at full lithiation.

of nano-particle. To model the fracturing of graphite, we have introduced a model for pulverised graphite based on a maximum deviatoric stress that the pulverised graphite can accommodate. We have presented the general model for a given yield stress of graphite, σ_{C}^{Y}, and a maximum deviatoric stress, $\sigma_{p}^{\max}$, but concentrated mainly on the case in which $\sigma_{\mathrm{C}}^{Y} = \sigma_{p}^{\max}$.

In this case, for the nano-particle consisting of a silicon core within a graphite shell, we have seen that the small yield stress of graphite causes the entire graphite shell to pulverise for relatively small silicon cores or at very low states of charge with larger silicon cores. Using the equations relating the lithium concentrations in each material to the position of the pulverised front, we were able to approximate the maximum initial volume of the silicon core such that the graphite shell does not fully pulverise as $V_{\mathrm{Si}}^{\mathrm{pulv}} = 6.6846 \times 10^{-5}$. We have approximated the SOC at which the graphite fully pulverises for larger silicon cores finding that the design that yields the highest capacity is a large silicon core at a low SOC. This is the same conclusion as for the initial silicon core volume which gives the largest capacity subject to maximum stress constraints in Section 2.6.2.3. We also estimate how the position of the pulverised front at full lithiation relates to the initial volume of the silicon core for small silicon cores, finding that s_{C} grows linearly with R_{Si}. Finally, by analysing the behaviour as $R_{\mathrm{Si}} \to 0$, we have estimated the scaling between the position of the pulverised front at full lithiation and the radius of the silicon core in this limit. We have used this analysis to find that in a large graphite matrix with small silicon inclusions, the maximum volume fraction of silicon that can be used to avoid the graphite becoming completely pulverised is approximately 5.2528×10^{-5}. This is extremely low and much less than have been used in past anodes based on silicon and graphite [140]. This discrepancy may occur for several reasons: anode particle geometry, differences in yield stress between different types of graphite, phenomena not considered in this model, or the anode still functioning with pulverised graphite.

We have also analysed this yielding model applied to a spherical nano-particle with a silicon layer and a central void. In this case, the silicon can also yield, and we model the post-yielding behaviour of the silicon using perfect plasticity. We have found the geometrical bounds on the outer radii of the central void and the silicon layer which determine the order in which the materials will yield and which will fully yield first. These bounds are only dependent on the ratio of the yield stresses of each material and the geometrical parameters of the nano-particle. These bounds can therefore be easily applied to nano-particles consisting of other materials. Finally, we found that for a silicon core and a graphite shell, adding a central void to the silicon core will not increase the maximum capacity of the nano-particle while ensuring some of the graphite is still elastic. However, if the graphite were to be strengthened such that its yield stress is increased, adding a central void can cause there to be an optimal initial volume of central core to increase this maximum capacity. This result can be useful in exploring other materials, such as using amorphous carbon as opposed to graphite. Note that if amorphous carbon were to be considered as the shell material, the pulverisation model may then not be as appropriate and intercalation does not occur so the chemical model will need to be modified slightly.

The complexity of the model in this chapter required the use of expensive computations and thus the model was not extended further to be suitable for modelling anodes in usual operation. We outline some of the limitations of the model here. Firstly, we only consider the first lithiation of the nano-particle, implied by the fully elastic graphite before any lithiation. In this case, the silicon would typically be crystalline before any lithiation as it has been shown to turn amorphous only after the first charge–discharge cycle. This is in contrast with the other models in this thesis in which we assume the silicon is amorphous. The OCV of crystalline and amorphous silicon are different [60], and the isotropic stiffness tensor assumption is not applicable for crystalline silicon. Therefore, there are some contradictions in the modelling of the silicon here.

The model becomes very complicated when delithiation after the yielding has occurred and subsequent charge–discharge cycles are considered. This is because the history of the material, through the position of the yielded fronts and the residual stresses between lithiating and delithiating would have to be tracked during the evolution of the system. We chose to focus solely on the first lithiation to avoid these complications and instead study how the initial volume of the silicon core affects this initial yield. However, the residual stresses that manifest in plastically deforming materials during repeated mechanical loading and unloading typically provide interesting insights into the long-term fatigue of materials, and thus incorporating this would be useful for studying degradation.

Lastly, in the nano-particle containing a central void, the silicon will plastically flow into the central void after yielding. We do not solve the model for the displacement and thus do not monitor this in our analysis. If the displacement at $r = R_V$ becomes less than $-R_V$, this implies the plastic silicon has closed the central void and contact has occurred at $r = 0$. The linear model does not account for this and so this effect may lead to unphysical behaviour. A simple way to account for this is to ensure that the initial volume of the silicon layer is less than $J_{\mathrm{Si}}^{\mathrm{c}} R_V^3$. Therefore, even in the unstressed case, the silicon will not expand so much that it should reach $r = 0$. This is likely the case in the analysis in Section 5.3.6 for the literature value for σ_{C}^{Y} as the silicon layers are very small in this case. However, it is not so for the larger σ_{C}^{Y} values. Despite these flaws in this simple model, it can provide insight into the yielding behaviour of the materials in the nano-particle.

Chapter 6

Conclusions

In this chapter, we summarise the main results from this thesis, address some of the limitations to the modelling approach taken, and suggest some future directions.

6.1 Main Results

In Chapter 2, we analysed the stress, displacement and lithium distribution in a multi-material nano-particle using a linear quasi-static chemo-mechanical model which incorporates coupling between the stress and the lithium concentration. We found that the lithium concentration is uniform in each material at equilbrium if the geometry has specific symmetries, and derived an effective OCV of a multi-material anode nano-particle that accounts for the stresses generated at equilibrium from the two materials. We also proposed several measures with which to optimise the initial volume of the silicon core, based on the expanded volume of the silicon core, the maximum stress generated, and the capacity of the nano-particle. The resulting optimal designs based on these measures are summarised in Section 2.7.

In Chapter 3, we applied the method of multiple scales to the linear chemo-mechanical model to calculate effective parameters for porous silicon. We found that taking the limit of small S^d_{Si} can linearise the resulting leading-order and first-order cell problems, resulting in a large saving of computational cost compared to solving the full nonlinear multiple-scales problem. Taking the large S^d_{Si} limit does not achieve this linearisation, but symmetric macroscale problems can reduce the computational cost of solving them by interpolating between solutions calculated across the range of possible macroscale variables. We used the effective parameters of the fully lithiated porous silicon to find nano-particle designs which decrease the expansion of the nano-particle while maintaining the same capacity as the non-porous nano-particle. Similarly, we found that incorporating a central void can also reduce the expansion due to the silicon displacing into the central void.

In Chapter 4, we analysed a geometrically nonlinear elasticity model applied to the core–shell geometry. We found that solutions to this model cease to exist above a certain SOC. The main conclusion from this analysis is that geometric nonlinearity is not sufficient to account for the large stresses induced in the graphite for large cores and high states of charge. Therefore, other mechanical behaviour must be incorporated into the model in these cases, for example nonlinear constitutive laws, plasticity, or cracking.

In Chapter 5, we incorporated the pulverisation of graphite and the plastic flow of silicon into the geometrically linear chemo-mechanical model from Chapter 2. Two key results from this chapter were the analytical approximations that can be made to determine the conditions such that the graphite does not fully pulverise and the effect of including a central void to the silicon in this model. We made several simplifications to give an approximation to the maximum volume fraction of silicon that can be introduced into a graphite matrix as nano-scale silicon inclusions. Such a composite anode material design is of interest to the Li-ion battery industry so this initial approximation should provide a useful input. We found that introducing a central void into the silicon core will not increase the maximum capacity such that the graphite has not fully pulverised when the nano-particle is fully lithiated, unless the graphite is strengthened in some way to increase the yield stress.

6.2 Modelling Limitations

The modelling approach taken in this thesis was to simplify the governing equations to enable as much analytical progress as possible. The linear elasticity assumption introduced in Chapter 2 is fairly restrictive to the application of this thesis: silicon. We addressed in which parameter regimes this linear model is still quantitatively valid for silicon in the results in Section 2.6. Even outside this range, the qualitative conclusions from Chapter 2 provide valuable insight into the mechanical behaviour of multi-material anodes. We used this linear model as the basis of the yielding model in Chapter 5 to allow us to make as much analytical progress as possible. As suggested in Section 4.6, the geometrically nonlinear, but constitutively linear elastic model with yielding mechanisms is likely the most quantitatively accurate model to pursue.

Further simplifications made to the chemical model throughout the thesis somewhat restrict the applicability of this model to anode nano-particles for practical use.

The equilbrium model assumes that the charging of the battery is slow enough that the inhomogeneities in the lithium distribution are smoothed sufficiently quickly by the diffusion of the lithium. Many effects due to lithium dynamics, including lithium inhomogeneities causing stresses within a single material, are not captured in this equilibrium model. One recent challenge for the battery industry is faster charging while avoiding damage to the anode [61], so inclusion of this feature would be key to this challenge. However, this equilibrium assumption is valid for faster charging rates when the diffusion occurs over a very small distance, and so can be valid in practice for nano-particles which are small enough. Additionally, the single-phase model of the lithium transport, governed by Fickian diffusion, is widely accepted to not be an accurate representation of lithiation of silicon [65, 66, 72, 73, 111]. Two-phase models with a lithium-rich region and a lithium-poor region are more representative of experimental observations so the single-phase model used in this work is most likely inaccurate.

We also make some geometric simplifications, only solving the models for a spherically symmetric nano-particle. While the nano-particles will not be perfect spheres, this assumption allows us to make a lot of analytical progress and we expect results for approximately spherical nano-particles to be qualitatively very similar. Secondly, the equilibrium model removes all length-scales from the problem. One reason for using nano-scale anode particles is the mitigation of the stress at this length-scale, as observed in experiments [66, 83] and in models [15, 92, 118]. Materials also behave differently on the nano-scale compared to that in the bulk due to surface effects [91, 138]. We have used parameter values and models suitable to bulk silicon and graphite so these may not be appropriate for nano-particles.

Finally, we do not compare any of our results in this thesis to experimental results as these are difficult and expensive to achieve in the equilibrium setting due to the slow charging that would be required. Due to this, it is not clear how valid the models presented here are, even in their respective valid parameter regimes.

6.3 Future Directions

In this final section we suggest some future directions that could be taken to build on the work within this thesis, largely addressing the limitations in the previous section.

Applying the linearised model to materials in which the linear regime is still appropriate at high states of charge could allow us to compare the effective OCVs shown in Figure 2.5 to experimental results. This would help to confirm the accuracy of the model under the assumptions that are stated in Chapter 2. The linear model could be extended to more complicated geometries than just spherical, searching for non-uniform solutions of the lithium concentration at equilibrium with multiple materials. Likewise, extending the model beyond the equilbrium state and investigating how the lithium concentration evolves over time for a given charging rate would address the limitation of not capturing the effects of inhomogeneous lithium concentrations. This has been widely studied for single materials [21, 25, 114] and cores surrounded by non-lithiating materials [44, 109], but investigating the effect of dynamics for nano-particles with core–shell geometry and multiple active materials is a very recent field of research [115].

The small and large S^d_{Si} limits in the multiple-scale analysis in Section 3.2 open up several directions to extend this work. We have seen that both reductions require the resulting cell problems to be solved for a range of macroscale variables, but this can fairly easily be achieved for the simple macroscale problem we consider here. Solving the cell problems for both small and large S^d_{Si} limits for one of the simple macroscale problems, and comparing the results to the case without stress-assisted diffusion, would allow us to see the effect that concentration variations on the microscale have on the effective material parameters of the porous silicon. These solutions could be used to analyse whether the inclusion of porous materials to the macroscale nano-particle could improve the expansion at partially lithiated states and not just the fully lithiated case we consider in Section 3.2.5. This multiple-scales analysis has been applied to modelling porous anodes in the past [57, 78, 89], but these works mostly neglect the inclusion of solid mechanics. Applying the multiple-scales problem resulting from the linear chemo-mechanical model to a periodic lattice of nano-particles can provide insight into how changes to the design of a single nano-particle can affect the macroscale displacement and stresses within an entire porous anode. This has been recently studied by Wu and Lu [116] but the coupling between the stress and concentration is neglected.

In Chapter 4, we chose to use a simplified version of the geometrically nonlinear elasticity model based on that from Cui *et al.* [25], neglecting the effects of stress-assisted diffusion. Incorporating this back into the nonlinear model, and investigating the effect this has on the SOC at which the solely elastic model breaks down, would help further understand the behaviour of this nonlinear model. Furthermore, we only analysed the problem for silicon and graphite and for $R_{\mathrm{Si}} = 0.5$. Investigating how the parameters affect the bifurcation in the solution to the model would assist in knowing when this solely elastic model can be used to obtain solutions and when it will fail.

Comparing the pulverisation model in Chapter 5 to more traditional cracking models using stress intensity factors would help validate the model used here. To ensure there is no unphysical displacement past $r = 0$ for the nano-particle design with the central void, comparing the results to a geometrically nonlinear model would address whether this omission is a significant issue or not. Comparison of the results in Figures 5.13 and 5.14 to those using a geometrically nonlinear model would help to validate the conclusions drawn here. As discussed in Section 5.4, extending the model to multiple charge–discharge cycles could help understand long-term degradation due to continuous yielding. Finally, further modelling of the anode design with several small silicon inclusions would be extremely interesting. The method of multiple scales could be utilised in this case for periodic arrays of silicon inclusions in the graphite matrix, and compared to the volume fraction of silicon result derived in Section 5.2.3.3 as $R_{\mathrm{Si}} \to 0$.

Appendix A

Deriving the Electrochemical Potential

In this appendix, we derive the chemical potential of the lithium intercalated in an anode material a, based on the derivation in [25].

A.1 Derivation of Full Stress-Dependent Electrochemical Potential

We begin by defining the total internal energy density per unit volume of material a as

$$\Pi_a^*(\mathbf{F}, c_a^*) = \varphi_a^*(c_a^*) + W_a^*(\mathbf{F}, c_a^*), \tag{A.1}$$

where $\varphi_a^*(c_a^*)$ is the internal chemical energy per unit volume after the stress-free expansion has occurred and $W_a^*(\mathbf{F}^*, c_a^*)$ is the strain energy after deformation per unit volume. All of these densities are measured in terms of a unit volume of the reference frame. We are able to split this internal energy in this way as we have multiplicatively decomposed the total deformation gradient as $\mathbf{F} = \mathbf{F}^e \mathbf{F}^{\mathrm{SF}}$. The chemical potential of lithium per mole of lithium is then given by

$$\mu_a^*(\mathbf{F}, c_a^*) = \left(\frac{\partial \Pi_a(\mathbf{F}, c_a^*)}{\partial c_a^*}\right)_{\mathbf{F}} = \frac{V_a^m}{x_a^{\max}} \left[\frac{\partial \varphi_a^*(c_a)}{\partial c_a} + \left(\frac{\partial W_a^*(\mathbf{F}, c_a)}{\partial c_a}\right)_{\mathbf{F}}\right], \tag{A.2}$$

where the first term in the bracket is the stress-independent part of the chemical potential and the second term in the bracket is the stress-dependent part of the chemical potential. As explained in Section 2.2.2, we can obtain the stress-independent part of the chemical potential from experimentally-obtained OCV data. We denote this stress-free chemical potential as $\tilde{\mu}_a^{\mathrm{SF},*}(c_a^*)$ and the stress-dependent chemical potential as $\tau_a(\mathbf{F}, c)$.

We now focus on deriving τ_a for a material with concentration-dependent mechanical parameters and with finite strains. As the strain energy density in material a, W_a^*, depends on the deformation and the stiffness $\mathbb{C}_a^*$, which is itself a function of the concentration c_a, we calculate $\partial W_a^*/\partial c_a$ by differentiating with a fixed stiffness $\mathbb{C}_a^*$ first and then differentiating with a fixed deformation, $\mathbf{F}$. Therefore, we have

$$\tau_a(\mathbf{F}, c) = \frac{V_a^m}{x_a^{\max}} \left[\left(\frac{\partial [J_a^c w_a^*(\mathbf{F}, c_a)]}{\partial F_{ij}^{\mathrm{SF}}} \frac{\partial F_{ij}^{\mathrm{SF}}}{\partial c_a} \right)_{\mathbf{F}, \mathbb{C}_a^*} + J_a^c \left(\frac{\partial w_a^*(\mathbf{F}, c_a)}{\partial c_a} \right)_{\mathbf{F}^e, \mathbf{F}^{\mathrm{SF}}} \right], \tag{A.3}$$

where we have written W_a^* as $J_a^c w_a^*$ and w_a^* is the strain energy after deformation per unit volume of the material after the stress-free expansion. This is similar to the the expression given in Eq. (14) of [25], but using the notation we introduced in Chapter 2.

We split the first derivative in (A.3) using the product rule to find

$$\frac{\partial [J_a^c w_a^*(\mathbf{F}, c_a)]}{\partial F_{ij}^{\mathrm{SF}}} = \left(\frac{\partial J_a^c}{\partial F_{ij}^{\mathrm{SF}}} \right)_{\mathbf{F}, \mathbb{C}_a^*} w^*(\mathbf{F}, c_a) + J_a^c \left(\frac{\partial w_a^*(\mathbf{F}, c_a)}{\partial F_{ij}^{\mathrm{SF}}} \right)_{\mathbf{F}, \mathbb{C}_a^*}, \tag{A.4}$$

and as $J_a^c = \det(\mathbf{F}^{\mathrm{SF}})$, we can use the identity

$$\frac{\partial \det(\mathbf{A})}{\partial \mathbf{A}} = \det(\mathbf{A}) \big(\mathbf{A}^{-1} \big)^{\mathrm{T}}, \tag{A.5}$$

for a general matrix $\mathbf{A}$, to see

$$\left(\frac{\partial J_a^c}{\partial F_{ij}^{\mathrm{SF}}} \right)_{\mathbf{F}, \mathbb{C}_a^*} = J_a^c f_{ji}^{\mathrm{SF}}, \tag{A.6}$$

where $\mathbf{f}^{\mathrm{SF}} = (\mathbf{F}^{\mathrm{SF}})^{-1}$. Using the chain rule, we can see

$$\begin{aligned} \left(\frac{\partial w_a^*(\mathbf{F}, c_a)}{\partial F_{ij}^{\mathrm{SF}}} \right)_{\mathbf{F}, \mathbb{C}_a^*} &= \left(\frac{\partial w_a^*(\mathbf{F}, c_a)}{\partial F_{mn}^e} \frac{\partial F_{mn}^e}{\partial F_{ij}^{\mathrm{SF}}} \right)_{\mathbf{F}, \mathbb{C}_a^*} && \text{(A.7)} \\ &= \left(\frac{\partial w_a^*(\mathbf{F}, c_a)}{\partial F_{mn}^e} \frac{\partial (F_{mk} f_{kn}^{\mathrm{SF}})}{\partial F_{ij}^{\mathrm{SF}}} \right)_{\mathbf{F}, \mathbb{C}_a^*} && \text{(A.8)} \\ &= \left(\frac{\partial w_a^*(\mathbf{F}, c_a)}{\partial F_{mn}^e} F_{mk} \frac{\partial f_{kn}^{\mathrm{SF}}}{\partial F_{ij}^{\mathrm{SF}}} \right)_{\mathbf{F}, \mathbb{C}_a^*}, && \text{(A.9)} \end{aligned}$$

where we have used the decomposition $\mathbf{F} = \mathbf{F}^e \mathbf{F}^{\mathrm{SF}}$ to give $\mathbf{F}^e = \mathbf{F}(\mathbf{F}^{\mathrm{SF}})^{-1}$. We can use the identity

$$\frac{\partial (\mathbf{A}^{-1})_{kl}}{\partial A_{ij}} = -(\mathbf{A}^{-1})_{ki} (\mathbf{A}^{-1})_{jl}, \tag{A.10}$$

to conclude

$$\left(\frac{\partial w_a^*(\mathbf{F}, c_a)}{\partial F_{ij}^{\mathrm{SF}}} \right)_{\mathbf{F}, \mathbb{C}_a^*} = -\left(\frac{\partial w_a^*(\mathbf{F}, c_a)}{\partial F_{mn}^e} \right)_{\mathbf{F}, \mathbb{C}_a^*} F_{mk} f_{ki}^{\mathrm{SF}} f_{jn}^{\mathrm{SF}}. \tag{A.11}$$

We substitute (A.6) and (A.11) into (A.4) to find

$$\frac{\partial[J_a^c w_a^*(\mathbf{F}, c_a)]}{\partial F_{ij}^{\mathrm{SF}}} = J_a^c f_{ji}^{\mathrm{SF}}\, w_a^*(\mathbf{F}, c_a) - J_a^c \left(\frac{\partial w_a^*(\mathbf{F}, c_a)}{\partial F_{mn}^e}\right)_{\mathbf{F},\mathbb{C}_a^*} F_{mk} f_{ki}^{\mathrm{SF}} f_{jn}^{\mathrm{SF}}, \tag{A.12}$$

which we write as

$$\frac{\partial[J_a^c w_a^*(\mathbf{F}, c_a)]}{\partial F_{ij}^{\mathrm{SF}}} = \Sigma_{jk} f_{ki}^{\mathrm{SF}}, \tag{A.13}$$

where

$$\Sigma_{jk} = \delta_{jk} W_a^*(\mathbf{F}, c_a) - J_a^c \left(\frac{\partial w_a^*(\mathbf{F}, c_a)}{\partial F_{mn}^e}\right)_{\mathbf{F},\mathbb{C}_a^*} F_{mk} f_{jn}^{\mathrm{SF}}. \tag{A.14}$$

This is known as the generalised Eshelby tensor in [25]. This can be reduced for hyperelastic materials which have the property

$$\frac{\partial w_a^*(\mathbf{F}, c_a)}{\partial F_{mn}^e} = \frac{1}{J_a^c} F_{nk}^{\mathrm{SF}} \sigma_{km}^{0*}, \tag{A.15}$$

where $\boldsymbol{\sigma}^{0*}$ is the first Piola-Kirchhoff stress tensor as defined in Section 4.1. This is related to the Cauchy stress tensor $\boldsymbol{\sigma}^*$ by (4.3). Substituting (4.3) and (A.15) into (A.14) reduces the general Eshelby tensor to the conventional Eshelby tensor [31, 117] given by

$$\begin{aligned}
\Sigma_{jk} &= \delta_{jk} W_a^*(\mathbf{F}, c_a) - J F_{nk}^{\mathrm{SF}} f_{kp} \sigma_{pm}^* F_{mk} f_{jn}^{\mathrm{SF}} \\
&= \delta_{jk} W_a^*(\mathbf{F}, c_a) - J \delta_{kj} f_{kp} \sigma_{pm}^* F_{mk} \\
&= \delta_{jk} W_a^*(\mathbf{F}, c_a) - J f_{jp} \sigma_{pm}^* F_{mk}.
\end{aligned} \tag{A.16}$$

Finally, we substitute (A.13) into (A.3) to yield

$$\tau(\mathbf{F}, c) = \frac{V_a^m}{x_a^{\max}} \left[\Sigma_{jk} f_{ki}^{\mathrm{SF}} \left(\frac{\partial F_{ij}^{\mathrm{SF}}}{\partial c_a}\right)_{\mathbf{F},\mathbb{C}_a^*} + J_a^c \left(\frac{\partial w_a^*(\mathbf{F}, c_a)}{\partial c_a}\right)_{\mathbf{F}^e,\mathbf{F}^{\mathrm{SF}}} \right]. \tag{A.17}$$

A.2 Reduction to Linear Stress-Dependent Electrochemical Potential

We now apply the assumptions we have used in Section 2.1.2 to reduce this general stress-dependent chemical potential (A.17) to the simple stress-dependent chemical potential in (2.34). Firstly, we assume that the stress-free expansion is isotropic so that $F_{ij}^{\mathrm{SF}} = (J_a^c)^{1/3}\delta_{ij}$, where $J_a^c = 1 + 3\eta_a x_a^{\max} c_a$, giving

$$\left(\frac{\partial F_{ij}^{\mathrm{SF}}}{\partial c_a}\right)_{\mathbf{F},\mathbb{C}_a^*} = \eta_a x_a^{\max} (J_a^c)^{-2/3} \delta_{ij} \tag{A.18}$$

and

$$f_{ki}^{\mathrm{SF}} = (J_a^c)^{-1/3}\delta_{ki}. \tag{A.19}$$

Substituting this into (A.17) yields

$$\tau(\mathbf{F}, c) = \frac{V_a^m}{x_a^{\max}}\left[\frac{\eta_a x_a^{\max}}{J_a^c}\Sigma_{kk} + J_a^c\left(\frac{\partial w_a^*(\mathbf{F}, c_a)}{\partial c_a}\right)_{\mathbf{F}^e, \mathbf{F}^{\mathrm{SF}}}\right], \tag{A.20}$$

and we note that the trace of (A.16) is given by

$$\begin{aligned}\Sigma_{kk} &= \delta_{kk}W_a^*(\mathbf{F}, c_a) - Jf_{kp}\sigma_{pm}^*F_{mk} \\ &= 3W_a^*(\mathbf{F}, c_a) - J\sigma_{kk}^*.\end{aligned} \tag{A.21}$$

We now study each term in (A.21), beginning with the strain energy per unit volume in the reference configuration W_a^*. If we assume the material is linearly elastic, as we have done in Chapter 2, we have

$$W_a^* = \frac{1}{2}J_a^c c_{ijkl}^{a,*}E_{ij}^e E_{kl}^e, \tag{A.22}$$

where $c_{ijkl}^{a,*}$ is the stiffness tensor of material a and E_{ij}^e is the elastic strain tensor, both in suffix notation. The product of the elastic strain tensors (2.7) is given by

$$\begin{aligned}E_{ij}^e E_{kl}^e = \frac{1}{4}&\left[(J_a^c)^{-2/3}\left\{\delta_{ij} + \frac{\partial u_i^*}{\partial X_j^*} + \frac{\partial u_j^*}{\partial X_i^*} + \frac{\partial u_i^*}{\partial X_p^*}\frac{\partial u_j^*}{\partial X_p^*}\right\} - \delta_{ij}\right] \\ &\times\left[(J_a^c)^{-2/3}\left\{\delta_{kl} + \frac{\partial u_k^*}{\partial X_l^*} + \frac{\partial u_l^*}{\partial X_k^*} + \frac{\partial u_k^*}{\partial X_p^*}\frac{\partial u_l^*}{\partial X_p^*}\right\} - \delta_{kl}\right]\end{aligned} \tag{A.23}$$

$$\begin{aligned}= \frac{1}{4}&\Bigg[(J_a^c)^{-2/3}\big((J_a^c)^{-2/3} - 1\big)\Bigg(\left\{\frac{\partial u_i^*}{\partial X_j^*} + \frac{\partial u_j^*}{\partial X_i^*} + \frac{\partial u_i^*}{\partial X_p^*}\frac{\partial u_j^*}{\partial X_p^*}\right\}\delta_{kl} \\ &+ \left\{\frac{\partial u_k^*}{\partial X_l^*} + \frac{\partial u_l^*}{\partial X_k^*} + \frac{\partial u_k^*}{\partial X_p^*}\frac{\partial u_l^*}{\partial X_p^*}\right\}\delta_{ij}\Bigg) + \big((J_a^c)^{-2/3} - 1\big)^2\delta_{ij}\delta_{kl} \\ &+(J_a^c)^{-4/3}\left\{\frac{\partial u_i^*}{\partial X_j^*} + \frac{\partial u_j^*}{\partial X_i^*} + \frac{\partial u_i^*}{\partial X_p^*}\frac{\partial u_j^*}{\partial X_p^*}\right\}\left\{\frac{\partial u_k^*}{\partial X_l^*} + \frac{\partial u_l^*}{\partial X_k^*} + \frac{\partial u_k^*}{\partial X_p^*}\frac{\partial u_l^*}{\partial X_p^*}\right\}\Bigg].\end{aligned} \tag{A.24}$$

Using the assumption in Section 2.1.2 that the quantity $\eta_a V_a^m c_a^{\max} = \eta_a x_a^{\max}$ is small for all materials a, we can approximate

$$(J_a^c)^{-2/3} = (1 + 3\eta_a x_a^{\max}c_a)^{-2/3} \approx 1 - 2\eta_a x_a^{\max}c_a, \tag{A.25}$$

$$(J_a^c)^{-4/3} \approx 1 - 4\eta_a x_a^{\max}c_a, \tag{A.26}$$

so that

$$
\begin{aligned}
(J_a^c)^{-2/3}\big((J_a^c)^{-2/3}-1\big) &\approx -2\eta_a x_a^{\max} c_a(1-2\eta_a x_a^{\max} c_a) \approx -2\eta_a x_a^{\max} c_a, && \text{(A.27a)}\\
\big((J_a^c)^{-2/3}-1\big)^2 &\approx 4(\eta_a x_a^{\max})^2 c_a^2, && \text{(A.27b)}\\
(J_a^c)^{-4/3} &\approx 1. && \text{(A.27c)}
\end{aligned}
$$

If we nondimensionalise $\boldsymbol{u}^*$ and $\boldsymbol{X}^*$ as in (2.8), we can ignore the quadratic terms in $\partial \boldsymbol{u}/\partial \boldsymbol{X}$ and we obtain

$$
\begin{aligned}
E_{ij}^e E_{kl}^e \approx \frac{1}{4}\Bigg[&- 2\eta_a\eta_1 x_a^{\max} x_1^{\max} c_a \Bigg(\left\{ \frac{\partial u_i}{\partial X_j} + \frac{\partial u_j}{\partial X_i} \right\}\delta_{kl} + \left\{ \frac{\partial u_k}{\partial X_l} + \frac{\partial u_l}{\partial X_k} \right\}\delta_{ij} \Bigg) \\
&+ 4(\eta_a x_a^{\max})^2 c_a^2 \delta_{ij}\delta_{kl} + (\eta_1 x_1^{\max})^2 \left\{ \frac{\partial u_i}{\partial X_j} + \frac{\partial u_j}{\partial X_i} \right\}\left\{ \frac{\partial u_k}{\partial X_l} + \frac{\partial u_l}{\partial X_k} \right\} \Bigg] \\
&+ \mathcal{O}\big((\eta_a x_a^{\max})^3\big).
\end{aligned} \tag{A.28}
$$

The second term in (A.21) can be written as

$$
J\sigma_{kk}^* = J_a^c \det(\mathbf{F}^e)\sigma_{kk}^*, \tag{A.29}
$$

and we can approximate using (A.25) to give

$$
\begin{aligned}
\mathbf{F}^e &= (J_a^c)^{-1/3}\left\{ \mathbf{1} + \frac{\partial \boldsymbol{u}^*}{\partial \boldsymbol{X}^*} \right\} \\
&\approx (1-\eta_a x_a^{\max} c_a)\left\{ \mathbf{1} + \frac{\partial \boldsymbol{u}^*}{\partial \boldsymbol{X}^*} \right\} \\
&= \mathbf{1} + \eta_1 x_1^{\max}\frac{\partial \boldsymbol{u}}{\partial \boldsymbol{X}} - \eta_a x_a^{\max} c_a \mathbf{1} - \eta_a\eta_1 x_a^{\max} x_1^{\max} c_a \frac{\partial \boldsymbol{u}}{\partial \boldsymbol{X}} \\
&= \mathbf{1} + \mathcal{O}(\eta_a x_a^{\max}),
\end{aligned} \tag{A.30}
$$

giving $\det(\mathbf{F}^e) \approx 1$. Substituting this approximation into (A.29) gives

$$
J\sigma_{kk}^* \approx J_a^c \sigma_{kk}^*, \tag{A.31}
$$

and using the nondimensionalisation of $\boldsymbol{\sigma}^*$ in (2.19) gives

$$
J\sigma_{kk}^* \approx G_1^* \eta_1 x_1^{\max}(1+3\eta_a x_a^{\max} c_a)\sigma_{kk} = \mathcal{O}(\eta_a x_a^{\max}), \tag{A.32}
$$

Therefore, the first term in (A.21) is $\mathcal{O}((\eta_a x_a^{\max})^2)$ and the second term is $\mathcal{O}(\eta_a x_a^{\max})$ and thus we may approximate

$$
\Sigma_{kk} \approx J_a^c \sigma_{kk}^*. \tag{A.33}
$$

The second term of (A.20) keeps the elastic and stress-free deformation gradients fixed, and thus is calculated by

$$J_a^c \left(\frac{\partial w_a^*(\mathbf{F}, c_a)}{\partial c_a} \right)_{\mathbf{F}^e, \mathbf{F}^{\mathrm{SF}}} = \frac{1}{2} J_a^c \frac{\partial c_{ijkl}^{a,*}}{\partial c_a} E_{ij}^e E_{kl}^e, \tag{A.34}$$

As shown in (A.28), the product $E_{ij}^e E_{kl}^e = \mathcal{O}((\eta_a x_a^{\max})^2)$. Therefore, under the assumptions in Section 2.1.3, this term is negligible compared to the leading-order term in the first term, given by (A.33), provided that

$$\frac{\partial c_{ijkl}^{a,*}}{\partial c_a} = o\big((\eta_a x_a^{\max})^{-1}\big). \tag{A.35}$$

For simplicity in this thesis, we are going to assume this is the case. Including the term in (A.34) would cause nonlinear u terms in the chemical potential. However, using the analysis in Section 2.3, these terms would only contribute to the term in brackets in (2.53) and so the solution $\mathrm{d}c_a/\mathrm{d}r = 0$, leading to the displacement given in (2.55), would still be valid. This may cause other solutions to (2.53) to be physically relevant, however. Taking the $\mathrm{d}c_a/\mathrm{d}r = 0$ solution, an additional consequence would be that the evaluation of the lithium concentration in each material, from solving (2.73) would have nonlinear terms, possibly introducing multiple values of c_{C} and c_{Si} which solve the chemical problem.

Therefore, for the assumptions in Chapter 2, we approximate

$$\tau(\mathbf{F}, c) \approx \frac{V_a^m}{x_a^{\max}} \left(\frac{\eta_a x_a^{\max}}{J_a^c} J_a^c \sigma_{kk}^* \right) = V_a^m \eta_a \mathrm{tr}(\boldsymbol{\sigma}^*), \tag{A.36}$$

as given in (2.34).

Appendix B

Other Solution to Radially Symmetric Linear Problem

In this appendix, we analyse the other possible solution to (2.53) with a radially-dependent concentration. This solution is given by

$$\begin{aligned}\frac{3\lambda_a+2G_a}{\lambda_a+2G_a}&\left[\left(\frac{\mathrm{d}u}{\mathrm{d}r}+\frac{2u}{r}\right)\frac{\mathrm{d}\lambda_a}{\mathrm{d}c_a}+2\frac{\mathrm{d}u}{\mathrm{d}r}\frac{\mathrm{d}G_a}{\mathrm{d}c_a}-\gamma_a\frac{\mathrm{d}(3\lambda_a+2G_a)}{\mathrm{d}c_a}c_a-\gamma_a(3\lambda_a+2G_a)\right]\\ &+\frac{1}{S_a^d}\frac{\mathrm{d}\mu_a^{\mathrm{SF}}}{\mathrm{d}c_a}-\frac{\mathrm{d}(3\lambda_a+2G_a)}{\mathrm{d}c_a}\left[\frac{\mathrm{d}u}{\mathrm{d}r}+\frac{2u}{r}-3\gamma_a c_a\right]+3\gamma_a(3\lambda_a+2G_a)=0.\end{aligned}\tag{B.1}$$

Collecting the constant, $\mathrm{d}u/\mathrm{d}r$, $\mathrm{d}\lambda_a/\mathrm{d}c_a$ and $\mathrm{d}G_a/\mathrm{d}c_a$ terms yields

$$\begin{aligned}&\frac{1}{S_a^d}\frac{\mathrm{d}\mu_a^{\mathrm{SF}}}{\mathrm{d}c_a}+\frac{4\gamma_a G_a(3\lambda_a+2G_a)}{\lambda_a+2G_a}+\frac{4}{\lambda_a+2G_a}\left(\lambda_a\frac{\mathrm{d}G_a}{\mathrm{d}c_a}-G_a\frac{\mathrm{d}\lambda_a}{\mathrm{d}c_a}\right)\frac{\mathrm{d}u}{\mathrm{d}r}\\ &\quad+\left(\frac{12G_a\gamma_a c_a}{\lambda_a+2G_a}-\frac{8G_a u}{(\lambda_a+2G_a)r}\right)\frac{\mathrm{d}\lambda_a}{\mathrm{d}c_a}+\left(\frac{8G_a\gamma_a c_a}{\lambda_a+2G_a}-\frac{4u}{r}\right)\frac{\mathrm{d}G_a}{\mathrm{d}c_a}=0\end{aligned}\tag{B.2}$$

Rearranging the $\mathrm{d}u/\mathrm{d}r$ terms and writing the two Lamé parameters in terms of the Young's modulus and the Poisson's ratio, given by

$$\lambda_a=\frac{E_a\nu_a}{(1+\nu_a)(1-2\nu_a)},\qquad G_a=\frac{E_a}{2(1+\nu_a)},\tag{B.3}$$

yields

$$\frac{4}{\lambda_a+2G_a}\left(\lambda_a\frac{\mathrm{d}G_a}{\mathrm{d}c_a}-G_a\frac{\mathrm{d}\lambda_a}{\mathrm{d}c_a}\right)\frac{\mathrm{d}u}{\mathrm{d}r}=\frac{4\lambda_a^2}{\lambda_a+2G_a}\frac{\mathrm{d}}{\mathrm{d}c_a}\left(\frac{G_a}{\lambda_a}\right)\frac{\mathrm{d}u}{\mathrm{d}r}\tag{B.4a}$$

$$=\frac{4E_a\nu_a^2}{(1-\nu_a^2)(1-2\nu_a)^2}\frac{\mathrm{d}}{\mathrm{d}c_a}\left(\frac{1-2\nu_a}{2\nu_a}\right)\frac{\mathrm{d}u}{\mathrm{d}r}.\tag{B.4b}$$

We can see that this term is only non-zero if the Poisson's ratio of material a is dependent on the lithium concentration. In this thesis, we take the Poisson's ratio to be independent of the lithium concentration, and thus this term can be removed from (B.2).

We can now write the solution u explicitly, given by

$$\begin{aligned}\left[\frac{8G_a}{\lambda_a+2G_a}\frac{\mathrm{d}\lambda_a}{\mathrm{d}c_a}-4\frac{\mathrm{d}G_a}{\mathrm{d}c_a}\right]\frac{u}{r}&=\frac{1}{S_a^d}\frac{\mathrm{d}\mu_a^{\mathrm{SF}}}{\mathrm{d}c_a}\\&+\frac{\gamma_a}{\lambda_a+2G_a}\left[4G_a(3\lambda_a+2G_a)+12G_ac_a\frac{\mathrm{d}\lambda_a}{\mathrm{d}c_a}+8G_ac_a\frac{\mathrm{d}G_a}{\mathrm{d}c_a}\right].\end{aligned}\tag{B.5}$$

Using (B.3) and assuming the Poisson's ratio is independent of c_a simplifies (B.5) to

$$\frac{1+2\nu_a}{(1+\nu_a)(1-\nu_a)}\frac{\mathrm{d}E_a}{\mathrm{d}c_a}\frac{u}{r}=\frac{1}{S_a^d}\frac{\mathrm{d}\mu_a^{\mathrm{SF}}}{\mathrm{d}c_a}+\frac{2\gamma_a}{1-\nu_a}\left[E_a+c_a\frac{\mathrm{d}E_a}{\mathrm{d}c_a}\right].\tag{B.6}$$

This solution seems unphysical for two reasons. Firstly, at $c_a = 0$ and $c_a = 1$, the solution, u, becomes extremely large due to the $\mathrm{d}\mu_a^{\mathrm{SF}}/\mathrm{d}c_a$ term. Secondly, this solution does not exist if the mechanical parameters are independent of the lithiation state, as (B.1) reduces to

$$\frac{\mathrm{d}\mu_a^{\mathrm{SF}}}{\mathrm{d}c_a}+\frac{4S_a^d\gamma_aG_a(3\lambda_a+2G_a)}{\lambda_a+2G_a}=0,\tag{B.7}$$

in this case. This would require $\mathrm{d}\mu_a^{\mathrm{SF}}/\mathrm{d}c_a$ to be constant and negative, which is not true for anode materials. If instead the Lamé parameters have a small dependence on lithiation state, the solution u becomes very large. This is true for both lithiation-independent and lithiation-dependent Poisson's ratios, given by (B.6) and (B.5), repectively, due to the terms multiplying the u/r term. It seems unphysical that as the lithiation dependence decreases, the radially-dependent concentration solution, u, becomes very large before it ceases to exist. Due to these reasons, we ignore this solution in Section 2.3 and proceed with the solution

$$\frac{\mathrm{d}c_a}{\mathrm{d}r}=0.\tag{B.8}$$

Appendix C

Small S^d_{Si} Derivation with Lithiation-Dependent Stiffness

In this appendix, we derive the F_0 and F_1 problems in (3.19) arising from taking the small S^d_{Si} limit, with a lithiation-dependent stiffness tensor, $\mathbb{C}_{\text{Si}}(c_{\text{Si}})$.

C.1 F_0 Problem

Using (3.20b) and (3.10c), we see that $c_{\text{Si}}^{(0,0)}$ is independent of $\hat{\mathbf{x}}$ in this case as well, so we can write (3.22) as

$$\hat{\boldsymbol{\nabla}} \cdot \big(\mathbb{C}_{\text{Si}}(c_{\text{Si}}^{(0,0)}) : \hat{\boldsymbol{\nabla}} \boldsymbol{u}^{(1,0)}\big) = 0 \qquad \text{in } \Omega_{\text{Si}}, \tag{C.1a}$$

$$\big(\mathbb{C}_{\text{Si}}(c_{\text{Si}}^{(0,0)}) : \hat{\boldsymbol{\nabla}} \boldsymbol{u}^{(1,0)}\big)\mathbf{n} = -\Big(\mathbb{C}_{\text{Si}}(c_{\text{Si}}^{(0,0)}) : \big(\boldsymbol{\nabla} \boldsymbol{u}^{(0)} - \gamma_{\text{Si}} c_{\text{Si}}^{(0,0)} \mathbf{1}\big)\Big)\mathbf{n} \qquad \text{on } \Gamma_e. \tag{C.1b}$$

The resulting cell problems will not simplify by using $\gamma_{\text{Si}} c_{\text{Si}}^{(0,0)}$ in the decomposition of $\boldsymbol{u}^{(1)}$ as in (3.24a), as it does in Section 3.2.2.1. Therefore, we decompose $\boldsymbol{u}^{(1)}$ by

$$\boldsymbol{u}^{(1,0)} = \mathcal{A}^{(0)} : \boldsymbol{\nabla} \boldsymbol{u}^{(0)} + \gamma_{\text{Si}} \mathbf{v}^{(0)} + \bar{\boldsymbol{u}}^{(1,0)}, \tag{C.2}$$

instead, where $\mathbf{v}^{(0)}$ is a vector of length three. Substituting (C.2) into (C.1) yields

$$\hat{\boldsymbol{\nabla}} \cdot \Big(\mathbb{C}_{\text{Si}}(c_{\text{Si}}^{(0,0)}) : \Big\{\hat{\boldsymbol{\nabla}} \big(\mathcal{A}^{(0)} : \boldsymbol{\nabla} \boldsymbol{u}^{(0)} + \gamma_{\text{Si}} \mathbf{v}^{(0)}\big)\Big\}\Big) = 0 \qquad \text{in } \hat{\Omega}_{\text{Si}}, \tag{C.3a}$$

$$\begin{aligned}\Big(\mathbb{C}_{\text{Si}}(c_{\text{Si}}^{(0,0)}) : \Big\{\hat{\boldsymbol{\nabla}} \big(\mathcal{A}^{(0)} : \boldsymbol{\nabla} \boldsymbol{u}^{(0)} + \gamma_{\text{Si}} \mathbf{v}^{(0)}\big)\Big\}\Big)\mathbf{n} \\ = -\Big[\mathbb{C}_{\text{Si}}(c_{\text{Si}}^{(0,0)}) : \Big(\boldsymbol{\nabla} \boldsymbol{u}^{(0)} - \gamma_{\text{Si}} c_{\text{Si}}^{(0,0)} \mathbf{1}\Big)\Big]\mathbf{n}\end{aligned} \qquad \text{on } \hat{\Gamma}_e, \tag{C.3b}$$

leading to the cell problems

$$\hat{\boldsymbol{\nabla}} \cdot \big(\mathbb{C}_{\text{Si}}(c_{\text{Si}}^{(0,0)}) : \hat{\boldsymbol{\nabla}} \mathcal{A}^{(0)}\big) = \mathbf{0} \qquad \text{in } \hat{\Omega}_{\text{Si}}, \tag{C.4a}$$

$$\big(\mathbb{C}_{\text{Si}}(c_{\text{Si}}^{(0,0)}) : \hat{\boldsymbol{\nabla}} \mathcal{A}^{(0)}\big)\mathbf{n} = -\mathbb{C}_{\text{Si}}(c_{\text{Si}}^{(0,0)}) \cdot \mathbf{n} \qquad \text{on } \hat{\Gamma}_e, \tag{C.4b}$$

and

$$\hat{\boldsymbol{\nabla}} \cdot \Big(\mathbb{C}_{\mathrm{Si}}\big(c_{\mathrm{Si}}^{(0,0)}\big) : \hat{\boldsymbol{\nabla}}\mathbf{v}^{(0)}\Big) = 0, \qquad \text{in } \hat{\Omega}_{\mathrm{Si}}, \tag{C.5a}$$

$$\Big(\mathbb{C}_{\mathrm{Si}}\big(c_{\mathrm{Si}}^{(0,0)}\big) : \hat{\boldsymbol{\nabla}}\mathbf{v}^{(0)}\Big)\mathbf{n} = c_{\mathrm{Si}}^{(0,0)}\Big(\mathbb{C}_{\mathrm{Si}}\big(c_{\mathrm{Si}}^{(0,0)}\big) : \mathbf{1}\Big)\mathbf{n}, \qquad \text{on } \hat{\Gamma}_e, \tag{C.5b}$$

with the usual periodicity and integral constraints given, for example, in (3.26c) and (3.26d). These problems depend on the leading-order concentration, $c_{\mathrm{Si}}^{(0,0)}$, through the lithiation-dependent stiffness tensor, $\mathbb{C}_{\mathrm{Si}}$.

C.2 $\boldsymbol{F}_1$ Problem

The first-order system in S_{Si}^d from substituting (3.20) into (3.12) is given by

$$\begin{aligned}\hat{\boldsymbol{\nabla}} \cdot \Big[&\mathbb{C}_{\mathrm{Si}}(c_{\mathrm{Si}}^{(0,0)}) : \Big\{\hat{\boldsymbol{\nabla}}\boldsymbol{u}^{(1,1)} - \gamma_{\mathrm{Si}} c_{\mathrm{Si}}^{(0,1)}\mathbf{1}\Big\} \\ &+ \mathbb{C}'_{\mathrm{Si}}(c_{\mathrm{Si}}^{(0,0)}) : \Big\{\hat{\boldsymbol{\nabla}}\boldsymbol{u}^{(1,0)} + \boldsymbol{\nabla}\boldsymbol{u}^{(0)} - \gamma_{\mathrm{Si}} c_{\mathrm{Si}}^{(0,0)}\mathbf{1}\Big\} c_{\mathrm{Si}}^{(0,1)}\Big] = 0 \qquad \text{in } \hat{\Omega}_{\mathrm{Si}},\end{aligned} \tag{C.6a}$$

$$\begin{aligned}\Big[&\mathbb{C}_{\mathrm{Si}}(c_{\mathrm{Si}}^{(0,0)}) : \Big\{\hat{\boldsymbol{\nabla}}\boldsymbol{u}^{(1,1)} - \gamma_{\mathrm{Si}} c_{\mathrm{Si}}^{(0,1)}\mathbf{1}\Big\} \\ &+ \mathbb{C}'_{\mathrm{Si}}(c_{\mathrm{Si}}^{(0,0)}) : \Big\{\hat{\boldsymbol{\nabla}}\boldsymbol{u}^{(1,0)} + \boldsymbol{\nabla}\boldsymbol{u}^{(0)} - \gamma_{\mathrm{Si}} c_{\mathrm{Si}}^{(0,0)}\mathbf{1}\Big\} c_{\mathrm{Si}}^{(0,1)}\Big]\mathbf{n} = 0 \qquad \text{on } \hat{\Gamma}_e,\end{aligned} \tag{C.6b}$$

where $c_{\mathrm{Si}}^{(0,1)}$ is given by (3.21b) and is dependent on both $\boldsymbol{\nabla}\boldsymbol{u}^{(0)}$ and $c_{\mathrm{Si}}^{(0,0)}$. From (3.21b), we can see that the second terms in the left-hand sides of (C.6) are nonlinear in $\boldsymbol{\nabla}\boldsymbol{u}^{(0)}$, and we cannot make a similar linear ansatz to (C.2) for the F_1 problem here. Similar to the nonlinear case in Section 3.2.1, the microscale displacement, $\boldsymbol{u}^{(1,1)}$, would need to be calculated at each macroscale position.

Therefore, the small S_{Si}^d cell problems are dependent on $c_{\mathrm{Si}}^{(0,0)}$ and $\boldsymbol{\nabla}\boldsymbol{u}^{(0)}$ in the lithiation-dependent stiffness case. These would in principle need to be solved for each macroscale position when the concentration is varying. However, as explained in Section 3.2.4, we know $c_{\mathrm{Si}}^{(0,0)}$ is restricted to $[0, 1]$, we can approximate the dependence of $\boldsymbol{u}^{(1)}$ on $c_{\mathrm{Si}}^{(0,0)}$ by solving the cell problems for a sample of $c_{\mathrm{Si}}^{(0,0)} \in [0, 1]$ and interpolating between these solutions. Then, when solving the macroscale problem, the effective parameters can be quickly calculated from this interpolation function. We can also do the same with $\boldsymbol{\nabla}\boldsymbol{u}^{(0)}$ using the spherical symmetry in the macroscale problem. However, the multiple-scales problem in this appendix does not greatly reduce the cost of solving the multiple-scales problem from the fully nonlinear problem with any size of S_{Si}^d.

Appendix D

Compressible Stresses, ODE and Outer Boundary Condition

In this appendix, we derive the 1st P–K stresses, the governing ODEs for u in r, and the boundary conditions at $r = 1$ for the nonlinear model in Chapter 4 for the compressible neo-Hookean and Blatz–Ko [8] constitutive laws.

D.1 Compressible Neo-Hookean

We can write the strain energy density (4.59a) in terms of the three diagonal elements of $\mathbf{F}^e$ in spherical coordinates, F^e_{rr}, $F^e_{\theta\theta}$ and $F^e_{\phi\phi}$ using (4.60a) and (4.60b), giving

$$\begin{aligned}\mathcal{W}^{\mathrm{NH}} = J^c_a\bigg[\frac{\lambda_a}{2}\Big(\log\big(F^e_{rr}F^e_{\theta\theta}F^e_{\phi\phi}\big)\Big)^2 - G_a\log\big(F^e_{rr}F^e_{\theta\theta}F^e_{\phi\phi}\big)&\\ + \frac{G_a}{2}\Big(\big(F^e_{rr}\big)^2 + \big(F^e_{\theta\theta}\big)^2 + \big(F^e_{\phi\phi}\big)^2\Big)\bigg].&\end{aligned} \tag{D.1}$$

Using (4.5), we can write the radial first P–K stress as

$$\begin{aligned}\sigma^0_{rr} &= \big(J^c_a\big)^{\frac{2}{3}}\frac{\partial}{\partial F^e_{rr}}\bigg[\frac{\lambda_a}{2}\Big(\log\big(F^e_{rr}F^e_{\theta\theta}F^e_{\phi\phi}\big)\Big)^2 - G_a\log\big(F^e_{rr}F^e_{\theta\theta}F^e_{\phi\phi}\big)\\ &\qquad + \frac{G_a}{2}\Big(\big(F^e_{rr}\big)^2 + \big(F^e_{\theta\theta}\big)^2 + \big(F^e_{\phi\phi}\big)^2\Big)\bigg]\\ &= \big(J^c_a\big)^{\frac{2}{3}}\bigg\{\lambda_a\log\big(F^e_{rr}F^e_{\theta\theta}F^e_{\phi\phi}\big)\frac{\partial}{\partial F^e_{rr}}\Big(\log\big(F^e_{rr}F^e_{\theta\theta}F^e_{\phi\phi}\big)\Big) - \frac{G_a}{F^e_{rr}} + G_aF^e_{rr}\bigg\}\\ &= \big(J^c_a\big)^{\frac{2}{3}}\bigg\{\frac{\lambda_a\log\big(F^e_{rr}F^e_{\theta\theta}F^e_{\phi\phi}\big)}{F^e_{rr}} - \frac{G_a}{F^e_{rr}} + G_aF^e_{rr}\bigg\},\end{aligned} \tag{D.2}$$

and the first P–K stress in the hoop direction as

$$\sigma^0_{\theta\theta} = \big(J^c_a\big)^{\frac{2}{3}}\bigg\{\frac{\lambda_a\log\big(F^e_{rr}F^e_{\theta\theta}F^e_{\phi\phi}\big)}{F^e_{\theta\theta}} - \frac{G_a}{F^e_{\theta\theta}} + G_aF^e_{\theta\theta}\bigg\}. \tag{D.3}$$

Taking the derivative of the radial 1st P–K stress (D.2) allows us to write the mechanical equilibrium equation (4.16) as

$$\begin{aligned}\frac{\lambda_a}{\left(F^e_{rr}\right)^2 F^e_{\theta\theta}F^e_{\phi\phi}}&\left[F^e_{\theta\theta}F^e_{\phi\phi}\frac{\partial F^e_{rr}}{\partial r}+F^e_{rr}F^e_{\phi\phi}\frac{\partial F^e_{\theta\theta}}{\partial r}+F^e_{rr}F^e_{\theta\theta}\frac{\partial F^e_{\phi\phi}}{\partial r}\right]+G_a\left(F^e_{rr}\right)^{-2}\frac{\partial F^e_{rr}}{\partial r}\\&+G_a\frac{\partial F^e_{rr}}{\partial r}-\lambda_a\log\left(F^e_{rr}F^e_{\theta\theta}F^e_{\phi\phi}\right)\left(F^e_{rr}\right)^{-2}\frac{\partial F^e_{rr}}{\partial r}+\frac{2\lambda_a\log\left(F^e_{rr}F^e_{\theta\theta}F^e_{\phi\phi}\right)}{rF^e_{rr}}\\&-\frac{2G_a}{rF^e_{rr}}+\frac{2G_aF^e_{rr}}{r}-\frac{2\lambda_a}{rF^e_{\theta\theta}}\log\left(F^e_{rr}F^e_{\theta\theta}F^e_{\phi\phi}\right)+\frac{2G_a}{rF^e_{\theta\theta}}-\frac{2G_aF^e_{\theta\theta}}{r}=0,\end{aligned}\tag{D.4}$$

which reduces to

$$\begin{aligned}\frac{\lambda_a}{(F^e_{rr})^2(F^e_{\theta\theta})^2}&\left[\left(F^e_{\theta\theta}\right)^2\frac{\partial F^e_{rr}}{\partial r}+2F^e_{rr}F^e_{\theta\theta}\frac{\partial F^e_{\theta\theta}}{\partial r}\right]+G_a\left(F^e_{rr}\right)^{-2}\frac{\partial F^e_{rr}}{\partial r}\\&+G_a\frac{\partial F^e_{rr}}{\partial r}-\lambda_a\log\left(F^e_{rr}\left(F^e_{\theta\theta}\right)^2\right)\left(F^e_{rr}\right)^{-2}\frac{\partial F^e_{rr}}{\partial r}+\frac{2\lambda_a\log\left(F^e_{rr}\left(F^e_{\theta\theta}\right)^2\right)}{rF^e_{rr}}\\&-\frac{2G_a}{rF^e_{rr}}+\frac{2G_aF^e_{rr}}{r}-\frac{2\lambda_a}{rF^e_{\theta\theta}}\log\left(F^e_{rr}\left(F^e_{\theta\theta}\right)^2\right)+\frac{2G_a}{rF^e_{\theta\theta}}-\frac{2G_aF^e_{\theta\theta}}{r}=0,\end{aligned}\tag{D.5}$$

when we apply the symmetry in θ and ϕ. Using (4.9), we can write

$$\frac{\partial F^e_{rr}}{\partial r}=\left(J^c_a\right)^{-\frac{1}{3}}\frac{\mathrm{d}^2u}{\mathrm{d}r^2},\qquad\frac{\partial F^e_{\theta\theta}}{\partial r}=\frac{\left(J^c_a\right)^{-\frac{1}{3}}}{r^2}\left(r\frac{\mathrm{d}u}{\mathrm{d}r}-u\right),\tag{D.6}$$

and substituting this into (D.5) yields the ODE for u in r, given as

$$\begin{aligned}&\left[1-\log\left(F^e_{rr}\left(F^e_{\theta\theta}\right)^2\right)+\frac{G_a}{\lambda_a}\left(1+\left(F^e_{rr}\right)^2\right)\right]\frac{\mathrm{d}^2u}{\mathrm{d}r^2}=\\&\qquad\frac{2G_a(J^c_a)^{\frac{1}{3}}}{\lambda_a r}\left[F^e_{rr}-\left(F^e_{rr}\right)^3-\frac{(F^e_{rr})^2}{F^e_{\theta\theta}}+F_{\theta\theta}\left(F^e_{rr}\right)^2\right]-\frac{2F^e_{rr}}{F^e_{\theta\theta}r^2}\left(r\frac{\mathrm{d}u}{\mathrm{d}r}-u\right)\\&\qquad\qquad+\frac{2(J^c_a)^{\frac{1}{3}}\log\left(F^e_{rr}(F^e_{\theta\theta})^2\right.}{r}\left(\frac{1}{F^e_{\theta\theta}}-\frac{1}{F^e_{rr}}\right).\end{aligned}\tag{D.7}$$

Using the identity (4.3), the radial 1st P–K stress (D.2) and the equations for F^e_{rr} and $F^e_{\theta\theta}$ (4.9), we can calculate the radial Cauchy stresses needed for the boundary conditions as

$$\sigma_{rr}=\frac{J^c_a}{(1+\frac{u}{r})^2}\left\{\frac{\lambda_a\ln\left((J^c_a)^{-1}\left(1+\frac{\mathrm{d}u}{\mathrm{d}r}\right)\left(1+\frac{u}{r}\right)^2\right)}{1+\frac{\mathrm{d}u}{\mathrm{d}r}}-\frac{G_a}{1+\frac{\mathrm{d}u}{\mathrm{d}r}}+G_a\left(1+\frac{\mathrm{d}u}{\mathrm{d}r}\right)\left(J^c_a\right)^{-\frac{2}{3}}\right\},\tag{D.8}$$

which can be rearranged to give $u(1)$ in terms of $\mathrm{d}u/\mathrm{d}r$ at $r=1$, where $\sigma_{rr}=0$. This gives

$$u(1)=\sqrt{\left(J^c_a\right)\left(1+\frac{\mathrm{d}u}{\mathrm{d}r}\right)^{-1}\exp\left[\frac{G_a}{\lambda_a}-\frac{G_a}{\lambda_a}\left(J^c_a\right)^{-\frac{2}{3}}\left(1+\left.\frac{\mathrm{d}u}{\mathrm{d}r}\right|_{r=1}\right)^2\right]}-1.\tag{D.9}$$

D.2 Blatz–Ko

Similarly, we can write the strain energy density for the Blatz–Ko constitutive law (4.59b) as

$$\mathcal{W}^{\mathrm{BK}} = \frac{J_a^c G_a}{2}[fW_1 + (1-f)W_2], \tag{D.10}$$

where

$$W_1 = \left[(F_{rr}^e)^2 + (F_{\theta\theta}^e)^2 + (F_{\phi\phi}^e)^2 - 3\right] + \frac{1}{\beta_a}\left[\left((F_{rr}^e)^2(F_{\theta\theta}^e)^2(F_{\phi\phi}^e)^2\right)^{-\beta_a} - 1\right], \tag{D.11a}$$

$$W_2 = \left[(F_{rr}^e)^{-2} + (F_{\theta\theta}^e)^{-2} + (F_{\phi\phi}^e)^{-2} - 3\right] + \frac{1}{\beta_a}\left[\left((F_{rr}^e)^2(F_{\theta\theta}^e)^2(F_{\phi\phi}^e)^2\right)^{\beta_a} - 1\right]. \tag{D.11b}$$

The radial first P–K stress is given by

$$\sigma_{rr}^0 = \frac{(J_a^c)^{\frac{2}{3}} G_a}{2}\left[f\frac{\partial W_1}{\partial F_{rr}^e} + (1-f)\frac{\partial W_2}{\partial F_{rr}^e}\right], \tag{D.12}$$

and

$$\frac{\partial W_1}{\partial F_{rr}^e} = 2\left[F_{rr}^e - (F_{rr}^e)^{-2\beta_a - 1}(F_{\theta\theta}^e)^{-2\beta_a}(F_{\phi\phi}^e)^{-2\beta_a}\right], \tag{D.13a}$$

$$\frac{\partial W_2}{\partial F_{rr}^e} = 2\left[(F_{rr}^e)^{2\beta_a - 1}(F_{\theta\theta}^e)^{2\beta_a}(F_{\phi\phi}^e)^{2\beta_a} - (F_{rr}^e)^{-3}\right]. \tag{D.13b}$$

The first P–K stress in the hoop direction is given by

$$\sigma_{\theta\theta}^0 = \frac{(J_a^c)^{\frac{2}{3}} G_a}{2}\left[f\frac{\partial W_1}{\partial F_{\theta\theta}^e} + (1-f)\frac{\partial W_2}{\partial F_{\theta\theta}^e}\right], \tag{D.14}$$

and

$$\frac{\partial W_1}{\partial F_{\theta\theta}^e} = 2\left[F_{\theta\theta}^e - (F_{rr}^e)^{-2\beta_a}(F_{\theta\theta}^e)^{-2\beta_a - 1}(F_{\phi\phi}^e)^{-2\beta_a}\right], \tag{D.15a}$$

$$\frac{\partial W_2}{\partial F_{\theta\theta}^e} = 2\left[(F_{rr}^e)^{2\beta_a}(F_{\theta\theta}^e)^{2\beta_a - 1}(F_{\phi\phi}^e)^{2\beta_a} - (F_{\theta\theta}^e)^{-3}\right]. \tag{D.15b}$$

Using (D.6), and that $\partial F^e_{\theta\theta}/\partial r = \partial F^e_{\phi\phi}/\partial r$, we take the derivatives

$$\frac{\partial (F^e_{rr})^{-3}}{\partial r} = -3(J^c_a)\frac{\mathrm{d}^2 u}{\mathrm{d}r^2}\left(1+\frac{\mathrm{d}u}{\mathrm{d}r}\right)^{-4}, \tag{D.16a}$$

$$\begin{aligned}
&\frac{\partial}{\partial r}\left[(F^e_{rr})^{-2\beta_a-1}(F^e_{\theta\theta})^{-2\beta_a}(F^e_{\phi\phi})^{-2\beta_a}\right] = \\
&\qquad (J^c_a)^{-\frac{1}{3}}(F^e_{rr})^{-2\beta_a-1}(F^e_{\theta\theta})^{-2\beta_a}(F^e_{\phi\phi})^{-2\beta_a}\bigg\{(-2\beta_a-1)\frac{\mathrm{d}^2 u}{\mathrm{d}r^2}(F^e_{rr})^{-1} \\
&\qquad\quad - 2\beta_a r^{-2}\left(r\frac{\mathrm{d}u}{\mathrm{d}r}-u\right)(F^e_{\theta\theta})^{-1} - 2\beta_a r^{-2}\left(r\frac{\mathrm{d}u}{\mathrm{d}r}-u\right)(F^e_{\phi\phi})^{-1}\bigg\},
\end{aligned} \tag{D.16b}$$

$$\begin{aligned}
&\frac{\partial}{\partial r}\left[(F^e_{rr})^{2\beta_a-1}(F^e_{\theta\theta})^{2\beta_a}(F^e_{\phi\phi})^{2\beta_a}\right] = \\
&\qquad (J^c_a)^{-\frac{1}{3}}(F^e_{rr})^{2\beta_a-1}(F^e_{\theta\theta})^{2\beta_a}(F^e_{\phi\phi})^{2\beta_a}\bigg\{(2\beta_a-1)\frac{\mathrm{d}^2 u}{\mathrm{d}r^2}(F^e_{rr})^{-1} \\
&\qquad\quad + 2\beta_a r^{-2}\left(r\frac{\mathrm{d}u}{\mathrm{d}r}-u\right)(F^e_{\theta\theta})^{-1} + 2\beta_a r^{-2}\left(r\frac{\mathrm{d}u}{\mathrm{d}r}-u\right)(F^e_{\phi\phi})^{-1}\bigg\}.
\end{aligned} \tag{D.16c}$$

We use these to write the mechanical equilibrium equation, (4.16), as

$$\begin{aligned}
&f(J^c_a)^{-\frac{1}{3}}\frac{\partial^2 u}{\partial r^2} + (J^c_a)^{-\frac{1}{3}}\bigg\{(2\beta_a+1)\frac{\mathrm{d}^2 u}{\mathrm{d}r^2}(F^e_{rr})^{-1} + 2\beta_a r^{-2}\left(r\frac{\mathrm{d}u}{\mathrm{d}r}-u\right)(F^e_{\theta\theta})^{-1} \\
&\qquad + 2\beta_a r^{-2}\left(r\frac{\mathrm{d}u}{\mathrm{d}r}-u\right)(F^e_{\phi\phi})^{-1}\bigg\}\Big[f(F^e_{rr})^{-2\beta_a-1}(F^e_{\theta\theta})^{-2\beta_a}(F^e_{\phi\phi})^{-2\beta_a} \\
&\qquad\qquad + (1-f)(F^e_{rr})^{2\beta_a-1}(F^e_{\theta\theta})^{2\beta_a}(F^e_{\phi\phi})^{2\beta_a}\Big] \\
&\quad + \frac{2}{r}\bigg\{f(F^e_{rr}-F^e_{\theta\theta}) - (1-f)\big((F^e_{rr})^{-3}-(F^e_{\theta\theta})^{-3}\big) \\
&\qquad\quad + f(F^e_{rr})^{-2\beta_a-1}(F^e_{\theta\theta})^{-2\beta_a-1}(F^e_{\phi\phi})^{-2\beta_a}(F^e_{rr}-F^e_{\theta\theta}) \\
&\qquad\qquad - (1-f)(F^e_{rr})^{2\beta_a-1}(F^e_{\theta\theta})^{2\beta_a-1}(F^e_{\phi\phi})^{2\beta_a}(F^e_{rr}-F^e_{\theta\theta})\bigg\} = 0.
\end{aligned} \tag{D.17}$$

We apply the symmetry in θ and ϕ to yield the ODE for u in r as

$$\begin{aligned}
&\bigg\{f + (2\beta_a+1)(F^e_{rr})^{-1}\Big[f(F^e_{rr})^{-2\beta_a-1}(F^e_{\theta\theta})^{-4\beta_a} + (1-f)(F^e_{rr})^{2\beta_a-1}(F^e_{\theta\theta})^{4\beta_a}\Big] \\
&\qquad - 2(1-f)(F^e_{rr})^{2\beta_a-2}(F^e_{\theta\theta})^{4\beta_a} + 3(1-f)(F^e_{rr})^{-4}\bigg\}\frac{\mathrm{d}^2 u}{\mathrm{d}r^2} \\
&= \frac{2}{r}(J^c_a)^{\frac{1}{3}}\bigg\{(1-f)\big[(F^e_{rr})^{-3}-(F^e_{\theta\theta})^{-3}\big] - f(F^e_{rr}-F^e_{\theta\theta}) \\
&\quad + \big[(F^e_{rr})^{-1}-(F^e_{\theta\theta})^{-1}\big]\big[f(F^e_{rr})^{-2\beta_a}(F^e_{\theta\theta})^{-4\beta_a} - (1-f)(F^e_{rr})^{2\beta_a}(F^e_{\theta\theta})^{4\beta_a}\big]\bigg\} \\
&\quad - \frac{4\beta_a}{r^2 F^e_{\theta\theta}}\left(r\frac{\mathrm{d}u}{\mathrm{d}r}-u\right)\Big[f(F^e_{rr})^{-2\beta_a-1}(F^e_{\theta\theta})^{-4\beta_a} + (1-f)(F^e_{rr})^{2\beta_a-1}(F^e_{\theta\theta})^{4\beta_a}\Big].
\end{aligned} \tag{D.18}$$

Finally, we can calculate the radial Cauchy stresses using (4.3) to give

$$\begin{aligned}\sigma_{rr} = \frac{(J_a^c)^{\frac{2}{3}}}{(1+u/r)^2}\Bigg\{ f\left[(J_a^c)^{-\frac{1}{3}}\left(1+\frac{\mathrm{d}u}{\mathrm{d}r}\right) - (J_a^c)^{\frac{6\beta_a+1}{3}}\left(1+\frac{\mathrm{d}u}{\mathrm{d}r}\right)^{-2\beta_a-1}\left(1+\frac{u}{r}\right)^{-4\beta_a}\right] \\ - (1-f)\left[J_a^c\left(1+\frac{\mathrm{d}u}{\mathrm{d}r}\right)^{-3} + (J_a^c)^{\frac{-6\beta_a+1}{3}}\left(1+\frac{\mathrm{d}u}{\mathrm{d}r}\right)^{2\beta_a-1}\left(1+\frac{u}{r}\right)^{4\beta}\right]\Bigg\}.\end{aligned} \tag{D.19}$$

The boundary condition at $r = 1$ is given by $\sigma_{rr} = 0$. We can rearrange (D.19) to yield the following two roots of $u(1)$ in terms of the displacement gradient, $\mathrm{d}u/\mathrm{d}r$, at $r = 1$. These are given by

$$u(1) = \left[(J_{\mathrm{C}}^c)^{\frac{6\beta_{\mathrm{C}}+2}{3}}\left(1+\left.\frac{\mathrm{d}u}{\mathrm{d}r}\right|_{r=1}\right)^{-2\beta_{\mathrm{C}}-2}\right]^{\frac{1}{4\beta_{\mathrm{C}}}} - 1, \tag{D.20a}$$

$$u(1) = \left[-\frac{f}{1-f}(J_{\mathrm{C}}^c)^{\frac{6\beta_{\mathrm{C}}-2}{3}}\left(1+\left.\frac{\mathrm{d}u}{\mathrm{d}r}\right|_{r=1}\right)^{-2\beta_{\mathrm{C}}+2}\right]^{\frac{1}{4\beta_{\mathrm{C}}}} - 1. \tag{D.20b}$$

However, $J_{\mathrm{C}}^c > 0$, $\mathrm{d}u/\mathrm{d}r > -1$, and $f/(1-f) > 0$, thus the term in the square bracket in (D.20b) is negative. Therefore, this root will only be real for particular values of β_a depending on the material in the shell. For a graphite shell, $\beta_{\mathrm{C}} = 0.889$ and $1/4\beta_{\mathrm{C}} = 0.28125$ which does yield complex values for $u(1)$ in (D.20b). Secondly, if $f = 1$, $u(1)$ is undefined in (D.20b). Therefore, we take (D.20a) as the expression for $u(1)$ for the Blatz–Ko constitutive law.

Appendix E

Regime Boundary Conditions

We present the boundary conditions and chemical potentials in each regime for the nano-particle with a central void shown in Figure 5.10. We then solve these conditions to find the integration constants in each regime and describe the method for solving these equations to find the displacement and lithium concentrations. The model for the yielding of the materials in this geometry is given in Sections 5.2.2 and 5.3, and the resulting general displacement, stresses and chemical potentials in each region of the nano-particle are referenced in Table 5.1. The general boundary conditions for this model are the continuity of displacement and normal stress between regions, zero traction on the boundary at $r = R_V$ and $r = 1$, and the yield condition being satisfied at s_{Si} and s_{C}. We use $\Lambda_a = 3\lambda_a + 2G_a$, for $a = \mathrm{Si}, \mathrm{C}$, throughout this appendix for ease of notation.

E.1 e.e

The e.e regime is solved to find A_{Si}, B_{Si}, A_{C} and B_{C} using the method in Chapter 2. These integration constants are given in terms of the concentrations, c_{Si} and c_{C}, in (3.2).

E.2 p.e.e

The boundary conditions in the p.e.e regime are given by

$$C_{\mathrm{Si}} = \frac{2\sigma^Y_{\mathrm{Si}}}{3}\log(R_V^3), \tag{E.1a}$$

$$C_{\mathrm{Si}} - \frac{2\sigma^Y_{\mathrm{Si}}}{3}\log(s_{\mathrm{Si}}^3) = \Lambda_{\mathrm{Si}}(A_{\mathrm{Si}} - \gamma_{\mathrm{Si}}c_{\mathrm{Si}}) - \frac{4G_{\mathrm{Si}}B_{\mathrm{Si}}}{s_{\mathrm{Si}}^3}, \tag{E.1b}$$

$$\frac{-6G_{\mathrm{Si}}B_{\mathrm{Si}}}{s_{\mathrm{Si}}^3} = \sigma^Y_{\mathrm{Si}}, \tag{E.1c}$$

$$\int_{R_V}^{s_{\mathrm{Si}}} \big(3\gamma_{\mathrm{Si}}c^p_{\mathrm{Si}}(\tilde{r}) + D_{\mathrm{Si}}(\tilde{r})\big)\tilde{r}^2\,\mathrm{d}\tilde{r} = A_{\mathrm{Si}}s_{\mathrm{Si}}^3 + B_{\mathrm{Si}} - E_{\mathrm{Si}}, \tag{E.1d}$$

$$\Lambda_{\mathrm{Si}}(A_{\mathrm{Si}} - \gamma_{\mathrm{Si}}c_{\mathrm{Si}}) - \frac{4G_{\mathrm{Si}}B_{\mathrm{Si}}}{R_{\mathrm{Si}}^3} = \Lambda_{\mathrm{C}}(A_{\mathrm{C}} - \gamma_{\mathrm{C}}c_{\mathrm{C}}) - \frac{4G_{\mathrm{C}}B_{\mathrm{C}}}{R_{\mathrm{Si}}^3}, \tag{E.1e}$$

$$A_{\mathrm{Si}}R_{\mathrm{Si}}^3 + B_{\mathrm{Si}} = A_{\mathrm{C}}R_{\mathrm{Si}}^3 + B_{\mathrm{C}}, \tag{E.1f}$$

$$\Lambda_{\mathrm{C}}(A_{\mathrm{C}} - \gamma_{\mathrm{C}}c_{\mathrm{C}}) = 4G_{\mathrm{C}}B_{\mathrm{C}}. \tag{E.1g}$$

Solving (E.1) yields the integration constants

$$A_{\mathrm{Si}} = \frac{2\sigma^Y_{\mathrm{Si}}}{3\Lambda_{\mathrm{Si}}}\left[\log\left(\frac{R_V^3}{s_{\mathrm{Si}}^3}\right) - 1\right] + \gamma_{\mathrm{Si}}c_{\mathrm{Si}}, \tag{E.2a}$$

$$B_{\mathrm{Si}} = \frac{-\sigma^Y_{\mathrm{Si}}s_{\mathrm{Si}}^3}{6G_{\mathrm{Si}}}, \tag{E.2b}$$

$$C_{\mathrm{Si}} = \frac{2\sigma^Y_{\mathrm{Si}}}{3}\log(R_V^3), \tag{E.2c}$$

$$D_{\mathrm{Si}}(r) = \frac{2\sigma^Y_{\mathrm{Si}}}{\Lambda_{\mathrm{Si}}|_{s_{\mathrm{Si}}=r}}\left[\log\left(\frac{R_V^3}{r^3}\right) - 1\right] + 3\gamma_{\mathrm{Si}}\big(c_{\mathrm{Si}}|_{s_{\mathrm{Si}}=r} - c^p_{\mathrm{Si}}(r)|_{s_{\mathrm{Si}}=r}\big), \tag{E.2d}$$

$$\begin{aligned} A_{\mathrm{C}} = \frac{4G_{\mathrm{C}}}{4G_{\mathrm{C}}R_{\mathrm{Si}}^3 + \Lambda_{\mathrm{C}}}\left\{\frac{2\sigma^Y_{\mathrm{Si}}R_{\mathrm{Si}}^3}{3\Lambda_{\mathrm{Si}}}\left[\log\left(\frac{R_V^3}{s_{\mathrm{Si}}^3}\right) - 1\right] + \gamma_{\mathrm{Si}}c_{\mathrm{Si}}R_{\mathrm{Si}}^3 - \frac{\sigma^Y_{\mathrm{Si}}s_{\mathrm{Si}}^3}{6G_{\mathrm{Si}}}\right\} \\ + \frac{\Lambda_{\mathrm{C}}}{4G_{\mathrm{C}}R_{\mathrm{Si}}^3 + \Lambda_{\mathrm{C}}}\gamma_{\mathrm{C}}c_{\mathrm{C}}, \end{aligned} \tag{E.2e}$$

$$\begin{aligned} B_{\mathrm{C}} = \frac{\Lambda_{\mathrm{C}}}{4G_{\mathrm{C}}R_{\mathrm{Si}}^3 + \Lambda_{\mathrm{C}}}\left\{\frac{2\sigma^Y_{\mathrm{Si}}R_{\mathrm{Si}}^3}{3\Lambda_{\mathrm{Si}}}\left[\log\left(\frac{R_V^3}{s_{\mathrm{Si}}^3}\right) - 1\right] + (\gamma_{\mathrm{Si}}c_{\mathrm{Si}} - \gamma_{\mathrm{C}}c_{\mathrm{C}})R_{\mathrm{Si}}^3 \right. \\ \left. - \frac{\sigma^Y_{\mathrm{Si}}s_{\mathrm{Si}}^3}{6G_{\mathrm{Si}}}\right\}. \end{aligned} \tag{E.2f}$$

where $D_{\mathrm{Si}}(r)$ is derived in a similar way to $D_{\mathrm{C}}(r)$ in Section 5.2.2.8, and a relationship between the lithium concentrations in Ω^e_{Si} and Ω^e_{C}, given by

$$\begin{aligned} c_{\mathrm{Si}} = \frac{1}{\gamma_{\mathrm{Si}}}\left\{\frac{\sigma^Y_{\mathrm{Si}}(4G_{\mathrm{C}}R_{\mathrm{Si}}^3 + \Lambda_{\mathrm{C}})}{6G_{\mathrm{C}}\Lambda_{\mathrm{C}}(1 - R_{\mathrm{Si}}^3)}\left[1 - \frac{s_{\mathrm{Si}}^3}{R_{\mathrm{Si}}^3} - \log\left(\frac{R_V^3}{s_{\mathrm{Si}}^3}\right)\right] + \gamma_{\mathrm{C}}c_{\mathrm{C}} \right. \\ \left. + \frac{2\sigma^Y_{\mathrm{Si}}}{3\Lambda_{\mathrm{Si}}}\left[1 - \log\left(\frac{R_V^3}{s_{\mathrm{Si}}^3}\right)\right] + \frac{\sigma^Y_{\mathrm{Si}}s_{\mathrm{Si}}^3}{6G_{\mathrm{Si}}R_{\mathrm{Si}}^3}\right\}. \end{aligned} \tag{E.3}$$

The chemical potential of the lithium in each region is given by

$$\mu = \mu_{\mathrm{Si}}^{\mathrm{SF}}\big(c_{\mathrm{Si}}^{p}(r)\big) - 2S_{\mathrm{Si}}^{d}\sigma_{\mathrm{Si}}^{Y}\left[\log\left(\frac{R_V^3}{r^3}\right) - 1\right] \qquad \text{in } \Omega_{\mathrm{Si}}^{p}, \tag{E.4a}$$

$$\mu = \mu_{\mathrm{Si}}^{\mathrm{SF}}(c_{\mathrm{Si}}) - 2S_{\mathrm{Si}}^{d}\sigma_{\mathrm{Si}}^{Y}\left[\log\left(\frac{R_V^3}{s_{\mathrm{Si}}^3}\right) - 1\right] \qquad \text{in } \Omega_{\mathrm{Si}}^{e}, \tag{E.4b}$$

$$\mu = \mu_{\mathrm{C}}^{\mathrm{SF}}(c_{\mathrm{C}}) - \frac{2S_{\mathrm{C}}^{d}\sigma_{\mathrm{Si}}^{Y}R_{\mathrm{Si}}^{3}}{1 - R_{\mathrm{Si}}^{3}}\left[1 - \frac{s_{\mathrm{Si}}^3}{R_{\mathrm{Si}}^3} - \log\left(\frac{R_V^3}{s_{\mathrm{Si}}^3}\right)\right] \qquad \text{in } \Omega_{\mathrm{C}}^{e}. \tag{E.4c}$$

It can be seen from (E.4a) and (E.4b) that the lithium concentration at $r = s_{\mathrm{Si}}$ is continuous, simplifying (E.2d) to just the first term.

To solve this system, we substitute (E.3) into (E.4b) and equate this to (E.4c) to yield a single equation for c_{C} for a given R_V, R_{Si} and s_{Si} which we can solve numerically. With lithiation-dependent Lamé parameters, (E.3) would need to be solved numerically for c_{Si} within the solver for c_{C} due to c_{Si} appearing in the Λ_{Si} and G_{Si} terms in the right-hand side. We then find c_{Si} and $c_{\mathrm{Si}}^{p}(r)$ for all the discrete values of $r \in [R_V, s_{\mathrm{Si}}]$ using (E.4a)-(E.4b), substitute the lithium concentrations into (E.1d) and solve for E_{Si}. This equation to solve is given by

$$\begin{aligned}
&\int_{R_V}^{s_{\mathrm{Si}}} 3\gamma_{\mathrm{Si}}c_{\mathrm{Si}}^{p}(\tilde{r})\tilde{r}^2 + \frac{2\sigma_{\mathrm{Si}}^{Y}\tilde{r}^2}{\Lambda_{\mathrm{Si}}|_{s_{\mathrm{Si}}=\tilde{r}}}\left[\log\left(\frac{R_V^3}{\tilde{r}^3}\right) - 1\right]\mathrm{d}\tilde{r} \\
&= \frac{2\sigma_{\mathrm{Si}}^{Y}s_{\mathrm{Si}}^{3}}{3\Lambda_{\mathrm{Si}}}\left[\log\left(\frac{R_V^3}{s_{\mathrm{Si}}^3}\right) - 1 - \frac{\Lambda_{\mathrm{Si}}}{4G_{\mathrm{Si}}}\right] + \gamma_{\mathrm{Si}}c_{\mathrm{Si}}s_{\mathrm{Si}}^{3} - E_{\mathrm{Si}}.
\end{aligned} \tag{E.5}$$

There are no bounds on E_{Si} as there are for c_{Si} when solving the e.p.e regime, and so solving this numerically is more difficult than solving for one of the concentration variables. However, if we only wish to calculate the position of s_{Si} as a function of c_0, we do not need to solve (E.5) at all as this can be obtained from the concentrations alone.

E.3 e.p.e

The boundary conditions in the e.p.e regime are given by

$$\Lambda_{\mathrm{Si}}(A_{\mathrm{Si}} - \gamma_{\mathrm{Si}} c_{\mathrm{Si}}) = \frac{4G_{\mathrm{Si}} B_{\mathrm{Si}}}{R_V^3}, \tag{E.6a}$$

$$A_{\mathrm{Si}} R_{\mathrm{Si}}^3 + B_{\mathrm{Si}} = E_{\mathrm{C}}, \tag{E.6b}$$

$$\Lambda_{\mathrm{Si}}(A_{\mathrm{Si}} - \gamma_{\mathrm{Si}} c_{\mathrm{Si}}) - \frac{4G_{\mathrm{Si}} B_{\mathrm{Si}}}{R_{\mathrm{Si}}^3} = C_{\mathrm{C}} + 2\sigma_p^{\max} \log(R_{\mathrm{Si}}), \tag{E.6c}$$

$$\int_{R_{\mathrm{Si}}}^{s_{\mathrm{C}}} \big(3\gamma_{\mathrm{C}} c_{\mathrm{C}}^p(\tilde{r}) + D_{\mathrm{C}}(\tilde{r})\big)\tilde{r}^2 \;\mathrm{d}\tilde{r} = A_{\mathrm{C}} s_{\mathrm{C}}^3 + B_{\mathrm{C}} - E_{\mathrm{C}}, \tag{E.6d}$$

$$C_{\mathrm{C}} + 2\sigma_p^{\max} \log(s_{\mathrm{C}}) = \Lambda_{\mathrm{C}}(A_{\mathrm{C}} - \gamma_{\mathrm{C}} c_{\mathrm{C}}) - \frac{4G_{\mathrm{C}} B_{\mathrm{C}}}{s_{\mathrm{C}}^3}, \tag{E.6e}$$

$$\frac{6G_{\mathrm{C}} B_{\mathrm{C}}}{s_{\mathrm{C}}^3} = \sigma_{\mathrm{C}}^Y, \tag{E.6f}$$

$$\Lambda_{\mathrm{C}}(A_{\mathrm{C}} - \gamma_{\mathrm{C}} c_{\mathrm{C}}) = 4G_{\mathrm{C}} B_{\mathrm{C}}. \tag{E.6g}$$

Solving (E.6) yields the expressions

$$A_{\mathrm{Si}} = \frac{2R_{\mathrm{Si}}^3}{3\Lambda_{\mathrm{Si}}(R_{\mathrm{Si}}^3 - R_V^3)} \left[\sigma_{\mathrm{C}}^Y (s_{\mathrm{C}}^3 - 1) + \sigma_p^{\max} \log\left(\frac{R_{\mathrm{Si}}^3}{s_{\mathrm{C}}^3}\right)\right] + \gamma_{\mathrm{Si}} c_{\mathrm{Si}}, \tag{E.7a}$$

$$B_{\mathrm{Si}} = \frac{R_{\mathrm{Si}}^3 R_V^3}{6G_{\mathrm{Si}}(R_{\mathrm{Si}}^3 - R_V^3)} \left[\sigma_{\mathrm{C}}^Y (s_{\mathrm{C}}^3 - 1) + \sigma_p^{\max} \log\left(\frac{R_{\mathrm{Si}}^3}{s_{\mathrm{C}}^3}\right)\right], \tag{E.7b}$$

$$A_{\mathrm{C}} = \frac{2\sigma_{\mathrm{C}}^Y s_{\mathrm{C}}^3}{3\Lambda_{\mathrm{C}}} + \gamma_{\mathrm{C}} c_{\mathrm{C}}, \tag{E.7c}$$

$$B_{\mathrm{C}} = \frac{\sigma_{\mathrm{C}}^Y s_{\mathrm{C}}^3}{6G_{\mathrm{C}}}, \tag{E.7d}$$

$$C_{\mathrm{C}} = \frac{2\sigma_{\mathrm{C}}^Y}{3}(s_{\mathrm{C}}^3 - 1) - \frac{2\sigma_p^{\max}}{3} \log(s_{\mathrm{C}}^3), \tag{E.7e}$$

$$D_{\mathrm{C}} = \frac{2\sigma_{\mathrm{C}}^Y r^3}{\Lambda_{\mathrm{C}}|_{s_C=r}} + 3\gamma_{\mathrm{C}}\big(c_{\mathrm{C}}|_{s_C=r} - c_{\mathrm{C}}^p(s_{\mathrm{C}})|_{s_C=r}\big), \tag{E.7f}$$

$$E_{\mathrm{C}} = \frac{R_{\mathrm{Si}}^3(4G_{\mathrm{Si}} R_{\mathrm{Si}}^3 + \Lambda_{\mathrm{Si}} R_V^3)}{6G_{\mathrm{Si}}\Lambda_{\mathrm{Si}}(R_{\mathrm{Si}}^3 - R_V^3)} \left[\sigma_{\mathrm{C}}^Y (s_{\mathrm{C}}^3 - 1) + \sigma_p^{\max} \log\left(\frac{R_{\mathrm{Si}}^3}{s_{\mathrm{C}}^3}\right)\right] + \gamma_{\mathrm{Si}} c_{\mathrm{Si}} R_{\mathrm{Si}}^3. \tag{E.7g}$$

The chemical potential of the lithium in this regime are given by

$$\mu = \mu_{\mathrm{Si}}^{\mathrm{SF}}(c_{\mathrm{Si}}) - \frac{2S_{\mathrm{Si}}^d R_{\mathrm{Si}}^3}{R_{\mathrm{Si}}^3 - R_V^3} \left[\sigma_{\mathrm{Si}}^Y (s_{\mathrm{C}}^3 - 1) + \sigma_p^{\max} \log\left(\frac{R_{\mathrm{Si}}^3}{s_{\mathrm{C}}^3}\right)\right] \qquad \text{in } \Omega_{\mathrm{Si}}, \tag{E.8a}$$

$$\mu = \mu_{\mathrm{C}}^{\mathrm{SF}}\big(c_{\mathrm{C}}^p(r)\big) - 2S_{\mathrm{C}}^d \left[\sigma_{\mathrm{C}}^Y (s_{\mathrm{C}}^3 - 1) + \sigma_p^{\max} \log\left(\frac{r^3}{s_{\mathrm{C}}^3}\right) + \sigma_p^{\max}\right] \qquad \text{in } \Omega_{\mathrm{C}}^p, \tag{E.8b}$$

$$\mu = \mu_{\mathrm{C}}^{\mathrm{SF}}(c_{\mathrm{C}}) - 2S_{\mathrm{C}}^d \sigma_{\mathrm{C}}^Y s_{\mathrm{C}}^3 \qquad \text{in } \Omega_{\mathrm{C}}^e, \tag{E.8c}$$

We substitute the integration constants (E.7) into (E.6d) to yield

$$\begin{aligned}\int_{R_{\mathrm{Si}}}^{s_{\mathrm{C}}} & 3\gamma_{\mathrm{C}}\big(c_{\mathrm{C}}^{p}(\tilde{r}) + c_{\mathrm{C}}|_{s_{\mathrm{C}}=r} - c_{\mathrm{C}}^{p}(s_{\mathrm{C}})|_{s_{\mathrm{C}}=r}\big)\tilde{r}^{2} + \frac{2\sigma_{\mathrm{C}}^{Y} r^{5}}{\Lambda_{\mathrm{C}}|_{s_{\mathrm{C}}=r}}\ \mathrm{d}\tilde{r} \\ &= \frac{2\sigma_{\mathrm{C}}^{Y} s_{\mathrm{C}}^{6}}{3\Lambda_{\mathrm{C}}} - \frac{R_{\mathrm{Si}}^{3}(4G_{\mathrm{Si}}R_{\mathrm{Si}}^{3} + \Lambda_{\mathrm{Si}}R_{V}^{3})}{6G_{\mathrm{Si}}\Lambda_{\mathrm{Si}}(R_{\mathrm{Si}}^{3} - R_{V}^{3})}\left[\sigma_{\mathrm{C}}^{Y}(s_{\mathrm{C}}^{3} - 1) + 3\sigma_{p}^{\max}\log\left(\frac{R_{\mathrm{Si}}}{s_{\mathrm{C}}}\right)\right] \\ &\qquad + \frac{\sigma_{\mathrm{C}}^{Y} s_{\mathrm{C}}^{3}}{6G_{\mathrm{C}}} + \gamma_{\mathrm{C}} c_{\mathrm{C}} s_{\mathrm{C}}^{3} - \gamma_{\mathrm{Si}} c_{\mathrm{Si}} R_{\mathrm{Si}}^{3}.\end{aligned} \tag{E.9}$$

This equation can be solved numerically for c_{Si} for a given s_{C}, R_V and R_{Si}, by solving for the c_{C} and c_{C}^{p} for the guessed value of c_{Si} using (E.8) and minimising the residual of (E.9). We increase s_{C} from $s_{\mathrm{C}} = R_{\mathrm{Si}}$ to $s_{\mathrm{C}} = 1$, solving for the lithium concentrations and displacement at each discrete value of s_{C}, using a similar method to that described in Section 5.2.2.8.

E.4 p.e.p.e

If both materials have only partially yielded, the nano-particle is in the p.e.p.e regime. The boundary conditions for the p.e.p.e regime are given by (E.6b)-(E.6g) and (E.1a)-(E.1d). Solving these boundary conditions gives A_{C}, B_{C}, D_{C}, A_{Si}, B_{Si}, C_{Si} and D_{Si} as (E.7c)-(E.7d), (E.7f), (E.2a)-(E.2d), respectively, and

$$C_{\mathrm{C}} = \frac{2\sigma_{\mathrm{Si}}^{Y}}{3}\log\left(\frac{R_V^3}{s_{\mathrm{Si}}^3}\right) - \frac{2\sigma_p^{\max}}{3}\log(R_{\mathrm{Si}}^3) + \frac{2\sigma_{\mathrm{Si}}^{Y}}{3}\left(\frac{s_{\mathrm{Si}}^3}{R_{\mathrm{Si}}^3} - 1\right), \tag{E.10a}$$

$$E_{\mathrm{C}} = \frac{2\sigma_{\mathrm{Si}}^{Y} R_{\mathrm{Si}}^3}{3\Lambda_{\mathrm{Si}}}\left[\log\left(\frac{R_V^3}{s_{\mathrm{Si}}^3}\right) - 1\right] + \gamma_{\mathrm{Si}} c_{\mathrm{Si}} R_{\mathrm{Si}}^3 - \frac{\sigma_{\mathrm{Si}}^{Y} s_{\mathrm{Si}}^3}{6G_{\mathrm{Si}}}. \tag{E.10b}$$

The boundary conditions for the p.e.p.e regime also yield a relationship between the two yielded fronts, given by

$$\sigma_{\mathrm{Si}}^{Y}\left[\log\left(\frac{s_{\mathrm{Si}}^3}{R_V^3}\right) + 1 - \frac{s_{\mathrm{Si}}^3}{R_{\mathrm{Si}}^3}\right] = \sigma_p^{\max}\log\left(\frac{s_{\mathrm{C}}^3}{R_{\mathrm{Si}}^3}\right) + \sigma_{\mathrm{C}}^{Y}(1 - s_{\mathrm{C}}^3). \tag{E.11}$$

Lastly, the chemical potential of the lithium in each region is given by (E.8c), (E.4a), (E.4b) and

$$\begin{aligned}\mu = \mu_{\mathrm{C}}^{\mathrm{SF}}\big(c_{\mathrm{C}}^{p}(r)\big) - 2S_{\mathrm{C}}^{d}\bigg[&\sigma_{\mathrm{Si}}^{Y}\log\left(\frac{R_V^3}{s_{\mathrm{Si}}^3}\right) + \sigma_p^{\max}\log\left(\frac{r^3}{R_{\mathrm{Si}}^3}\right) \\ &+ \sigma_{\mathrm{Si}}^{Y}\left(\frac{s_{\mathrm{Si}}^3}{R_{\mathrm{Si}}^3} - 1\right) + \sigma_p^{\max}\bigg] \qquad \text{in } \Omega_{\mathrm{C}}^{p},\end{aligned} \tag{E.12}$$

Therefore, for a given R_V, R_{Si} and s_{C}, we numerically solve (E.11) to find s_{Si} and substitute A_{C}, B_{C}, D_{C}, E_{C} and s_{Si} into (E.6d) to yield

$$\begin{aligned}\int_{R_{\mathrm{Si}}}^{s_{\mathrm{C}}} 3\gamma_{\mathrm{C}}\big(c_{\mathrm{C}}^p(\tilde{r}) + c_{\mathrm{C}}|_{s_{\mathrm{C}}=r} - c_{\mathrm{C}}^p(s_{\mathrm{C}})|_{s_{\mathrm{C}}=r}\big)\tilde{r}^2 + \frac{2\sigma_{\mathrm{C}}^Y r^5}{\Lambda_{\mathrm{C}}|_{s_{\mathrm{C}}=r}}\ \mathrm{d}\tilde{r} \\ = \frac{2\sigma_{\mathrm{C}}^Y s_{\mathrm{C}}^6}{3\Lambda_{\mathrm{C}}} + \frac{\sigma_{\mathrm{C}}^Y s_{\mathrm{C}}^3}{6G_{\mathrm{C}}} - \frac{2\sigma_{\mathrm{Si}}^Y R_{\mathrm{Si}}^3}{3\Lambda_{\mathrm{Si}}}\left[\log\left(\frac{R_V^3}{s_{\mathrm{Si}}^3}\right) - 1\right] + \frac{\sigma_{\mathrm{Si}}^Y s_{\mathrm{Si}}^3}{6G_{\mathrm{Si}}} \\ + \gamma_{\mathrm{C}} c_{\mathrm{C}} s_{\mathrm{C}}^3 - \gamma_{\mathrm{Si}} c_{\mathrm{Si}} R_{\mathrm{Si}}^3,\end{aligned} \tag{E.13}$$

and solve for c_{Si}. Within the function to evaluate the residual of (E.13), we calculate c_{C} and $c_{\mathrm{C}}^p(r)$ for $r \in [R_{\mathrm{Si}}, s_{\mathrm{C}}]$ by equating (E.4b) to (E.8c) and (E.12), respectively. To find the displacement in Ω_{Si}^p, $c_{\mathrm{Si}}^p(r)$ is calculated by equating (E.4b) to (E.4a) for $r \in [R_V, s_{\mathrm{Si}}]$, and solving (E.5) for E_{Si}.

E.5 p.e

The boundary conditions in the p.e regime are given by (E.1a), (E.1g) and

$$C_{\mathrm{Si}} - \frac{2\sigma_{\mathrm{Si}}^Y}{3}\log(R_{\mathrm{Si}}^3) = \Lambda_{\mathrm{C}}(A_{\mathrm{C}} - \gamma_{\mathrm{C}} c_{\mathrm{C}}) - \frac{4G_{\mathrm{C}}B_{\mathrm{C}}}{R_{\mathrm{Si}}^3}, \tag{E.14a}$$

$$\int_{R_V}^{R_{\mathrm{Si}}} \big(3\gamma_{\mathrm{Si}} c_{\mathrm{Si}}^p(\tilde{r}) + D_{\mathrm{Si}}(\tilde{r})\big)\tilde{r}^2\ \mathrm{d}\tilde{r} = A_{\mathrm{C}} R_{\mathrm{Si}}^3 + B_{\mathrm{C}} - E_{\mathrm{Si}}. \tag{E.14b}$$

The expressions for C_{Si} and D_{Si} in this regime are given by (E.2c) and (E.2d), respectively. If the Lamé parameters are assumed lithiation-dependent, $D_{\mathrm{Si}}(r)$ will have to be calculated using the values of c_{Si} when the nano-particle is in the p.e.e regime for $s_{\mathrm{Si}} \in [R_V, R_{\mathrm{Si}}]$. The integration constants A_{C} and B_{C} are given by

$$A_{\mathrm{C}} = \frac{2\sigma_{\mathrm{Si}}^Y R_{\mathrm{Si}}^3}{3\Lambda_{\mathrm{C}}(R_{\mathrm{Si}}^3 - 1)}\log\left(\frac{R_V^3}{R_{\mathrm{Si}}^3}\right) + \gamma_{\mathrm{C}} c_{\mathrm{C}}, \tag{E.15a}$$

$$B_{\mathrm{C}} = \frac{\sigma_{\mathrm{Si}}^Y R_{\mathrm{Si}}^3}{6G_{\mathrm{C}}(R_{\mathrm{Si}}^3 - 1)}\log\left(\frac{R_V^3}{R_{\mathrm{Si}}^3}\right). \tag{E.15b}$$

Lastly, the lithium concentration in Ω_{Si}^p and Ω_{C}^e is determined by

$$\mu_{\mathrm{Si}}^{\mathrm{SF}}\big(c_{\mathrm{Si}}^p(r)\big) - 2S_{\mathrm{Si}}^d \sigma_{\mathrm{Si}}^Y\left[\log\left(\frac{R_V^3}{r^3}\right) - 1\right] = \mu_{\mathrm{C}}^{\mathrm{SF}}(c_{\mathrm{C}}) - \frac{2S_{\mathrm{C}}^d \sigma_{\mathrm{Si}}^Y R_{\mathrm{Si}}^3}{R_{\mathrm{Si}}^3 - 1}\log\left(\frac{R_V^3}{R_{\mathrm{Si}}^3}\right). \tag{E.16}$$

As s_{Si} is fixed at $s_{\mathrm{Si}} = R_{\mathrm{Si}}$, we instead increase c_{C} from the value at which s_{Si} first reaches R_{Si}. We calculate $c_{\mathrm{Si}}^p(r)$ for $r \in [R_V, R_{\mathrm{Si}}]$ using (E.16), and solve (E.14b) for E_{Si}. If the graphite is fully lithiated before the plastic silicon, we fix $c_{\mathrm{C}} = 1$ and increase $c_{\mathrm{Si}}^p(R_{\mathrm{Si}})$ until $c_{\mathrm{Si}}^p(R_{\mathrm{Si}}) = 1$ because c_{Si}^p is smallest at $r = R_{\mathrm{Si}}$, as seen from (E.16). Thus, we can calculate the displacement in the nano-particle in this regime for all values of the SOC.

E.6 e.p

The boundary conditions in the e.p regime are given by (E.6a)-(E.6c) and

$$C_{\mathrm{C}} + 2\sigma_p^{\max}\log(1) = 0. \tag{E.17}$$

We solve this system of equations to give

$$A_{\mathrm{Si}} = \frac{2\sigma_p^{\max}R_{\mathrm{Si}}^3}{3\Lambda_{\mathrm{Si}}(R_{\mathrm{Si}}^3 - R_V^3)}\log(R_{\mathrm{Si}}^3) + \gamma_{\mathrm{Si}}c_{\mathrm{Si}}, \tag{E.18a}$$

$$B_{\mathrm{Si}} = \frac{\sigma_p^{\max}R_V^3R_{\mathrm{Si}}^3}{6G_{\mathrm{Si}}(R_{\mathrm{Si}}^3 - R_V^3)}\log(R_{\mathrm{Si}}^3), \tag{E.18b}$$

$$C_{\mathrm{C}} = 0, \tag{E.18c}$$

$$E_{\mathrm{C}} = \frac{\sigma_p^{\max}R_{\mathrm{Si}}^3(4G_{\mathrm{Si}}R_{\mathrm{Si}}^3 + \Lambda_{\mathrm{Si}}R_V^3)}{6G_{\mathrm{Si}}\Lambda_{\mathrm{Si}}(R_{\mathrm{Si}}^3 - R_V^3)}\log(R_{\mathrm{Si}}^3) + \gamma_{\mathrm{Si}}c_{\mathrm{Si}}R_{\mathrm{Si}}^3. \tag{E.18d}$$

The lithium concentrations are determined from

$$\mu_{\mathrm{Si}}^{\mathrm{SF}}(c_{\mathrm{Si}}) - \frac{2S_{\mathrm{Si}}^d\sigma_p^{\max}R_{\mathrm{Si}}^3}{R_{\mathrm{Si}}^3 - R_V^3}\log(R_{\mathrm{Si}}^3) = \mu_{\mathrm{C}}^{\mathrm{SF}}\big(c_{\mathrm{C}}^p(r)\big) - 2S_{\mathrm{C}}^d\sigma_p^{\max}\big(\log(r^3)+1\big). \tag{E.19}$$

If the Lamé parameters are assumed to be lithiation-dependent, $D_{\mathrm{C}}(r)$ is calculated from c_{C} values in the e.p.e regime for $s_{\mathrm{C}} \in [R_{\mathrm{Si}}, 1]$.

Similarly to the p.e regime, there is no yielded front position to increase in this regime so we instead increase the value of c_{Si} from the value at which $s_{\mathrm{C}} = 1$, using (E.19) to find $c_{\mathrm{C}}^p(r)$ for each c_{Si} value. If the silicon is fully lithiated before the pulverised graphite, we instead increase $c_{\mathrm{C}}^p(R_{\mathrm{Si}})$ until $c_{\mathrm{C}}^p(R_{\mathrm{Si}}) = 1$ because c_{C}^p is smallest at $r = R_{\mathrm{Si}}$, as seen from (E.19).

E.7 p.p.e

The boundary conditions for this regime are given by (E.1a), (E.6d)-(E.6g) and

$$C_{\mathrm{Si}} - \frac{2\sigma_{\mathrm{Si}}^Y}{3}\log(R_{\mathrm{Si}}^3) = C_{\mathrm{C}} + \frac{2\sigma_p^{\max}}{3}\log(R_{\mathrm{Si}}^3), \tag{E.20a}$$

$$\int_{R_V}^{R_{\mathrm{Si}}}\big(3\gamma_{\mathrm{Si}}c_{\mathrm{Si}}^p(\tilde{r}) + D_{\mathrm{Si}}(\tilde{r})\big)\tilde{r}^2\,\mathrm{d}\tilde{r} = E_{\mathrm{C}} - E_{\mathrm{Si}}, \tag{E.20b}$$

$$\int_{R_{\mathrm{Si}}}^{s_{\mathrm{C}}}\big(3\gamma_{\mathrm{C}}c_{\mathrm{C}}^p(\tilde{r} + D_{\mathrm{C}}(\tilde{r})\big)\tilde{r}^2\,\mathrm{d}\tilde{r} = A_{\mathrm{C}}s_{\mathrm{C}}^3 + B_{\mathrm{C}} - E_{\mathrm{C}}. \tag{E.20c}$$

We solve these boundary conditions for A_{C}, B_{C}, C_{Si} and C_{C}, which are given by (E.7c), (E.7d), (E.2c) and

$$C_{\mathrm{C}} = \frac{2\sigma_{\mathrm{Si}}^Y}{3}\log\left(\frac{R_V^3}{R_{\mathrm{Si}}^3}\right) - \frac{2\sigma_p^{\max}}{3}\log(R_{\mathrm{Si}}^3), \tag{E.21}$$

respectively, and $D_{\mathrm{Si}}(r)$ and $D_{\mathrm{C}}(r)$ are given by (E.2d) and (E.7f), respectively. The chemical potential of the lithium in the different regions is given by (E.4a), (E.8c) and

$$\mu = \mu_{\mathrm{C}}^{\mathrm{SF}}(c_{\mathrm{C}}) - 2S_{\mathrm{C}}^{d}\left[\sigma_{\mathrm{Si}}^{Y}\log\left(\frac{R_V^3}{R_{\mathrm{Si}}^3}\right) + \sigma_p^{\max}\log\left(\frac{r^3}{R_{\mathrm{Si}}^3}\right) + 2\sigma_p^{\max}\right] \text{ in } \Omega_{\mathrm{C}}^{p}. \tag{E.22}$$

We substitute A_{C}, B_{C} and C_{C} into (E.6e) to obtain an algebraic equation for s_{C}, given by

$$\sigma_{\mathrm{Si}}^{Y}\log\left(\frac{R_V^3}{R_{\mathrm{Si}}^3}\right) + \sigma_p^{\max}\log\left(\frac{s_{\mathrm{C}}^3}{R_{\mathrm{Si}}^3}\right) = \sigma_{\mathrm{C}}^{Y}(s_{\mathrm{C}}^3 - 1). \tag{E.23}$$

Because this is an algebraic equation only depending on the initial geometry of the nano-particle and the yield stresses of each material, the pulverised front s_{C} must remain constant under the current assumptions.

Similarly to the e.p and p.e regimes, we solve for the displacement and concentrations for a given c_{C}, increasing c_{C} from the value at which the silicon fully yields to $c_{\mathrm{C}} = 1$. We do this by substituting c_{C} into (E.4a) and (E.22) and solving for $c_{\mathrm{Si}}^{p}(r)$ and $c_{\mathrm{C}}^{p}(r)$, for $r = [R_V, R_{\mathrm{Si}}]$ and $r = [R_{\mathrm{Si}}, s_{\mathrm{C}}]$, respectively. We substitute the integration constants into (E.20c) to give

$$\begin{aligned}
&\int_{R_{\mathrm{Si}}}^{s_{\mathrm{C}}} 3\gamma_{\mathrm{C}}\big(c_{\mathrm{C}}^{p}(\tilde{r}) + c_{\mathrm{C}}|_{s_{\mathrm{C}}=r} - c_{\mathrm{C}}^{p}(s_{\mathrm{C}})|_{s_{\mathrm{C}}=r}\big)\tilde{r}^2 + \frac{2\sigma_{\mathrm{C}}^{Y} r^5}{\Lambda_{\mathrm{C}}|_{s_{\mathrm{C}}=r}}\,\mathrm{d}\tilde{r} \\
&= \frac{2\sigma_{\mathrm{C}}^{Y} s_{\mathrm{C}}^6}{3\Lambda_{\mathrm{C}}} + \gamma_{\mathrm{C}} c_{\mathrm{C}} s_{\mathrm{C}}^3 + \frac{\sigma_{\mathrm{C}}^{Y} s_{\mathrm{C}}^3}{6G_{\mathrm{C}}} - E_{\mathrm{Si}} \\
&\qquad - \int_{R_V}^{R_{\mathrm{Si}}} 3\gamma_{\mathrm{Si}} c_{\mathrm{Si}}^{p}(\tilde{r})\tilde{r}^2 + \frac{2\sigma_{\mathrm{Si}}^{Y}\tilde{r}^2}{\Lambda_{\mathrm{Si}}|_{s_{\mathrm{Si}}=r}}\left[\log\left(\frac{R_V^3}{\tilde{r}^3}\right) - 1\right]\mathrm{d}\tilde{r}
\end{aligned} \tag{E.24}$$

and solve for E_{Si} to fully solve the system.

E.8 p.e.p

In this regime, the boundary conditions are given by (E.6b)-(E.6c), (E.1a)-(E.1d) and (E.17). We can solve for A_{Si}, B_{Si}, C_{Si}, C_{C} and E_{C}, given by (E.2a), (E.2b), (E.2c), (E.18c) and (E.10b), respectively. The functions $D_{\mathrm{Si}}(r)$ and $D_{\mathrm{C}}(r)$ are given by (E.2d) and (E.7f), respectively. The chemical potential in each regime is given by (E.4a), (E.4b), and

$$\mu = \mu_{\mathrm{C}}^{\mathrm{SF}}\big(c_{\mathrm{C}}^{p}(r)\big) - 2S_{\mathrm{C}}^{d}\sigma_p^{\max}\big(\log(r^3) + 1\big) \qquad \text{in } \Omega_{\mathrm{C}}^{p}. \tag{E.25}$$

Similarly to the p.p.e regime, we can substitute these integration constants into (E.6c) to find an algebraic expression for s_{Si}, given by

$$\sigma_p^{\max}\log(R_{\text{Si}}^3) + \sigma_{\text{Si}}^Y \log\left(\frac{s_{\text{Si}}^3}{R_V^3}\right) = \sigma_{\text{Si}}^Y\left(\frac{s_{\text{Si}}^3}{R_{\text{Si}}^3} - 1\right). \tag{E.26}$$

Therefore, in the p.e.p regime, s_{Si} is fixed. Because the position of the plastic front is fixed, we solve for the displacement and concentrations for increasing values of c_{Si} by solving (E.5) for E_{Si}. Similarly to other regimes, if c_{Si} reaches $c_{\text{Si}} = 1$ before the nano-particle is fully lithiated, we then increase $c_{\text{C}}^p(R_{\text{Si}})$ until $c_{\text{C}}^p(R_{\text{Si}}) = 1$ as $c_{\text{C}}^p(r)$ is smallest at $r = R_{\text{Si}}$.

E.9 p.p

Lastly, if both the materials fully yield, the boundary conditions in the p.p regime are given by (E.1a), (E.17), (E.20a) and (E.20b). We can solve for C_{Si} and C_{C}, giving (E.18c) and (E.2c), respectively. We then substitute these into (E.20a) to yield

$$\sigma_{\text{Si}}^Y \log\left(\frac{R_V^3}{R_{\text{Si}}^3}\right) = \sigma_p^{\max}\log(R_{\text{Si}}^3). \tag{E.27}$$

This is an algebraic equation for the geometric and yield constants of the materials and thus the p.p regime will only occur if (E.27) is satisfied. The equation relating c_{Si}^p and c_{C}^p in this regime is

$$\mu_{\text{Si}}^{\text{SF}}\big(c_{\text{Si}}^p(r)\big) - 2S_{\text{Si}}^d\sigma_{\text{Si}}^Y\left[\log\left(\frac{R_V^3}{r^3}\right) - 1\right] = \mu_{\text{C}}^{\text{SF}}\big(c_{\text{C}}^p(r)\big) - 2S_{\text{C}}^d\sigma_p^{\max}\big[\log(r^3) + 1\big]. \tag{E.28}$$

If (E.27) is satisfied, however, we cannot solve this system fully as there is only one equation relating E_{Si} and E_{C}.

Bibliography

[1] M. S. Alnæs, J. Blechta, J. Hake, A. Johansson, B. Kehlet, A. Logg, C. Richardson, J. Ring, M. E. Rognes, and G. N. Wells. The fenics project version 1.5. *Archive of Numerical Software*, 3(100), 2015.

[2] S. Atlung, K. West, and T. Jacobsen. Dynamic aspects of solid solution cathodes for electrochemical power sources. *Journal of The Electrochemical Society*, 126(8):1311–1321, 1979.

[3] T. M. Bandhauer, S. Garimella, and T. F. Fuller. A critical review of thermal issues in lithium-ion batteries. *Journal of the Electrochemical Society*, 158(3):R1–R25, 2011.

[4] M. Z. Bazant. Theory of chemical kinetics and charge transfer based on nonequilibrium thermodynamics. *Accounts of Chemical Research*, 46(5):1144–1160, 2013.

[5] L. Y. Beaulieu, K. W. Eberman, R. L. Turner, L. J. Krause, and J. R. Dahn. Colossal reversible volume changes in lithium alloys. *Electrochemical and Solid-State Letters*, 4(9):A137–A140, 2001.

[6] C. R. Birkl, E. McTurk, M. R. Roberts, P. G. Bruce, and D. A. Howey. A parametric open circuit voltage model for lithium-ion batteries. *Journal of The Electrochemical Society*, 162(12):A2271–A2280, 2015.

[7] A. M. Bizeray, J. Kim, S. R. Duncan, and D. A. Howey. Identifiability and parameter estimation of the single particle lithium-ion battery model. *IEEE Transactions on Control Systems Technology*, 2018.

[8] P. J. Blatz and W. L. Ko. Application of finite elastic theory to the deformation of rubbery materials. *Transactions of the Society of Rheology*, 6(1):223–252, 1962.

[9] A. F. Bower, P. R. Guduru, and V. A. Sethuraman. A Finite Strain Model of Stress, Diffusion, Plastic Flow and Electrochemical Reactions in a Lithium-Ion Half-Cell. *Journal of the Mechanics and Physics of Solids*, 59(4):1–41, 2010.

[10] Q. M. Bui and H. C. Elman. Semi-smooth newton methods for nonlinear complementarity formulation of compositional two-phase flow in porous media. *arXiv preprint arXiv:1805.05801*, 2018.

[11] R. Burridge and J. B. Keller. Poroelasticity equations derived from microstructure. *The Journal of the Acoustical Society of America*, 70(4):1140–1146, 1981.

[12] John W Cahn and John E Hilliard. Free energy of a nonuniform system. I. Interfacial free energy. *The Journal of Chemical Physics*, 28(2):258–267, 1958.

[13] J. Chakraborty, C. P. Please, A. Goriely, and S. J. Chapman. Combining mechanical and chemical effects in the deformation and failure of a cylindrical electrode particle in a Li-ion battery. *International Journal of Solids and Structures*, 54:66–81, 2015.

[14] C. K. Chan, H. Peng, G. Liu, K. McIlwrath, X. F. Zhang, R. A. Huggins, and Y. Cui. High-performance lithium battery anodes using silicon nanowires. *Nature Nanotechnology*, 3(1):31–35, 2008.

[15] B. Chen, J. Zhou, and R. Cai. Analytical model for crack propagation in spherical nano electrodes of lithium-ion batteries. *Electrochimica Acta*, 210:7–14, 2016.

[16] C. Chen and O. L. Mangasarian. A class of smoothing functions for nonlinear and mixed complementarity problems. *Computational Optimization and Applications*, 5(2):97–138, 1996.

[17] L. Chen, F. Fan, L. Hong, J. Chen, Y. Z. Ji, S. L. Zhang, T. Zhu, and L. Q. Chen. A Phase-Field Model Coupled with Large Elasto-Plastic Deformation: Application to Lithiated Silicon Electrodes. *Journal of the Electrochemical Society*, 161(11):F3164–F3172, 2014.

[18] M. J. Chen, L. S. Kimpton, J. P. Whiteley, M. Castilho, J. Malda, C. P. Please, S. L. Waters, and H. M. Byrne. Multiscale modelling and homogenisation of fibre-reinforced hydrogels for tissue engineering. *European Journal of Applied Mathematics*, pages 1–29, 2019.

[19] Y. Chen, Q. Z. Huang, J. Wang, Q. Wang, and J. M. Xue. Synthesis of monodispersed SnO_2@C composite hollow spheres for lithium ion battery anode applications. *Journal of Materials Chemistry*, 21(43):17448–17453, 2011.

[20] M. J. Chon, V. A. Sethuraman, A. McCormick, V. Srinivasan, and P. R. Guduru. Real-time measurement of stress and damage evolution during initial lithiation of crystalline silicon. *Physical Review Letters*, 107(4):045503, 2011.

[21] J. Christensen and J. Newman. Stress generation and fracture in lithium insertion materials. *Journal of Solid State Electrochemistry*, 10(5):293–319, 2006.

[22] F. Ciucci and W. Lai. Derivation of micro/macro lithium battery models from homogenization. *Transport in Porous Media*, 88(2):249–270, 2011.

[23] L. Cui, R. Ruffo, C. K. Chan, H. Peng, and Y. Cui. Crystalline–amorphous core–shell silicon nanowires for high capacity and high current battery electrodes. *Nano Letters*, 9(1):491–495, 2008.

[24] Z. Cui, F. Gao, Z. Cui, and J. Qu. A second nearest-neighbor embedded atom method interatomic potential for Li–Si alloys. *Journal of Power Sources*, 207:150–159, 2012.

[25] Z. Cui, F. Gao, and J. Qu. A finite deformation stress-dependent chemical potential and its applications to lithium-ion batteries. *Journal of the Mechanics and Physics of Solids*, 60(7):1280–1295, 2012.

[26] Z. Cui, F. Gao, and J. Qu. Interface-reaction controlled diffusion in binary solids with applications to lithiation of silicon in lithium-ion batteries. *Journal of the Mechanics and Physics of Solids*, 61(2):293–310, 2013.

[27] Z. Cui, F. Gao, and J. M. Qu. On the perturbation solution of interface-reaction controlled diffusion in solids. *Acta Mechanica Sinica/Lixue Xuebao*, 28(4):1049–1057, 2012.

[28] D. Deng and J. Y. Lee. Hollow core–shell mesospheres of crystalline SnO_2 nanoparticle aggregates for high capacity Li^+-ion storage. *Chemistry of Materials*, 20(5):1841–1846, 2008.

[29] J. Doke. `www.mathworks.com/matlabcentral/fileexchange/7173-grabit`, Retrieved in 2017.

[30] J. Dölle. *Investigation of Si/C-based anodes for Li-ion batteries.* PhD thesis, 2014.

[31] J. D. Eshelby. The force on an elastic singularity. *Philosophical Transactions of the Royal Society of London. Series A, Mathematical and Physical Sciences*, 244(877):87–112, 1951.

[32] S. Esmizadeh, H. Haftbaradaran, and F. Mossaiby. An investigation of the critical conditions leading to deintercalation induced fracture in two-phase elastic electrode particles using a moving interphase core-shell model. *European Journal of Mechanics, A/Solids*, 74:96–111, 2019.

[33] R. D. Falgout and U. M. Yang. hypre: A library of high performance preconditioners. In *International Conference on Computational Science*, pages 632–641. Springer, 2002.

[34] F. Fan, S. Huang, H. Yang, M. Raju, D. Datta, V. B. Shenoy, A. C. T. Van Duin, S. Zhang, and T. Zhu. Mechanical properties of amorphous $\mathrm{Li_xSi}$ alloys: a reactive force field study. *Modelling and Simulation in Materials Science and Engineering*, 21(7):074002, 2013.

[35] S. Fang, L. Shen, G. Xu, P. Nie, J. Wang, H. Dou, and X. Zhang. Rational design of void-involved $\mathrm{Si@TiO_2}$ nanospheres as high-performance anode material for lithium-ion batteries. *ACS Applied Materials & Interfaces*, 6(9):6497–6503, 2014.

[36] A. Fischer. A special newton-type optimization method. *Optimization*, 24(3-4):269–284, 1992.

[37] D. M. Follstaedt, J. A. Knapp, and S. M. Myers. Mechanical properties of ion-implanted amorphous silicon. *Journal of Materials Research*, 19(1):338–346, 2004.

[38] J. M. Foster, S. J. Chapman, G. Richardson, and B. Protas. A mathematical model for mechanically-induced deterioration of the binder in lithium-ion electrodes. *SIAM Journal on Applied Mathematics*, 77(6):2172–2198, 2017.

[39] J. M. Foster, X. Huang, M. Jiang, S. J. Chapman, B. Protas, and G. Richardson. Causes of binder damage in porous battery electrodes and strategies to prevent it. *Journal of Power Sources*, 350:140–151, 2017.

[40] T. F. Fuller, M. Doyle, and J. Newman. Simulation and optimization of the dual lithium ion insertion cell. *Journal of the Electrochemical Society*, 141(1):1–10, 1994.

[41] Y. F. Gao and M. Zhou. Strong stress-enhanced diffusion in amorphous lithium alloy nanowire electrodes. *Journal of Applied Physics*, 109(1):14310, 2011.

[42] Y. F. Gao and M. Zhou. Coupled mechano-diffusional driving forces for fracture in electrode materials. *Journal of Power Sources*, 230:176–193, 2013.

[43] C. Geuzaine and J. Remacle. Gmsh: A 3-D finite element mesh generator with built-in pre- and post- processing facilities. *International Journal for Numerical Methods in Engineering*, 79(11):1309–1331, 2009.

[44] F. Hao and D. Fang. Diffusion-induced stresses of spherical core–shell electrodes in lithium-ion batteries: The effects of the shell and surface/interface stress. *Journal of the Electrochemical Society*, 160(4):A595–A600, 2013.

[45] T. D. Hatchard and J. R. Dahn. In situ XRD and electrochemical study of the reaction of lithium with amorphous silicon. *Journal of The Electrochemical Society*, 151(6):A838, 2004.

[46] M. G. Hennessy and I. R. Moyles. Asymptotic reduction, solution, and homogenisation of a thermo-electrochemical model for a lithium-ion battery. *arXiv preprint arXiv:1907.02775*, 2019.

[47] N. S. Hieu, J. C. Lim, and J. K. Lee. Free-standing silicon nanorods on copper foil as anode for lithium-ion batteries. *Microelectronic Engineering*, 89:138–140, 2012.

[48] P. Howell, G. Kozyreff, and J. Ockendon. *Applied Solid Mechanics*, volume 43. Cambridge University Press, 2009.

[49] L. Hu, H. Wu, Y. Gao, A. Cao, H. Li, J. McDough, X. Xie, M. Zhou, and Y. Cui. Silicon–carbon nanotube coaxial sponge as Li-ion anodes with high areal capacity. *Advanced Energy Materials*, 1(4):523–527, 2011.

[50] J. Y. Huang, L. Zhong, C. M. Wang, J. P. Sullivan, W. Xu, L. Q. Zhang, S. X. Mao, N. S. Hudak, X. H. Liu, A. Subramanian, F. Hongyou, L. Qi, A. Kushima, and J. Li. In situ observation of the electrochemical lithiation of a single SnO_2 nanowire electrode. *Science*, 330(6010):1515–1520, 2010.

[51] S. Huang, F. Fan, J. Li, S. Zhang, and T. Zhu. Stress generation during lithiation of high-capacity electrode particles in lithium ion batteries. *Acta Materialia*, 61(12):4354–4364, 2013.

[52] P. Jakobsen. Introduction to the method of multiple scales. *arXiv preprint arXiv:1312.3651*, 2013.

[53] Z. Jia and W. K. Liu. Analytical model on stress-regulated lithiation kinetics and fracture of Si–C yolk–shell anodes for lithium-ion batteries. *Journal of The Electrochemical Society*, 163(6):A940–A946, 2016.

[54] J. Kierzenka and L. F. Shampine. A bvp solver that controls residual and error. *Journal of Numerical Analysis, Industrial and Applied Mathematics*, 3(1-2):27–41, 2008.

[55] H. Kim, M. Seo, M. Park, and J. Cho. A critical size of silicon nano-anodes for lithium rechargeable batteries. *Angewandte Chemie International Edition*, 49(12):2146–2149, 2010.

[56] K. Kumaresan, G. Sikha, and R. E. White. Thermal model for a Li-ion cell. *Journal of the Electrochemical Society*, 155(2):A164–A171, 2008.

[57] W. Lai and F. Ciucci. Mathematical modeling of porous battery electrodes–Revisit of Newman's model. *Electrochimica Acta*, 56(11):4369–4377, 2011.

[58] F. Larché and J. W. Cahn. A linear theory of thermochemical equilibrium of solids under stress. *Acta Metallurgica*, 21(8):1051–1063, 1973.

[59] C. Laslau, L. Xie, and C. Robinson. The next-generation battery roadmap: Quantifying how solid-state, lithium-sulfur, and other batteries will emerge after 2020. *Presentation*, 2015.

[60] J. Li and J. R. Dahn. An in situ X-ray diffraction study of the reaction of Li with crystalline Si. *Journal of The Electrochemical Society*, 154(3):A156–A161, 2007.

[61] J. Liu. Addressing the grand challenges in energy storage. *Advanced Functional Materials*, 23(8):924–928, 2013.

[62] L. Liu, J. Lyu, T. Li, and T. Zhao. Well-constructed silicon-based materials as high-performance lithium-ion battery anodes. *Nanoscale*, 8(2):701–722, 2016.

[63] N. Liu, Z. Lu, J. Zhao, M. T. McDowell, H. Lee, W. Zhao, and Y. Cui. A pomegranate-inspired nanoscale design for large-volume-change lithium battery anodes. *Nature Nanotechnology*, 9(3):187–192, 2014.

[64] N. Liu, H. Wu, M. T. McDowell, Y. Yao, C. M. Wang, and Y. Cui. A yolk–shell design for stabilized and scalable Li-ion battery alloy anodes. *Nano Letters*, 12(6):3315–3321, 2012.

[65] X. H. Liu, F. Fan, H. Yang, S. Zhang, J. Y. Huang, and T. Zhu. Self-limiting lithiation in silicon nanowires. *ACS Nano*, 7(2):1495–1503, 2013.

[66] X. H. Liu, L. Zhong, S. Huang, S. X. Mao, T. Zhu, and J. Y. Huang. Size-dependent fracture of silicon nanoparticles during lithiation. *ACS Nano*, 6(2):1522–1531, 2012.

[67] Y. Liu, L. Pengyu, M. Jun, B. Ruobing, and L. D. Hui. Stress fields in hollow core–shell spherical electrodes of lithium-ion batteries. *Proceedings of the Royal Society A: Mathematical, Physical and Engineering Sciences*, 470(2172):1–20, 2014.

[68] X. W. Lou, Y. Wang, C. Yuan, J. Y. Lee, and L. A. Archer. Template-free synthesis of SnO_2 hollow nanostructures with high lithium storage capacity. *Advanced Materials*, 18(17):2325–2329, 2006.

[69] A. Magasinski, P. Dixon, B. Hertzberg, A. Kvit, J. Ayala, and G. Yushin. High-performance lithium-ion anodes using a hierarchical bottom-up approach. *Nature Materials*, 9(4):353–358, 2010.

[70] L. G. B. Manhani, L. C. Pardini, and N. F. Levy. Assessement of tensile strength of graphites by the iosipescu coupon test. *Materials Research*, 10(3):233–239, 2007.

[71] S. G. Marquis, V. Sulzer, R. Timms, C. P. Please, and S. J. Chapman. An asymptotic derivation of a single particle model with electrolyte. *arXiv preprint arXiv:1905.12553*, 2019.

[72] M. T. McDowell, S. W. Lee, J. T. Harris, B. A. Korgel, C. Wang, W. D. Nix, and Y. Cui. In situ TEM of two-phase lithiation of amorphous silicon nanospheres. *Nano Letters*, 13(2):758–764, 2013.

[73] M. T. McDowell, I. Ryu, S. W. Lee, C. Wang, W. D. Nix, and Y. Cui. Studying the kinetics of crystalline silicon nanoparticle lithiation with in situ transmission electron microscopy. *Advanced Materials*, 24(45):6034–6041, 2012.

[74] D. D. Morrison, J. D. Riley, and J. F. Zancanaro. Multiple shooting method for two-point boundary value problems. *Communications of the ACM*, 5(12):613–614, 1962.

[75] A. Mukhopadhyay and B. W. Sheldon. Deformation and stress in electrode materials for Li-ion batteries. *Progress in Materials Science*, 63:58–116, 2014.

[76] S. Nejad, D. T. Gladwin, and D. A. Stone. A systematic review of lumped-parameter equivalent circuit models for real-time estimation of lithium-ion battery states. *Journal of Power Sources*, 316:183–196, 2016.

[77] J. Newman and K. E. Thomas-Alyea. *Electrochemical Systems*. John Wiley & Sons, 2012.

[78] J. Newman and W. Tiedemann. Porous-electrode theory with battery applications. *AIChE Journal*, 21(1):25–41, 1975.

[79] Nexeon. Nexeon - About Li-ion batteries: `www.nexeon.co.uk/technology-2/about-li-ion-batteries`, Accessed on 18/07/2017.

[80] G. Ning and B. N. Popov. Cycle life modeling of lithium-ion batteries. *Journal of The Electrochemical Society*, 151(10):A1584–A1591, 2004.

[81] C. Ouyang and L. Q. Chen. Physics towards next generation Li secondary batteries materials: A short review from computational materials design perspective. *Science China Physics, Mechanics and Astronomy*, 56(12):2278–2292, 2013.

[82] C. R. Pals and J. Newman. Thermal modeling of the lithium/polymer battery I. discharge behavior of a single cell. *Journal of the Electrochemical Society*, 142(10):3274–3281, 1995.

[83] M. Park, K. Kim, J. Kim, and J. Cho. Flexible dimensional control of high-capacity Li-ion battery anodes: From 0D hollow to 3D porous germanium nanoparticle assemblies. *Advanced Materials*, 22(3):415–418, 2010.

[84] M. B. Pinson and M. Z. Bazant. Theory of SEI formation in rechargeable batteries: capacity fade, accelerated aging and lifetime prediction. *Journal of the Electrochemical Society*, 160(2):A243–A250, 2013.

[85] Y. Qi, H. Guo, L. G. Hector, and A. Timmons. Threefold increase in the Young's modulus of graphite negative electrode during lithium intercalation. *Journal of The Electrochemical Society*, 157(5):A558–A566, 2010.

[86] Y. Qi, L. G. Hector, C. James, and K. J. Kim. Lithium concentration dependent elastic properties of battery electrode materials from first principles calculations. *Journal of The Electrochemical Society*, 161(11):F3010–F3018, 2014.

[87] A. M. Ramos and C. P. Please. Some comments on the Butler–Volmer equation for modeling lithium-ion batteries. *arXiv preprint arXiv:1503.05912*, 2015.

[88] Y. Reynier, R. Yazami, and B. Fultz. The entropy and enthalpy of lithium intercalation into graphite. *Journal of Power Sources*, 119-121:850–855, 2003.

[89] G. Richardson, G. Denuault, and C. P. Please. Multiscale modelling and analysis of lithium-ion battery charge and discharge. *Journal of Engineering Mathematics*, 72(1):41–72, 2012.

[90] G. Richardson, I. Korotkin, R. Ranom, R. Castle, and J. M. Foster. Generalised single particle models for high-rate operation of graded lithium-ion electrodes: systematic derivation and validation. *arXiv preprint arXiv:1907.09410*, 2019.

[91] E. Roduner. Size matters: why nanomaterials are different. *Chemical Society Reviews*, 35(7):583–592, 2006.

[92] I. Ryu, J. W. Choi, Y. Cui, and W. D. Nix. Size-dependent fracture of Si nanowire battery anodes. *Journal of the Mechanics and Physics of Solids*, 59(9):1717–1730, 2011.

[93] Y. Saad. A flexible inner-outer preconditioned GMRES algorithm. *SIAM Journal on Scientific Computing*, 14(2):461–469, 1993.

[94] S. Santhanagopalan, Q. Guo, P. Ramadass, and R. E. White. Review of models for predicting the cycling performance of lithium-ion batteries. *Journal of Power Sources*, 156(2):620–628, 2006.

[95] A. Sarkar, P. Shrotriya, and A. Chandra. Fracture modeling of lithium-silicon battery based on variable elastic moduli. *Journal of The Electrochemical Society*, 164(11):E3606–E3612, 2017.

[96] M. Seo, M. Park, K. T. Lee, K. Kim, J. Kim, and J. Cho. High performance Ge nanowire anode sheathed with carbon for lithium rechargeable batteries. *Energy & Environmental Science*, 4(2):425–428, 2011.

[97] V. A. Sethuraman, V. Srinivasan, A. F. Bower, and P. R. Guduru. In situ measurements of stress-potential coupling in lithiated silicon. *Journal of The Electrochemical Society*, 157(11):A1253–A1261, 2010.

[98] Vijay A. Sethuraman, M. J. Chon, M. Shimshak, V. Srinivasan, and P. R. Guduru. In situ measurements of stress evolution in silicon thin films during electrochemical litiation and delithiation. *Journal of Power Sources*, 195(15):5062–5066, 2010.

[99] V. B. Shenoy, P. Johari, and Y. Qi. Elastic softening of amorphous and crystalline Li–Si phases with increasing Li concentration: a first-principles study. *Journal of Power Sources*, 195(19):6825–6830, 2010.

[100] S. Shi, J. Gao, Y. Liu, Y. Zhao, Q. Wu, W. Ju, C. Ouyang, and R. Xiao. Multiscale computation methods: Their applications in lithium-ion battery research and development. *Chinese Physics B*, 25(1):018212, 2015.

[101] H. Song, Z. Cao, X. Chen, H. Lu, M. Jia, Z. Zhang, Y. Lai, J. Li, and Y. Liu. Capacity fade of $LiFePO_4$/graphite cell at elevated temperature. *Journal of Solid State Electrochemistry*, 17(3):599–605, 2013.

[102] J. Song, S. Chen, M. Zhou, T. Xu, D. Lv, M. L. Gordin, T. Long, M. Melnyk, and D. Wang. Micro-sized silicon–carbon composites composed of carbon-coated sub-10nm Si primary particles as high-performance anode materials for lithium-ion batteries. *Journal of Materials Chemistry A*, 2(5):1257–1262, 2014.

[103] T. Song, J. Xia, J. H. Lee, D. H. Lee, M. S. Kwon, J. M. Choi, J. Wu, S. K. Doo, H. Chang, W. I. Park, D. S. Zang, H. Kim, Y. Huang, K. C. Hwang, J. A. Rogers, and U. Paik. Arrays of sealed silicon nanotubes as anodes for lithium-ion batteries. *Nano Letters*, 10(5):1710–1716, 2010.

[104] R. Stojanovic, S. Djuric, and L. Vujoševic. On finite thermal deformations. *Archives of Mechanics*, 16:103–108, 1964.

[105] N. Swaminathan, J. Qu, and Y. Sun. An electro-chemo-mechanical theory of defects in ionic solids. Part II. Examples. *Philosophical Magazine*, 87(11):1723–1742, 2007.

[106] K. Takahashi, K. Higa, S. Mair, M. Chintapalli, N. Balsara, and V. Srinivasan. Mechanical degradation of graphite/PVDF composite electrodes: a model–experimental study. *Journal of The Electrochemical Society*, 163(3):A385–A395, 2016.

[107] K. Takahashi and V. Srinivasan. Examination of graphite particle cracking as a failure mode in lithium-ion batteries: a model-experimental study. *Journal of The Electrochemical Society*, 162(4):A635–A645, 2015.

[108] A. Wang, S. Kadam, H. Li, S. Shi, and Y. Qi. Review on modeling of the anode solid electrolyte interphase (SEI) for lithium-ion batteries. *npj Computational Materials*, 4(1):15, 2018.

[109] C. Wang, Z. Ma, Y. Wang, and C. Lu. Failure prediction of high-capacity electrode materials in lithium-ion batteries. *Journal of The Electrochemical Society*, 163(7):A1157–A1163, 2016.

[110] C. Wang, H. Wu, Z. Chen, M. T. McDowell, Y. Cui, and Z. Bao. Self-healing chemistry enables the stable operation of silicon microparticle anodes for high-energy lithium-ion batteries. *Nature Chemistry*, 5(12):1042–8, 2013.

[111] J. W. Wang, Y. He, F. Fan, X. H. Liu, S. Xia, Y. Liu, C. T. Harris, H. Li, J. Y. Huang, S. X. Mao, and Z. Ting. Two-phase electrochemical lithiation in amorphous silicon. *Nano Letters*, 13(2):709–715, 2013.

[112] J. W. Wang, H. Luo, Y. Liu, Y. He, F. Fan, Z. Zhang, S. X. Mao, C. Wang, and T. Zhu. Tuning the outward to inward swelling in lithiated silicon nanotubes via surface oxide coating. *Nano Letters*, 2016.

[113] M. Wang and X. Xiao. Investigation of the chemo-mechanical coupling in lithiation/delithiation of amorphous Si through simulations of Si thin films and Si nanospheres. *Journal of Power Sources*, 326:365–376, 2016.

[114] B. Wu. *Modeling and design of lithium-ion batteries: Mechanics and electrochemistry.* PhD thesis, 2019.

[115] B. Wu and W. Lu. Mechanical modeling of particles with active core–shell structures for lithium-ion battery electrodes. *The Journal of Physical Chemistry C*, 121(35):19022–19030, 2017.

[116] B. Wu and W. Lu. A consistently coupled multiscale mechanical–electrochemical battery model with particle interaction and its validation. *Journal of the Mechanics and Physics of Solids*, 125:89–111, 2019.

[117] C. H. Wu. The role of Eshelby stress in composition-generated and stress-assisted diffusion. *Journal of the Mechanics and Physics of Solids*, 49(8):1771–1794, 2001.

[118] H. Wu, Z. Xie, Y. Wang, C. Lu, and Z. Ma. Modeling diffusion-induced stress on two-phase lithiation in lithium-ion batteries. *European Journal of Mechanics, A/Solids*, 71(April):320–325, 2018.

[119] H. Wu, G. Zheng, N. Liu, T. J. Carney, Y. Yang, and Y. Cui. Engineering empty space between Si nanoparticles for lithium-ion battery anodes. *Nano Letters*, 12(2):904–909, 2012.

[120] C. Xu, L. Weng, B. Chen, J. Zhou, and R. Cai. An analytical model for the fracture behavior in hollow cylindrical anodes. *International Journal of Mechanical Sciences*, 157:87–97, 2019.

[121] Y. Xu, G. Yin, Y. Ma, P. Zuo, and X. Cheng. Nanosized core/shell silicon@carbon anode material for lithium-ion batteries with polyvinylidene fluoride as carbon source. *Journal of Materials Chemistry*, 20(16):3216–3220, 2010.

[122] H. Yang, S. Sun, and C. Yang. Nonlinearly preconditioned semismooth newton methods for variational inequality solution of two-phase flow in porous media. *Journal of Computational Physics*, 332:1–20, 2017.

[123] S. Yoon, C. Park, and H. Sohn. Electrochemical characterizations of germanium and carbon-coated germanium composite anode for lithium-ion batteries. *Electrochemical and Solid-State Letters*, 11(4):A42–A45, 2008.

[124] M. Yoshio, H. Wang, K. Fukuda, T. Umeno, N. Dimov, and Z. Ogumi. Carbon-coated Si as a lithium-ion battery anode material. *Journal of The Electrochemical Society*, 149(12):A1598, 2002.

[125] P. Yu, B. N. Popov, J. A. Ritter, and R. E. White. Determination of the lithium-ion diffusion coefficient in graphite. *Journal of The Electrochemical Society*, 146(1):8–14, 1999.

[126] M. R. Zamfir, H. T. Nguyen, E. Moyen, Y. H. Lee, and D. Pribat. Silicon nanowires for Li-based battery anodes: a review. *Journal of Materials Chemistry A*, 1(34):9566–9586, 2013.

[127] L. Zhan, Y. Wang, W. Qiao, L. Ling, and S. Yang. Hollow carbon spheres with encapsulation of Co_3O_4 nanoparticles as anode material for lithium-ion batteries. *Electrochimica Acta*, 78:440–445, 2012.

[128] K. Zhang, Y. Li, J. Wu, B. Zheng, and F. Yang. Lithiation-induced buckling of wire-based electrodes in lithium-ion batteries: A phase-field model coupled with large deformation. *International Journal of Solids and Structures*, 144-145:289–300, 2018.

[129] T. Zhang, D. Li, Z. Tao, and J. Chen. Understanding electrode materials of rechargeable lithium batteries via DFT calculations. *Progress in Natural Science: Materials International*, 23(3):256–272, 2013.

[130] W. Zhang. A review of the electrochemical performance of alloy anodes for lithium-ion batteries. *Journal of Power Sources*, 196(1):13–24, 2011.

[131] X. Zhang, W. Shyy, and A. M. Sastry. Numerical simulation of intercalation-induced stress in Li-ion battery electrode particles. *Journal of the Electrochemical Society*, 154(10):A910–A916, 2007.

[132] K. Zhao, M. Pharr, L. Hartle, J. J. Vlassak, and Z. Suo. Fracture and debonding in lithium-ion batteries with electrodes of hollow core–shell nanostructures. *Journal of Power Sources*, 218:6–14, 2012.

[133] K. Zhao, M. Pharr, Q. Wan, W. L. Wang, E. Kaxiras, J. J. Vlassak, and Z. Suo. Concurrent reaction and plasticity during initial lithiation of crystalline silicon in lithium-ion batteries. *Journal of The Electrochemical Society*, 159(3):A238–A243, 2012.

[134] K. Zhao, G. A. Tritsaris, M. Pharr, W. L. Wang, O. Okeke, Z. Suo, J. J. Vlassak, and E. Kaxiras. Reactive flow in silicon electrodes assisted by the insertion of lithium. *Nano Letters*, 12(8):4397–4403, 2012.

[135] Y. Zhao, P. Stein, Y. Bai, M. Al-Siraj, Y. Yang, and B. Xu. A review on modeling of electro-chemo-mechanics in lithium-ion batteries. *Journal of Power Sources*, 413:259–283, 2019.

[136] Y. Zhao, B. Xu, P. Stein, and D. Gross. Phase-field study of electrochemical reactions at exterior and interior interfaces in Li-ion battery electrode particles. *Computer Methods in Applied Mechanics and Engineering*, 312:428–446, 2016.

[137] J. Zhu, J. Zhou, B. Chen, and T. Liu, Z.and Liu. Dislocation effect on diffusion-induced stress for lithiation in hollow spherical electrode. *Journal of Solid State Electrochemistry*, 20(1):37–46, 2016.

[138] Y. Zhu, F. Xu, Q. Qin, W. Y. Fung, and W. Lu. Mechanical properties of vapor–liquid–solid synthesized silicon nanowires. *Nano Letters*, 9(11):3934–3939, 2009.

[139] C. Zou, L. Zhang, X. Hu, Z. Wang, T. Wik, and M. Pecht. A review of fractional-order techniques applied to lithium-ion batteries, lead-acid batteries, and supercapacitors. *Journal of Power Sources*, 390:286–296, 2018.

[140] X. Zuo, J. Zhu, P. Müller-Buschbaum, and Y. Cheng. Silicon based lithium-ion battery anodes: A chronicle perspective review. *Nano Energy*, 31:113–143, 2017.